



## Department of Precision and Microsystems Engineering

### Design of a membrane for a lung-on-a-chip device.

S.A.M. den Boer

Report no : 2022.072  
Supervisor 1 : Prof. Dr. U. Staufer  
Supervisor 2 : Dr. M. Mastrangeli  
Specialisation : MNE  
Type of report : Thesis Report  
Date : 18 October 2022





# Design of a membrane for a lung-on-chip device

Design and testing of a membrane concept incorporating a dynamic pore size to study the alveolar-capillary barrier *in vitro*.

S.A.M. den Boer

to obtain the degree of Master of Science  
in Mechanical Engineering and Biomedical Engineering  
at the Delft University of Technology,  
to be defended publicly on Monday October 31, 2022 at 12:30 PM.

Student number:	4469178
Project duration:	September 5, 2021 – October 31, 2022
Thesis committee:	Prof. dr. U. Staufer, TU Delft, Chairman
	Dr. ir. M. Mastrangeli, TU Delft, Supervisor
	Prof. dr. R. Rottier, Erasmus Medical Center, External supervisor
	Dr. P. Boukany, TU Delft, Committee member
	Dr. E. Fratila-Apachitei, TU Delft, Committee member

An electronic version of this thesis is available at <http://repository.tudelft.nl/>.





# Preface

This master thesis report is the final part of an Individual Double Degree master's program combining Mechanical Engineering (High Tech Engineering) and Biomedical Engineering (Medical Devices) at the Delft University of Technology. The project was conducted in collaboration with the Erasmus Medical Center in Rotterdam. The project and research covered in this report have not been without the occasional hurdles, and the guidance and advice of my supervisors, PhD candidates, fellow students, and family and friends have been immensely appreciated. Therefore, I would like to thank the following people in particular.

First, I would like to thank my main supervisors. Prof. Urs Staufer, my supervisor from High Tech Engineering, and Dr. Massimo Mastrangeli, my supervisor from Biomedical Engineering, thank you for your continuous support and attention. I greatly appreciated our discussions on this fascinating topic during our weekly meetings. From the Erasmus Medical Center, I would like to thank Prof. Robbert Rottier very much for all your helpful insights into the world of cell cultures and lung physiology. It was always a warm welcome at the EMC, and no question was too simple to ask.

Furthermore, I would like to thank Dr. Clémentine Boutry for your endless enthusiasm and our discussions on POMaC. It has been indispensable for the course of this research. I would also like to thank Eveline Matroos for your help and commitment to organising everything surrounding the master.

From the Erasmus Medical Center, I would like to thank Cinta Iriondo Martinez, Floor Benthem and Kari-Pekka Skarp for sharing your knowledge on setting up cell cultures. From the TU Delft, I would like to thank Pieter van Altena for your help with the Nanoindenter. Ahmed Sharaf, for your expertise with the Nanoscribe and the HMDS coating. Moreover, I want to thank all not yet mentioned lab staff in the EMC, EKL and 3ME laboratories for helping me find, order and handle the chemicals, setting up the experiments and sharing knowledge.

Lastly, the support and encouragement of family and friends were greatly appreciated and helped during the more challenging parts of the project.

Thank you all, and I do not doubt that I will see you soon!

*S.A.M. den Boer  
Delft, October 2022*



# Abstract

*In vitro* models are fundamental in studying cell behaviour, the physiological function of organs, and their response to drugs and toxins [1–3]. However, the shortage of accurate and reliable *in vitro* models calls for the development of *in vitro* lung models that better recapitulate lung physiology and pathology [2, 4]. Lung-on-a-chip models are promising alternatives to animal and traditional *in vitro* models [5–10]. To date, most membranes used in these models are made of poly(dimethylsiloxane), which has significant disadvantages, such as high ad- and absorption of small molecules [2, 5]. Moreover, there is a need to establish adequate membrane pore sizes throughout the cell culture duration. This study aims to design and test the viability of a novel LOC membrane containing a dynamic membrane pore size to recapitulate the pulmonary alveolar-capillary barrier. The possibility of fabricating a membrane with an adjustable pore size is investigated to allow for confluent monolayer formation, while also providing immune cell migration across the membrane.

Poly(octamethylene maleate (anhydride) citrate) (POMaC) is evaluated as a membrane material due to its versatility, elasticity and degradation properties. Several aspects are studied to evaluate the concept. The first aspect is whether spincoating could be a fabrication method for creating a uniform thin film. Second, it is evaluated whether conical pillars printed with 2-photon polymerization could serve as a mould on the substrate to create the pores. Third, the cytotoxicity of POMaC for primary lung cells is evaluated with a toxicity assay using eluates. Furthermore, POMaC is a very versatile material, and its mechanical properties differ significantly with different monomer ratios and curing methods. Therefore, the stiffness properties, degradation rate and imaging properties are evaluated. Stiffness is evaluated by nanoindentation measurements, degradability is measured optically under static and dynamic flow conditions, and the imaging properties are evaluated optically and using autofluorescence measurements. Lastly, membrane integration is studied using various bonding methods, including oxygen plasma.

The results show that POMaC can be spincoated into  $\sim 13\text{ }\mu\text{m}$  thin, uniform layers and detached from the substrate. Furthermore, well shaped pillars that could be used as a structural mould can be created. These results provide promising support for a combination of fabricating and detaching a thin membrane while utilising the coned pillars. The stiffness was in the expected range, and the bioimaging properties were found to be suitable. The degradation results did not support the hypothesis that a structural pore size could increase, which likely impedes the increase of pore diameter necessary for immune cell transmigration. POMaC exhibited layer-by-layer softening and swelling. A model of the degradation characteristics of POMaC is proposed. Furthermore, alternative approaches for creating a membrane with a dynamic pore size are introduced. Additionally, more research is advised to be conducted on the cytotoxicity of POMaC to primary lung cells. If a dynamical pore size could successfully be incorporated in a thin membrane on which both epithelial and endothelial cells can be grown, it would be a big step forward in *in vitro* cell culture studies.





# Contents

Preface	iii
Abstract	v
Nomenclature	xi
1 Introduction	1
1.1 The alveolar-capillary barrier . . . . .	2
1.2 The LOC environment . . . . .	3
1.3 State-of-the-art in LOC . . . . .	4
1.4 Research question . . . . .	4
1.5 Report structure. . . . .	5
2 Background theory	7
2.1 Lung physiology . . . . .	7
2.2 Cell types used for in vitro modelling. . . . .	9
2.3 In vitro lung models . . . . .	11
2.3.1 State-of-the-art . . . . .	12
2.3.2 Prior work in the PME group. . . . .	13
2.4 LOC membrane requirements . . . . .	14
2.5 Membrane material. . . . .	20
2.5.1 The downside of PDMS membranes . . . . .	20
2.5.2 An alternative material: POMaC . . . . .	21
2.5.2.1 Background information . . . . .	22
2.5.2.2 Additional material specifications . . . . .	27
2.6 Membrane fabrication . . . . .	29
2.6.1 Fabricating pores . . . . .	29
2.6.2 Membrane integration methods . . . . .	31
3 Concept introduction	33
4 Methodology	37
4.1 Synthesizing POMaC . . . . .	37
4.2 POMaC moulding. . . . .	38
4.2.1 Moulding POMaC in a 3D printed mould . . . . .	39
4.2.2 Moulding POMaC in a PDMS mould . . . . .	39
4.3 Spincoating POMaC. . . . .	39
4.4 Pillar fabrication by 2PP-printing . . . . .	41
4.5 POMaC stiffness quantification . . . . .	43
4.6 POMaC degradation . . . . .	44
4.7 POMaC bonding . . . . .	47
4.8 POMaC cytotoxicity assay. . . . .	48
4.8.1 Sample dimensions . . . . .	48
4.8.2 Mould fabrication . . . . .	49
4.8.3 POMaC sample fabrication . . . . .	49
4.8.4 Cell culture protocol . . . . .	50
4.9 Autofluorescence of POMaC . . . . .	51
5 Results	53
5.1 POMaC synthesis and curing . . . . .	53
5.2 POMaC moulding . . . . .	53

5.3	Spincoating . . . . .	54
5.3.1	Layer thickness . . . . .	55
5.4	Micropillar fabrication . . . . .	57
5.5	POMaC stiffness quantification . . . . .	61
5.6	Degradation. . . . .	64
5.7	POMaC bonding . . . . .	66
5.8	Cytotoxicity of POMaC and photoinitiators . . . . .	66
5.9	Autofluorescence of POMaC . . . . .	68
6	Discussion . . . . .	71
6.1	Interpretation of findings . . . . .	71
6.2	A broader view . . . . .	78
7	Conclusion . . . . .	81
A	Methodology . . . . .	85
A.1	Detailed drawing of 3D-printed moulds. . . . .	85
A.1.1	POMaC and PDMS moulding . . . . .	85
A.1.2	Toxicity assay . . . . .	86
A.1.3	Degradability assessment . . . . .	87
A.2	Overview of several spincoating experiments . . . . .	89
A.3	Substrate priming methodology . . . . .	90
A.3.1	PTFE priming procedure. . . . .	90
A.3.2	HMDS priming procedure . . . . .	90
A.3.3	Pluronic F-127 priming procedure for spincoating. . . . .	90
A.4	Overview of dose test parameters . . . . .	91
A.5	Calculations of biodegradability mould dimensions . . . . .	92
A.6	Calculations of toxicology mould dimensions. . . . .	93
A.7	Exposure times in autofluorescence testing. . . . .	94
B	DeScribe Code . . . . .	95
B.1	singlemouldpillardata.gwl . . . . .	95
B.2	Dose test 1 . . . . .	96
B.3	Dose test 2 . . . . .	97
B.4	Dose test 3 . . . . .	98
B.5	Dose test 4 . . . . .	99
B.5.1	Main code . . . . .	99
B.5.2	Additional codes . . . . .	100
B.6	Dose test 5 . . . . .	106
B.6.1	Main code . . . . .	106
B.6.2	Additional codes . . . . .	106
B.7	Array test 1 . . . . .	114
B.7.1	Main code . . . . .	114
B.7.2	Additional code . . . . .	115
B.8	Array test 2 . . . . .	116
B.8.1	Main code . . . . .	116
B.8.2	Additional code . . . . .	117
B.9	Array test 3 . . . . .	118
B.10	Array test 4 . . . . .	119
C	Results . . . . .	121
C.1	Profilometry measurement results . . . . .	121
C.1.1	Matlab code for mean thickness calculation . . . . .	121
C.1.2	Images of the areas used in the profilometry measurement . . . . .	125
C.2	Matlab code for effective Young's modulus calculation . . . . .	127
C.3	Toxicology cell culture results . . . . .	129
C.4	Autofluorescence results for the 1 mm thick samples . . . . .	131



---

D	Future research	135
D.1	Fabrication of a membrane containing a pillar imprint . . . . .	135
D.2	Permeability measurement . . . . .	136
	Bibliography	137
E	Literature Review	145



# Nomenclature

Table 1: List of abbreviations.

Abbreviation	Description
2PP	2-photon polymerization
AE cells	Tracheo-bronchial epithelial cells
AETI	Alveolar Epithelial Type 1 cells (squamous)
AETII	Alveolar Epithelial Type 2 cells (cuboidal)
ALI	Air-liquid interface
AOC	Alveoli-on-a-chip
Calu-3 cells	Human airway epithelial cells
CE	Collagen-elastin
cFBs	Human cardiac fibroblasts
COPD	Chronic obstructive pulmonary disease
DI water	Deionized water
DMEM	Dulbecco's Modified Eagle's Medium
DMSO	Dimethylsulfoxide
ECM	Extracellular matrix
EKL	Else Kooi Lab
EMC	Erasmus Medical Center
EPOMaC	Ester bond crosslinked POMaC
EPPOMaC	Ester bond crosslinked photopolymerized POMaC
FDA	Food and drug administration
FEPM	Tetrafluoroethylene-propylene
GelMa	Gelatin methacrylate
hAECs	Primary human airway epithelial cells
hBSMC	Human bronchial smooth muscle cells
HDI	1,6-hexamethylene diisocyanate
hESCs	Human embryonic stem cells
HMDS	Hexamethyldisilazane
hMSCs	Human mesenchymal stem cells
HMVEC-L	Primary human lung microvascular endothelial cells
HPMEC	Human pulmonary microvascular endothelial cells
HUVEC	Primary human umbilical vein endothelial cells
$I_{UV}$	Intensity of the UV point source
IL-8	Interleukin-8
IPA	Isopropanol
iPSC	Induced pluripotent stem cells
Irgacure 2959	2-hydroxy-1-[4(hydroxyethoxy)phenyl]-2-methyl-1 propanone
ITO	Indium-tin oxide
KSFM	Keratinocyte Serum-Free Growth Medium
LFS	Low Force Stereolithography
LOC	Lung-on-a-chip
LP	Laser power
MCAF/MCP-1	Monocyte chemotactic and activating factor
NSL	Nanosphere lithography
OOc	Organ-on-a-chip
PBEC	Primary human bronchial epithelial cells



---

PBS	Phosphate buffered saline solution
PC	polycarbonate
PCL	poly( $\epsilon$ )-caprolactone
PDMS	Poly(dimethylsiloxane)
PEG	Polyethylene glycol
PEGDA	Polyethylene glycol diacrylate
PET	Polyethylene terephthalate
PGA	Poly(glycolide)
PGMEA	Propylene glycol monomethyl ether acetate
PGS	Poly(glycerol sebacate)
PGSA	Poly(glycerol sebacate) acrylate
pH-PAEC	Primary human pulmonary alveolar epithelial cells
PICO	Itaconic acid-crosslinked poly(octamethylene citrate)
PLA	Poly(lactic acid)
PLGA	Poly(lactic-co-glycolic acid)
PLLA	Poly(L-lactide)
PME	Department of Precision and Microsystems Engineering
PMNs	Polymorphonuclear neutrophils
POC	Poly(octamethylene citrate)
POMaC	Poly(octamethylene maleate (anhydride) citrate)
POMaC, 2.5h	POMaC synthesized for 2.5 hours
POMaC, 3h	POMaC synthesized for 3 hours
PPOMaC	Photopolymerized POMaC
Pre-POMaC	POMaC prepolymer
PTFE	Poly(tetrafluoroethylene) (Teflon)
SEBS	Styrene-ethylene-butylene-styrene
SEI	Secondary electron imaging
SEM	Scanning electron microscope
SLA	Stereolithography
SS	Scanning speed
TEER	Transepithelial electrical resistance
TPO	Diphenyl-2,4,6-trimethyl benzoyl phosphine oxide
UV	Ultraviolet
VSI	Vertical Scanning Interferometry
WCA	Water contact angle

---

# Introduction

Among the leading causes of death worldwide are lung diseases [4]. The gas-exchanging region of the lungs is the human body's largest internal surface area directly exposed to the external environment. It is, besides being a vital aspect of human life, also a region susceptible to disease and injury [11]. In recent years it has become evident that the emergence of respiratory viruses, such as SARS-CoV-2, can have an enormous impact on society [4]. This further emphasizes the relevance of research on lung diseases and physiology [4]. Generally, research is conducted with *in vitro* models, and *in vivo* animal models before clinical trials are conducted. The term *in vitro* describes procedures outside of living organisms, whereas *in vivo* covers research done with or within an entire living organism.

*In vitro* models are fundamental in studying cell behaviour, the physiological function of organs, and their response to drugs and toxins [1–3]. These physiological functions are often hard to determine since there is a shortage of accurate and reliable *in vitro* models [2]. *In vitro* human lung models often fail to recapitulate the *in vivo* environment, and preclinical animal models are increasingly being questioned because of ethical issues and the general lack of predictability for human diseases [4, 6, 10]. One of the main concerns regarding predictability is that animal tissues vary greatly from human tissues concerning their anatomy, immune system, and inflammatory response [12]. Moreover, 90% of preclinical animal studies do not accurately predict the outcome of human clinical trials [13]. Furthermore, the success rate in the clinical phase generally is only about 10% to 20% [3]. This low success rate leads to the disregard of unsuccessful drugs in a late stage of their development, as promising results in these models do not ensure equally successful results in humans [6, 10]. Moreover, potentially successful drugs can be disregarded unnecessarily in the earlier phase of animal and *in vitro* testing. When considering the immense financial expense of drug development and the long development time required, the pressing need for means to quickly and reliably assess drug efficacy and safety at an early stage becomes apparent [6, 14]. Therefore, there is an increasing need for developing *in vitro* lung models that better recapitulate human lung tissue [4].

Traditionally, *in vitro* models are organized mostly as 2D cell cultures, on, for example, Petri dishes or well plates [1, 9]. These cell cultures lack dynamical cues and fail to mimic the complex nature of tissues, as well as the structural, mechanical, and functional properties that this complex nature entails [9, 10]. Furthermore, 2D *in vitro* cultures are generally monocultures [10]. A disadvantage of using a monoculture is that it does not recapitulate accurately, among others, cell morphology, cell division, cell secretion and physiological functions [10]. Apart from 2D cell cultures, 3D cell cultures have been created with cells that are grown in an extracellular matrix (ECM) gel to include more tissue-specific functions [6]. However, these 3D models often fail to accurately capture the functional and structural complexity that *in vivo* tissues exhibit [2, 6]. The architecture and spatial design of 3D models have been limited, and dynamic mechanical and biochemical cues, which are fundamental in organ function and development, are generally not incorporated either [15].

Organ-on-a-chip (OOC) models are promising alternatives for animal models and traditional *in vitro* models [5–10]. The first OOC device mimicking the lungs was the device designed by Huh et al. in 2010 [15]. They defined OOCs as "microfluidic cell cultures with continuously perfused chambers inhabited by living cells arranged to simulate tissue- and organ-level physiology, created with microchip manufacturing" [15, 16].

OOCs allow for precise mimicking of the dynamic micro-environment by incorporating microfluidics, living cells, and dynamical cues *in vitro*. Thereby better recapitulating the *in vivo* tissue-tissue interfaces, the microarchitectures and environments than traditional cell culture systems, and thus facilitating a more accurate prediction of cell behaviour [10]. For example, they allow for mimicking the circulation in the body by allowing continuous perfusion of the cells [9].

So far, various barrier tissue interfaces have been recapitulated by microfluidic models, such as the blood-brain barrier, the gut, and the lungs' blood-air barrier [5]. To date, OOC models, and more specifically lung-on-a-chip (LOC) models, that precisely and effectively reproduce complete drug responses and disease mechanisms, have not been developed [6]. A LOC model indicates any OOC model that recapitulates part of the lung. This study focuses on recapitulating the alveolar-capillary barrier, thus more specifically, on alveoli-on-a-chips (AOCs).

LOC models are currently being used for lung disease modelling, cytotoxicity studies, cancer diagnosis and drug screening assays [11]. Various respiratory diseases that are studied using LOC devices include: lung cancer, pulmonary oedema, pulmonary thrombosis, asthma, chronic obstructive pulmonary disease (COPD), cystic and pulmonary fibrosis, and pulmonary hypertension [10, 17, 18]. LOC models are also used to study the effect of air pollution [3], and emergent respiratory viruses, such as SARS-CoV-2, which can have a significant impact on society [4, 13]. Moreover, LOC models allow the study of lung physiology [3]. A lot of the mechanisms present in the lung are still not well understood, and LOC devices can play a prominent role in helping to discover these physiological mechanisms [3].

### 1.1. The alveolar-capillary barrier

The lungs are the primary organ within the respiratory system. Within the alveoli, they allow oxygen and carbon dioxide exchange through the alveolar-capillary barrier, also known as the respiratory membrane [19] (Fig. 1.1 A). This thin membrane consists of epithelial and endothelial cells on top of a thin fused basement membrane [20]. The alveoli are inflated and deflated during breathing, stretching the respiratory membrane. Lung tissue is subjected to enormous expansions, undergoing strains of 10% to 20% [21].

The alveolar-capillary barrier contains more than 40 different cell types [22, 23]. Facing the capillary lumen, it consists of endothelial cells, and facing the alveolar lumen, it consists of epithelial cells with a surfactant layer [23] (Fig. 1.1 B). Between these two cell layers, the fused basement membranes form the interstitium. This space is made up of various cells, particularly fibroblasts, and an ECM containing elastic fibres, collagen fibrils, and laminin, which provides mechanical integrity [21]. Myofibroblasts span the inter-alveolar septum through pores connecting both sides of this septum, which contributes to the mechanical stability [23]. An innate immune system is also present, as macrophages transit freely around the alveolar lumen, responding to foreign microorganisms [24]. Moreover, white blood cells, such as neutrophils, migrate between the capillary and alveolar lumen [3].

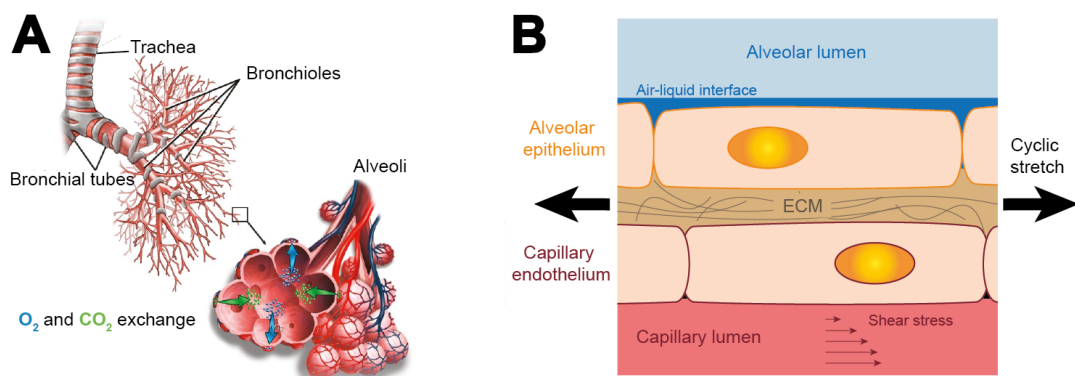


Figure 1.1: Schematic of the lungs and the alveolar-capillary barrier. (A) Overview of the airways and the alveoli [25]. (B) The alveolar-capillary barrier, based on Nonaka et al. [26].

## 1.2. The LOC environment

*In vitro* models need to mimic the *in vivo* environment and its ECM as closely as possible. The effect of breathing, by which a periodic strain is applied to the cells, is deemed to be vital in regulating lung functions [22]. Such a strain can be mimicked by incorporating a flexible polymeric membrane in the LOC and cyclically stretching it [5]. However, so far, this effect has not been intensively modelled [22]. Three-dimensional ECMs have been used to create tissue-specific phenotypes, but their architecture and spatial design have been limited [2]. Dynamic, mechanical, and biochemical cues fundamental in organ function and development and immune characteristics are minimally incorporated as well [2].

Knudsen et al. [23] state that various structural requirements must be met to create efficient oxygen and carbon dioxide diffusion through the barrier. First, a large surface area must be present. Second, the diffusion barrier must be thin since *in vivo*, the alveolar-capillary barrier is about 1  $\mu\text{m}$  thick [23, 27]. Third, the membrane must be stable, which is maintained by the surfactant layer and the connective tissue within the lung. Last, in order to recreate breathing movements, the barrier must be flexible and elastic [23]. Several additional requirements need to be met in a LOC that will be further discussed in Section 2.4.

A simple schematic of an intersection of the membrane environment is shown in Figure 1.2. As stated previously, a cyclic stretch needs to be applied. This stretch can be applied with a frequency of 0.2 Hz, and a strain on the membrane (orange) of 10% to 20%, to mimic normal breathing. On the side of the capillary lumen, a continuous media flow that simulates the blood flow should ideally be present. Whereas, on the side of the alveolar lumen, a constant gas flow, simulating airflow, should ideally be present to implement an air-liquid interface (ALI). An ALI is the combination of the epithelial cells and the surfactant layer, which is secreted by the cells in the presence of air. Both flows exercise shear stress on the cells seeded on the membrane. The mean wall shear stress on endothelial cells in microvessels *in vivo* was found to be 1.54  $\text{N/m}^2$  by Koutsiaris et al. [28]. The shear stress exerted by the airflow is assumed negligible. Furthermore, a thin and porous membrane (indicated in orange) needs to be present to mimic the *in vivo* gas and nutrient exchange [23].

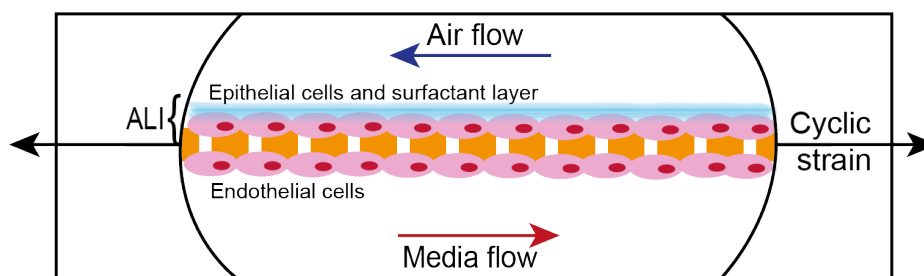


Figure 1.2: Schematic side view of a LOC. The porous membrane is indicated in orange.

To date, most membranes used in LOC models are made of poly(dimethylsiloxane) (PDMS) [2, 5]. PDMS is low cost, elastic, optically transparent, easy to process using soft-lithography, gas permeable and biocompatible [5, 7]. However, it has high adsorption and absorption of small hydrophobic molecules, which limits its application in drug evaluation studies [5, 7, 8]. Moreover, its intrinsic stiffness and molecular composition are distinctly different from alveolar lung tissue [5]. It also has a high water vapour permeability, which causes osmolarity shifts and thus influences homeostasis [8]. Therefore, other materials than PDMS will be analyzed to create a new membrane design. Possible alternative material groups include, for example, thermoplastic polymers, hydrogels and thermoplastic elastomers.

The material included should be elastic, sterilisable and biocompatible to facilitate cell viability. Besides that, the membrane material used should be optically transparent to facilitate high-resolution microscopic analyses for reliable cell characterization and assessment [7, 8]. The device should ideally also allow for cell culture experiments having a duration of minimally two weeks, up to four weeks. Lastly, recovering the used membrane to allow for additional testing of the cultured cells is desired.

### 1.3. State-of-the-art in LOC

Based on the Literature Review, it was found that although there has been much advancement in the field of LOC devices in recent years, there are still many improvements possible in the current designs. First, the use of PDMS as a material in OOCs is undesirable due to its high ad- and absorption of small molecules, which influences the accuracy of drug evaluation studies. The alveolar-capillary barrier that is aimed to be recapitulated is an elastic and exceptionally thin porous barrier. When not using PDMS as a membrane material, only a limited number of studies were able to include a thin ( $\leq 10 \mu\text{m}$ ) membrane. Moreover, alternative materials are often rigid or lack mechanical strength. Generally, membranes created with alternative materials were static and used in short-term cell culture studies.

Second, a significant amount of LOC devices do not include a cyclic stretching of the membrane, a media flow and an ALI simultaneously. Stretching should be included in order to recapitulate the effect of breathing on the cells, and a media flow and ALI should be included to recapitulate the presence of blood flow and air, respectively. Thereby, these LOCs do not recapitulate the shear stress and the strain on the cells, as displayed *in vivo*.

Third, different phases of the cell culture may necessitate or benefit from diverse membrane characteristics. Therefore, research containing dynamic membranes, which change throughout the cell culture, will be studied in more detail in Section 2.4. The focus will be placed on the pore size within the membrane. In the first phase, during monolayer formation, a membrane should be non-porous or contain small-sized pores so that cells do not travel through the membrane. Moreover, it should be wettable and bioactive, promoting cell adhesion and growth. For the second phase, the membrane needs to be permeable and porous to allow transport of nutrients, signalling molecules, and immune cells across it. Furthermore, it has become clear that the membrane needs to be elastic enough to undergo a cyclic strain while being robust enough to last the entire cell culture.

Thus, the need for a novel membrane for LOC devices became apparent in the literature review. The requirements for an ideal LOC membrane to recapitulate the alveolar-capillary barrier, were set as follows: The membrane should sustain a cyclic in-plane stretch of at least 20%, an ALI along with a physiological fluid flow, and it should have a thickness of  $\leq 10 \mu\text{m}$ . Furthermore, it should have an adequate pore size, be made of a material that has better ad- and absorption properties than the conventionally used PDMS, and it should be possible to culture cells for up to 4 weeks.

### 1.4. Research question

This thesis project aims to design and test a novel LOC membrane to recapitulate the pulmonary alveolar-capillary barrier. This barrier is the blood-air barrier in the lungs' gas exchanging region. However, designing and testing a membrane with all the previously mentioned properties, next to testing and improving the prior LOC design by the Department of Precision and Microsystems Engineering (PME) [1], would be a too large knowledge gap and research subject to cover in the limited time span of a master's thesis. Therefore, a small part of this overall aim is researched. In the Literature Review, the need to establish adequate pore sizes in the membrane throughout the cell cultures became apparent. This includes the starting pore size, which is used when culturing the monolayers and during cell differentiation, and secondly, the pore size which is desired to allow for immune cell migration across the membrane when strain and an ALI are applied. As explained previously, these two pore sizes ideally need to have different pore diameters. Therefore, the possibility of adjusting this pore size throughout the cell culture will be investigated.

Thus, the research question of this thesis is: **How to fabricate a LOC membrane containing a dynamic membrane pore size to be able to study the monolayer formation, adherence, and immune cell transmigration?** The membrane design should allow for the incorporation of an ALI, physiological fluid flow and in-plane cyclic stretch.

Subquestions that will be studied in this research include:

1. What material should be used as a membrane material? This will be studied by focusing on:
  - 1.1 material cytotoxicity and biocompatibility,
  - 1.2 material stiffness,
  - 1.3 material degradation and long-term stability,

- 1.4 and (bio)imaging properties of the material.
2. How to fabricate a thin membrane containing a dynamic pore size? This is addressed by studying:
  - 2.1 How to fabricate a uniform and thin membrane?
  - 2.2 How to fabricate a dynamic pore size within the membrane?
  - 2.3 How to integrate the membrane into the previously designed PDMS LOC device?

## 1.5. Report structure

This thesis report, to answer the research questions, first discusses in Chapter 2 the relevant background theory. In Chapter 3 the membrane concept for a membrane with dynamic pores is introduced. Chapter 4 covers the methodology used in the various experiments. The results are presented in Chapter 5. The discussion and interpretation of the results follow in Chapter 6. Finally, a conclusion and future outlook are presented in Chapter 7. This report's chapters all include content regarding both of the master's programs in Mechanical Engineering and Biomedical Engineering.



# 2

## Background theory

This Chapter covers the relevant background theory for this research. Additional background information is included in the Literature Review located at the end of this report. First, the lung physiology and the characteristics of the alveoli are covered. Subsequently, the relevant parameters that need to be considered in the design of a LOC membrane are discussed. Additionally, the LOC device designed previously in the PME Department [1] will be covered. Lastly, the possibilities for an alternative material for a LOC membrane and possible fabrication methods for a thin and porous membrane will be covered.

### 2.1. Lung physiology

The human respiratory system allows for gas exchange between blood circulating in the body and the external environment [19]. The lungs are the primary organ within this respiratory system, and it allows the exchange of oxygen and carbon dioxide [3]. This system exists of the conducting zone, and the respiratory zone [19]. The conducting zone is merely the region where the air is transported to and from the gas exchanging region [19]. Whereas the respiratory zone is the region where the gas exchange actually takes place, and it starts where the terminal bronchioles turn into the respiratory bronchioles (Fig. 2.1) [24]. This region is where the acini are located, which consist of bronchioles, alveolar ducts, and alveoli [19]. There are over 30 000 acini present in the adult human lung, and each acinus holds roughly 10 000 alveoli [11]. Overall, this accounts for about 300 million alveoli, which make up most of the human lung volume [24]. Around every alveolus, a dense network of pulmonary capillaries is present.

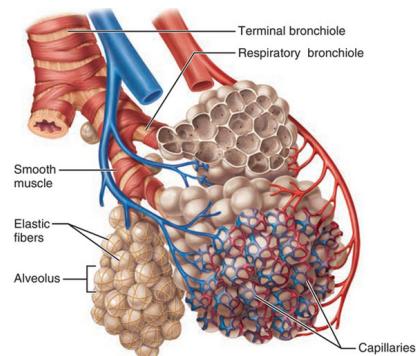


Figure 2.1: View of capillary-alveolar relationships [24].

The gas exchange itself happens *via* diffusion through the respiratory membrane, also called the alveolar-capillary barrier (Fig. 2.2) [24]. This thin membrane spans between the alveolar lumen and the capillary lumen. This membrane is so thin that a single sheet of tissue paper is about 15 times thicker [24]. It is comprised of epithelial and endothelial cells, which are located on different sides of a fused basement membrane. Between the alveoli, there is also a membrane, the inter-alveolar membrane, containing pores of Kohn with a diameter of about 10  $\mu\text{m}$  to 15  $\mu\text{m}$  [3]. These alveolar pores equalize the air pressure throughout the alveoli and provide secondary air routes to alveoli otherwise unreachable due to disease [24].

The alveoli are roughly ordered in a honeycomb structure with polyhedral-shaped cavities [11]. This causes the general morphology of the alveolar blasts to be hexagonal [29]. The diameter of the individual alveoli ranges from 200 to 300  $\mu\text{m}$  [3, 29].

On the side of the capillary lumen, endothelial cells are present, creating a monolayer called the endothelium [3]. Whereas, on the side of the alveolar lumen, the alveolar-capillary barrier consists of a single layer of epithelial cells covered by a thin layer of liquid surfactant. The surfactant forms the barrier between the air



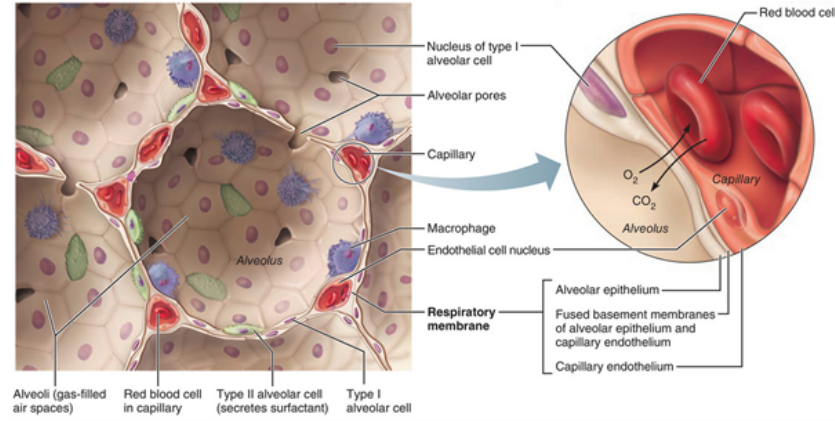


Figure 2.2: Detailed anatomy of the alveolar membranes [24].

and the tissue, called the air-liquid interface [19, 20]. The epithelial cell layer secretes the surfactant, which consists of alveolar lining fluid [3, 20]. This layer of about  $0.1\text{--}0.2\ \mu\text{m}$  thick protects the epithelial cells from being exposed directly to the air and plays a significant role in the immune defence of the alveoli [3, 11]. The surfactant layer also decreases the air-liquid surface tension, which promotes molecule diffusion across the membrane [29]. Upon film compression, which happens during exhalation, the surface tension is almost equal to zero [11]. Along the alveolar lumen, alveolar macrophages transit around freely, which continuously respond to infectious microorganisms that are breathed in [24].

Both the capillary endothelial and alveolar epithelial cell layers have a basement membrane, which poses as a structural support and bonding site for the adjacent cells [30]. Each basement membrane has a thickness of about  $50\ \text{nm}$ . They are fused together to create the alveolar interstitium [20]. This barrier forms the connective tissue between the alveoli and the blood vessel. The thickness of the interstitium itself ranges from  $0.2\ \mu\text{m}$  to  $0.5\ \mu\text{m}$  [3]. The complete alveolar-capillary barrier, including the cell monolayers, has a mean thickness of  $1.1\ \mu\text{m}$  [3, 20, 27]. But at the gas exchange location, where the membrane is thinnest in order to allow for efficient gas, solutes and protein diffusion, it has a thickness of  $0.62\ \mu\text{m}$  [20, 29].

The ECM, of which the interstitium consists, provides the lung with its most vital functionality [20]. The ECM contains roughly 60 different cell types [20], among which elastin and collagen IV fibrils are abundantly present. These fibers have a diameter ranging from  $10$  to  $100\ \text{nm}$  [3, 29, 31]. Cells present in the lungs include, for example, epithelial cells, smooth muscle cells, endothelial cells, and a specific set of fibroblasts [19, 20]. The fibroblasts produce elastin that composes a third of the total lung dry mass [3, 27]. It creates a highly elastic intricate woven network of nanofibers, which supports cells [31]. Furthermore, the basement membrane is porous, and it contains two types of pores [20]. The specific pore sizes are still undetermined, but it is suggested that one pore type has a size smaller than  $2.5\ \text{nm}$  and a less common second pore type has a diameter of less than  $400\ \text{nm}$  [20].

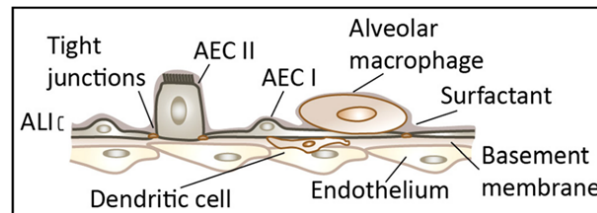


Figure 2.3: Schematic of the alveolar-capillary barrier, showing the cellular composition and the ALI [11].

The epithelial layer consists mainly of squamous type I (AET I) and to a lesser degree cuboidal type II (AET II) alveolar cells (Fig. 2.3) [3, 24, 29]. AET I cells make up about 95% of the alveolar wall. They maintain homeostasis and contribute to particle transport, and gas exchange [3, 29]. They are also connected through the basement membrane's ECM to the capillary endothelial cells [29]. AET II cells secrete the surfactant layer, stimulated by cell stretching [3, 29]. This surfactant is constantly produced and subsequently broken down

and reabsorbed by macrophages [3]. The half-life time of surfactant is 5 to 10 hours [3]. AET II cells also play a prominent role in the immune system by producing antimicrobial proteins [24]. The size of an epithelial cell ranges between 10  $\mu\text{m}$  for AET II cells and 50- 100  $\mu\text{m}$  for AET I cells [32].

The AET I cells form a continuous layer with tight junctions, showing little leakage of particles [3]. Tight junctions are cell-cell adhesions, which tightly connect cells, allowing for paracellular and transcellular transport. Besides that, these junctions play a significant role in controlling intracellular signals, and cellular polarity [30]. The AET I cells are only replaced by differentiated AET II cells, which constantly renew [3].

The endothelial cell layer is a semi-selective barrier, managing the transport of particles and migration of white blood cells between the capillary lumen and the neighbouring alveolar tissue [3]. It has been shown by transmission electron microscopy that alveolar fibroblasts are connected to AET I and AET II cells through basement membrane apertures. Furthermore, the same may be possible with endothelial cells, and thus the endothelium may also be directly connected to the epithelium *via* fibroblasts [30].

The dynamical aspects will be covered now that the alveoli's anatomical structure and dimensions have been discussed. Firstly, the lung displays unique mechanical forces: every respiratory cycle, a periodic mechanical force is exerted on the alveolar membrane. This dynamical force makes the lung a challenging tissue to mimic *in vivo* [33]. Physiological stretching of the alveoli is vital in tissue and cell development and in maintaining homeostasis [34]. The alveoli are inflated and stretched during inspiration and deflated during expiration. At rest, both phases are around 1.5 to 2 seconds, with a 1-second pause in between [3]. This results in a regular breathing frequency of around 0.20 Hz [20]. The alveolar basement membrane generally undergoes a linear strain of 4% during this rest condition [20]. During exercise and deep breathing, the respiratory frequency can rise 3 to 5 fold [3, 20]. The corresponding linear strain roughly goes up to 12%. This strain range is the physiological strain range [29]. Birukov et al. [35] state, based on clinical observations and models, that a linear mechanical strain greater than 15% may be marked as pathophysiological. In comparison, Tas et al. [34] state that overdistension of the lung happens when the strain goes over 20%. Doryab et al. [20] also state that in pathological conditions, strains up to 20% have been observed.

Table 2.1: Characteristics of the alveoli.

Feature	Value
Thickness basement membrane	~50 nm
Total barrier thickness	~0.6 $\mu\text{m}$
Pore size	< 2.5 nm and < 400 nm
Breathing frequency	0.2 Hz
Physiological linear strain range	4% -12%
Stiffness	< 10 kPa

Regarding tissue stiffness, Pasman et al. [4] state that lung tissue has a Young's modulus of 400 Pa. According to Doryab et al. [20], the alveolar tissue has a Young's modulus of around 1-2 kPa. Furthermore, the Young's modulus of an alveolar wall is roughly 5 kPa, for a wall with an average thickness of 8  $\mu\text{m}$ . However, this is a gross oversimplification by Cavalcante et al. due to not taking into account the wall structure [36]. Generally, the stiffness of the alveolar-capillary barrier is assumed to be less than 10 kPa.

To date, it has not been possible to exactly recapitulate these variables and the alveolar barrier structure within a LOC membrane simultaneously. Moreover, the obtainable stretch, membrane porosity and stability depend on, for example, the membrane thickness, structural design and the type of materials chosen for the membrane. As such, it might not be possible or necessary to fully mimic every variable exactly, as long as the LOC membrane mimics the native environment adequately enough. An overview of characteristics that the alveoli exhibit is shown in Table 2.1.

## 2.2. Cell types used for *in vitro* modelling

For *in vitro* cell cultures, various cell types can be chosen. The leading choice is between primary cells and immortalized cell lines, but also induced pluripotent stem cells (iPSC) have recently been tried to culture [3]. The following Section is an overview of these cell types. Table 2.2 gives a summary of the advantages and disadvantages of each cell type that is discussed in this Section.

**Human primary cells:** Primary cells are directly derived from donor tissue, using specific enzymes [1, 3]. Ideally, primary cells are used for cell cultures since they more closely resemble the *in vivo* cell properties [4]. However, this is often challenging since primary cells are more costly, more challenging to culture and have a limited lifespan [1, 3, 4].

**Primary epithelial cell types include:** Primary human pulmonary alveolar epithelial cells (pH-PAEC), primary human bronchial epithelial cells (PBEC), primary human airway epithelial cells (hAECs) [12, 13, 37], and tracheo-bronchial epithelial cells (AE) [38][1]. hAECs have the best characteristics that simulate *in vivo* behaviour [3].

**Primary endothelial cell types include:** primary human umbilical vein endothelial cells (HUVEC) [27, 39–42], human pulmonary microvascular endothelial cells (HPMEC) and primary human lung microvascular endothelial cells (HMVEC-L) [1, 3, 4, 20, 22, 43]. Besides the frequently applied HPMEC lines, also HUVECs are a non cancerous, and a very commonly used cell line [3].

Table 2.2: Overview of the advantages and disadvantages of the various cell types.

Cell type	Advantages	Disadvantages
Human primary cells	Close resemblance to <i>in vivo</i> cell properties	Costly Challenging to culture Limited life-span
Immortalized cell lines	Increased life-span Easier to culture	Less resemblance to <i>in vivo</i> properties
iPSCs	Differentiable into various tissues Increased biological accuracy	No clear differentiation protocol

**Immortalized cell lines:** Since primary cells prove more challenging to use in cell cultures, for the reasons mentioned previously, often immortalized cell lines are used [4]. The lifespan of cells is increased in immortalized cell lines, which are derived from primary cell lines. In order to make them immortalized, a mutation can be induced, by which they keep dividing [3]. Thus, they keep proliferating, and they subsequently can be grown *in vitro* long-term [3]. However, due to the changes they undergo, they often do not exhibit the same phenotypes as native cells [3].

**Immortalized epithelial cell types include:** Lung cancer cells (NCI-H1437) [44], pulmonary alveolar epithelial cells (NCI-H441) [6, 20], human airway epithelial cell line (Calu-3) [19, 45], adenocarcinomic human alveolar basal epithelial cells (A549) [27, 29, 39, 42, 46, 47], human bronchial epithelium cells (BEAS-2B) [1, 14, 48]. A commonly used and thoroughly characterized epithelial cell line is the A549 cell line, although these have been found to form weak junctions. [3]. Since the A549 cell line barely exhibits barrier function, they are less suitable for lung barrier modelling [4]. The NCI-H441 cell line particularly allows for a tight epithelium layer and the generation of surfactant [3]. Also, Calu-3 cell lines have been extensively used to model lung barriers since they have proper barrier function, have good availability and are relatively easy to culture [4].

**Immortalized endothelial cell types include:** Lung cancer cells (NCI-H1237) [1].

**Induced pluripotent stem cell lines:** iPSC lines are donor cells reprogrammed into stem cells [9]. These stem cells can subsequently be differentiated into any kind of tissue [1, 3]. iPSCs have the ability to replace primary or immortalized cell lines, and they can increase the biological accuracy by permitting experiments on cells from multiple sources [3]. iPSCs have already been used in lung organoids [9], kidney-on-a-chip [49] and in mimicking the blood-brain barrier [10]. However, the differentiation protocols for lung tissue are not adequate yet, and they need further research [3, 10].

**Other cell types:** Other cell types have also been included in various research on the alveolar-capillary barrier. These include, but are not limited to, fibroblasts (primary human lung fibroblasts), dendritic cells, human bronchial smooth muscle cells (hBSMCs), or pulmonary macrophages [1, 3].

Pasman et al. [4] demonstrated that when compared to monocultures, implementing a coculture with both endothelial and epithelial cells exhibited various benefits. This includes, for example, improved barrier function [4]. Nevertheless, many studies still apply monocultures. For each cell culture study, an adequate cell type must be chosen by taking the aforementioned advantages and disadvantages into account.

## 2.3. *In vitro* lung models

This Section gives background information on *in vitro* lung models, the state-of-art and relevant characteristics that LOC devices and membranes can exhibit, and prior work on LOCs in the PME Department relevant to this research is covered. Additional information on the state-of-art of LOC devices, the differences in LOC device layout, membrane straining types, and examples of representative LOC devices are included in the Literature Review included at the end of this report.

### 2D cell cultures

2D cell cultures, such as plastic or glass culture dishes or well plates, have been a broadly used method due to their low cost and their ability to provide a means for standardized and consistent studies [9, 27]. Typically a single cell type is studied in these cell cultures, however, a simple cell culture does not contain the complex functionality, and physiological/pathological conditions found *in vivo*, where multiple cell types are present, which continuously give and receive signals and cues from each other [9, 10, 27]. Transwell inserts are a popular choice and have been used to recreate an ALI with a coculture and a permeable membrane, often between smooth muscle cells and epithelial cells [3, 11, 19]. However, generally rigid, bioinert membrane materials such as polyethylene terephthalate (PET) are used. These have high stiffness and do not mimic the ECM, both chemically and structurally [19]. Most importantly, these 2D cell cultures fail to provide dynamical and mechanical cues to the cells, which include strain, compression and tension, shear stresses, and the various tissue-specific dimensions and geometrical structures [10]. These cues affect cell behaviour by influencing cell differentiation, proliferation, contractility motility, and organ development [10]. The dynamic shear stress-dependent response also influences the progression of several diseases such as COPD and asthma, and it should be included if diseases such as these are studied [12].

### Organoids

The limitations in 2D cell cultures (and in animal models) caused a shift in research to more extended 3D models, such as organoids, which are multicellular 3D cultures containing clusters of cells, set up using stem cells or tumour cells [10, 27]. These 3D models generally use biocompatible polymers or natural materials as a scaffold for three-dimensional growth of tissue [27]. More complex 3D cell cultures can provide longer incubation times and an ECM or scaffolding in which multiple cell types can grow, allowing for a more biomimetic environment [20, 39]. Also, the tissue-specific structure and shape, and cell-cell or cell-matrix interactions, which influence physiological functions, can be more closely mimicked [3, 27]. Therefore, these are proving to be better models for cell migration, differentiation, growth, and general cell survival [3]. Multicell cocultures with up to 5 different cell types have been achieved [20]. Nonetheless, these models, being static cultures, generally fail to provide an ALI, and they omit the dynamics to mimic the breathing mechanisms [39].

### LOC devices

Current developments in microfabrication techniques have allowed for the incorporation of various biomechanical characteristics into *in vivo* models, such as mechanical stimuli, microfluidics and a 3D microarchitecture [3]. Mechanical stimuli, such as the breathing movement, influence not only cell development and tissue regeneration, but also disease onset, and advancement [20]. Moreover, adding microfluidics not only allows for more extended study durations by continuously providing nutrients to the cells, but it also allows for the incorporation of fluid shear effects and the effects of physical, chemical and electrical stimuli [9].

### LOC characteristics

The inclusion of an ALI is relevant due to several factors. It increases monolayer integrity, allows primary cells to differentiate into epithelial cells, and incorporated air increases surfactant secretion [11, 15]. Including an ALI also improves the molecular barrier function compared to submerged conditions [15]. It reasonably also produces stronger tight junctions since Huh et al. [15] found an increased electrical resistance over the cell layer under ALI conditions in their study. Moreover, including a medium flow in the device is essential since the subsequent shear stress on the endothelial cells exerts several effects: endothelial cells align along the flow direction, and the permeability of the cell layer and cell morphology are influenced [3]. Besides that, the shear stress also influences inflammation and protein expression, and most critically, it influences the cells' ability to form a tight monolayer [3]. In contrast, the shear stresses can also injure the underlying endothelial cells when the stresses become too large [46].

The simulation of a breathing movement by including a cyclic stretch on the cells is relevant because it affects multiple cellular behaviours by inducing morphological, biochemical, metabolic and genetic changes in the cells [15, 50]. These include, but are not limited to, tight junction formation, cell proliferation, mi-

gration and differentiation, and surfactant secretion [20, 30]. Due to the strain, cells experience mechanical forces at their focal adhesions. From there on, this signal is transmitted to the cytoskeleton, which remodels accordingly. The type of strain (1D, 2D or 3D), its magnitude and frequency all have a significant influence on cell behaviour [50]. For example, Stucki et al. [41] showed that cyclic stretching of the membrane affects barrier permeability of the epithelial layer, and Huh et al. [15] found that applying a realistic cyclic stretch enhances nanoparticle transport through the alveolar-capillary barrier. Furthermore, the metabolic activity of dynamically stretched cells was also higher than that of static cells [10]. Besides that, endothelial cells align perpendicular to the straining direction, and cyclic (over)stretching influences the onset and development of various diseases, such as ARDS-like cell injury [3, 46]. Since strain significantly affects cellular behaviours, mechanical stimuli are vital in simulating the native (patho)physiological cell environment [20].

Lastly, the membrane must be thin enough. Membranes in LOC devices are often about 10  $\mu\text{m}$  thick or thicker, which is a factor 20 to 50 thicker than the *in vivo* counterpart. Consequently, inter-cellular exchanges, such as translocation and diffusion, which are vital aspects in simulating the native environment, can not be accurately represented [3, 11]. Besides that, most devices and their membranes are made with PDMS [39], which has several disadvantages such as ab- and adsorption of hydrophobic molecules, which will be further explained in Section 2.5.1. As such, membranes should ideally be designed using materials other than PDMS. Currently, membranes mainly focus on structurally supporting the cells placed on the membrane. However, compared to *in vivo* basement membranes, they are generally too thick and not elastic enough [30]. As Douville et al. [46] state, solid and fluid mechanical stresses significantly influence the cell culture and should be taken into account in recapitulating alveoli. Therefore, these stresses should be incorporated with A: a breathing motion and B: a fluid flow. Furthermore, an ALI and a thin membrane are essential.

### 2.3.1. State-of-the-art

Based on the Literature Review, it was found that only a limited number of studies focussing on LOCs were able to include a thin membrane ( $<10 \mu\text{m}$ ), and only two had a membrane equal or thinner than 1  $\mu\text{m}$  to the author's knowledge [3, 29]. Moreover, when a thin membrane was incorporated, it was generally static or not yet tested for long-term cell cultures. For example, no thin membranes made of a different material than PDMS had a cell culture containing a cyclic stretch for longer than 48 hours. The studies that did include a thin membrane with the possibility of short-term stretching include the design by Laniece [3], Stucki et al. [41], Doryab et al. [30] and Zamprogno et al. [5]. All four studies incorporated a triaxial, out-of-plane stretch (bulging).

Second, many devices had both an ALI, a media flow, and a cyclic stretch incorporated in their devices. Although not all studies were able to apply the cyclic stretch and the media flow or ALI at the same time on the membrane [3, 22]. This means that these LOCs do not simulate shear stress on the cells, while the cells are also subjected to a strain, as displayed *in vivo*. There are also differences present in the type of stretch that was applied. One of the more common stretching types is the bulging stretch. In-plane stretch was also widely present in the literature, although often in combination with thicker membranes.

Third, as explained by Doryab et al. [30] different phases of the cell culture may necessitate for or benefit of diverse membrane requirements. Therefore, research containing changing membranes throughout the cell culture were studied. These include membranes that are (partly) biodegradable. Rezaei et al. [51] designed a biodegradable scaffold not suitable for stretching or an ALI. Zhang et al. [52] made a Poly(octamethylene maleate (anhydride) citrate) (POMaC) scaffold, which could contain an ALI, but no strain was applied to the membrane. Doryab et al. [30] made a membrane with varying pore size. Zamprogno et al. [5] designed a biodegradable membrane with a support structure. As such, inspiration can be taken from these designs.

Fourth, there are various promising material alternatives proposed for PDMS. Alternative materials also allow for alternative manufacturing methods and membrane structures, such as electrospun fibres or a rigid support structure. Support structures generally contain a hexagonal shape. Most alternative materials were still incorporated in devices that did not mimic the breathing motion, often due to the rigidity or the limited mechanical strength of the used material. For example, glass [44], PET, polycarbonate (PC), poly(tetrafluoroethylene) (PTFE) [38, 47], polyester [12] and silicon [14] were incorporated as a rigid substitute. Promising materials replacing PDMS that were subjected to a strain include; gelatin [3, 29], poly(lactic-co-glycolic acid) (PLGA) [27] and poly( $\epsilon$ )-caprolactone (PCL) [30, 53] in the case of electrospinning. Furthermore, gelatin methacrylate (GelMa) [13] and a collagen-elastin (CE)-hydrogel [5] were proposed as hydrogel alternatives.

In conclusion, several designs of LOC devices have incorporated a combination of breathing movements, biodegradability, media and airflow while closely mimicking the lungs' ECM. However, there are still no LOC devices to the author's knowledge that do not use PDMS, and which contain simultaneously: an ALI, media flow, cyclic in-plane physiological stretching, and a membrane with a thickness under  $10\text{ }\mu\text{m}$  that allows for both endothelial and epithelial cell studies spanning multiple weeks. Besides that, generally, little information is present on the motivation of the chosen pore size and its effect on the cell culture. Furthermore, few studies consider that dynamic membranes could have a beneficial effect on cells in different phases of the cell culture. The possibilities of filling this knowledge gap need to be researched for the reasons stated previously, and will be further explored in the coming chapters. Research into an adequate membrane will be conducted using the device previously designed by the PME Department due to its availability and previous promising results [1].

### 2.3.2. Prior work in the PME group

The PME Department at the Delft University of Technology designed a LOC device to recapitulate the alveolar-capillary barrier [1]. The membrane, which is to be designed in this project, is intended to be placed within this LOC device. The design of the LOC consists of two stacked channels, in between which a membrane is located. The device can provide an ALI with both a gas and media flow. The media flow in the basal chamber is designed to exert a shear stress of  $0.55\text{ Pa}$  on the endothelial cells at a  $2.6\text{ ml/min}$  flow rate. The LOC is resealable, due to PDMS slabs placed on top of the chip (Fig. 2.6). The cells can be seeded on the membrane by direct pipetting, and they can be retrieved after the experiment for additional analyses. Furthermore, the LOC is compatible with confocal microscopy and optical sensors to measure pH and  $\text{O}_2$  and  $\text{CO}_2$  concentrations. It is also possible to include transepithelial electrical resistance (TEER) and temperature sensors. All the materials used (PDMS, glass) have good optical transparency allowing live imaging of the cells [1].

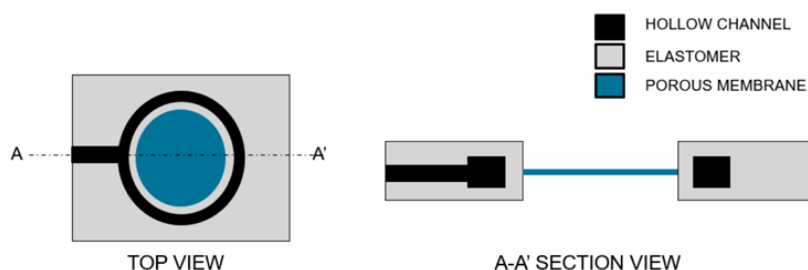


Figure 2.4: Schematic of the LOC device designed in the PME Department [1].

The device (Fig. 2.4) uses a hollow actuation ring (black), which bends the PDMS elastomeric wall inwards when negative pressure is applied. This inward bending stretches the membrane (blue) biaxially, up to 20% linear strain. To incorporate cyclic strain, a triangular wave cycle with  $0.2\text{ Hz}$  was used. The PDMS channels were fabricated using soft-lithography, and they were sandwiched between glass layers (Fig. 2.5). Plasma bonding was used to bond the channels to the actuator [1].

The overall dimensions of the LOC are included in Figure 2.6. The total length and width of the channel through which medium flows are  $2\text{ cm}$  and  $3.2\text{ mm}$ , respectively. The central membrane hole was designed to have a diameter of  $3.1\text{ mm}$ , and the cell supporting surface of the membrane had a diameter of  $3\text{ mm}$  [1].

This device is designed for an endothelial and epithelial cell coculture, providing cyclic strain and shear stress. However, the membrane is made of PDMS, which has several disadvantages that will be further explained in Section 2.5.1. PBECs remained viable for at least 16 days in culture on the PDMS membrane within the device,

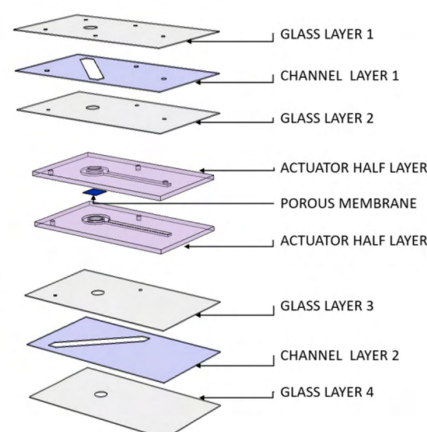


Figure 2.5: Layered view of the LOC designed in the PME Department [1].

and they formed a monolayer after five days. The design also allows for scale-up by manufacturing an array of LOCs next to each other so that multiple cell cultures can be performed simultaneously [1].

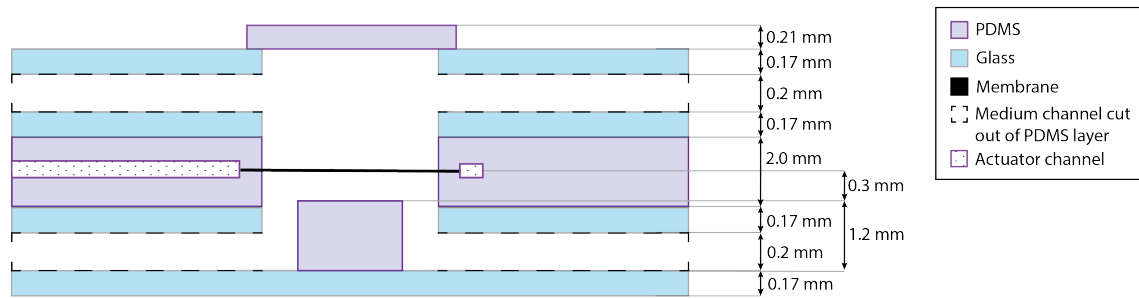


Figure 2.6: Schematic side view and dimensions of the LOC device designed by the PME Department [1].

## 2.4. LOC membrane requirements

There are various types of cell-supporting membranes. The membrane is usually a thin porous membrane [39]. The general membrane thickness is around  $10\ \mu\text{m}$ . Pores present in the membrane range between  $0.4\ \mu\text{m}$  and  $50\ \mu\text{m}$ , with most pore sizes below  $10\ \mu\text{m}$ . Although membranes with no pores are also used [44, 46]. The membrane topology ranges from smooth, textureless membranes to 2.5D/3D membranes such as electrospun membranes, which contain a distinct fibrous texture. A material that is often used as a membrane material is PDMS, but also various synthetic polymers and hydrogels have recently been researched. When designing a LOC device, great care should be taken to ensure that the device layout, type of strain, and membrane type correspond with the desired functionality of the device. Even though significant advancement in the design of LOC devices has been made in the past two decades, there are still many limitations in the current designs. This Section covers the background information on LOC membranes, and discusses the requirements for a LOC membrane. When setting these requirements, it was kept in mind that this membrane is to be used in the prior designed LOC in the PME Department.

Based on the Literature Review, a set of requirements was formed for a LOC membrane to recapitulate the alveolar-capillary barrier and to obtain the required functionality within the LOC. Table 2.3 gives a brief overview of the requirements. Each requirement is further elaborated on in the rest of this Section.

Table 2.3: Overview of membrane requirements.

Membrane requirement	Value
Membrane diameter	3 mm
Membrane thickness	$\leq 10\ \mu\text{m}$
Pore size	$\leq 3\ \mu\text{m}$ in Phase 1, $\geq 3\ \mu\text{m}$ and $\leq 8\ \mu\text{m}$ in Phase 2
Permeability	$\sim 4.3 \times 10^{-6}\ \text{cm/s}$ to proteins
Chemical inertness	Minimal molecule ab- and adsorption and chemical reactivity
Biocompatibility	Long-term biocompatibility must be present
Wettability	$\text{WCA} < 70^\circ$
Stiffness	1 kPa - 300 kPa
Actuation pressure	$\leq -800\ \text{mbar}$
Strain	$\geq 20\%$
Stretching frequency	0.2 Hz
Shear stress on endothelial cells	$\sim 1.54\ \text{N/m}^2$
Optical transparency	Adequate for confocal microscopy
Sterilizable	70% ethanol or 5% $\text{H}_2\text{O}_2$
Sustain x number of cycles	$\sim 5 \times 10^5$ cycles
Membrane integration	Leaktight, detachable after experiments



### Cell culture phases

According to Doryab et al. [30], two phases can be discerned during cell culture growth. In Phase 1, alveolar epithelial cells adhere to the membrane. They proliferate and grow into a connecting monolayer, forming tight junctions. In this phase, the membrane is still fully submerged on both sides of the membrane, and no stretch is yet applied. In Phase 2, the cell layer will be further cultured under ALI conditions. ALI conditions mean the media is interchanged with a gas flow on the apical side, initiating epithelial cell differentiation and acclimatization. During this acclimatization, cells will polarize and secrete surfactant. In the second phase, the cells are continuously secreting a cell-secreted ECM, which forms a layer underneath the cells between them and the membrane. After the cells have formed a monolayer during this phase, a cyclic strain can be applied [30].

Thus, for each phase, different membrane characteristics are desired. Figure 2.7 gives a schematic overview of how the different characteristics could change throughout the phases. The phases begin with cell seeding, after which a monolayer is formed. Once this monolayer has been formed, the ALI is introduced (Fig. 2.7 D). In Phase 1, a membrane should be bioactive, promoting cell adhesion and growth, besides being wettable and non-porous or containing small pores (Fig. 2.7 A and B). It should contain small pores so that cells do not travel through the membrane. The elasticity of the membrane is not critical yet, as no strain is yet applied. These characteristics are optimal for cell monolayer formation [30]. Next, after the ALI has been introduced and the cells have differentiated, a cyclic strain can be applied to the membrane (Fig. 2.7 C). For this second phase, the membrane needs to be permeable and porous to allow the transport of nutrients, signalling molecules and immune cells. Furthermore, the membrane needs to have an elasticity that recapitulates the human lung's ECM while being tough enough to undergo a cyclic strain (Fig. 2.7 A and B) [30].

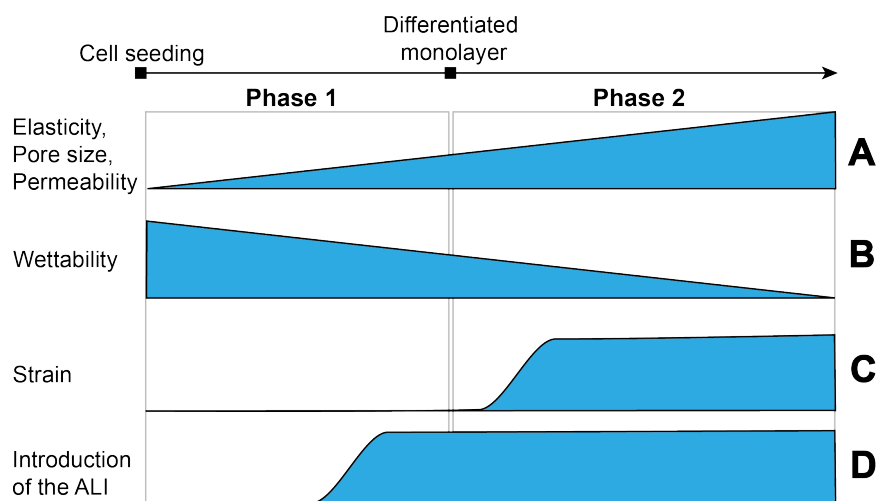


Figure 2.7: Schematic representation of the membrane properties throughout a cell culture. Based on Doryab et al. [30].

### Membrane dimensions

The membrane is designed to fit in the LOC design created prior by the PME Department [1] and should therefore have suitable dimensions. These dimensions include a membrane diameter of 3 mm, excluding the membrane edges used for the membrane integration. Furthermore, a membrane with microscale thickness is needed to allow for efficient gas exchange [27]. The membrane thickness should mimic the alveolar-capillary barrier thickness as closely as possible, which is made up of 2 basement membranes of 50 nm each, creating a membrane with a thickness of 0.1  $\mu\text{m}$  overall [27]. Generally, a LOC membrane has a thickness of around 10  $\mu\text{m}$ , and few membranes have been designed to be thinner than that. Most membrane thicknesses have been determined by the manufacturing possibilities rather than a biologically based choice. This limitation is due to the trade-off between membrane thickness and membrane strength and the achievable manufacturing resolution. Thus, the thickness should adequately recapitulate the *in vivo* properties while considering the materials and manufacturing methods. The device dimensions should also allow the cell culture to be studied under a confocal microscope. When using the device of the PME department [1], a membrane with



a thickness of 10  $\mu\text{m}$  has been found to fit within the working distance of a confocal microscope (HCX PL Fluotar L 40x objective).

### Pore size and permeability

The alveolar-capillary barrier aimed to be recreated is an elastic and exceptionally thin porous membrane. Doryab et al. [30] state that in order to allow for transport of e.g. nutrients and immune cells across the membrane barrier, three things need to be taken into account: a low membrane thickness; a large pore size (up to 8  $\mu\text{m}$ ); and high porosity (around 9%).

**Pore size:** Standard transwell inserts generally have a pore size between 0.4  $\mu\text{m}$  and 8  $\mu\text{m}$  (Corning Incorporated, Corning, NY). Most LOC devices also contain pore sizes within this range, though some membranes do not contain pores [19, 44, 46, 54]. However, many studies do not elaborate on their decision to choose a specific pore size.

**Nutrient and cell transfer through the membrane:** A permeable and porous membrane is desired to facilitate nutrient and protein exchange through the membrane. For example, Pasman et al. [4] found that in static cell cultures, a higher cell density was possible on more permeable membranes since those facilitated a better nutrient supply. Furthermore, the possibility of immune cell and protein migration across the membrane is desired to recapitulate the *in vivo* environment more accurately. For example, neutrophil movement needs to be observed to measure lung inflammation, as an indication of lung inflammation is the process of neutrophil displacement from the micro-vascular channel to the alveolar chamber [10]. Also, the cytokine interleukin-8 (IL-8) gene expression and subsequent protein release happen when inflammation is present [30, 35]. Moreover, pore size influences macrophage migration through the membrane. Besides that, pore size influences cell differentiation, proliferation, adhesion, growth and viability [55].

**The pore size dilemma:** Cell migration speed through pores diminishes linearly with decreasing pore size, meaning that the lower response to increasing mechanical confinement is not a 'stop or go' arrangement but a gradual process largely dependent on cell deformation [56]. Cell deformation is limited by the nucleus, the largest and most rigid cell organelle. Thus, cell migration efficacy is a joint function of substrate porosity, and nuclear deformability [56]. Wolf et al. [56] found that maximal cell deformation was generally reached when the nucleus deformed to 10% of its original cross-section, reaching the migration limit. This migration limit ranged from 10  $\mu\text{m}^2$  for tumour cells to 1  $\mu\text{m}^2$  for polymorphonuclear neutrophils (PMNs) [56].

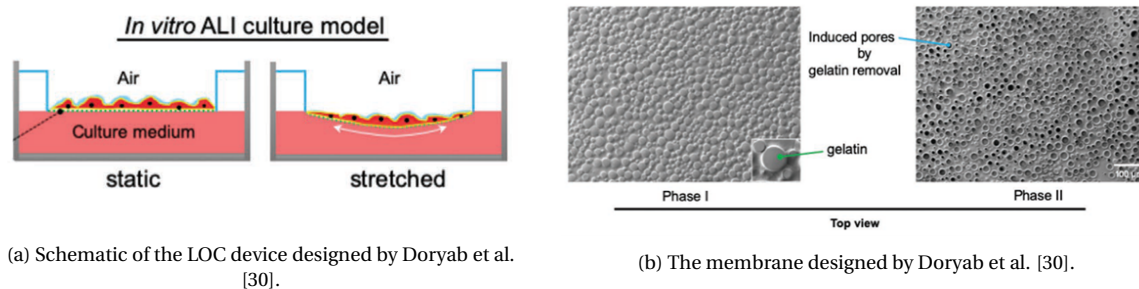
Regarding lung cells, Doryab et al. [30] state that in the first phase, no pores need to be present in the membrane. If pores are present, the maximum pore size is between 1-3  $\mu\text{m}$  to avoid epithelial and endothelial cells from travelling through (or into) the membrane. This migration is to be prevented since these cells need to form a confluent monolayer on their respective membrane sides. Zhang et al. [55] also state that 2.5 – 3.5  $\mu\text{m}$  is the minimum pore size through which cells can infiltrate and migrate. However, sufficient nutrient supply should still be present in this phase, especially on a poreless membrane where no nutrients can travel through the membrane. Pasman et al. [4] demonstrated that cells could grow more poorly on a poreless membrane compared to a membrane with pores. In the LOC design used in this study, a media flow containing nutrients is present on both sides of the membrane before the ALI is introduced, diminishing the need for pores in this phase.

To allow for innate cell migration, such as macrophage and neutrophil migration across the membrane, Doryab et al. [30] stated that in Phase 2, a pore size larger than 3  $\mu\text{m}$ , up to 8  $\mu\text{m}$  is desired. For example, Zhang et al. [57] reported that through their 10  $\mu\text{m}$  diameter pores perfused human monocytes (THP-1) and macrophages were able to transmigrate which indicates that a pore size of this dimension could be suitable for recapitulating the immune system. On larger pore sizes than 8  $\mu\text{m}$ , which is larger than a single epithelial cell, Doryab et al. [30] determined that no confluent monolayers could be formed [30].

Thus, the dilemma arises that immune cells cannot pass through the membrane when pore sizes are smaller than 3  $\mu\text{m}$  (e.g. the often used 0.4  $\mu\text{m}$ ). However, when the pore sizes are larger than 3  $\mu\text{m}$ , endothelial and epithelial cells can pass through the membrane, which hinders their adherence and monolayer formation.

A solution for this dilemma has been proposed by Doryab et al. [30] with their PCL and gelatin composite membrane (Fig. 2.8). They created a membrane with a variable pore size up to 8  $\mu\text{m}$ , on which a confluent epithelial cell layer was cultured. Initially, the membrane contained no pores. The porosity was also variable throughout the cell study up to  $9.4 \pm 0.2\%$ . Although a cyclic out-of-plane strain of 25% could be applied to this membrane, this was only experimentally tested for 48 hours under submerged conditions [30]. Besides

that, this membrane only contained a monoculture of epithelial cells. Thus, although this is a promising approach to pore sizes, the membrane in this design has not yet been proven suitable for long-term cocultures containing both endothelial and epithelial cells. Moreover, the LOC used in this study is designed for in-plane stretching of the membrane.



(a) Schematic of the LOC device designed by Doryab et al. [30].

(b) The membrane designed by Doryab et al. [30].

Figure 2.8: The LOC device designed by Doryab et al. [30].

Furthermore, Huang et al. [13] demonstrated that uniform pores are preferable to random pores in experiments, even though the (average) pore size might be the same. Pasman et al. [4] also linked a less homogeneous pore distribution and a less confluent monolayer. This is noteworthy, since LOC devices often contain a range of randomly distributed pores and pore sizes [3, 29, 30, 53, 58].

Thus, an ideal membrane should have a uniform pore size below  $3\ \mu\text{m}$  in the first phase, where a confluent monolayer is created. After this monolayer is created, larger pore sizes are desired to mimic the *in vivo* trans-membrane processes such as neutrophil migration more closely. However, little literature is present on pore sizes and their effects in endothelial and epithelial *in vitro* cell cultures.

**Permeability and porosity:** The membrane is expected to have an increased permeability under dynamic loading conditions compared to static conditions. This increase is because the pore size increases when strain is applied to the membrane. For example, Doryab et al. [30] found that pore size increased by a factor of 1.10 when a strain of 21% was applied. Even with increased permeability, the membrane combined with the cell layer should act as a watertight barrier between the upper and lower chambers. As a reference for the permeability value, Zhang et al. [52] stated that the permeability of mammalian capillaries to proteins is about  $4.3 \times 10^{-6}\ \text{cm/s}$ . Regarding the porosity, Doryab et al. [30] aim at a porosity of 9%, whereas Nissar [1] aims at a porosity of 3% - 3.5%.

### Biocompatibility and chemical inertness

The membrane should react minimally with any other chemical compounds present in the cell culture. Furthermore, it must be non-absorbent to molecules in the medium. These molecules can include drugs, proteins and growth factors [30]. This is relevant because this interaction with molecules can influence the accuracy of drug screening experiments [49].

Furthermore, the membrane material should be biocompatible. Both endothelial and epithelial cells should be able to create a confluent monolayer on the membrane without any cytotoxic effects [7, 27]. Moreover, the material should remain biocompatible for the whole study duration so that long-term cell viability can be acquired. Although, once the cells have formed a confluent monolayer and they have started to secrete their own ECM, their contact with the membrane becomes less [20, 33]. Thus, since the contact diminishes, the biocompatibility of the membrane also becomes less crucial.

### Hydrophilicity and wettability

The cell substrate must have certain hydrophilicity and wettability, in order for cells to adhere adequately to the surface. A hydrophobic material would need a surface pre-treatment to enhance cell adherence. This surface treatment is, for example, done with a collagen coating, as is often done on a PDMS surface [39]. Regarding the wettability, Doryab et al. [30] state that a water contact angle of less than  $70^\circ$  is favourable ( $\text{WCA} \leq 70^\circ$ ). A WCA of less than  $90^\circ$  indicates a hydrophilic surface. Most synthetic materials used in OOC applications are hydrophobic. Therefore, this characteristic need to be taken into account when selecting materials.

The required wettability may also change throughout the cell culture stadia. A higher wettability is desired during the first phase to improve cell monolayer formation. In the second phase, the cells have started to secrete their own ECM, which creates a layer between the support membrane and the cell layer. Since the cells have already formed a continuous layer including tight junctions and are not in direct contact with the membrane anymore, the membrane may in this stage have a slightly diminished surface wettability (Fig. 2.7) [30].

### Membrane stiffness

The membrane must be stiff enough to support the adjacent cells, but also elastic enough to sustain cyclic breathing movements. The pressure actuator (Elveflow, OB1 MK3+ microfluidic flow controller) used for the LOC device of the PME Department [1] can exert a negative pressure of 800 mbar on the membrane. The membrane should be elastic enough to provide the desired strain under this pressure or less.

Besides that, membrane stiffness influences cell behaviour. The stiffness of the ECM has an influence on cell migration (e.g. by mechanotransduction), differentiation, cell division and maintaining homeostasis [59]. Zamprogno et al. [60] found, for example, that human fibroblast cell spread is reduced on soft surfaces compared to stiffer surfaces. The stiffness also influences cytoskeleton formation [59]. Softer membranes diminish tight junction formation and augment the distribution of actin, whereas stiffer membranes enhance the formation of F-actin cytoskeleton [30]. The stiffness of the membrane may also differ when various diseases are studied. For example, the collagen content increases in pulmonary fibrosis, which stiffens the alveolar-capillary barrier tissue.

Preferably, the membrane mimics the stiffness of the *in vivo* basement membrane [61]. The stiffness of an alveolar wall ranges in the literature between a Young's modulus of 1 kPa and 300 kPa, but is generally assumed  $< 10$  kPa [20, 30]. Osario et al. [61] for example, stated an elastic modulus of 3.4 kPa in uniaxial tension, and Paman et al. [4] stated a Young's modulus of lung tissue of 400 Pa or lower. It is relevant to note that in the design of a membrane, the overall membrane stiffness should be widely considered next to the material stiffness, since this greatly influences the membrane stretch that can be obtained and transferred to the adhered cells.

Throughout the cell culture the stiffness may vary. When no stretch is yet applied in the first phase, the membrane may be less elastic. In Phase 1 the membrane also largely has a support function and may therefore be stiffer than native alveolar-capillary barrier tissue. The elasticity becomes an important variable and needs to have a significant value when stretch is applied and the membrane is deformed (Fig. 2.7).

### Cyclic stretch

The membrane should be able to sustain cyclic stretch for several weeks to recapitulate the breathing motion. The physiological strain range is between 4% and 12% [20, 29]. Strains over 20% are considered pathophysiological [34, 35]. Since an adequate membrane should be able to recapitulate the complete (patho)physiological strain range, a strain of at least 20% must be sustained by the membrane in order to be able to mimic the whole range of physiological breathing movements and to also be able to recapitulate a pathophysiological environment.

The cyclic stretch, which exerts a strain on the cells, influences multiple cellular behaviours [15]. Due to the strain, cells experience mechanical forces at their focal adhesions. From there on, this signal is transmitted to the cytoskeleton, which remodels accordingly [50]. Cyclic stretching enhances the formation of tight junctions [30]. Furthermore, it influences: pulmonary epithelial cell proliferation; differentiation; surfactant secretion; and migration [20]. It also influences disease onset and advancement. These effects occur since mechanical stimulation affects specific signalling pathways, which influence gene expression and protein synthesis [20]. For example, a strain between 15% and 20% on endothelial cells increases fibroblast growth factor release, activation of monocyte chemotactic and activating factor (MCAF/MCP-1), and production of the inflammatory cytokine IL-8 [35]. Besides that, overstretching of the alveolar membrane can cause a disruption of the tight junctions, causing damage to the cell monolayer and loss of cells [20, 35]. This increases vascular leakage, which can lead to oedema [33]. Thus, mechanical stimuli are vital in recapitulating the (patho)physiological circumstances to study the effect of possible treatments in an *in vitro* environment [20].

The type of cyclic stretch is often a sinusoidal cyclic stretch, as applied by Doryab et al. [20] and Stucki et al. [41], but it can also be a triangular cyclic stretch, as applied by Nissar [1] and Stucki et al. [22] three years

later. The cyclic motion mimics the breathing motion, generally with a frequency of 0.2 Hz [13]. The type of strain (1D, 2D or 3D), its magnitude and frequency all significantly influence cell behaviour [50]. Various types of strain are present in LOC devices, as discussed in the Literature Review. Biaxial or triaxial stretch simulates the *in vivo* environment more closely than uniaxial stretch. Huh et al. [15] observed that cells align to the loading direction perpendicularly when uniaxially stretched. This does not resemble the *in vivo* cell behaviour and thus, biaxial or triaxial stretching should be selected over uniaxial stretching. In contrast, there is little information present in the literature on whether cells behave differently when subjected to a two-dimensional or three-dimensional stretch and whether this influences how well cells can be cultured.



Figure 2.9: Schematic illustration of media and gas flow alongside an in-plane stretched membrane and an out-of-plane stretched membrane. Red arrows indicate the stretching direction.

Out-of-plane biaxial or triaxial stretching, or bulging, of small diameter membranes, does resemble the *in vivo* type of stretching since the alveoli also exhibit a bulging of the membrane. However, often devices can not provide a media flow at the same time as bulging the membrane [41], because the same chambers are used for both purposes. Furthermore, if a media flow is provided, the shear stress exerted by the fluid flow passing by the membrane exerts a different effect on out-of-plane stretched membranes than on in-plane stretched membranes. The media will flow parallel to the membrane for in-plane stretched membranes, creating a uniform shear flow over the membrane. In out-of-plane stretch, the flow will not uniformly exert a shear on the membrane since the channel itself will not deform along with the membrane (Fig. 2.9). This creates areas where shear stress will be higher than other areas. In the human body, the pulmonary vessel can generally be assumed to also deform along with the alveolar membrane, avoiding these local variations in shear stresses (Fig. 2.10).

Although the fluid flow in these devices is generally low, this aspect still needs to be considered. Besides that, on larger diameter membranes bidirectional in-plane stretching exerts roughly the same effect as triaxial out-of-plane stretching, regarding the applied surface area strain. Therefore, an in-plane biaxial stretch is best applied to the membrane. Furthermore, in a membrane that uses a bulging stretch, there is at least one actuation channel that exerts the pressure difference needed to bulge the membrane. Since this research aims to have two channels with medium flow (both gas and liquid), two flow channels should be present. The actuation for this membrane stretch is therefore controlled *via* separate actuation channels that run around the sides of the membrane (Fig. 2.4).

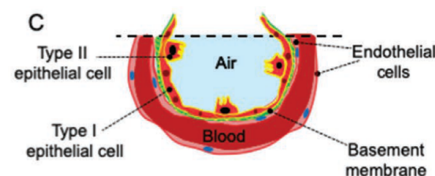


Figure 2.10: Schematic of the alveolar-capillary barrier [30].

### The air-liquid interface and shear stress

The ALI is an essential feature of healthy lungs. An ALI consists of the epithelial cell layer, on which a thin liquid surfactant layer is present and its boundary with the air. This surfactant layer separates the epithelial cells from the air [11]. The presence of air increases surfactant production, which is crucial in maintaining the stability of the membrane [10, 11]. Furthermore, including airflow also introduces a more biomimetic permeability by decreasing the surface tension [10].

Douville et al. [46] note the importance of including both solid and fluid stresses within the device. Besides cyclic membrane straining, the LOC should also include a media flow on the basal side of the membrane and a gas flow on the apical side. Both flows, especially the media flow, can exert a shear stress on the adjacent cells, and this may play a role in the mechanoregulation of the cell layers [19]. It also plays a vital role in pathology, and disease mechanisms [46].

In conclusion, the LOC device should include both an ALI and physiological shear stress. The shear stress exerted on endothelial cells due to blood flow ranges between 0.28 – 9.55 N/m<sup>2</sup>, with a mean value of 1.54

$\text{N/m}^2$ . The shear stress in the smallest capillaries is in the higher range [28]. Besides mimicking the physiological shear stress, the ALI should remain intact under cyclic stretch: no medium leaches to the air interface side; and no cells detach from the membrane [30]. Furthermore, an open reservoir generally makes it difficult to create fluid stresses by a pressurized fluid flow, so the fluid channels should be able to be closed off if a pressurized fluid flow is desired [46].

### Handling requirements

Various handling requirements also need to be met to make the chip suitable for laboratory use. These requirements include the possibility for direct on-chip cell seeding, confocal microscope analyses, ease of use and membrane recovery. Furthermore, the membrane needs to be designed such that it can be reproducibly manufactured. A closed chip configuration is unfavourable regarding the standard handling principles applied in both the Erasmus Medical Center (EMC), as well as in laboratories and the pharmaceutical industry [52]. Therefore, an open chip configuration is preferred to practically seed the cells on the chip and allow live imaging. The device prior designed by the PME Department [1] contains a resealable chip configuration that can later be opened when cell seeding or imaging is done.

The device, including its membrane should also be sterilizable. At the EMC this is done with 70% ethanol or 5%  $\text{H}_2\text{O}_2$ . Also Jin et al. [53], Tas et al. [34] and Shresta et al. [10], for example, used these sterilization methods. Other sterilization techniques found in literature include: ultraviolet (UV) sterilization [3, 16, 46, 51], ozone sterilization [5, 41], ethylene oxide [62] or a combination of ethanol and peracetic acid [63].

### Cell culture

The chip is designed for studies ranging from 2 to 4 weeks. At a breathing frequency of 0.2 Hz a study of four weeks contains just less than  $5 \times 10^5$  stretching cycles. Therefore, the membrane must maintain its intended properties for this duration at least. The type of cells that are desired to be cultured on the membrane are primary endothelial and epithelial cells. Since these cells are relatively hard to culture, also cancer cells could be tested initially in order to obtain a proof of concept.

### Membrane integration

The membrane should be detachable after the cell culture experiments to allow for additional testing. The membrane integration should therefore allow for suitable membrane removal. Besides that, the membrane integration should be robust enough to resist and prevent leakage or membrane detachment during cyclic stretching.

The requirements presented above should ideally all be taken into account when designing an adequate membrane for a LOC device.

## 2.5. Membrane material

The mechanical characteristics of a membrane, such as the geometric stiffness, elastic modulus, viscoelasticity, surface hardness, tension and compression, and shear stress all influence cell activity [55]. Additional characteristics that are important in LOC membrane design include: optical transparency; the flexibility of the material; whether it ab- or adsorbs small molecules, and whether it is biocompatible and sterilizable. PDMS has been a widely used material in LOC devices, but it exhibits a range of disadvantages. This Section first discusses the disadvantages of PDMS, before the selected alternative material is introduced in Section 2.5.2, based on the requirements introduced in Section 2.4. Further background information on the various material groups that have been used as LOC materials, and their advantages and disadvantages is included in Appendix E in Chapter 3 on the materials and manufacturing methods for LOC devices.

### 2.5.1. The downside of PDMS membranes

Most OOC models are made of PDMS as their main structural and cell-interacting component [2, 5, 7, 8, 34, 39]. PDMS is a soft and versatile polymer [64]. Its elastic modulus is generally around 1 MPa, but its stiffness can accurately be controlled between 0.8 MPa and 10 MPa, while still allowing 20% uniaxial strain [64]. PDMS can be used in a broad range of temperatures, spanning from  $-100^\circ\text{C}$  to  $200^\circ\text{C}$  [64]. To fabricate PDMS structures, generally soft-lithography is used.

Using PDMS has several advantages; it is elastic, optically transparent, biocompatible, bioinert and has relatively good mechanical characteristics [5, 7, 16, 64]. Its biocompatibility allows for long-term cell cultures [7].

Moreover, its flexibility allows recapitulating the strain and elasticity present in native tissues [7]. Furthermore, it has an excellent gas permeability, which is needed in an alveolar membrane [7, 40]. Besides that, it is easy to mould and to use in soft-lithography, and it has low material costs [7, 8].

Although this makes PDMS seem like a very suitable material for a LOC device, there are several drawbacks. It is hydrophobic, so it needs surface treatment to enhance wettability, and cell adhesion [30]. Besides that, it has high adsorption and absorption of small hydrophobic molecules. Especially when there is a large surface-to-volume ratio, as is the case with a membrane. This ad- and absorption limits its application in drug evaluation studies [5, 7, 8]. When the PDMS absorbs these molecules, there is (1) a reduction in the drug or cell-signalling compounds that exert an effect on the cell culture, (2) cross-contamination, (3) increased background fluorescence, and this all impairs accurate interpretations of the drug toxicity and efficacy/dose-response effect, thereby limiting drug evaluation studies [7, 8]. Furthermore, uncured oligomers present in the PDMS can leach out into the surrounding environment [8]. Moreover, its intrinsic stiffness (1 MPa vs 2 kPa) and molecular composition are distinctly different from alveolar lung tissue [5]. It also has a high water vapour permeability, which causes osmolarity shifts and thus influences homeostasis [8]. Additionally, it is autofluorescent to some extent, and it is incompatible with organic solvents [7]. Finally, it also poses a challenge when high volume manufacturing is desired due to the development time when using master moulds [7, 8].

Therefore, materials other than PDMS need to be analyzed to create a new membrane design. For devices that recapitulate the physiological motion of breathing, highly elastomeric materials are desired [15]. Besides that, the membrane material must still be optically clear to facilitate high-resolution microscopic analyses [8]. Possible material groups include hydrogels, such as Matrigel or CE/gelatin hydrogels. Moreover, in order to create more elastic membranes that still have a diminished small molecule absorption, elastomeric materials such as polyurethane, styrene-ethylene-butylene-styrene (SEBS), tetrafluoroethylene-propylene (FEPM), polyethylene glycol diacrylate (PEGDA), POMaC, or itaconic acid-crosslinked poly(octamethylene citrate) (PICO) can be used [7].

### 2.5.2. An alternative material: POMaC

The most promising biomaterials for tissue engineering, according to Wang et al. [65] and Davenport Huyer et al. [66], are polyester biomaterials, which are a class of synthetic biodegradable polymer materials. This is due to their controllable mechanical properties, good biodegradation and biocompatibility [65, 66]. Notable polyester materials approved by the Food and Drug Administration (FDA) include polycaprolactone, poly(glycolide) (PGA), poly(L-lactide) (PLLA) and poly(lactic) acid (PLA), but their use in soft tissue engineering is limited due to their high stiffness [66, 67].

Compared with traditional biodegradable synthetic polymers, citrate-based polymers, such as the poly(octamethylene citrate) (POC) polymer, exhibit various advantages: simple synthesis; controllable structure; good biocompatibility; and the capacity for additional functional modification [65]. However, further functionalization of POC polymers is necessary since the conventional POC polymer is water-insoluble and limited with a narrow scope of mechanical properties, bioactivities and functions [65]. Therefore, many variations of citrate-based elastomers have been created. A very promising POC-based material for soft tissue applications is POMaC, which provides large material elongation (up to 534 %), controlled physical structure and properties, while maintaining good biocompatibility [65]. This material was developed by Tran et al. [67], by replacing maleic acid by maleic anhydride.

Several advantages of using POMaC include:

(1) The POMaC polymer network structure recapitulates the natural tissue structure. Collagen and elastin are crosslinked polymers that provide elasticity to the natural ECM in the same way that crosslinks in POMaC confer elasticity [67].

(2) Moreover, fabrication employs a simple synthesis method under mild conditions. UV crosslinking gives the advantage of short polymerization times and facilitating a wide range of geometries [67].

(3) Additionally, the dual crosslinking method and monomer ratio give rise to controllable mechanical and degradable properties [68]. The formed ester bonds are degradable by hydrolysis [57]. Their presence in the polymer backbone and as crosslinks provides degradability to the crosslinked polymer network [67]. The mechanical and degradation properties can also be further fine-tuned by adjusting the monomer ratio [67].

(4) A fourth advantage is that the monomers are inexpensive and widely used in biomaterials [67]. Citric acid participates in the pre-polymer formation through a simple polycondensation and it provides pendant functional groups within the biomaterial [67]. Available pendant functional groups (free -COOH and -OH groups) can not only be utilized to form ester bonds, but they can also be modified with a variety of biologically relevant factors, controlling cell adhesion and function [67]. The next Section will provide more detailed information on POMaC.

### 2.5.2.1. Background information

POMaC is a citrate-based polyester thermoset elastomer which closely mimics the mechanical properties of a wide range of soft biological tissues [67]. Citric acid is part of the tricarboxylic acid cycle [65]. Citrate-based biomaterials have become an important tool in advances in biomaterials science and engineering due to their versatile material and biological characteristics such as unique antioxidant anti-inflammatory, antimicrobial, adhesive properties [69] and low thrombogenicity [57, 65]. These elastomers possess controllable mechanical properties, good biodegradability and excellent biocompatibility and angiogenesis ability, which is foundational to their use in biomedical applications [65]. POMaC is an elastomer which minimizes, though not fully eliminates, small molecule absorption [7].

POMaC consists of the inexpensive monomers citric acid, maleic anhydride and 1,8-octanediol and it exhibits a dual crosslinking mechanism [67]. It can be cured by UV photopolymerization and/or by thermal crosslinking [67] [65], allowing for rapid assembly [57]. These different curing methods are shown in Figure 2.12.

The pre-polymer (pre-POMaC) is fabricated by mixing the monomers and heating the mixture at 140°C for several hours under nitrogen conditions, initiating a polycondensation reaction (Fig. 2.11). In this reaction which builds up the polymer backbone, ester bonds are formed between the monomers and H<sub>2</sub>O is released [67]. The specific build-up of the pre-POMaC backbone is shown in Figure 2.12. The ester bonds in the backbone are shown in blue and the vinyl carbons which remain from the maleic anhydride in red. A carboxylic acid (-COOH) group and a hydroxyl (-OH) group (shown in green) are remaining pendant functional groups from the citric acid. These pendant functional groups can be utilized to form additional degradable ester crosslinks, or to modify the polymer with a wide variety of biologically relevant factors such as proteins, polypeptides or antibodies, which control and promote cell proliferation and adhesion [65, 67]. After the heating step, the pre-POMaC is separated by precipitation [68].

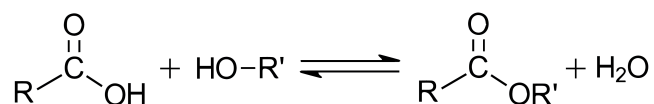


Figure 2.11: An overview of the polycondensation reaction which takes place when ester bonds are created in the polymer, upon heating of the material.

The pre-POMaC can be further polymerized *via* a dual crosslinking mechanism. Additional ester crosslinks can be formed by heating the pre-POMaC (Fig. 2.12 C), in a polycondensation reaction *via* the free functional groups (green) creating ester bond crosslinked POMaC (EPOMaC) [67]. Another crosslinking mechanism, initiated by UV light, is carbon-carbon crosslinking *via* free radical polymerization, forming photocrosslinked POMaC (PPOMaC) (Fig. 2.12 B) [67, 68]. This crosslinking mechanism takes place *via* the vinyl group (red) and consists of an initiation, a propagation and a termination step.

In the initiation step, the increased energy level due to UV light breaks molecular bonds within the added photoinitiator, which leaves each remaining side of the initial molecule containing a free radical. This reaction for two photoinitiators, 2-hydroxy-1-[4(hydroxyethoxy)phenyl]-2-methyl-1 propanone (Irgacure 2959) and diphenyl-2,4,6-trimethyl benzoyl phosphine oxide (TPO), are shown in Figures 2.13 A and 2.13 C respectively [70–72]. In the propagation step, the cleaved molecule containing a free radical reacts with the vinyl group within the pre-POMaC, creating carbon-carbon crosslinks, according to the reaction shown in Figure 2.13 B [72]. This chain reaction is terminated when a free radical encounters a second free radical, forming a stable bond. The chemical structure of both a vinyl group and an ester bond are shown in Figure 2.14.



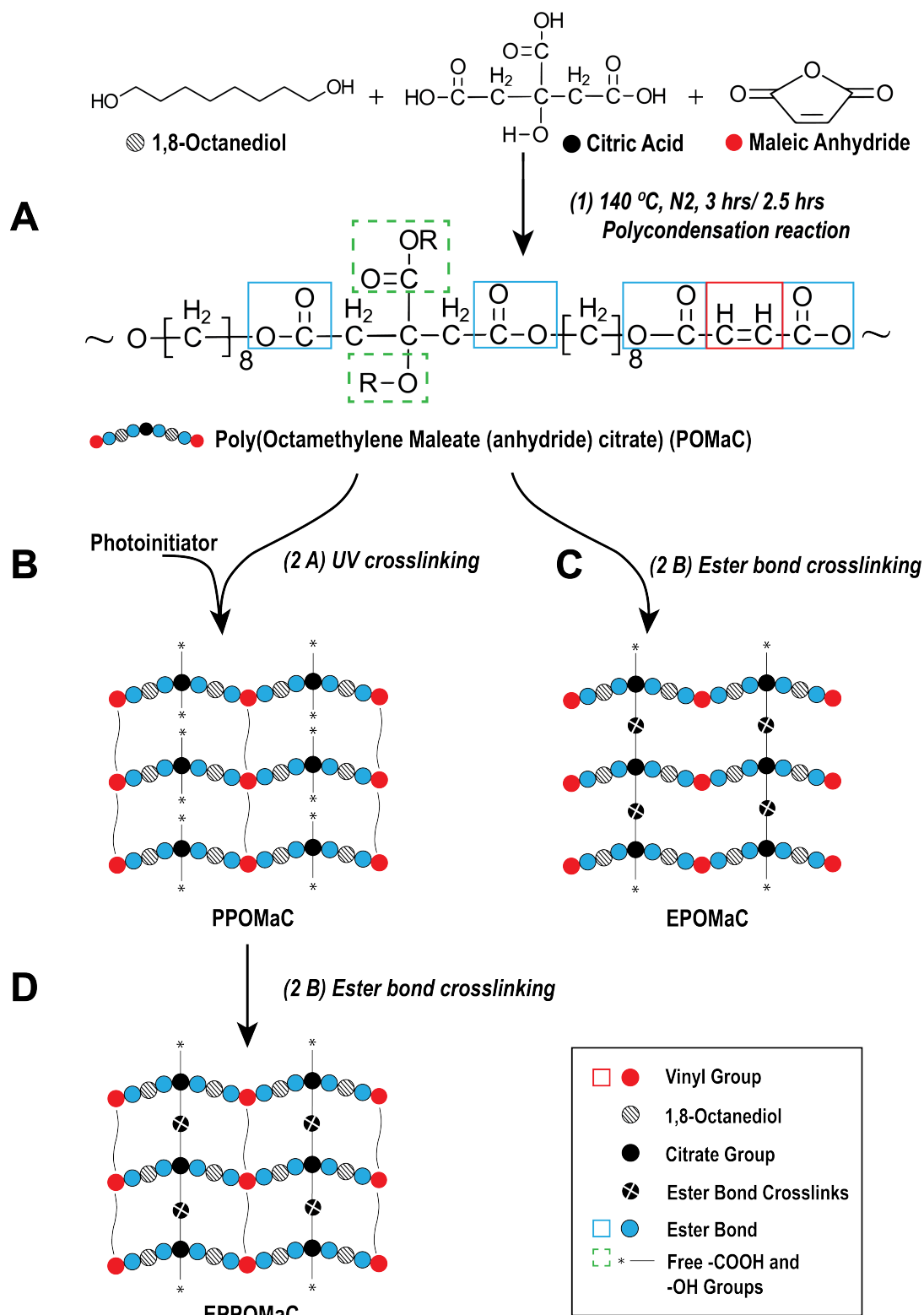


Figure 2.12: A schematic overview of the POMaC synthesis and crosslinking mechanisms. (A) The monomers citric acid, maleic anhydride and 1,8-octanediol undergo a polycondensation reaction, building the polymer backbone and incorporating vinyl carbons (red) and ester bonds (blue). Free functional groups remain present (green). (B) After addition of a photoinitiator to the pre-POMaC, with UV light exposure free radical polymerization is initiated. The polymerization happens through the vinyl bonds (red), creating PPOMaC. Free functional groups remain present (green). (C) A second crosslinking mechanism for pre-POMaC is through polycondensation, providing EPOMaC through the free functional groups of citric acid (green). (D) After UV photopolymerization, the PPOMaC can be further crosslinked through free functional groups (green) creating EPPOMaC. Based on Tran et al. [67], Zhang et al. [73] and Boutry et al. [68].



During photopolymerization, the free functional groups remaining from citric acid are not yet utilized, and these can subsequently be used in post-polymerization to form ester bonds in a polycondensation reaction. This combination creates ester bond crosslinked photocrosslinked POMaC (EPPOMaC) (Fig. 2.12 D) [67].

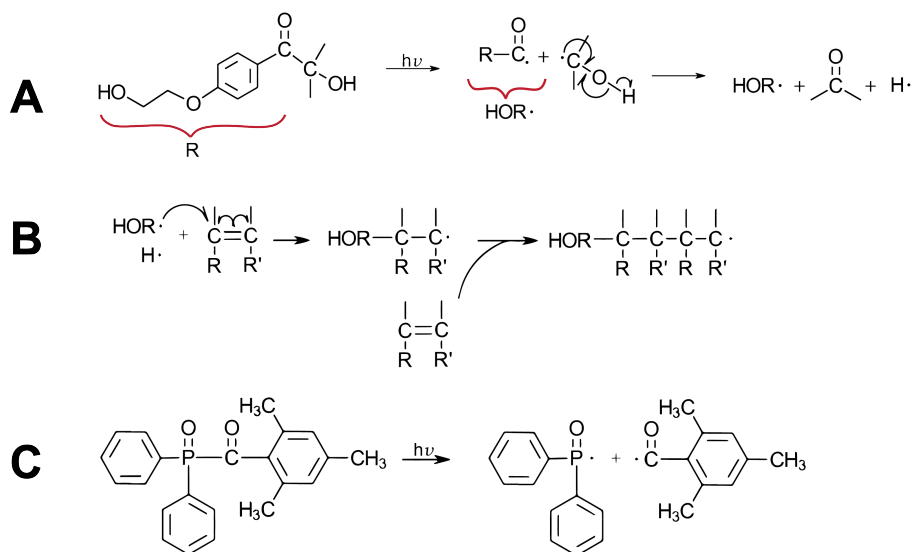


Figure 2.13: An overview of the photopolymerization mechanism. (A) Initiation step of the photoinitiator Irgacure 2959.

The molecule is cleaved upon UV irradiation presenting free radicals within the material. Based on Zhang et al. and Liang [70, 72]. (B) Propagation step of the photoinitiator Irgacure 2959. The molecules containing a free radical react and bond with the vinyl groups, initiating a chain reaction throughout the material due to the remaining presence of free radicals. Based on work of Liang [72]. (C) Initiation step of the photoinitiator TPO. The molecule is cleaved upon UV irradiation presenting free radicals within the material. The propagation mechanism is similar to the reaction shown in

B. Based on Ruhland et al. [71].

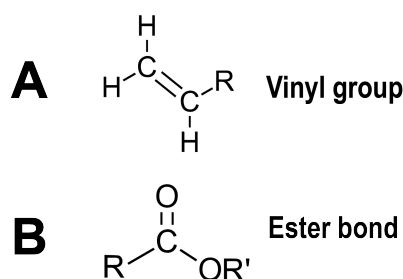


Figure 2.14: (A) a vinyl group and (B) an ester bond.

The most used photoinitiator for POMaC is Irgacure 2959 [67]. In combination with POMaC, it has been used in a concentration of 1 wt% [67, 68] and 5 wt% [52, 66, 74]. Another photoinitiator widely used in curing polymers is TPO. TPO has a relatively high photoinitiation efficiency, which could leave relatively fewer unreacted free radicals within the polymer [75]. Moreover, Irgacure 2959 is suitable for hydrophilic polymers. TPO is suitable for both hydrophilic and hydrophobic polymers. Wang et al. [75] used 1 wt% TPO to cure various prepolymers.

Complete curing of the polymer is critical, as any unreacted photoinitiator and unreacted free radicals might elicit cytotoxic reactions. Moreover, high concentrations of Irgacure 2959 and TPO increase cytotoxicity [75, 76]. Irgacure 2959 at low concentrations ( $\leq 0.015\%$  w/v) was found to be cytocompatible [76]. A 1 wt% TPO concentration in poly(glycerol sebacate) acrylate (PGSA) polymer was also found to be cytocompatible [75].

### Biodegradability

Polymer erosion can be classified as either bulk erosion or surface erosion [77]. In bulk erosion the rate in which water penetrates into the material exceeds the rate in which the polymer is broken down into water-soluble fragments [78]. In surface erosion, the water penetration rate into the polymer is slower than the polymer breakdown into soluble fragments [78]. Therefore, bulk erosion causes a reduction in molecular weight and mechanical strength throughout the specimen (Fig. 2.15 A) whereas, surface erosion results in specimen thinning (Fig. 2.15 B) while preserving bulk integrity and characteristics [77, 78].

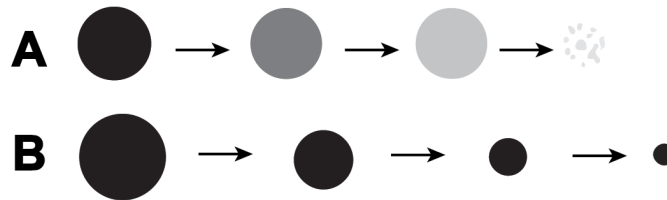


Figure 2.15: Schematic of the degradation behaviour of materials by (A) bulk erosion and (B) surface erosion [77].

Bulk erosion generally occurs in two phases. In the first phase, water penetrates the bulk of the material where it converts long polymer chains into shorter, eventually water-soluble, fragments [78, 79]. This causes a decrease in the molecular weight of the polymer essentially from the beginning of the hydrolytic degradation process [77]. Structural integrity of the matrix is initially maintained due to the remaining (cross)links. This molecular weight reduction is followed by a decrease in the mechanical and physical properties as water begins to fragment the material [78]. Mass loss is notably delayed until short chain fragments are fully detached from the polymer network [77]. Expectedly, the loss in material strength precedes mass loss [77]. The second phase includes enzymatic attack on the short polymer fragments [78, 79]. Metabolizing of these fragments results in rapid polymer mass loss. [78]. This order of events is illustrated in Figure 2.16 A.

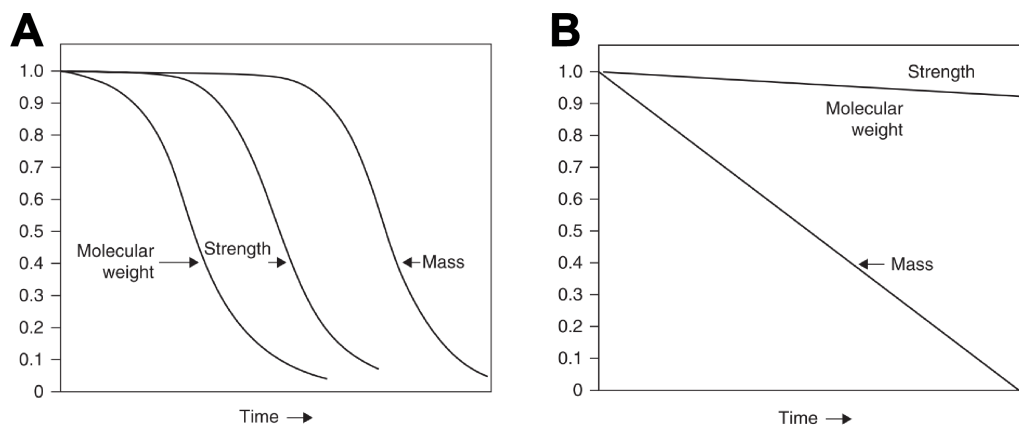


Figure 2.16: Generic curves illustrating the sequence of (A) the bulk erosion process and (B) the surface erosion process of degradable polymers over time [77, 78].

In surface erosion, the degradation reactions are limited to the surface of the polymer and the rate of hydrolysis of bonds is relatively fast compared to the diffusion rate of water into the bulk material [77]. Slow loss of mechanical strength relative to mass loss occurs meaning that a material maintains almost its full mechanical strength over the course of degradation [80]. Both the mass and mechanical strength decrease linearly over time, where mass loss precedes the loss of mechanical strength and molecular weight which remain about the same over time (Fig. 2.16 B) [77, 80].

Most biodegradable polyesters that are currently available, such as PLLA, PLA, or PGA, degrade by a bulk erosion process which predominantly involves simple hydrolysis of main chain (carboxylic) ester bonds [77–79, 81]. Although, some polymers undergo surface erosion characteristics: polyanhydrides and poly(orthoesters),

due to their very hydrolytically labile bonds (which react rapidly with water) in the polymer backbone [77]. This surface erosion is due to more hydrophobic parts that limit water penetration into the bulk material, limiting the hydrolysis of the ortho ester bonds to the surface layer and hydrolysis of the labile bonds too fast to allow water penetration into the bulk material [82]. For example, poly(glycerol sebacate) (PGS) has been reported to undergo surface erosion *in vivo*, by an unknown mechanism [83], exhibiting slow loss of mechanical strength relative to mass loss [80]. PGS also has the main degradation mechanism of cleavage of the ester linkages [80].

Literature reports that the degradation behaviour of POMaC is based on surface erosion instead of bulk erosion, thus in a layer-by-layer manner [66–68, 84], which allows for a linear loss of mechanical properties during degradation [84]. This makes POMaC especially suited for applications requiring mechanical strength and stretch fatigue resistance [84]. Daniele et al. [85], whose research is yet to be peer reviewed, found a linear mass loss of POMaC, with a mass loss rate of ~0.02% and ~1.7% in deionized (DI) water and phosphate buffered saline solution (PBS) respectively [85].

POMaC is an organic material exhibiting biodegradability, allowing for decomposition by cells. Its breakdown products are fully soluble [67]. In addition, POMaC exhibits excellent biocompatibility upon degradation [68]. POMaC undergoes biodegradation by hydrolysis of carboxylic ester bonds (Fig. 2.17 A), due to scission of hydrolytically unstable bonds in the polymer backbone and ester bond crosslinks [57, 67].

The carbon-carbon bonds created by UV crosslinking are generally not considered to be degradable bonds, as no labile bonds are present [77]. However, due to *in vivo* cellular action (enzymatic activity, cellular degradation), such bonds could undergo scission in which radical species are formed [77]. Moreover, the bonds present in the polymer backbone mainly exist of hydrolysable ester bonds.

The presence of hydrophilic degradable copolymers within the polymer network provides an increased degradation rate with respect to many polyethylene glycol (PEG) hydrogels [67].

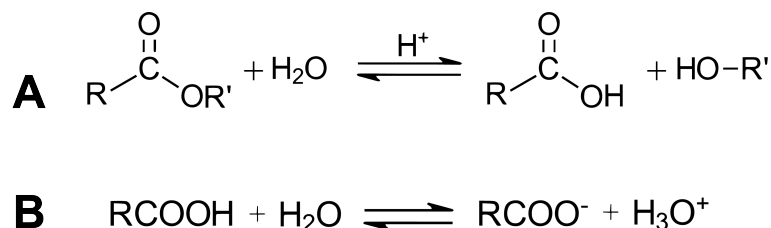


Figure 2.17: (A) Overview of the hydrolysis reaction, where ester bonds are broken down to a carboxylic acid and an alcohol group. (B) A carboxylic acid group can act as a proton donor [86].

The rate of ester bond degradation is influenced by the pH level, since the ester bonds are affected by acidic ( $\text{H}_3\text{O}^+$ ) or basic ( $\text{OH}^-$ ) species [81, 87]. For this reason, for example, Tran et al. [67] could find increased degradation rate of POMaC in NaOH solution when compared to a PBS solution. Upon degradation, a carboxyl group ( $-\text{COOH}$ ), (Fig. 2.17 A) is present in the network. Carboxylic acids are Brønsted-Lowry acids since they are proton ( $\text{H}^+$ ) donors (Fig. 2.17 B) [86, 88]. Weak acids such as these typically only partially dissociate into their conjugates in neutral aqueous solutions. POMaC degradation could be slightly autocatalytic since one of the reaction products, the carboxylic acid end group ( $-\text{COOH}$ ) accelerates the hydrolysis reaction by serving as proton donor, and since  $\text{H}^+$  acts as a catalyst in this reaction, it enables the acid-catalyzed reaction mechanism [81, 89, 90].

This auto-catalytic effect of the presence of carboxylic acid end groups in polymers, was also reported by Tracy [91] who noticed that water uptake and degradation rate increased when replacing ester end groups with carboxylic acid end groups since these acid end groups enhance the hydrophilicity of the polymer and act as a catalyst in degradation [78]. Presumably, POMaC would also exhibit this auto-catalytic effect, since the method of degradation is also primarily by carboxylic ester hydrolysis and thus largely comparable.

Both the mechanical and degradation properties of citrate-based elastomers, such as POMaC, can be controlled by adjusting the molar ratio of the initial monomers, and the crosslinking method, temperature and

time during synthesis and curing [65] since this has an influence on the type of polymer bonds, their density, and the average molecular weight of the polymer. Increasing the crosslinking time, for example, increases the crosslinking density [65]. The crosslinking density of a polymer influences the strength of the material, the degree of swelling, and the diffusion of a solute through the material which influences the rate of degradation [92]. Tran et al. [67] found that when increasing crosslinking through ester bond formation resulted in longer degradation rates. Moreover, the average molecular weight of the formed polymer is dependent on the POMaC synthesis and curing procedure. A lower average molecular weight (shorter chains) increases the degradation rate [81].

Adjusting the monomer ratio also influences the rate of degradation. For example, the rate of degradation heavily relies on the citric acid monomer ratio [57]. Increasing citric acid content increases the number of hydrolysable ester bonds and thus increases degradation rate. On the other hand, a higher maleic anhydride ratio results in slower degradation since this provides more non-hydrolysable photocrosslinks [67].

Photocrosslinks within the material that are non-hydrolysable remain during degradation and maintain the mechanical cohesion [68]. This means that POMaC cured only by ester bond crosslinking and missing these non-hydrolysable crosslinks, has a higher degradation rate than also photocrosslinked POMaC [68]. For this reason, the curing method also has an influence on the degradation rate, since that influences the presence and density of hydrolysable ester bonds and non-hydrolysable carbon-carbon crosslinks. This difference in degradation rate for POMaC with different monomer ratios and curing method can be observed in the degradation rates found by Tran et al. [67], where *PPOMaC 4* (citric acid: maleic anhydride: 1,8-octanediol ratio of 3:2:5, resp.) was degraded by  $77.50 \pm 1.93\%$ , and *EPPOMaC 8 (2 days)* (1:4:5 ratio, resp.) degraded only  $18.45 \pm 4.44\%$  by week 10 in PBS [67].

A further indication of the degradation rate is given by Zhang et al. [57] who found that their 50  $\mu\text{m}$  thick POMaC channel wall did not degrade appreciably in one week. Furthermore, biodegradation studies showed that POMaC polymer disks (8 mm diameter and 1 mm height) persisted *in vivo* for at least 5 weeks [57]. In general, polymer degradation is accelerated by a greater hydrophilicity in the polymer backbone or end groups and greater reactivity among hydrolytic groups in the backbone [78].

Other factors affecting degradation include: flow rate; strain; porosity; temperature; composition and enzymes [81]. According to Urbina et al. [79] multiple studies reported that the rate of hydrolysis increases faster at a higher temperature [79, 81]. Moreover, degradation rate can be increased by the presence of cells within the cell culture due to the action of various enzymes [65]. For example, fungi and bacteria can further assimilate the degraded polymer [79].

### 2.5.2.2. Additional material specifications

Several other relevant parameters of POMaC include: the elastic properties; biocompatibility; optical transparency and fluorescent properties; swelling properties and the bonding ability to other materials. This Section elaborates on these aspects and the information present in literature.

#### Elastic properties

POMaC is able to closely mimic the mechanical properties of a wide range of soft biological tissues due to its relatively low stiffness [67]. The material properties, such as the stiffness and the degradation profiles of POMaC, depend on the monomer ratio, the UV and heat exposure, and additions of porogens [57, 67]. For example, Tran et al. [67] found that upon reduction of the maleic anhydride molar concentration the elastic modulus decreased, the elongation at break increased and the crosslinking density decreased [67]. Zhang et al. [57] reported a stiffness range of POMaC between  $53 \pm 8$  to  $1423 \pm 651$  kPa. Tran et al. [67] reported a range between 0.03 and 1.54 MPa, with an ultimate tensile strength of  $\sim 0.99$  MPa. The elongation at break was reported by Tran et al. [67] to be between 48% and 534% strain. Boutry et al. [68] could apply a constant strain of 10%, releasing to 5% strain, to POMaC for 20,000 cycles. As stated, these values depend on the type of POMaC and fabrication method chosen.

#### Biocompatibility

POMaC has good cell and tissue biocompatibility, according to *in vitro* and *in vivo* evaluation conducted by Tran et al. [67] on EPPOMaC discs, who reported good cell adhesion and proliferation of 3T3 fibroblasts. Also research by Boutry et al. [68] found excellent biocompatibility in *in vitro* and in *in vivo* rat models, with stable operation over 2 to 3 weeks. Zhang et al. [57] found that one week after implantation of the AngioChip

cardiac tissues, native angiogenesis occurred around the implant. Moreover, the cardiac patch fabricated by Montgomery et al. [65] possessed vascularization, macrophage recruitment, and cell survival comparable to those of surgical patches.

POMaC has predominantly been utilised with cardiac cells. Zhang et al. [57] focused mainly on cardiac and hepatic (liver) cells and studied them on POMaC for 7 days, creating a fully endothelialized lumen within their scaffold. Also Zhao et al. [93] focussed on culturing cardiac cells. The cells cultured on POMaC so far include: human mesenchymal stem cells (hMSCs) [57]; human embryonic stem cells (hESCs) [57]; HUVECs [57]; Primary rat hepatocytes mixed with primary rat fibroblasts [57]; NIH 3T3 fibroblasts [67] and human cardiac fibroblasts (cFBs) [93]. A study with epithelial lung cells has not yet been conducted to the author's knowledge.

Three different ECM proteins have been used as coating to effectively support cell adhesion on POC scaffolds: fibronectin; laminin; and collagen [65]. Regarding sterilization of POMaC, steam sterilization is not possible since the penetrating high pressure steam would initiate hydrolysis of the polymer [81]. In addition sterilization by irradiation could adjust the mechanical properties by influencing the degree of crosslinking [81]. POMaC has been sterilized by using 70% ethanol [67].

### Bioimaging properties

POMaC is an optically transparent material, and Zhang et al. [57] used confocal microscopy to image cells. Furthermore, regarding the fluorescent properties of POMaC, Zhang et al. [57] reported no limitation. An image of their set-up under fluorescent light is shown in Figure 2.18, where the cultured endothelial cells are seen to light up green. Zhao et al. [93] reported an intrinsic autofluorescence when illuminated with blue light ( $\lambda_{ex} = 350\text{nm}$  /  $\lambda_{em} = 470\text{nm}$ ). Citrate-based elastomers exhibit good photoluminescence characteristics upon functional modification with for example, amino acids, siloxanes or polyamides, due to their specific chemical structures [65, 69].

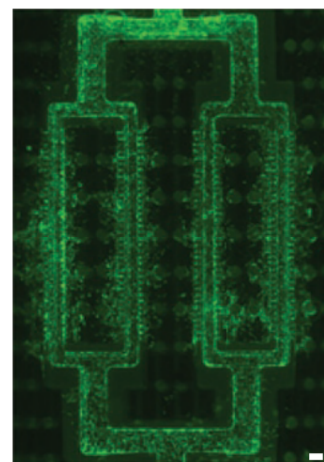


Figure 2.18: Fluorescent image of endothelial cells (green) on the AngioChip. Scale bar, 100  $\mu\text{m}$  [57].

### Swelling properties

Tran et al. [67] calculated the swelling properties of POMaC in dimethylsulfoxide (DMSO) and PBS using its dry and wet weight. Their results showed that EPPOMaC showed the least swelling, followed by EPOMaC and PPOMaC, respectively. Moreover, swelling is inversely related to the concentration of maleic anhydride in the polymer network and to the duration of the ester bond crosslinking time [67]. They found that swelling in PBS for EPPOMaC (UV irradiated for 10 minutes) decreased after heat curing for 2 days instead of 1 day, from around 150% to around 50%, respectively [67].

### POMaC bonding to other materials

To integrate the designed membrane into the LOC device, a strong and elastic integration bond is needed between the POMaC membrane and the PDMS device. Zhang et al. [57] reported that POMaC exhibits strong (temporary) adhesion to glass and a weak adhesion to PDMS. Zhang et al. [57] reported that POMaC exhibited a weak adhesion to PDMS when being photo-crosslinked on PDMS, due to oxygen-induced inhibition of the free radical polymerization on the POMaC surface connected to the PDMS. This creates a non-polymerized POMaC layer at this interface, causing the weak adhesion [57].

It is important that the bond between the POMaC membrane and the PDMS device does not impede the material elasticity. The place on the edge of the membrane where the materials should bind is also the place where the actuator is located which stretches the membrane. This stretching happens by creating a negative pressure which strains the membrane and the actuator part of the chip (Section 2.6). Thus an elastic bond is essential. Montgomery et al. [74] used cyanoacrylate glue to bind POMaC and PDMS together in tensile tests. However, this bond is a rigid non-elastic bond, and therefore this bonding method was discarded.

### Previous applications of POMaC

Citrate based materials have been used as a new type of surgical fixation biomaterial 'Citregen' in order to promote tissue healing after material degradation. This material has been approved by the FDA for fixation screws and it manufactured and sold by Acuitive Technologies, Inc. [65]. Several examples of cell constructs for which POMaC specifically has been used are the fabrication of a scaffold for parenchymal cells, called the AngioChip by Zhang et al. [57]. This scaffold was fabricated using a 3D stamping technique using a layer thickness of 25  $\mu\text{m}$  [57]. Tran et al. [67] utilised a PDMS mould to cure the POMaC and form a microchannel for tissue engineering applications. Moreover, Boutry et al. [68] made an implantable pressure and strain sensor covered by POMaC, and Zhao et al. [93] used POMaC in their Biowire II platform as a wire around which cardiac cells could attach to enable drug testing under electrical pacing. POMaC has been broadly used for cardiac tissue engineering and vascular engineering due to its excellent elastomeric mechanical properties [65, 84]. Montgomery et al. constructed a flexible shape-memory POMaC scaffold polymer with a microfabricated lattice to create patches for minimally invasive delivery of functional tissues [65].

## 2.6. Membrane fabrication

OOC devices are typically manufactured using soft-lithography. Other applied manufacturing techniques include electrospinning, micromoulding, microetching, micromilling, solid object printing, 3D printing, photopolymerization, laser etching, and injection moulding [9]. These fabrication techniques are discussed in greater detail in the Literature Review. Furthermore, a LOC device ideally must be produced in a way that is low-cost, high throughput and applicable repetitively. In order to make LOCs low-cost and broadly available, the throughput must be on a significant scale or at least able to scale up. In combination with the material, the manufacturing method has a significant influence on the device's eventual structural resolution and properties. Selecting a correct manufacturing method is therefore of great importance.

The most common fabrication techniques using POMaC are 3D-stamping and soft-lithography by PDMS-POMaC moulding. 3D-stamping of POMaC was used by Zhang et al. [52] for their AngioChip. This technique involves pre-patterning POMaC sheets within PDMS moulds and stamping these sheets layer-by-layer on top of each other on a glass base substrate. POMaC layer thickness went down to 25  $\mu\text{m}$ , with 10 to 20  $\mu\text{m}$  holes [52]. Secondly, since POMaC exhibits weak adherence to PDMS, POMaC can be cured in a PDMS mould and subsequently extracted [52]. This method was applied by Zhang et al. [52], Davenport Huyer et al. [66], Montgomery et al. [74] and Boutry et al. [68], among others.

Another widely used method to create uniform thin films is spincoating. Spincoating has been used with a broad range of polymers such as PDMS, GelMa, or POMaC [1, 13, 94, 95]. Spincoating works by placing a drop of viscous medium on a substrate which is placed under a certain r.p.m. for a specific time, to create a thin film. POMaC has been spincoated and UV cured with a layer thickness of 35  $\mu\text{m}$  on silicon at 500 r.p.m. for 45 seconds and subsequently 1500 r.p.m. for 1 minute [95]. Daniele et al. [85], not yet peer-reviewed, also conducted spincoating experiments with POMaC. They spincoated a POMaC layer of  $412 \pm 13 \mu\text{m}$  with a 20 wt% dextran solution in MilliQ water as a sacrificial layer. In order to control POMaC film thickness, a spreading agent (e.g. dioxane) was deemed necessary. Curing was first done by UV light using 5 wt% Irgacure 2959 as a photoinitiator, and oven post-polymerization was subsequently applied [85]. Various parameters have an effect on the uniformity and stability of the spincoated layer: the type of material and its viscosity during spincoating; the spincoating parameters; the type of substrate and substrate priming; the curing method; and the method of membrane detachment.

### 2.6.1. Fabricating pores

Pores in a membrane are often created simultaneously and with the same manufacturing technique used to fabricate the membrane itself. For example, in soft-lithography, 3D printing and electrospinning, the pores can be formed during the fabrication process. However, these pores generally have a relatively large diameter. In soft-lithography, which uses moulding, pore sizes rarely are below 10  $\mu\text{m}$ . In 3D printing, the printing resolution limits the pore size, which is already a limitation in the fabrication process. Electrospinning gives a wide range of possible pore sizes, depending on, e.g. the spinning time, fibre diameter and material used.

Other fabrication methods used to create pores in LOC membranes include: track etching, laser etched pores, nanosphere lithography (NSL) and block-copolymers. Track etching can fabricate pores ranging from 10 nm to tens of micrometers in diameter with a pore density ranging from 1 to  $10^{10} \text{ cm}^{-2}$  [96]. Laser etching is suited for small surfaces and pores larger than several micrometres [37]. Nanosphere lithography can



achieve a resolution smaller than the conventional photolithography resolution limit of  $2\text{ }\mu\text{m}$ , reaching pore sizes below  $500\text{ nm}$ , relying on the use of self-assembling nanospheres in the etch mask fabrication [97]. The block-copolymer technique uses a combination of block polymers, which microphase-separate. By chemically etching one of the block polymers away, monoliths with a porous structure are fabricated [98]. This technique is suited for relatively small surfaces and mesopores, which are pores between  $2\text{ nm}$  and  $50\text{ nm}$  [99]. However, electrospinning, block-copolymers and track etching give a random pore distribution. As stated in Section 2.4, a uniform pore distribution is preferable to random pore distribution [13]. Moreover, NSL and block-copolymers provide pores much smaller than the  $3\text{ }\mu\text{m}$  to  $8\text{ }\mu\text{m}$  aimed for.

Another approach to create pores is to use a degrading material. This approach was used by Doryab et al. [30] and Huang et al. [13]. Doryab et al. [30] designed a hybrid AOC membrane that was non-porous during cell seeding and the initial growth phase. When cell stretching and an ALI were introduced, the membrane became porous to allow for cell migration and nutrient exchange in a later stage of the cell culture. The membrane was thinner than  $5\text{ }\mu\text{m}$  and made of gelatin and PCL. The membrane was fabricated by spincoating a PCL and gelatin emulsion. The gelatin bubbles present in the PCL membrane initially provide increased surface wettability, favourable in cell adherence and growth. When cells grow and proliferate, they will secrete their own ECM. This ECM will allow the cells to migrate to less wettable materials, in this case, the PCL. Subsequently, they will form a continuous monolayer spanning both the gelatin and the PCL regions. Eventually, the gelatin will gradually degrade, leaving pores in the PCL membrane. This degradation also increases the elasticity since the more elastic PCL will remain, and the stiffer gelatin will dissolve. The pore size ranged between  $1.1$  and  $7.9\text{ }\mu\text{m}$  and had a mean of  $4.5 \pm 1.7\text{ }\mu\text{m}$  [30]. This membrane poses a very interesting and promising approach to the use of biodegradable membranes.

Huang et al. [13] created pores prior to cell culture by creating an inverse opal GelMA structure, recapitulating the *in vivo* alveolar sac dimensions and the interconnecting windows. The structure was created by curing GelMA around alginate microbeads, which were subsequently dissolved. Each alveoli pore had a diameter of  $200\text{ }\mu\text{m}$ , and within their design, they were able to recreate about 7050 alveoli. The total membrane thickness was less than  $3\text{ mm}$ , and the scaffold structure itself had a thickness of  $546.4\text{ }\mu\text{m}$ , which consisted of about three stacked layers of simulated alveoli [13]. Overall, this is a relatively thick membrane (Fig. 2.19).

Like the design by Huang et al. [13], there have been other studies into creating a three-dimensional hydrogel scaffold for lung cells [13, 44, 51]. However, it remains an issue that a three-dimensional scaffold does not directly resemble a membrane. The human body contains a dense network of capillaries encapsulating and wrapping around the alveoli. If a three-dimensional scaffold is created, a design needs to ensure that the scaffold is not too porous or too thick. Simultaneously, thin barriers need to exist between the endothelial and epithelial cells, while nutrients should reach all the cultured cells. This means that a barrier or membrane with limited porosity and thickness should always be present.

#### Micropore fabrication in POMaC

Currently, nanopore fabrication in POMaC is possible with the use of porogen leaching. The AngioChip of Zhang et al. [57] contained both micro and nanopores in the walls. The smallest micropores had a diameter of  $10\text{ }\mu\text{m}$  and was created using 3D stamping techniques. The nanopores, incorporated to further enhance oxygen and nutrient exchange, were created using porogen leaching [57]. Tran et al. [67] fabricated porous POMaC scaffolds by mixing pre-POMaC with 1,4-dioxane and sieved sodium chloride salts in a  $106\text{ }\mu\text{m}$  to  $150\text{ }\mu\text{m}$  size range before curing. By immersion in DI water, the salts were leached out and a porous structure remained.

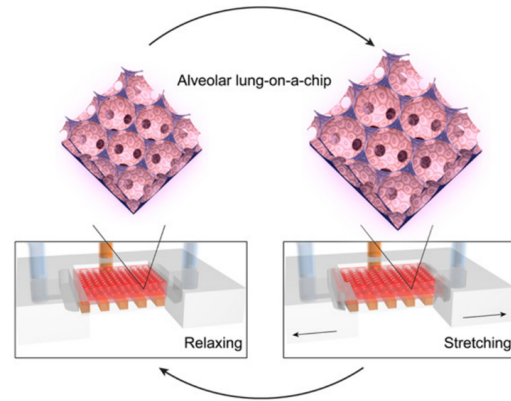


Figure 2.19: The LOC device designed by Huang et al. [13].

### 2.6.2. Membrane integration methods

When no cyclic stretch needs to be applied, a standard integration frequently used with various membrane materials is to sandwich the membrane between two layers of PDMS. These layers are sealed together by slow-curing liquid PDMS between them. This was done by Nalayanda et al. [47], who used a porous PET membrane. This method, however, produces a membrane integration that is often not strong enough to remain intact when cyclic stretching is applied. When using a PDMS membrane in a PDMS device, the integration bond is often a lot stronger than when using different materials, allowing for straining of the membrane. Oxygen or corona plasma treatment can bond the membrane and the rest of the device together. This treatment was done in the devices of both Jain et al. [43], Douville et al. [46] and Nissar [1]. They were able to create a leak-tight membrane undergoing a cyclic bulging stretch.

For the design of a good membrane integration when an in-plane strain is applied on the membrane, several factors play a role: First, the materials of the contact surfaces of the membrane and the device should be compatible. This means that a strong bond between these surfaces should be possible. Second, the strength of this bond can be increased by a larger contact surface area. Last, a clamping device could help with further eliminating any possible leakage.

This chapter provided an overview of different manufacturing methods that are promising, or have been used with POMaC. The next chapter will discuss the proposed concept for the LOC membrane, using the information provided in the previous chapters.





# 3

## Concept introduction

The aim of this research is to evaluate the possibility of creating a membrane with a dynamic pore size, meaning that it features a pore size that increases during the cell culture. This dynamic pore size aims to allow for confluent monolayer formation while also providing immune cell migration across the membrane in a later phase of the cell culture. This membrane could, in future, be used to conduct further research on the effect that pore size has on cell cultures. Based on the Literature Review, summarized in Table 2.3, the aim is to create a membrane that is about 10  $\mu\text{m}$  thick. Pore sizes should start with a diameter smaller than 3  $\mu\text{m}$ , and increase to a diameter between 3  $\mu\text{m}$  and 8  $\mu\text{m}$  once a confluent cell layer has been formed and the ALI is introduced. Moreover, uniform pore size and a homogeneous spatial pore distribution are preferable to randomly distributed pore sizes, and inhomogeneously located pores [4, 13]. The stiffness of the membrane should ideally approach alveolar lung tissue stiffness, to mimic the stiffness of the *in vivo* alveolar wall. Lung tissue has a reported range between 1 kPa and 300 kPa, with most literature stating a stiffness lower than 10 kPa [20, 30]. This Section discusses the concept proposed for an AOC membrane with a dynamic pore size.

### Material

The concept for the membrane designed in this study depends on degradability of the membrane material. The basic concept of the membrane is that when membrane material degrades away during cell culture, the pore size increases (Fig. 3.1). POMaC could be a suitable material in this regard, since it degrades by surface erosion [68, 84]. Moreover, it has lower small molecule absorption than PDMS and long-term reported biocompatibility for a large range of cells. In addition, it allows for large strains, is sterilizable and optically transparent. Also, the elastic modulus of this material could fit within the desired range for this membrane.

### Fabrication

It is desirable to create an array of uniform pores in the membrane. To achieve this, fabrication by moulding could be promising. The possibility of creating small conical pillars that could be used as a mould to imprint the pore structure in POMaC is researched and tested in this study. Figure 3.1 shows a schematic of the fabrication steps to create the membrane. To fabricate the conical pillars, it will be evaluated whether 2-photon polymerization (2PP)-printing could be a suitable option (Fig. 3.1 B). On top of these pillars a thin layer of POMaC is to be deposited and cured (Fig. 3.1 C). After detaching, the POMaC contains the pillared imprint within its layer (Fig. 3.1 D). Upon degradation of this layer, which for POMaC happens layer-by-layer, it is hypothesized that the pore size increases (Fig. 3.1 F).

### Dimensions

The dimensions of the designed conical pillars are shown in Figure 3.2. The pillars have a height of 9  $\mu\text{m}$ . The base of the cones is set at 10  $\mu\text{m}$  and the top is set at 2  $\mu\text{m}$ . The top of the cones is kept flat, to facilitate easier removal of the membrane from them. 2PP-printing is a widely used method to create structures at this scale.

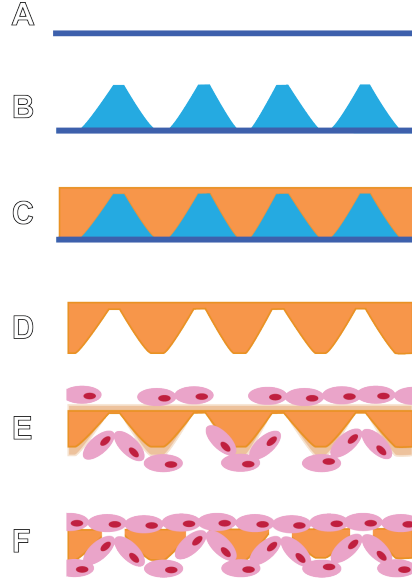


Figure 3.1: A schematic of the concept for the fabrication of a membrane with a dynamic pore size. (A) A substrate is chosen (dark blue). (B) On the substrate coned pillars are fabricated (light blue). (C) On top of the substrate and the pillars a polymer layer (orange) is spincoated. (D) The polymer layer is detached, creating a membrane with a structural imprint from the pillars. (E) during cell culture on the membrane, the membrane slowly biodegrades. (F) When the cell layers are confluent, the pore size in the membrane increases, due to material degradation.

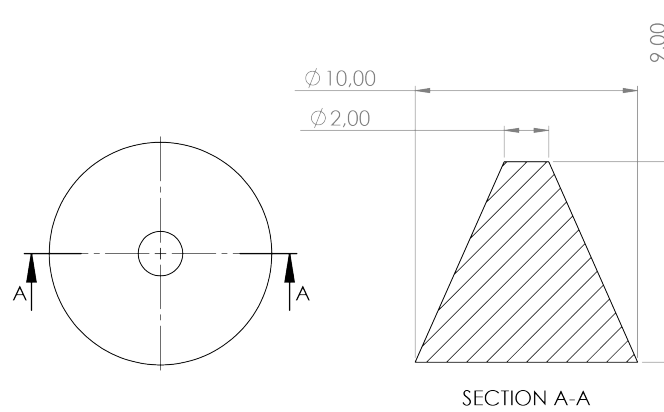


Figure 3.2: A drawing of the concept dimensions for a single pillar. (Left) Top view of the pillar. (Right) Section view of the pillar. Dimensions are in  $\mu\text{m}$ .

If a  $10\ \mu\text{m}$  thick membrane is created on top of this mould, an additional layer of  $1\ \mu\text{m}$  thick POMaC is present on top of the pillars. This layer initially creates a poreless and smooth membrane in which pores slowly should be formed. In the beginning of the cell culture no pores are needed yet and the pore diameter is to be smaller than  $3\ \mu\text{m}$ . A confluent cell layer is generally present after about one week. After this week, the pore diameter is to increase beyond  $3\ \mu\text{m}$ . With the proposed dimensions, the degradability rate in this concept should be about  $0.5\ \mu\text{m}$  per week to create pores with a diameter larger than  $3\ \mu\text{m}$  by the second week (Fig. 3.3).

Equations 3.1 to 3.5 describe how the degradation rate per week can be calculated, based on the membrane dimensions. There are two critical points in the dimension of the membrane. First, the membrane needs to contain an open pore, where the additional top layer ( $t_{add}$ ) is fully degraded away. The amount of degradation needed to obtain an open pore is indicated with  $l_{deg1}$  (Eq. 3.1). Second, the pore diameter needs to increase to the desired pore diameter. The amount of degradation needed for this is denoted with  $l_{deg2}$  (Eq. 3.5).

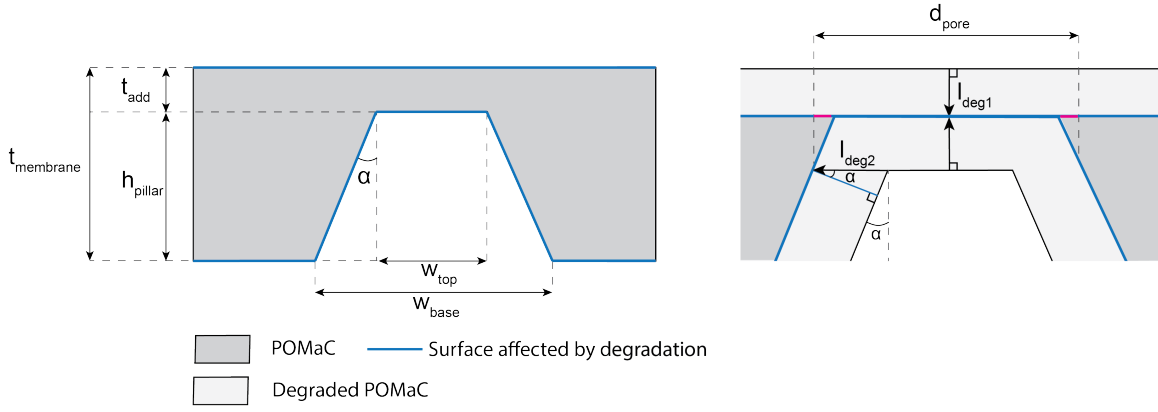


Figure 3.3: Schematic of a pore in the membrane. (left) The general membrane dimensions. (right) A close-up of the relevant membrane dimensions and parameters during degradation. The blue line indicates the POMaC degradation boundary.

$$l_{deg1} = \frac{t_{membrane} - h_{pillar}}{2} \quad (3.1)$$

Where:  $l_{deg1}$  = the amount of degradation desired in order to obtain an open pore.  
 $t_{membrane}$  = the thickness of the fabricated pillar.  
 $h_{pillar}$  = the height of the conical pillar.

$$\alpha = \tan^{-1} \left( \frac{w_{base} - w_{top}}{2h_{pillar}} \right) \quad (3.2)$$

Where:  $\alpha$  = the angle of the designed pillars, in this design  $24^\circ$ .  
 $h_{pillar}$  = the height of the designed pillar, in this concept  $9 \mu\text{m}$ .  
 $w_{base}$  = the width of the base of the pillar, here  $10 \mu\text{m}$ .  
 $w_{top}$  = the width of the top of the pillar, here  $2 \mu\text{m}$ .

$$l_{pore} = \frac{d_{pore} - w_{top}}{2} \quad (3.3)$$

Where:  $l_{pore}$  = the increase in pore radius that needs to be present to obtain the ideal pore size after one week.  
 $d_{pore}$  = the desired pore size after one week, here  $3 \mu\text{m}$ .

$$l_{deg2} = l_{pore} \cdot \cos(\alpha) \quad (3.4)$$

Where:  $l_{deg2}$  = the degradation desired to increase the pore size to the desired diameter after one week (Fig. 3.3).

The combined equation is shown in Equation 3.1.

$$l_{deg2} = \frac{d_{pore} - w_{top}}{2} \cdot \cos \left( \tan^{-1} \left( \frac{2h_{pillar}}{w_{base} - w_{top}} \right) \right) \quad (3.5)$$

The combined effect of  $l_{deg1}$  and  $l_{deg2}$ , indicated by the pink line in Figure 3.3 is not included in the calculations, since its effect is negligible (about  $0.2 \mu\text{m}$  for a  $10 \mu\text{m}$  thick POMaC membrane).

Based on the geometry set in this design,  $l_{deg1}$  and  $l_{deg2}$  are  $0.50 \mu\text{m}$  and  $0.46 \mu\text{m}$ , respectively. This means that in order to obtain an open pore with a diameter of  $3 \mu\text{m}$  by week 1, a degradation rate of  $0.5 \mu\text{m}$  is ideal. The pore will then have a diameter of  $3.1 \mu\text{m}$ . Depending on the actual degradation rate of the used POMaC, the height and angle of the pillars or the thickness of the additional POMaC layer can be adjusted.

In these calculations an ideal surface erosion model is assumed. Moreover, in assuming the calculated degradation rate as the ideal rate of degradation of POMaC, no effect of cell activity, flow or temperature on the degradation rate is yet incorporated. It is also assumed that no shrinkage or expansion of the membrane takes place once it is detached from the mould. Also, it is assumed that the larger bottom pore size  $w_{base}$  does not allow cell migration, due to the smaller pore diameter at the top of the membrane. By using a conical pore structure, less POMaC has to degrade to achieve an increase in pore size during the cell culture. Furthermore, based on the observed POMaC degradation rate, the pillar dimensions can be adjusted accordingly.

### Porosity

The porosity of the membrane, based on literature should be between 3% and 9% for an optimal ALI [1, 30]. The porosity of the membrane changes with the pore size and the pitch of the pores (distance between pore centers) (Eq 3.6). Figure 3.4 illustrates the porosity increase within the membrane for various pitches and pore radii. As the membrane degrades, pore size increases. The ideal porosity, based on literature, is indicated in grey. No pitch provides for every pore radius a porosity within this range. A pitch of 35  $\mu\text{m}$  was deemed optimal, as it gives a porosity of 3% at a pore diameter roughly of 3.4  $\mu\text{m}$  and at a pore size of 5.9  $\mu\text{m}$  a porosity of 9%. In order to obtain a pillar array of 3 x 3 mm, with a pillar pitch of 35  $\mu\text{m}$ , 86 x 86 pillars should be fabricated.

$$Porosity(\%) = \frac{\pi r^2}{pitch^2} \cdot 100\% \quad (3.6)$$

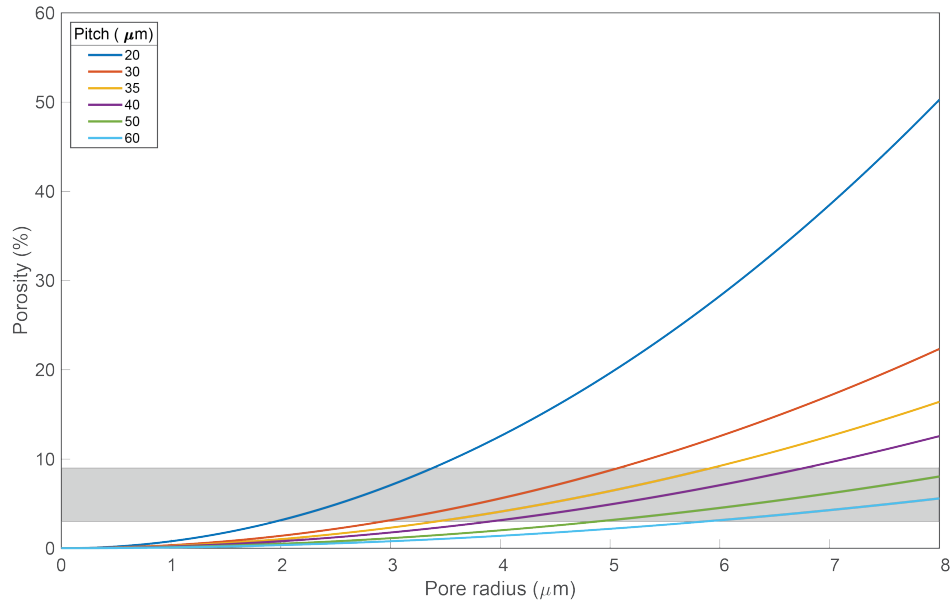


Figure 3.4: The porosity of the membrane as function of the pore diameter indicates for various pitches between the pillars.

In this Chapter, a concept for a LOC membrane was proposed. Chapter 4 will focus on the methodology used to evaluate the proposed concept.

# 4

## Methodology

To evaluate the concept viability, several aspects were studied. First, the optimal method of synthesizing and curing POMaC was studied. Second, it was determined whether a thin film of POMaC can be created and detached from a substrate. It was evaluated whether spincoating could serve as fabrication method for creating a uniform thin film. To create the pore structure, it was assessed whether a mould with 2PP-printed pillars could be created on the substrate. Third, the biocompatibility and toxicity of POMaC for lung cells was evaluated. Therefore, a toxicity assay with the use of an eluate was conducted on primary lung cells.

Furthermore, since POMaC is a very versatile material, its mechanical properties differ greatly with different monomer ratios and curing methods. Therefore, the stiffness properties and degradation rate were evaluated. Regarding the degradation rate, the volumetric degradation rate is relevant, since this influences the membrane dimensions and therefore the pore size. A method to determine the volumetric degradation rate was designed. Fifth, autofluorescence of POMaC was studied, to assess whether this could influence fluorescent cell culture imaging. Lastly, membrane integration should be leaktight. Since the prior designed LOC is made of PDMS, bonding between PDMS and POMaC was assessed.

This Chapter covers the materials and experimental methods used in this research. The POMaC synthesis was conducted at the Else Kooi Lab (EKL) located at the Delft University of Technology. The moulding, spincoating and curing of POMaC, in addition to the 2PP-printing, stiffness, and degradation measurements, were done at the 3ME faculty of the Delft University of Technology. The bonding experiment took place at both EKL and the 3ME faculty. The autofluorescence measurement, cytotoxicity assay and cell cultures were conducted at the EMC in Rotterdam. 3D printing of the moulds was conducted at all three facilities.

### 4.1. Synthesizing POMaC

Pre-POMaC is synthesized in a controlled condensation reaction (Fig. 2.12) with three different monomers; 1,8-octanediol (Sigma-Aldrich, CAS 629-41-4), citric acid (Sigma-Aldrich, CAS 77-92-9) and maleic acid (Sigma-Aldrich, CAS 110-16-7) [67]. The molar ratio for mixing these monomers is 5:1:4, respectively, based on Zhang et al. [57] and the POMaC 8 of Tran et al. [67]. The synthesis method is based on the methodology used by Boutry et al. [68], Zhang et al. [73], and Tran et al. [67].

#### Synthesizing methodology

The three monomers were mixed in a 250 ml three-necked flask with a round bottom. All glasswork was cleaned with acetone, isopropanol (IPA), DI water and dried with a nitrogen air gun. The flask content was placed under a nitrogen atmosphere and gradually heated to 140 °C while being magnetically stirred at 200 r.p.m. (Fig. 4.1 A). Two types of pre-POMaC were fabricated: one that was heated for 2.5 hours (POMaC, 2.5h) and one that was heated for 3 hours (POMaC, 3h). As a purification step, the contents were dissolved in 1,4 dioxane (99.8%, Sigma-Aldrich, CAS 123-91-1) and *via* precipitation dropwise added to DI water to remove any unreacted oligomers and monomers (Fig. 4.1 B). Lastly, the precipitated POMaC was collected and lyophilized (dried) overnight under nitrogen conditions (Fig. 4.1 C).

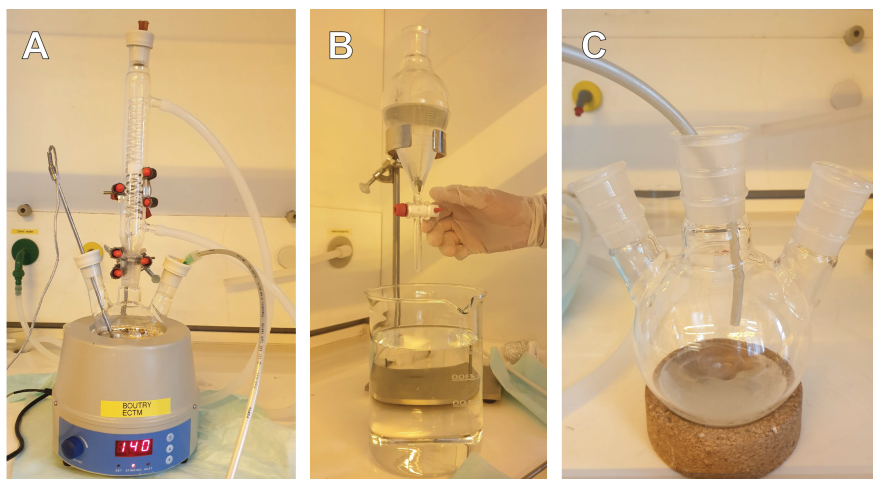


Figure 4.1: (A) Heating the monomer mixture to 140 °C to initiate the poly-condensation reaction. (B) The precipitation step to purify the material. (C) The lyophilization step.

### Photoinitiators

Two types of photoinitiators were evaluated: Irgacure 2959 (Sigma-Aldrich, CAS 106797-53-9) and TPO (Sigma-Aldrich, CAS 75980-60-8). The amount of photoinitiator added is 5 wt% and 1 wt% respectively, based on research by Zhang et al. [57], Tran et al. [67] and Wang et al. [75]. The POMaC was heated on a hot plate at 80 °C for 1 min. before adding the photoinitiator and mixing with a magnetic stirrer for 5 min. at the same temperature.

### Curing methods

Various curing methods were applied to evaluate different polymer characteristics. PPOMaC networks are formed through free radical polymerization [67]. The pre-POMaC containing photoinitiator was placed under a UV point source (Bluepoint 4 Ecocure, Hönle, Germany) at a distance of 1 to 2.5 cm, containing a UVA-intensity of 2000 - 14000 mW/cm<sup>2</sup> and a wavelength range between 310 and 570 nm, initiating the polymerization reaction. The UV light intensity at the substrate is inversely proportional to the square of the distance from the UV source [100]. Polymerization times differed and will be further elaborated on in the respective experimental sections. PPOMaC can be further crosslinked by ester bonding to create EPPOMaC, or pre-POMaC can solely be crosslinked by ester bonding to create EPOMaC (Fig. 2.12). Ester bonds were formed *via* oven post-polymerization at 80°C for either 48 hours or 72 hours, based on methodology of Tran et al. [67].

### Storing

The pre-polymer was wrapped in aluminium foil and stored in a dark fridge at 4°C. Since these polymers are hydrolytically unstable, any moisture present can degrade the material in storage [77]. Moreover, crosslinking can be initiated by both heat and UV light. The polymers are stored at a low temperature to eliminate the formation of bonds and limit the moisture present.

## 4.2. POMaC moulding

It was evaluated whether POMaC could be moulded into various structures using both 3D printed moulds and PDMS moulds. The 3D printed moulds had a square area of 16 x 16 mm<sup>2</sup> and a thickness of 1 mm. A pillar with a diameter of 3 mm was placed in the middle of the mould, to create a hole in the 1 mm thick POMaC sample, so the sample could also be utilized to evaluate POMaC thin film detachment from the substrate (Section 4.7). The fabricated PDMS mould creates a POMaC sample with a square area of 18 x 18 mm<sup>2</sup> and a thickness of 2 mm, with a hole of 3.5 mm in diameter in the middle. The PDMS mould was fabricated using a 3D printed mould, of which the dimensional drawing can be found in Appendix A.1.1 as well. The dimensional drawings of all the 3D printed moulds are included in Appendix A.1.1.

The POMaC in the moulds was cured both with UV light and heat. Heat curing was conducted by oven-curing at 80°C for 48 and 72 hours, based on research by Tran et al. [67]. The samples were post-cured with UV light for 30 minutes at 100% light intensity ( $I_{UV} = 100\%$ ) with a UV point source (Bluepoint 4 Ecocure) at a source

height of 1.5 cm above the substrate. The 3D printed moulds were fabricated on a DLP 3D printer (Max X, Asiga, Australia) with clear resin (Tech Clear, Moin, Germany). Post-processing consisted of cleaning in an IPA bath for 10 minutes and post-curing with a UV flood light.

#### 4.2.1. Moulding POMaC in a 3D printed mould

Directly moulding POMaC in a 3D printed mould was evaluated *via* the following method: The 3D printed mould was placed in a 5% Pluronic F-127 (Sigma-Aldrich, CAS 9003-11-6) solution for 5 minutes and air dried. Subsequently, POMaC (3h, with 1 wt% TPO) was heated at 80°C on a hot plate for 1 minute to decrease its viscosity and ease its pouring into the mould. After pouring, the POMaC was UV cured for 30 minutes (2x15 min,  $I_{UV} = 100\%$ ) with the UV point source, which was placed 2.5 cm above the mould to cure a wider area. Subsequently, the mould was placed in the oven for 48 hours at 80°C. UV post-curing was equal to the first curing step. The sample was extracted from the mould by placing it in DI water for 2 days.

#### 4.2.2. Moulding POMaC in a PDMS mould

##### Fabricating a PDMS mould

The following procedure was followed, to make a PDMS mould: First, the 3D printed moulds and glass microscope slides were placed in a 5% Pluronic F-127 solution for 5 minutes and subsequently air dried. Then uncured PDMS (Sylgard-184, Dow Chemical, USA) with a 1:15 (w/w) (base: curing agent) was added to the 3D printed mould. The mould was placed in a desiccator at -900 mbar for 30 minutes or until all air bubbles disappeared. The mould was then covered with the glass slides without creating air bubbles, bonded with small rubber bands, and placed in the oven at 75°C for 3 hours to cure the PDMS. After oven curing, the mould was cooled down to room temperature. The mould was placed in IPA for 10 minutes to release the PDMS from the mould and the glass slide. This causes the PDMS to swell and thus eases its release [1]. Lastly, the PDMS mould was cleaned with DI water and left to dry.

##### Fabricating a POMaC sample

The following steps were taken to cure POMaC in the PDMS moulds: The PDMS moulds were placed in a 5% solution of Pluronic F-127 for 5 minutes and air dried. Then, POMaC (3h, 1 wt% TPO) was heated at 80°C on a hot plate for 1 minute to decrease its viscosity and to ease pouring into the PDMS mould. After pouring, it was placed in the desiccator overnight for 14 hours to release all bubbles. Any remaining gas bubbles were scraped off or pricked through. The sample was UV cured for 30 minutes (2x15 min,  $I_{UV} = 100\%$ ) with the UV point source placed 2.5 cm above the mould to cure a wider area. Next, the mould was placed in the oven for 48 hours at 80°C. The PDMS mould with POMaC was subsequently UV post-cured for 30 minutes. The height of the UV lamp was 2.5 cm above the sample. Afterwards, the mould was placed in PBS for a day, to facilitate easy removal of the POMaC from the mould.

##### Deviations from methodology above

Samples that were oven cured for 72 hours instead of 48 hours, not subjected to UV curing, or not placed in the desiccator were also evaluated. Also, samples were fabricated where the UV curing step prior to oven curing was omitted. Moreover, various concentrations of Pluronic F-127 (1%, 5% and 10%) were evaluated as a surface primer.

### 4.3. Spincoating POMaC

The option of spincoating POMaC was researched, to produce a thin membrane. Various variables affect the uniformity and stability of the spincoated layer: the type of POMaC; POMaC viscosity during spincoating; the spincoating parameters; the type of substrate and substrate priming; the curing method; and the method of membrane detachment. Pre-POMaC (2.5h and 3h), with 5 wt% Irgacure 2959 was used to assess the spincoating possibilities. POMaC is stored at 4 °C, at which temperature it exhibits a high viscosity. Since preheating POMaC decreases the viscosity, POMaC at room temperature and POMaC preheated in the oven for 20 min. at 50 °C were used in the experiments. An overview of several experiments is included in Appendix A.2.

##### Substrate

The types of substrate used were glass, due to its ready availability, and silicon. Silicon was chosen since adherence of 2PP-printed structures is stronger to silicon than to glass, making it a more optimal substrate for pore fabrication with 2PP-printed moulds. Four substrate primings were tested to evaluate the adherence of POMaC to the substrate: no priming; a polymerized PTFE layer (Slick<sup>TM</sup> Sheet, Oil Slick, Bellingham, USA); Pluronic F-127 coating (Sigma-Aldrich, CAS 9003-11-6); and an hexamethyldisilazane (HMDS) (Sigma-



Aldrich, CAS 999-97-3) coating. The methods used to prime the substrate are listed in Appendix A.3. PDMS as a substrate primer was not tested since this would necessitate an extra spincoating step which might impair the substrates surface smoothness.

The substrate priming, besides affecting layer uniformity and stability, aids in membrane detachment. Non-toxic Pluronic F-127 dissolves in aqueous solutions, allowing for the detachment of the thin layer by acting as a sacrificial layer. It is a hydrogel used in tissue engineering as a mould, track patterning, and sacrificial material [101]. HMDS is a silanization agent that increases surface hydrophobicity and decreases the adherence of added compounds. It can be applied on surfaces containing hydroxyl groups (-OH), such as glass and metal oxide surfaces [102]. Nontoxic PTFE exhibits high hydrophobicity and chemical inertness, diminishing adherence of added compounds [103] (Fig. 4.2).

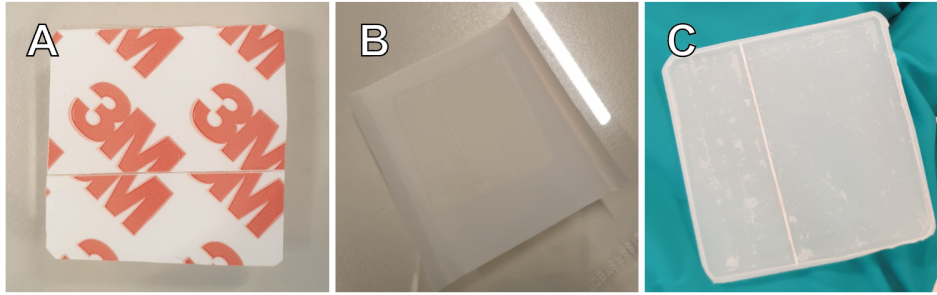


Figure 4.2: An overview of creating a PTFE layer on the substrate.

### Spincoating parameters

After substrate priming, about 2 mL of POMaC was placed in the middle of the substrate and aligned with the center point of the spincoater (Spin150i, SPS-POLOS, Germany). The spincoating parameters were based on spincoating parameters for PDMS and are listed in Table 4.1 [1]. The objective is to obtain a POMaC layer of about 10  $\mu\text{m}$ . POMaC is more viscous than PDMS, so the expectation is that the POMaC layer will be slightly thicker than indicated in the table.

Table 4.1: Overview of the used spincoating parameters and the corresponding layer thickness for PDMS [1].

Spinning acceleration	Spinning speed	Spinning duration	Thickness for PDMS
1000 r.p.m./s	2500 r.p.m.	5 min.	10 $\mu\text{m}$
1000 r.p.m./s	1000 r.p.m.	2.5 min.	40 $\mu\text{m}$
1000 r.p.m./s	400 r.p.m.	1 min.	200 $\mu\text{m}$

### Curing methods

Both UV and heat curing methods were applied. Heat curing was conducted *via* a hot plate between 100°C, and 150°C. UV curing was conducted initially with the Photopol UV light curing unit (Photopol light, Dental-farm, Italy) and subsequently with the UV point source (Bluepoint 4 Ecocure). Curing lengths ranged between 15 and 30 min. The exact curing method is included in Appendix A.2.

### Membrane detachment

The substrate with the membrane was placed in a PBS solution or DI water for 1 to 2 days to detach the membrane. The PBS solution was fabricated by dissolving a phosphate buffered saline tablet (Sigma-Aldrich, LOT SLCK3649) in 200 ml DI water. The membrane was subsequently detached using tweezers, an attached POMaC support structure, or tape to divide the detachment force over a larger area of the membrane to diminish the chance of rupturing the membrane.

### Layer thickness measurement

The thickness of the POMaC spincoated layer was measured with a White Light Interferometer (3D Optical Profilometer, Bruker). POMaC is transparent, and silicon is a reflective material. Therefore, the interferometry measurement was taken in the range where no reflecting light interferes with the measurement. The measurement was taken under green light illumination with a 2.5x objective, and a Vertical Scanning Interferometry (VSI) processing method was used.

#### 4.4. Pillar fabrication by 2PP-printing

The possibility of using 2PP-printed moulds is evaluated to fabricate a conical structure within the membrane (Ch. 3). This was assessed with the Photonic Professional GT+ (Nanoscribe GmbH & Co.), which is a 3D printer designed for ultra-precise and rapid microfabrication [104]. 2PP is based on direct laser writing, where two photons are absorbed simultaneously by a single molecule when light intensity exceeds the polymerization threshold. (Fig. 4.3) [105]. With respect to one photon absorption, 2-photon absorption exhibits a much smaller area where light intensity exceeds the polymerization threshold, initiating polymerization only within the focal spot, allowing for a high resolution and localized printing [105]. This 2PP-printer has an average output power of <180 mW and peak power of 25 kW [104].

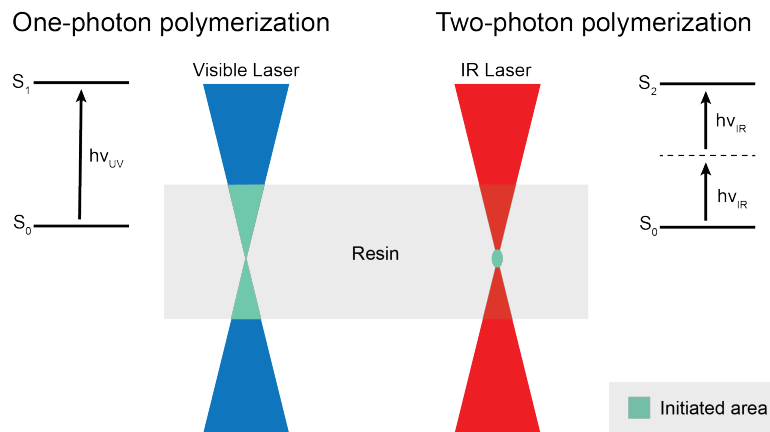


Figure 4.3: Schematic comparison of one photon polymerization and two-photon polymerization. The area where polymerization is initiated is limited to only the focal spot in two-photon polymerization.  $S_1$  indicates a first excited state, and  $S_2$  indicates a second excited state. Based on Anderson et al. [106].

The printing configuration used was Dip-in Laser Lithography (DiLL) (Fig. 4.4) [104, 106]. The smallest feature size and the total printable volume are determined by the combination of objective, dose and resin type [104]. Furthermore, the slicing and hatching lines are the horizontal and vertical printing lines that the printer follows. The typical slicing and hatching distances for the 25x and 63x objective are  $1\ \mu\text{m}$  and  $0.5\ \mu\text{m}$ , and  $0.3\ \mu\text{m}$  and  $0.2\ \mu\text{m}$ , respectively [104]. The 25x objective has a theoretical lateral (xy) and axial (z) resolution of 595 nm and 3313 nm, respectively. In comparison, the 63x objective has a resolution of 340 nm and 826 nm, respectively (Tab. 4.2). The smallest part of the conical pillar has a dimension of  $2\ \mu\text{m}$  (Fig. 3.2). Therefore, both the 63x and the 25x objectives are evaluated, where the 25x objective has the advantage that printing speed and printing field are higher than for the 63x objective [104].

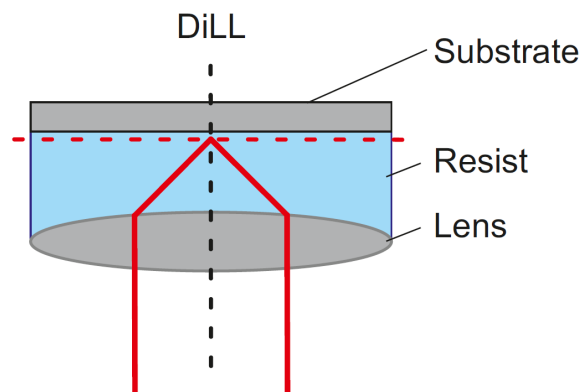


Figure 4.4: Schematic of the Dip-in Laser Lithography (DiLL) configuration [104].

Table 4.2: Photonic Professional GT+ Nanoscribe 2PP-printer parameters.

	25x Objective	63x Objective
Standard slicing distance	1 $\mu\text{m}$	0.3 $\mu\text{m}$
Standard hatching distance	0.5 $\mu\text{m}$	0.2 $\mu\text{m}$
Theoretical lateral resolution	595 nm	340 nm
Theoretical axial resolution	3313 nm	826 nm

The prints were conducted in the galvo scanning mode instead of the piezo scanning mode since this optimizes print time. Hatch lines were taken both one way ( $\uparrow\uparrow$ ) and alternate ( $\uparrow\downarrow$ ). During the dose tests, the dose was kept constant as much as possible while changing the laser power (LP, %) and scanning speed (SS,  $\mu\text{m/s}$ ). The equation for the dose is given in Eq 4.1, where  $n = 2$  since the technique uses 2-photon polymerization [104].

$$Dose = \frac{LP^n}{SS} \quad (4.1)$$

The resins used were IP-S (IP-S, Nanoscribe GmbH, LOT 1-600-0157) for the 25x objective and IP-Dip (IP-Dip, Nanoscribe GmbH, LOT 1-600-0410) for the 63x objective. All prints were conducted on silicon wafers or indium-tin oxide (ITO)-coated glass substrates. Silicon was selected as the final substrate, due to increased attachment of the 2PP-resin, compared to the other ITO-coated glass option. When using silicon as substrate, there may be interference problems where light is reflected off the surface, which creates extra unwanted cured areas or areas exposed to a too high dose. A lower LP or higher SS could be used to mitigate this effect.

Standard printing protocol included cleaning the sample beforehand with acetone and IPA and subsequently blow drying the sample with nitrogen. After cleaning, samples underwent a plasma oxygen treatment to enhance the bond of the polymer structure to the substrate. This treatment was conducted on a plasma cleaner (FEMTO plasma cleaner, Diener Electronic, Germany) for 15 min at 0.14 mbar and the power set at 80%. After printing, the sample was developed in propylene glycol monomethyl ether acetate (PGMEA) for 25 minutes to dissolve any unreacted resin and subsequently placed in IPA for 5 minutes. Afterwards, the structure was delicately air-dried with an air gun.

Several dose and array printing tests were conducted to select the optimal printing parameters. The dose tests were conducted to find the optimal printing parameters for the conical pillars. Subsequently, several array printing tests were conducted to test the uniformity and dimension accuracy of the printed array. The pitch used in these array tests was 20  $\mu\text{m}$ . An overview of the parameters used can be found in Appendix A.4. The job execution software used was NanoWrite (Nanoscribe GmbH), and the print job creation software used was DeScribe (Nanoscribe GmbH). The DeScribe codes used for the printing tests are included in Appendix B. During all prints, the PowerScaling used was 1. The PowerScaling times the LP determines the actual laser emission of the printer [104]. In order to speed up the printing process, the GalvoAcceleration parameter was increased from 1 to 10. In addition, the use of the Swift printing mode was evaluated. The Swift Mode can increase print speeds up to ten times by combining an outer structure shell with a coarsely sliced and hatched core [104]. The Swift Mode could decrease the surface quality compared to printing in the solid mode. Moreover, UV post-curing of the print is generally not required but could increase overall stability [104].

Imaging of the pillars was conducted using a scanning electron microscope (SEM) (JSM-6010LA analytical scanning electron microscope, JEOL, Japan). The imaging was done using Secondary Electron Imaging (SEI), measuring the surface morphology with an electron acceleration voltage of 10 kV or 15 kV. A gold coating was applied to make the surface of the samples conductive, using gold sputtering at 30 mA for 30 seconds. The gold sputterer used was the JFC-1300 auto fine coater (JEOL, Japan).

## 4.5. POMaC stiffness quantification

Indentation tests have been widely applied to study the mechanical properties of soft materials such as soft polymers and biological tissues, e.g. articular cartilage and subcutaneous tissues [107, 108]. These tests measure material stiffness very locally and, as such, have been used to quantify the difference between the surface and the interior of polymers, such as PDMS [108]. The effective Young's modulus at the surface of the POMaC sample was measured with the Optics11 Life Piuma Nanoindenter (Optics11 Life, the Netherlands) (Fig. 4.5). Three different samples containing POMaC (3h, 1 wt% TPO) were tested, listed in Table 4.3. All samples had the same dimensions and were 2 mm thick. The samples were cured with UV light and oven curing at 80 °C for 48 hours. The difference between the samples is A) the UV light intensity during curing and B) the duration the sample has been submerged.

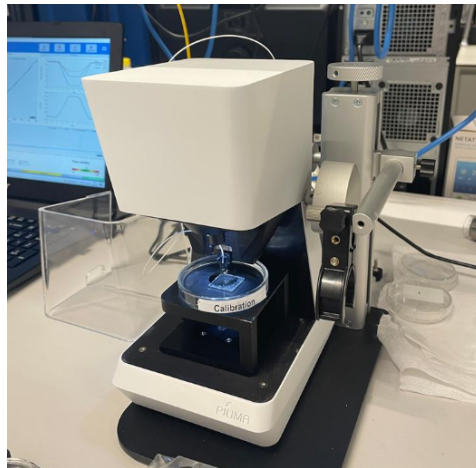


Figure 4.5: The test set-up with the Piuma Nanoindenter and a submerged sample.

Table 4.3: Samples evaluated for their effective Young's moduli.

Sample	POMaC type	UV curing intensity ( $I_{UV}$ )	Oven curing	Submersion
1.	EPPOMaC (TPO)	100% for 30 min.	80°C for 48 hours	<1 hour in DI water
2.	EPPOMaC (TPO)	60% for 30 min.	80°C for 48 hours	<1 hour in DI water
3.	EPPOMaC (TPO)	100% for 30 min.	80°C for 48 hours	2 weeks in PBS

When in contact with the sample surface, the Nanoindenter cantilever deflects depending on the stiffness of the surface. An optical interferometer measures this deflection. The measurements were conducted in PBS and DI water, as this aids measurements on surfaces with adhesive properties. The first two samples were placed in DI water for a relatively short time; they were submerged only during the measurement, which took about an hour and 30 minutes, respectively. The third sample was submerged in PBS for 2 weeks to measure the effect of long-term submersion. The measurement took place in fresh PBS.

To avoid the stiffness of the underlying substrate affecting the measurement, maximally 5% of the total sample thickness can be taken as cantilever indentation depth [109]. Since the samples have a thickness of 2 mm, they can be indented for 10  $\mu\text{m}$ . Moreover, the type of cantilever affects the allowed indentation depth. The probe used for the measurements of the first two samples had a cantilever stiffness of 3.62 N/m and a tip radius of 29  $\mu\text{m}$ . For the third sample, the probe had a cantilever stiffness of 3.71 N/m and a tip radius of 28.5  $\mu\text{m}$ . The indentation limitation of the probes is 3  $\mu\text{m}$ , including a 0.9  $\mu\text{m}$  safety margin. Therefore, the indentation depth was set at 3  $\mu\text{m}$ .

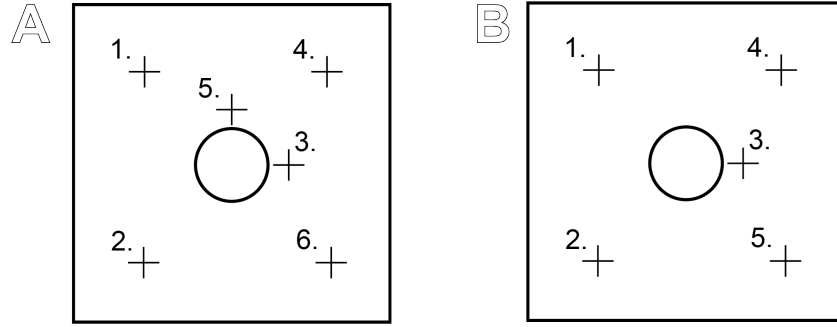


Figure 4.6: An overview of the measurement points for the various samples. A) The measurement points for Sample 1 and Sample 3. B) The measurement points for Sample 2.

A matrix scan was conducted at several locations on the samples (Fig. 4.6). This scan measured 9 points close together in a 3 by 3 square with 100  $\mu\text{m}$  between each measurement point. A matrix scan provides multiple measurement points without measuring exactly the same point multiple times, as previously measuring might influence the subsequent measurements.

With nanoindentation, the effective Young's Modulus is calculated. This modulus takes an assumed Poisson's ratio into account. The Poisson's ratio ( $\nu$ ) is assumed to be 0.5 for soft (elastic) materials, with a bulk modulus higher than the shear modulus [109]. The correlation between the effective Young's modulus and the Young's modulus is given by

$$E = E_{eff}(1 - \nu^2) \quad (4.2)$$

where  $E$  is the Young's modulus,  $E_{eff}$  is the effective Young's modulus, and  $\nu$  is the Poisson's ratio [109]. The model used as fit to calculate the effective Young's modulus is the Hertzian model, where a single fit with  $P_{max} = 100\%$  was used, meaning that all measurement data of the indentation are taken into account. The Hertzian model is commonly used for measuring the elasticity of purely elastic linear materials in the kPa stiffness range [109], and it does not take into account viscoelastic behaviour [108]. The effective Young's modulus with respect to the applied load in the Hertzian model is given by

$$P = \frac{4}{3} E_{eff} R^{\frac{1}{2}} h^{\frac{3}{2}} \quad (4.3)$$

Where  $P$  is the indentation load,  $R$  is the radius of the round indenter tip, and  $h$  is the indentation depth [109].

## 4.6. POMaC degradation

The concept for a dynamical pore size in the membrane rests upon the principle of the degradation of the membrane material (Ch. 3). As the material degrades away, the pore diameter is hypothesised to increase *via* surface degradation. Therefore, the effect of POMaC degradation on its geometry is measured. The biodegradability rate changes with the monomer ratio, synthesis, and curing method. Thus, the degradability process of the specific type of POMaC used in this study should be characterised. Moreover, measuring the degradability rate should be conducted *via* a relatively simple method in order to be able to get fast insight into the rate of degradation once a part of the previously mentioned aspects has been altered. A simple assessment method allows future research to fine-tune the degradation rate of the material for its respective applications.

The environment within the LOC was recapitulated regarding the shear stress at the material surface and the medium flow present to measure the degradation rate. A channel was designed with embedded structures (App. A.1.3). These structures can be filled with POMaC and are slowly exposed when the material degrades away (Fig. 4.7). The structures consist of steps with a set height from each other. Each step exposed indicates a certain layer height that the POMaC has degraded away. For fabrication of the set-up, 3D printing of the mould was selected due to versatile geometry and rapid fabrication options.

### Dimensions

The flow rate in the LOC is set at 137.5 ml/h [1], which gives a shear stress of 0.55 Pa at the top and bottom of

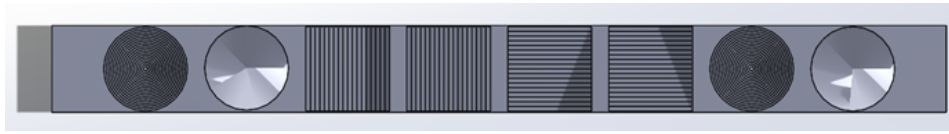


Figure 4.7: Schematic of the insert with embedded structures placed in the channel. The exact dimensions are included in Appendix A.1.3.

the LOC channels, according to Hele-Shaw flow (Equation 4.4). Where  $\tau$  is the shear stress,  $\eta$  is the viscosity,  $Q$  is the flow rate, and  $w$  and  $h$  are the channel width and height, respectively. To have a similar flow effect on the POMaC as in the LOC, the shear stress in the degradation measurement set-up is also aimed at 0.55 Pa. In order to calculate the dimensions of the biodegradability channel, a Matlab script was used, which can be found in Appendix A.5.

$$\tau = \frac{6\eta Q}{wh^2} \quad (4.4)$$

The width of the channel was set at 5 mm. Under equal shear stress at the channel surface, the channel height depends on the volumetric flow rate. The higher the channel height, the higher the flow rate needed (Fig. 4.8). The viscosity of PBS is assumed constant since Yeom et al. [110] showed that the viscosity of PBS is hardly flow-dependent. Selecting a realistic channel height of 3 mm requires a volumetric flow rate of 135 ml/min (Fig. 4.8).

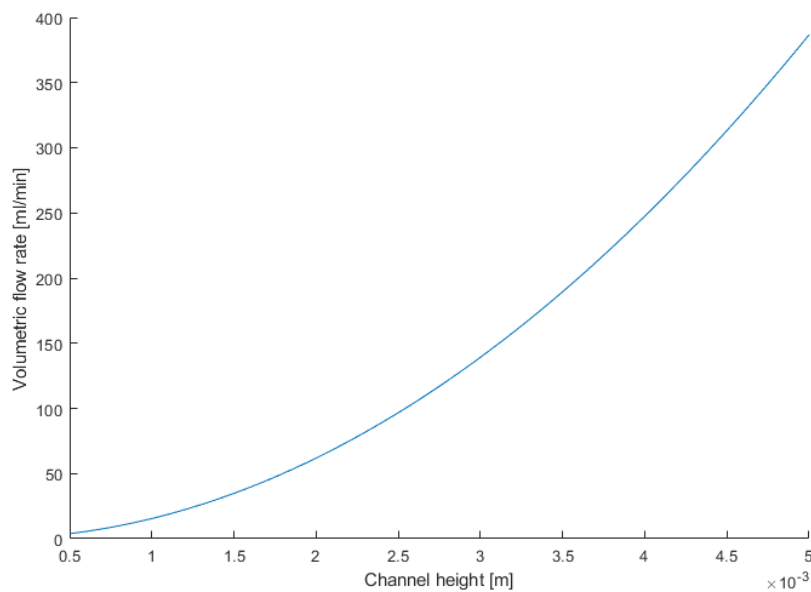


Figure 4.8: The channel height versus the volumetric flow rate for a constant shear stress (0.55 Pa) and a channel width of 0.5 cm.

The height and width of the fabricated channel are 3 mm and 5 mm, respectively. The channel length is 19 cm, restricted by the 3D printbed. The casing thickness around the channel is 3 mm, and the flow channel inlets are placed in the middle of the flow channel.

Since the shear stress is aimed to be a constant value, the dynamic flow has to be fully developed to mitigate any entrance effects, which is after the channel entrance length [111]. The entrance length would have to be 12 cm to get a fully developed laminar flow (App. A.5.). This length would make the complete design too long for 3D printing. Moreover, in the LOC device, a turbulent flow is present. In most practical engineering applications, the entrance effect becomes insignificant beyond a pipe length of 10 times the diameter [111,

112]. For a non-circular channel, the hydraulic diameter  $d_h$  can be calculated as follows:

$$d_h = 4 \cdot \frac{h \cdot w}{2w + 2h} \quad (4.5)$$

This gives a minimal entrance length for turbulent flow of 3.8 cm. Therefore, an entrance length of 5 cm is included in the channel. The exit length may be smaller than the entrance length and is therefore set at 3 cm [111, 112].

Various embedded structure geometries are used in the channel, both inverted cones and square stairs (Fig. 4.7). Structures are similar at the beginning, and the end of the channel and the structures are placed in multiple orientations to mitigate the effect of location and orientation in the channel (App. A.1.3). There is little initial guess on the biodegradability rate since it depends significantly on the type of POMaC used. Therefore, the step size was taken as small as possible. The vertical step size in the structures is set at 0.11 mm, at the limit of the 3D printer resolution. Each structure consists of 18 steps. A total POMaC layer thickness of 2 mm was selected since that was the thickest layer cured up to then and could, therefore, certainly be cured. The radius of the structures covers (almost) the whole range of the channel to observe the effect of degradation over the whole channel width. The dimensions are optimized for a 3D printer resolution of 27  $\mu\text{m}$ .

### Fabrication

For fabricating the channel mould, the methodology for the toxicity assay moulds was used (Section 4.8). The sole difference is that after the first 10 minutes in the UV post-curing step, weights were placed on the biodegradability moulds to prevent bending of the long structures. This bending would prevent the top and bottom parts of the channel from fitting together and forming a leak-tight channel. After post-curing the parts were completely straight. Next, the biodegradability mould top and bottom parts were cooled down to room temperature, placed on top of each other and taped together to preserve a lasting fitting shape. The mould was made leak tight by adding a layer of polyurethane tape (eVatmaster Consulting GmbH, Germany) between the two channel parts. This tape is a transparent, reusable tape which prevents any leaks. The channel mould surface in contact with the tape was cleaned with ethanol and dried prior. Additional elastic bands and clips were used to increase the tightening force.

### Set-up

Syringe pumps do not support the recirculation of media. In contrast, peristaltic pumps allow for recirculation, although peristaltic pumps provide a pulsed flow. Despite the pulsed flow, a peristaltic pump (MCP-Process IP65, Ismatec, Germany) was selected for the experiment. This pump theoretically has a flow rate of up to 230 ml/min for an inner tube diameter of 3.2 mm. However, the set-up for this pump only provided a maximum flow rate of 65 ml/min, where 135 ml/min would have been ideal. A future design of the channel should therefore have a height of 1.4 mm. Alternatively, another pump could be used. This was not done in this study due to time constraints.

The medium used was Dulbecco's Modified Eagle's Medium (DMEM) medium. This medium was used since it has roughly the same composition as the medium used in cell cultures aimed to be eventually realized on the membrane. The experiment was conducted at room temperature. The degradation rate might be slightly higher during cell culture due to temperature differences and the presence of cells.

The PPOMaC was added to the channel as follows: The 3D printed mould was cleaned with ethanol, IPA, and water and dried. Then pre-POMaC, (3h, 1 wt% TPO) was heated for 20 min. at 50°C to decrease the viscosity, and it was subsequently added to the mould. The mould was placed in the desiccator to remove any air. Next, any excess POMaC was scraped off using a flat blade. The POMaC was cured under the UV point source, with  $I_{UV} = 100\%$  for 30 minutes at a height of 1.5 cm. Since there are various structures containing POMaC and they can not fit under the UV lamp simultaneously, the structures not exposed to UV were covered with aluminium foil.

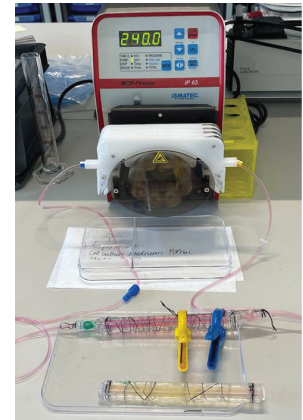


Figure 4.9: The experimental set-up with both the channels under static and dynamic flow conditions.



Both the degradation rate under dynamic flow and under static conditions are relevant since both conditions are present in the LOC. Therefore, POMaC is evaluated under both static and dynamic flow conditions. Images during the experiment were taken on a digital microscope (VHX-6000 digital microscope, Keyence International, Belgium). Figure 4.9 shows the experimental set-up used.

## 4.7. POMaC bonding

Several options were studied for integrating the POMaC membrane into the PDMS LOC device with a strong and elastic bond: fabricating the complete device out of POMaC, and PDMS to POMaC bonding using various methods.

### POMaC-POMaC bonding

Since moulding of POMaC was possible (Section 5.2), fabricating the whole device out of POMaC could be an option. In this approach, it was assessed to what extent POMaC could be bonded to POMaC. This was tested by spreading a thin layer of uncured POMaC between two fully cured slabs of POMaC using a spatula. The structure was UV cured for 30 min. under the UV point source,  $I_{UV} = 100\%$ , at a height of 1.5 cm. Subsequently, it was placed on a hot plate for 30 min. at  $150\text{ }^{\circ}\text{C}$ . Next, the bond strength was tested by pulling on the respective slabs with tweezers.

### PDMS-POMaC bonding

Whether POMaC could be bonded to the PDMS LOC chip directly was tested using three different methods: (1) directly bonding PDMS and POMaC together using UV and heat curing; (2) bonding the two materials together by placing either liquid PDMS or POMaC in between and subsequently UV or heat curing; and (3) using oxygen plasma on the PDMS surface to activate it, before bonding it to POMaC.

Plasma surface pre-treatment is commonly used for bonding polymers, such as PDMS, by activating the surface [113]. Domansky et al. [113], for example, performed surface bonding of PDMS and polyurethane *via* air plasma treatment. During surface activation, the surface energy increases and short-lived highly reactive species are produced in the plasma and bound to the surface. With oxygen plasma, mainly hydroxyl groups are formed. In PDMS, for example, these replace the present methyl groups [114]. When the hydroxyl groups fabricated on the polymer surface come into contact, a condensation reaction occurs, where a covalent bond is formed, and water is expelled [114] (Fig. 4.10). Oxygen plasma treatment could allow for a bond that maintains the elasticity needed when bonding the membrane to the LOC since it does not introduce a stiff material.

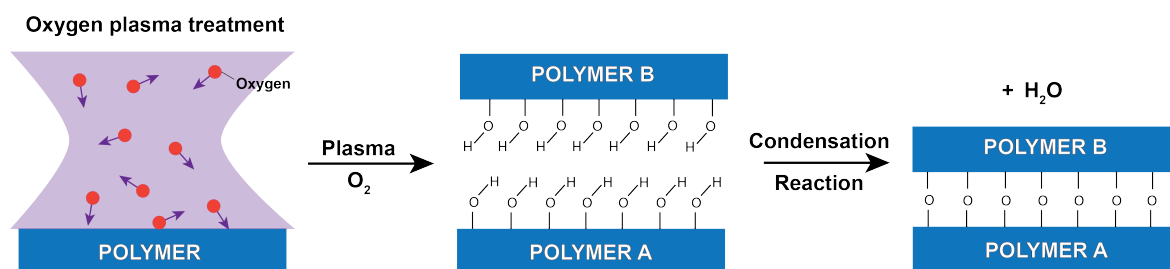


Figure 4.10: Schematic illustration of the mechanism of polymer bonding by oxygen plasma surface activation. Hydroxyl groups are added to the surface during plasma activation. A condensation reaction is initiated by placing two activated surfaces onto each other, where the formed hydroxyl groups react into water and an a covalent bond. Loose adaptation of Ramakrishna [114].

(1) To test whether POMaC and PDMS could be directly bonded, previously cured POMaC and PDMS samples were placed on top of each other and exposed to UV light for 30 min. at  $I_{UV} = 100\%$  under the UV point source at a distance of 1.5 cm. Afterwards, the samples were oven-cured at  $85\text{ }^{\circ}\text{C}$  for 1 hour, after which the bond strength was tested by pulling on the material with tweezers.

(2) To test the bonding of POMaC to PDMS with a liquid POMaC layer, a PDMS LOC actuator layer was attached to a thin spincoated POMaC layer, using a thin uncured liquid POMaC layer in between. The spincoated and cured POMaC was spincoated on a silicon substrate primed with HMDS. The liquid POMaC layer



was subsequently cured for 30 min under the UV point source at  $I_{UV} = 100\%$  at a height of 1.5 cm. Subsequently, the substrate was oven post-cured at 85 °C for 1 hour. After curing, the whole substrate, including the PDMS, was submerged in DI water to loosen the adherence of the spincoated membrane to the substrate. Subsequently, the adherence of PDMS to POMaC was tested. The same methodology was used for testing the bond using a liquid PDMS layer.

(3) To test the bonding of POMaC to PDMS using oxygen plasma, a cured PDMS piece was placed in the plasma cleaner (ATTO plasma cleaner, Diener Electronic, Germany). Two tests were performed. First, only the PDMS was exposed to plasma at a power of 100 W (50% intensity) for 1 minute. Second, exposure at a power of 200 W (100 % intensity) for 3 minutes was conducted on both the PDMS and POMaC samples. After exposure, the PDMS and POMaC samples were placed on top of each other and left for 30 minutes. Next, the sample adherence was evaluated by pulling with tweezers on the respective samples.

#### 4.8. POMaC cytotoxicity assay

A toxicity assay was conducted to evaluate the cytotoxicity of POMaC and the photoinitiators Irgacure 2959 and TPO. A cytotoxicity assay uses an eluate of a material to study to what extent cell apoptosis and metabolism are present to get an indication of the cytocompatibility of the material [115]. An eluate results from elution and is the solution of solvent and dissolved matter. It is obtained by extracting material from a base material, in this case POMaC, by placing it in a solvent, here cell culture medium [115, 116]. This eluate, containing degraded POMaC, is added to a healthy cell culture. By tracking cell viability after adding the eluate, cytotoxic effects of the material on the cell culture can be studied.

The cytotoxicity of 4 different POMaC configurations were evaluated (Tab. 4.4). The differences between the eluate samples were: A) the type and concentration of photoinitiator present in the POMaC and the curing method and B) the elution time. The elution time is the period that a POMaC sample is in contact with the cell culture medium, during which it leaches. The elution times evaluated are one, two and five days. A further explanation will given in Section 4.8.4. To evaluate the cytotoxicity of pure POMaC, EPOMaC without any photoinitiator was utilized (Sample 1). An EPOMaC sample with an uncured photoinitiator was tested to study how the cell culture would be affected when the uncured photoinitiator remained present in the material (Sample 2). Only oven curing was used to cure these samples. Additionally, PPOMaC samples with different photoinitiators (Irgacure 2959 and TPO) were studied to evaluate their cytotoxicity combined with POMaC (Samples 3 and 4).

Table 4.4: Samples evaluated in the toxicity assay.

Sample	Type of POMaC, photoinitiator	Curing method
1.	EPOMaC, no photoinitiator	Oven curing, 80°C for 72 hrs.
2.	EPOMaC, uncured 1 wt% TPO	Oven curing, 80°C for 72 hrs.
3.	PPOMaC, 5 wt% Irgacure 2959	UV curing, $I_{UV} = 100\%$ , $h = 1.5$ cm, 45 min.
4.	PPOMaC, 1 wt% TPO	UV curing, $I_{UV} = 60\%$ , $h = 1.5$ cm, 30 min.

##### 4.8.1. Sample dimensions

The amount of eluate fabricated is 10 ml to have enough cell culture medium to exchange medium every two to three days (allowing for three exchanges overall) for all experimental runs on a 48-well plate. The concentration of eluate in the toxicity assay was taken as the highest possible eluate concentration that the cells could theoretically encounter in the LOC device. Therefore, the same medium: POMaC volume ratio in the toxicity assay is used, as the medium: POMaC volume ratio of the membrane in the LOC device in the static state. This static state is taken as the volume of the POMaC membrane and the volume of the cell culture medium present when the complete lower LOC channel is filled and no flow, tubing, or extra medium is present.

The dimensions of the LOC were taken as stated in Section 2.3.2. The thickness of the membrane is ideally 10  $\mu\text{m}$ . However, this is a very thin membrane, and the feasibility of fabricating this thickness is not yet apparent. Therefore, a thicker membrane (60  $\mu\text{m}$ ) is used in the dimension calculations of the sample since POMaC should be nontoxic for a possible thicker membrane incorporated in the LOC as well.

Ideally, the sample also has the same aspect ratio as the membrane. However, since the membrane has a very

high aspect ratio and to preserve handleability, the thickness of the disc sample was set at 1 mm. Keeping the medium: POMaC volume ratio constant provided a disc with a thickness of 1 mm and a diameter of 2 cm to be placed in 10 ml cell culture medium. The complete calculations can be found in Appendix A.6. The corresponding mould dimensions for the 3D printed moulds can be found in Appendix A.1.2.

### 4.8.2. Mould fabrication

Figure 4.11 shows a schematic of the experimental protocol.

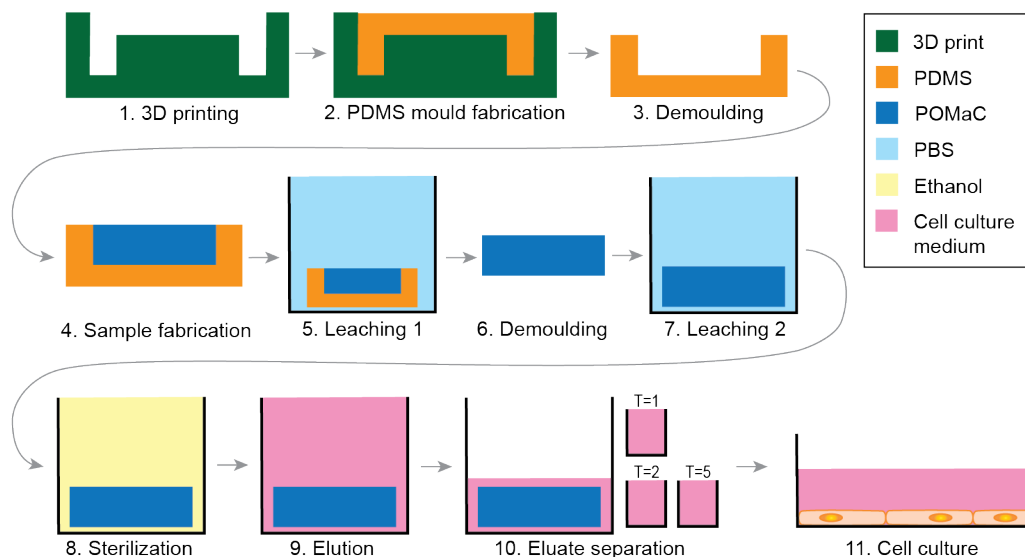


Figure 4.11: Schematic illustration of the experimental protocol.

PDMS moulding was used to fabricate the POMaC structures. PDMS moulds were fabricated by curing liquid PDMS in a 3D printed mould (Fig. 4.11 step 1-3.). The 3D printed moulds for the toxicity and degradability measurements were printed on a high-resolution stereolithography (SLA) printer (Form 3B+, Formlabs, USA). This SLA printer uses Low Force Stereolithography (LFS) with 250 mW laser power. The resolution used to print the moulds is 25  $\mu\text{m}$ , and the resin used for printing is the Clear Resin V4 (Formlabs, USA). This material has cured an ultimate tensile strength of 65 MPa and a tensile modulus of 2.8 GPa. It has a heat deflection temperature of 73.1  $^{\circ}\text{C}$  at 4.55 bar, meaning that at an applied load of 4.55 bar, the mould starts to deform at 73  $^{\circ}\text{C}$  [117]. It was found that the mould for the POMaC samples did not deform when placed at 80  $^{\circ}\text{C}$  in the oven for two days.

After printing, the prints were placed in the freezer for about an hour to ease release from the print plate. The supports were broken with a knife. Subsequently, the structures were placed in an IPA bath (>99.8% (GC), Honeywell/Riedel-de Haën, CAS 67-63-0) for 15 minutes and blown free of any remaining resin and IPA with an airgun. This process was repeated. The moulds were post-cured at 60  $^{\circ}\text{C}$  for 40 minutes. The PDMS moulds were fabricated using the 3D printed moulds according to the protocol described in Section 4.2.2.

### 4.8.3. POMaC sample fabrication

To fabricate the POMaC samples using PDMS moulding, depicted in Figure 4.11 step 4, the following protocol was used:

1. The PDMS moulds were placed in a 5% Pluronic F-127 solution for 5 minutes and, subsequently, air dried.
2. Then POMaC was preheated for 20 minutes at 50  $^{\circ}\text{C}$  in the oven to decrease the viscosity and to ease its pouring into the PDMS mould.
3. Subsequently, a specific type of POMaC was poured into the dry PDMS mould, and any excess POMaC was scraped off the top using a flat knife. No glass plate was added to allow for easier removal when

cured. No desiccator step was used as it was found that without this step, fewer air bubbles were formed during oven curing.

**To fabricate an EPPOMaC sample:**

- 4.A.1. An initial UV curing step was conducted using the UV point source. The UV source was placed 1.5 cm above the sample. The samples containing TPO were cured at  $I_{UV} = 100\%$  for 3 x 15 min. Samples containing Irgacure 2959 were cured for 2 x 15 min at  $I_{UV} = 60\%$ .

**Note:** Various UV curing lengths and intensities were tried. This is the advised protocol for the samples used in the cytotoxicity assay based on the previous experiments.

- 4.A.2. The moulds were placed in the oven at 80 °C for 48 hours.

- 4.A.3. After oven curing, the sample was UV post-cured for 2x15 min. at  $I_{UV} = 100\%$  with the UV point source 1.5 cm above the sample.

**Note:** No EPPOMaC samples were used in the toxicology experiment, only EPOMaC and PPOMaC samples.

**To fabricate an EPOMaC sample:**

- 4.B. An EPOMaC sample is only ester-crosslinked by oven curing, so no photocrosslinking was applied. The EPOMaC samples for the toxicology experiments were oven cured at 80 °C for 72 hours, based on research by Zhang et al. [57].

**To fabricate a PPOMaC sample:**

- 4.C. The samples were photo-crosslinked using the UV point source. The UV lamp was placed at a height of 1.5 cm above the sample. The samples containing TPO were cured at  $I_{UV} = 100\%$  for 3 x 15 min. Samples containing Irgacure 2959 were cured at  $I_{UV} = 60\%$  for 2 x 15 min.
5. For all samples, the mould was placed in PBS for one day after curing to leach out the remaining uncured polymer and photoinitiator and to facilitate easy removal of POMaC from the mould. Samples containing uncured photoinitiator were wrapped in aluminium foil to prevent the photoinitiator from post-curing.

#### 4.8.4. Cell culture protocol

All samples were placed in PBS for 24 hours to leach out. After 24 hours, they were demoulded from the PDMS mould and placed in PBS again for 24 hours (Fig. 4.11 step 5-7). Subsequently, the samples were used at the EMC for an autofluorescence test (Section 4.9). Subsequently, the samples were sterilised in 70% ethanol for 10 seconds, air dried for 50 seconds and washed twice in PBS (Fig. 4.11 step 8). Afterwards, they were immersed in 10 ml Keratinocyte Serum-Free Growth Medium (KSFM) cell culture medium for specified elution times in the incubator at 37.0 °C and 5.0% CO<sub>2</sub> (Fig. 4.11 step 9).

After 1, 2, and 5 days 3 ml of the medium was separated from the POMaC discs and placed in sterile tubes to create eluates with various contact times (T=1, T=2 and T=5) with POMaC (Fig. 4.11 step 10). Each time 3 ml of medium was separated and placed in a new sterile tube. The separated eluates were placed in the incubator until they were added to the cell culture (Fig. 4.11 step 11). Table 4.5 gives an overview of the elution time, the four different samples and the run number of each well. For each configuration, two wells were utilised to minimise any deviant effects.

The type of cells used are PBECs (PBEC D23 P6) since these are more sensitive to environmental conditions than immortalized cell lines. A 48-well plate was used with about 50 000 cells per plate. Twenty-four hours after the cells were inoculated, the eluates were added. Since the POMaC discs have a dimension scaled to the highest concentration that cells could experience in the LOC, all of the well's medium is replaced with a medium that has been in contact with POMaC for a specific time. As a control, eight wells containing pure KSFM medium are used. The 48-well plates were placed in the incubator at 37.0 °C and 5.0% CO<sub>2</sub>. One, two and five days after adding the eluate to the cells, the viability of the cells were evaluated. This was done using brightfield imaging (Revolve microscope, Echo, USA). The cell culture medium was refreshed after 48 hours.

Table 4.5: Overview of experimental runs, regarding elution times and sample types.

Sample:	Days in contact with POMaC	Run number
EPOMaC, No photoinitiator	T=1	1, 2
	T=2	3, 4
	T=5	5, 6
EPOMaC, Uncured 1 wt% TPO	T=1	7, 8
	T=2	9, 10
	T=5	11, 12
PPOMaC, 5 wt% Irgacure 2595	T=1	13, 14
	T=2	15, 16
	T=5	17, 18
PPOMaC, 1 wt% TPO	T=1	19, 20
	T=2	21, 22
	T=5	23, 24
Control	(T=0)	25- 31

## 4.9. Autofluorescence of POMaC

The membrane in the LOC device is to be imaged using confocal microscopy, including the use of fluorescent stains. Therefore, the membrane should exhibit as little fluorescence as possible since this could interfere with the imaging of the cells. The amount of autofluorescence POMaC exhibits is assessed for various often-used fluorescent wavelengths. Both samples with and without photoinitiators are evaluated.

The thickness of the material and the exposure time used for imaging influence the perceived fluorescence of the material. Therefore, POMaC samples of two different thicknesses are studied. The first six samples are 1 mm thick samples, fabricated as stated in Section 4.8. The 1 mm thick samples, which had been submerged in PBS for at least two days, were placed in a polystyrene Petri dish during imaging. Additionally, a thin layer of POMaC on glass (about  $\sim 200 \mu\text{m}$ ) thicker than the eventual membrane, was tested for its autofluorescence. Moreover, a previously fluorescently stained cell culture slide was placed on top to use realistic exposure time settings. This allowed for evaluating whether the intrinsic autofluorescence of a thin POMaC layer would pose a limitation when imaging a cell culture. Moreover, a thin PDMS layer with a 1:15 curing agent to base ratio on glass was tested to compare its fluorescence under similar circumstances to POMaC. Table 4.6 gives an overview of the tested samples.

For the fabrication of the thin POMaC layer, POMaC (3h, 1wt% TPO) was preheated for 20 min at  $50^\circ\text{C}$ . Subsequently, around 2 ml of POMaC was placed on a glass slide which was cleaned with acetone, IPA and DI water, respectively. This slide was placed in a spincoater (Spin150i, SPS-POLOS), and the program for a  $200 \mu\text{m}$  thick layer was run (Section 4.3). Curing was done by placing the slide under the UV point source for 4 x 15 min,  $I_{UV} = 100\%$  at a height of 2 cm.

Table 4.6: Overview of samples used for the autofluorescence experiment.

Sample:	Type of POMaC, photoinitiator	Sample thickness
1.	EPPOMaC, 5% Irgacure 2595	1 mm
2.	EPPOMaC, 1 wt% TPO	1 mm
3.	EPOMaC, No photoinitiator	1 mm
4.	EPOMaC, Uncured 1 wt% TPO	1 mm
5.	PPOMaC, 5% Irgacure 2595	1 mm
6.	PPOMaC, 1 wt% TPO	1 mm
7.	PPOMaC, 1 wt% TPO	$\sim 200 \mu\text{m}$
8.	PDMS, 1:15 curing agent:base	$\sim 200 \mu\text{m}$

The fluorescence is measured on the ECHO Revolve Microscope (Revolve, Echo, USA). Four different wavelengths are tested, corresponding to four different widely applied stains [118–121]. Table 4.7 summarizes the stains and their corresponding maximum excitation and emission wavelength tested.

Table 4.7: The different wavelength ranges tested and their corresponding stains. The wavelengths are as specified by the manufacturer. The excitation and emission maxima are stated respectively.

Wavelength	Corresponding stain	Colour in image
350 nm - 470 nm [118]	DAPI (4',6-diamidino-2-phenylindole)	Blue
490 nm - 520 nm [119]	FITC (Fluorescein-5-isothiocyanate)	Green
596 nm - 615 nm [120]	TXRED	Cyan
649 nm - 666 nm [121]	CY5	Yellow

For each sample, a brightfield image and fluorescent images were taken. The intensity of the fluorescent colour in the image depends on the exposure time used to capture the images. The exposure times used for the 1 mm thick and the  $\sim 200 \mu\text{m}$  thin samples are listed in Appendix A.7. The samples in Table 4.6 were tested for their autofluorescent properties in the middle of the sample and at the edge. Both their fluorescence for single stains and a fluorescent overlay with brightfield were imaged. All photos were taken with a 2x objective.

# 5

## Results

This Chapter covers results found during the experiments listed in the methodology. An interpretation of the consequences of these results on the membrane concept will be provided in the discussion (Ch. 6). Supporting information is included in Appendix C.

### 5.1. POMaC synthesis and curing

All pre-polymers were fabricated using a 5:1:4 molar ratio of 1,8-octanediol, citric acid and maleic acid, respectively, through a poly-condensation reaction. The pre-polymer is a viscous, transparent liquid at room temperature. It was observed that the viscosity of the pre-polymer depends on the heating time of the monomer mixture under nitrogen conditions due to the crosslinking density created within the pre-polymer. Heating for 3 hours during synthesis provided a higher viscosity that could be cured faster than its counterpart heated for 2.5 hours. Due to its shorter curing time, pre-POMaC (3h) was used for most experiments. Moreover, the viscosity was found to be temperature dependent: increasing the POMaC temperature significantly decreased the viscosity, improving the material handleability. Therefore, POMaC was heated up at 50°C for 20 minutes in the oven before using it in either moulding or spincoating.

Furthermore, a significant difference between the use of the two different photoinitiators was observed. POMaC containing 5 wt% Irgacure 2959 cured significantly faster than POMaC containing 1 wt% TPO, when curing with the same UV intensity for equal durations. This difference is possibly attributable to the higher photoinitiator concentration of Irgacure 2959. Additionally, POMaC containing 5 wt% Irgacure 2959 showed yellowing (Fig. 5.1 A) when exposed to high intensity UV for prolonged times (~30 minutes). POMaC containing 1 wt% TPO remained fully transparent after curing (Fig. 5.1 B and C). Thus, there is a trade-off in curing speed versus complete transparency.

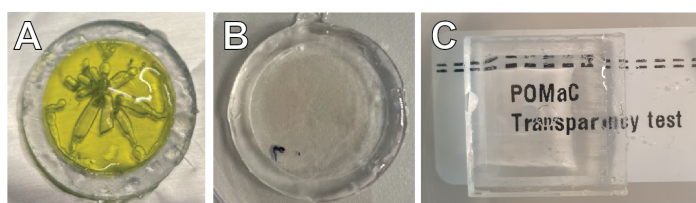


Figure 5.1: (A) EPPOMaC containing 5 wt% Irgacure 2959 cured for 30 min. at  $I_{UV} = 100\%$  and oven cured for 48 hrs. at 80 °C. (B) PPOMaC containing 1wt% TPO cured for 45 min. at  $I_{UV} = 100\%$  and oven cured for 48 hrs. at 80 °C. (C) Transparency of a 2 mm thick EPPOMaC sample containing 1 wt% TPO post-curing in a 3 mm thick PDMS mould.

### 5.2. POMaC moulding

Moulding POMaC directly in the stiff 3D printed moulds was not possible because of detachment difficulties due to POMaCs strong adhesion to the 3D printed mould and the rigidity of the 3D printed mould. Using flexible PDMS moulds to mould POMaC proved to be the most suitable solution. EPPOMaC and PPOMaC

samples could be extracted from the PDMS moulds relatively easy. EPOMaC samples, on the other hand, due to only being ester crosslinked, exhibited very low stiffness, limiting its demoulding. For example, it was found that solely oven-curing the sample for 48 hours left the POMaC sample too soft to extract. Post-curing the sample with UV significantly increased the mechanical strength of the POMaC to the point that it was detachable from the PDMS mould. When UV curing the sample before and after oven-curing for 30 min., the sample was more prone to tearing than only UV curing a single time for 30 min. Another option was to oven cure the POMaC for 72 hours to increase crosslinking density, though extraction was still challenging due to low stiffness, stickiness and large POMaC deformation.

The POMaC sample was detachable from PDMS moulds treated with 5% Pluronic F-127 when submerged in DI water or PBS for 1 to 2 days. A 1% Pluronic F-127 concentration was too low to make the sample easily detachable. A higher concentration of Pluronic F-127 of 10% would form ridges when drying, altering the mould surface and leaving an imprint on the POMaC sample. Therefore, 5% Pluronic F-127 was used as surface priming in PDMS moulds and curing *via* 48 hours of oven curing at 80°C and UV post-curing for 30 minutes posed the best means of moulding a POMaC sample (Fig. 5.2).

Furthermore, the moulds containing POMaC placed in the low pressure desiccator overnight prior to oven-curing were found to contain large air bubbles even after 14 hours in a desiccator. Any bubbles present at the start of oven curing would not disappear and, therefore, be present in the final sample. Moulds not placed in the desiccator contained no bubbles at the start and end of oven curing. Therefore, unlike in moulding PDMS, not using a desiccator proved more optimal in moulding POMaC.

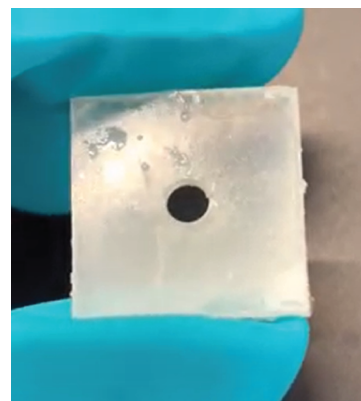


Figure 5.2: POMaC sample fabricated by moulding in PDMS.

### 5.3. Spincoating

In evaluating whether a thin and uniform layer of POMaC could be spincoated, several aspects were found to influence the layer quality: the pre-POMaC viscosity; the substrate priming; the curing method, time and temperature and the spincoating parameters. Additionally, membrane detachment was studied, which proved to be very dependent on the type of substrate priming.

As mentioned, pre-POMaC (3h) exhibited a higher viscosity and faster curing than pre-POMaC (2.5h). Pre-POMaC (3h) was used due to its faster curing. However, when using more viscous POMaC, film rupture, creating a 'spiderweb effect' was observable, where void spaces appear in the POMaC, causing an unstable and non-uniform layer (Fig. 5.3 H). Especially the 3 hours heated pre-POMaC used at room temperature showed high viscosity and generated an unstable thin spincoated POMaC layer in every instance. Therefore, preheating the material at 50°C for 20 min. to reduce its viscosity before spincoating was found to provide better results than POMaC at room temperature.

POMaC adhered well to unprimed glass or silicon during spincoating and curing, providing a uniform layer (Fig. 5.3 E). On highly hydrophobic surfaces, such as PTFE, POMaC had too little adherence, exhibiting unstable layer formation (Fig. 5.3 A). Within minutes post spincoating, an initially uniform POMaC layer would shrink to form separate POMaC droplets. HMDS and a Pluronic F-127 solution were promising since these provide a sacrificial layer, allowing detachment of the POMaC from the substrate. A 1% Pluronic F-127 solution, though providing better results than PTFE, did not provide a stable and uniform layer during spincoating and curing (Fig. 5.3 G and H). HMDS, on the other hand, did provide a stable and uniform layer throughout spincoating and curing (Fig. 5.3 D). No difference between glass and silicon as substrate was observed.

Thin POMaC layer detachment from unprimed glass and silicon proved to be very difficult, if not impossible, by pulling the material or submerging it in an aqueous solution. This underlined the need for a surface primer. POMaC detachment from PTFE was remarkably easy. Figure 5.3 B and C show the PTFE substrate before and after detachment, showing no residue is left behind when detaching the POMaC with tweezers using hardly any pulling force. Detachment of POMaC on HMDS and Pluronic F-127 was also possible after submerging it in an aqueous solution such as PBS. Thicker layers ( $> 40 \mu\text{m}$ ) could also be detached using tape (Fig. 5.3 F). Thus, regarding the detachment and obtainable POMaC layer uniformity and stability on various surface primers, an HMDS priming on silicon provided the best results.



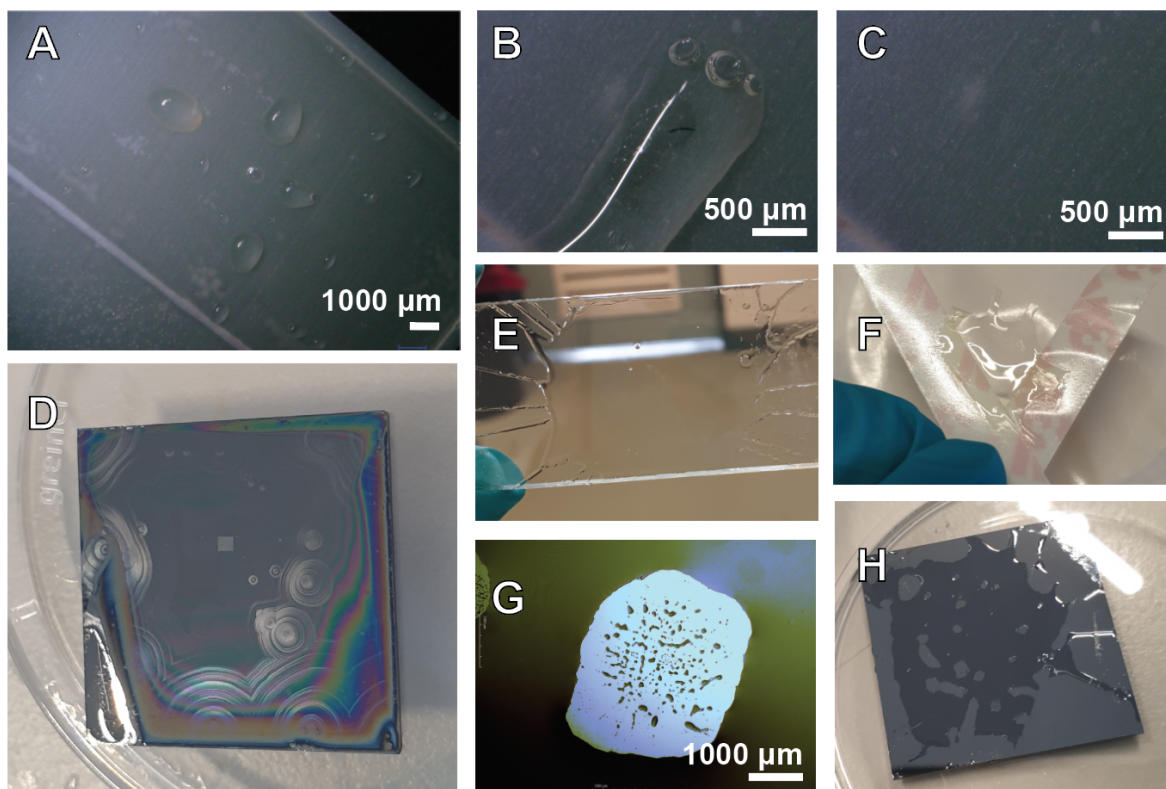


Figure 5.3: An overview of the spincoating results. (A) POMaC spincoated on PTFE, film rupture and droplet formation visible. (B) POMaC on PTFE before detachment. (C) The PTFE surface after POMaC detachment, showing no residue. (D) A uniform layer of spincoated and cured POMaC on a HMDS surface priming on silicon. The square in the middle of the substrate contained 2PP-printed pillars. (E) A uniform and stable spincoated POMaC layer on glass with no substrate priming before curing. (F) Detachment of a POMaC layer using 3M tape. (G) Film rupture of the POMaC layer on a surface primed with Pluronic F-127 before curing. (H) Film rupture and non-uniformity of the POMaC layer on a surface primed with Pluronic F-127 after curing.

It was found that the curing method plays an essential factor in the uniformity of the film. Heat curing at too high temperatures creates void spaces in the spincoated membrane due to film rupture and shrinkage. A possibility to mitigate this is to increase the curing temperature slowly. However, since an uncured thin POMaC layer also creeps up over time, the long curing time associated with a slowly increasing curing temperature made it challenging to fabricate a uniform thin membrane by heat curing. The same phenomenon was observed when curing a thin layer of POMaC with UV light at a high intensity for a long time. Therefore, it was determined solely UV cure the POMaC spincoated sample at a suitable intensity. The best curing parameters were UV curing for 30 min. (2 x 15 min.), with a UV source intensity of  $I_{UV} = 100\%$  and a source height of 2 cm above the substrate.

### 5.3.1. Layer thickness

The thickness of a spincoated POMaC layer on a silicon substrate primed with HMDS was measured using white light interferometry. The spincoating parameters used to spincoat this layer were the same parameters used to spincoat a 10  $\mu\text{m}$  thick PDMS layer (Tab. 4.1) [1]. The thickness was measured at 5 different areas along a cut edge of the spincoated POMaC layer (Fig. 5.4). All data points within each area (Fig. 5.4 B) were combined in histogram plots, shown in Figure 5.5. The left and right peaks indicate the substrate surface's height with respect to the POMaC layer height, respectively. Small pieces of POMaC left on the substrate and layer irregularities, such as the presence of air bubbles (Fig. 5.4 D), might cause a spread in the peaks.



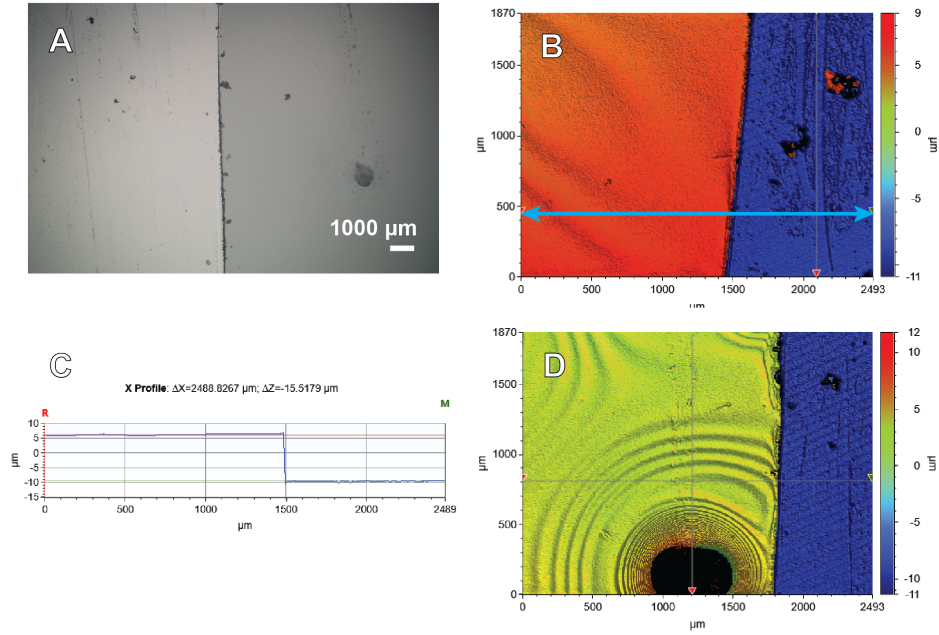


Figure 5.4: (A) A brightfield image of the cut made across the POMaC layer to measure the layer thickness. (B) White light interferometry image of one of the areas used to obtain surface height data. Red: POMaC. Blue: silicon substrate. (C) An example graph of height difference data obtained with white light interferometry along a straight line. The graph corresponds with the height along the blue line in Figure 5.4 B. (D) White light interferometry image of an area used to obtain surface height data. A surface irregularity can be seen in the lower part of the area (black). Yellow: POMaC. Blue: silicon substrate.

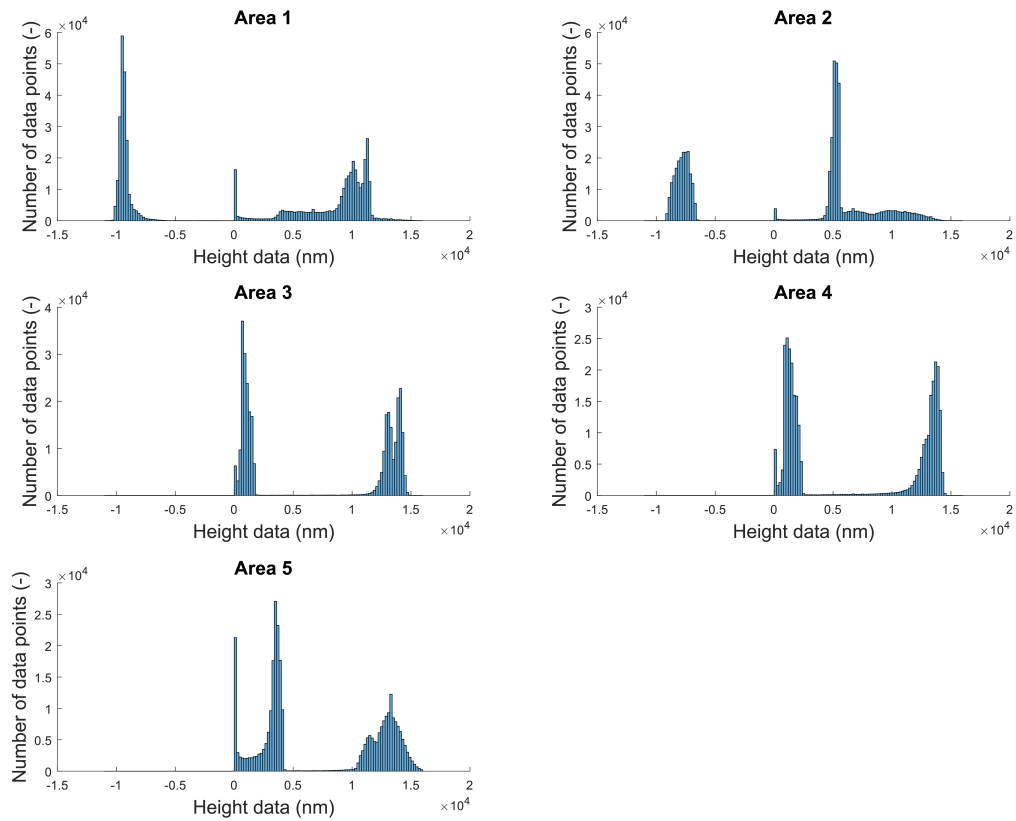


Figure 5.5: Histograms showing the height distribution of the spincoated POMaC layer and the substrate surface for five different measured areas. The left and right peaks indicate the substrate and the POMaC layer height, respectively.

To calculate the mean POMaC layer thickness, a cropped data set of all points within a peak was created with which the mean ( $\mu$ ) and standard deviation ( $\sigma$ ) were calculated. The thickness of the POMaC layer ( $\mu_i \pm \sigma_i$ ) was calculated by subtracting the mean POMaC layer height ( $\mu_{PLH}$ ) by the mean substrate surface height ( $\mu_{SSH}$ ), using Equation 5.1. An overview of the obtained mean thicknesses and their standard deviations for each area is included in Table 5.1. The overall mean layer thickness was found to be  $13 \pm 5 \mu\text{m}$  (Eq. 5.2). A mean and standard deviation instead of a fitted Gaussian curve was used due to surface unevenness, causing a spread in the peaks. The Matlab code utilized to analyze the results is included in Appendix C.1.1. The white light interferometry images are included in Appendix C.1, and the raw data set is included in the Supplementary files.

$$\mu_i \pm \sigma_i = (\mu_{PLH} - \mu_{SSH}) \pm \sqrt{\sigma_{PLH}^2 + \sigma_{SSH}^2} \quad (5.1)$$

$$\mu_{overall} \pm \sigma_{overall} = \frac{1}{5} \sum_{i=1}^5 \mu_i \pm \sqrt{\sum_{i=1}^5 \sigma_i^2} \quad (5.2)$$

Table 5.1: Measured height difference (mean  $\pm$  standard deviation) between the substrate and the top of the spincoated layer of five areas on a cut POMaC spincoated layer.

Measurement	Height difference ( $\mu\text{m}$ )
1.	$18 \pm 3$
2.	$14 \pm 3$
3.	$12 \pm 1$
4.	$12 \pm 2$
5.	$10 \pm 3$

## 5.4. Micropillar fabrication

Several laser exposure dose tests were conducted to evaluate the possibility of creating a micropillar mould using 2PP-printing. A summary of the results is provided in Table 5.2. The first dose test exhibited an inaccurate pillar geometry, due to a too high LP (Fig. 5.6). The range of SS tested did not have a significant effect on the geometry of the printed pillars. The second dose test was aborted and did therefore not provide results. In the third dose test, the LP range was lowered and the SS was kept equal to the conditions in the first dose test. The pillar geometry was significantly better, though a 'wing-shaped' defect was observed on all pillars at the same location on the structure (Fig 5.7 B). This shape could be due to printing parameters, irradiation dose, the reflective property of the silicon substrate, or the limited resolution of the 25x objective. Moreover, the pillars exposed to a lower dose exhibited the most accurate geometry of the respective dose test (Fig 5.7 C). Again SS had no substantial effect on the geometry, but a lower LP proved more optimal.

Table 5.2: Summary of the results of the various dose tests conducted and listed in Table A.2.

Test	Result
Dose test 1	Inaccurate pillar geometry, LP too high, no significant difference with SS.
Dose test 2	Interface failed, aborted.
Dose test 3	Inaccurate pillar geometry, lower LP gave better results, no significant difference with SS.
Dose test 4	Inaccurate pillar geometry.
Dose test 5	Some pillars showed well-defined geometry, no 'wing-shaped' defects present. Projected hatch lines were an issue. The best result was found using parameters of Area 1.
Array test 1	Array print possible with 25x objective.
Array test 2	Array print possible with 63x objective.
Array test 3	A LP of 50% provided consistently well-defined pillar geometry.
Array test 4	The best printing parameters were successfully incorporated in an array.

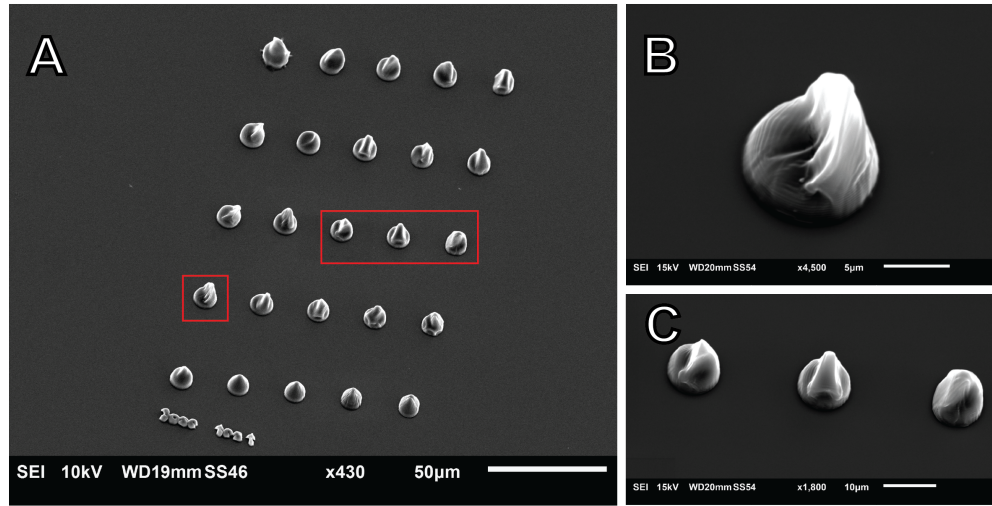


Figure 5.6: SEM images showing pillars fabricated in Dose test 1. (A) Overview of the complete pillar array. LP increases from bottom to top and SS increases from left to right. (B) Close-up of the pillar indicated with the small red square. (C) Close-up of the pillars indicated with the larger red rectangle. All images were taken under a 30° angle.

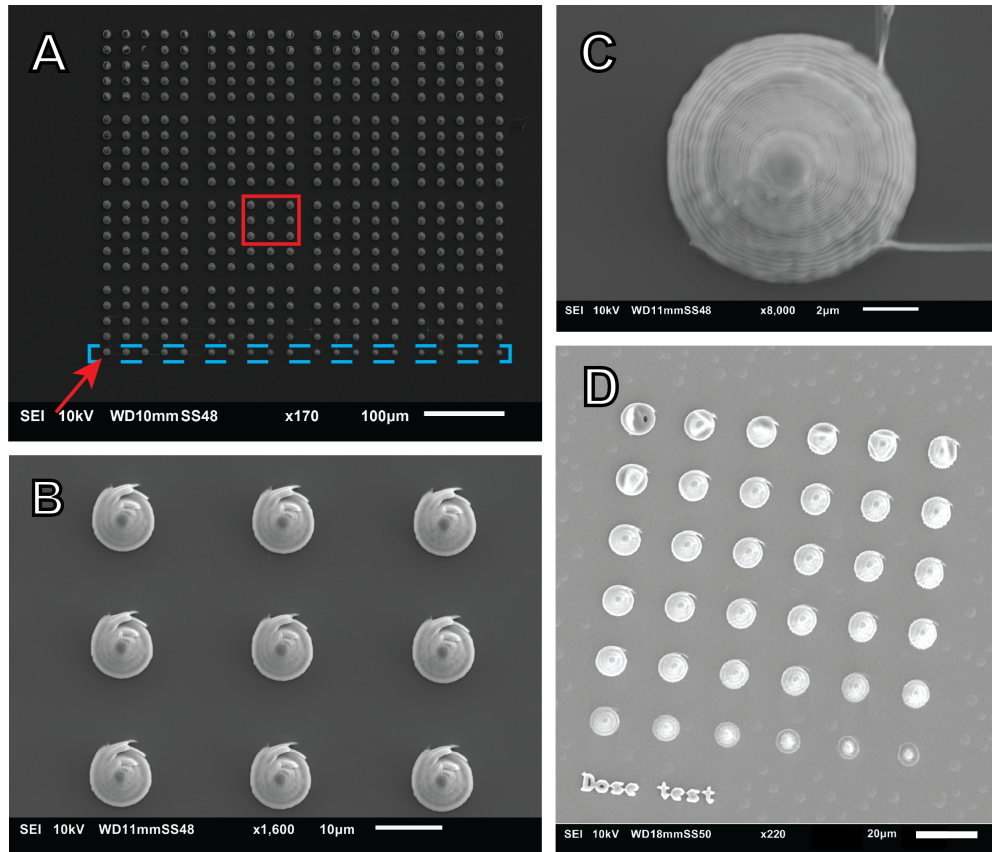


Figure 5.7: SEM images showing pillars of Dose test 3 and 4. (A) Top view overview of the complete pillar array fabricated in Dose test 3. LP increases from bottom to top and SS increases from left to right. The blue dashed box indicates all pillars without a 'wing-shaped' defect. (B) Pillars exhibiting the 'wing-shaped' defect. Close-up of the pillars indicated with the red square in Figure A. (C) Close-up of the pillar exposed to a low LP which does not exhibit the 'wing-shaped' defect, indicated by the red arrow in Figure A. (D) SEM image of the top view of pillars created in Dose test 4 (Area 2). Geometric defects can be seen at the top side of the pillars.

Therefore, in the fourth dose test, several printing parameters were evaluated. An increased slicing and hatching distance were used, since increasing these distances causes a lower local exposure dose. Moreover, a larger amount of shell contours was tested, since this could have provided a more accurate and well-defined geometry. The range of LP and SS was kept equal for each condition tested (App. A.4). However, it was observed that the 'wing-shaped' defect was still present (Fig. 5.7 D).

Since the 'wing-shaped' defect was still present, the 63x objective was tested in Dose test 5 to evaluate the effect of an objective with a higher resolution. Both the standard and an adjusted slicing and hatching distance and shell contour count were used. In order to evaluate the cause of the geometric defect the samples were designed with and without contour. Moreover, a range of LP and SS were evaluated (App. A.4). Besides that, for Area 4, a swift printing mode was tested. It was observed that none of the pillars printed with the 63x objective showed the 'wing-shaped' defects. Furthermore, the pillars that were printed with the standard system settings (Area 2), exhibited significantly projected hatch lines (Fig. 5.8 A). Moreover, for several pillars exposed to a low dose, the top came loose (Fig. 5.8 B). Using the swift mode (Area 4), under higher SS, the hatching lines became significantly pronounced, showing a diminishing surface quality (Fig. 5.8 C). The most promising pillars of each area were selected and compared (Fig. 5.8 D, E and F) and the printing parameters used for these pillars are summarized in Table 5.3. Pillars from Area 2 were not included as all pillars exhibited poor geometry. Based on the results, pillar 1 (Fig. 5.8 D), with a LP between 40% and 60% was promising and thus selected for the third array print test.

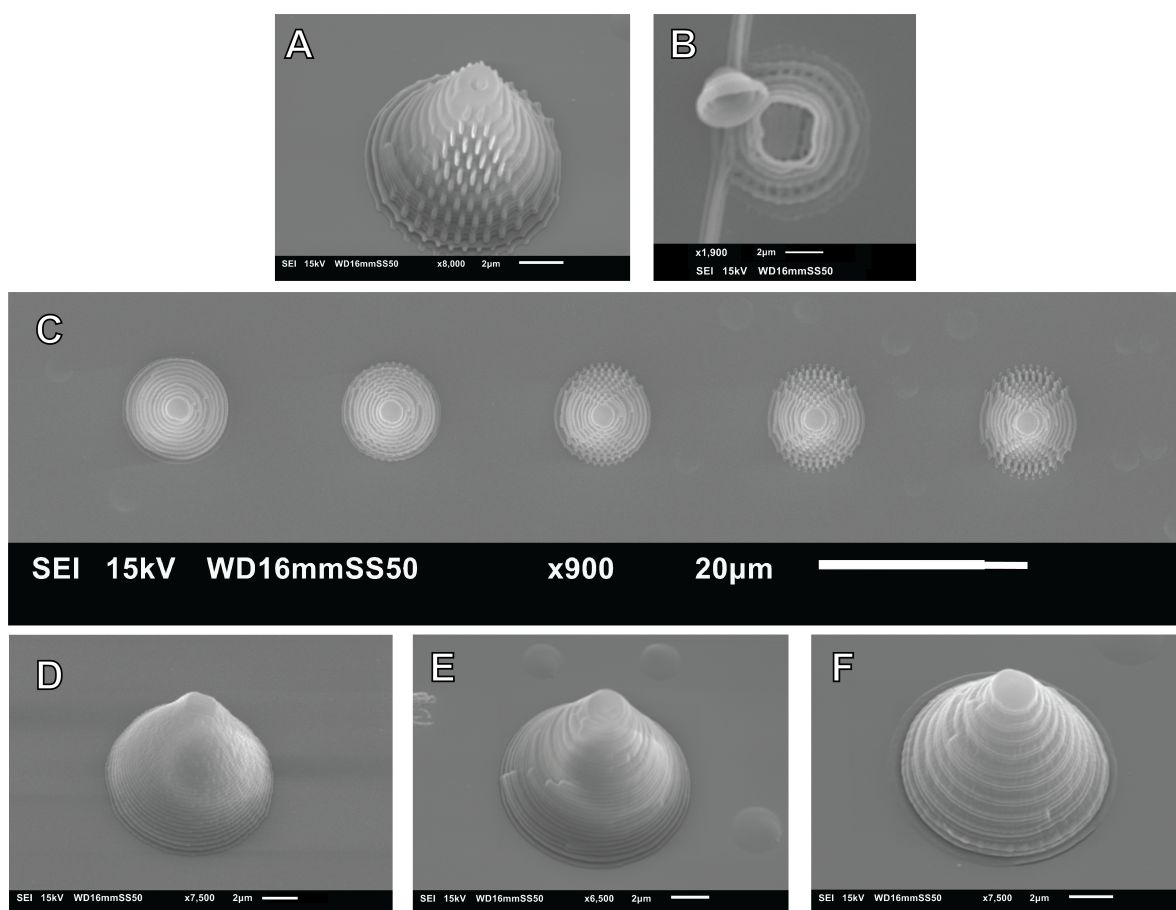


Figure 5.8: SEM images showing pillars created in Dose test 5. (A) Pillar in Area 2, showing projecting hatch lines. Imaged under a 30° angle. (B) Pillar in Area 2, showing the top of the shell of the pillar detached. (C) Pillar row in Area 4. With increasing SS, hatch lines become more pronounced. SS increases from left to right. (D) Pillar 1, located in Area 1. Imaged under a 30° angle. (E) Pillar 2, located in Area 3. Imaged under a 30° angle. (F) Pillar 3, located in Area 4. Imaged under a 30° angle.



Table 5.3: Overview of the parameters used for several promising pillars of Dose test 5, shown in Figure 5.8 D, E and F. The printing time is a DeScribe software calculation if a 3 x 3 mm array of pillars is to be printed (81 x 81 pillars) with a 63x objective.

Pillar	Area	LP (%)	SS ( $\mu\text{m/s}$ )	Slicing, hatching distance	Contour lines	Printing time
Pillar 1	Area 1	60	10000	0.3 $\mu\text{m}$ , 0.2 $\mu\text{m}$	0	9:42 hrs.
Pillar 2	Area 3	40	15000	0.3 $\mu\text{m}$ , 0.2 $\mu\text{m}$	2	10:43 hrs.
Pillar 3	Area 4	90	10000	0.9 $\mu\text{m}$ , 0.35 $\mu\text{m}$	2	7:49 hrs.

The first and second array prints showed that using the 25x and 63x objective, respectively, a good array print could be conducted where the pillars remained in contact with to the surface during development and which showed accurate pillar distribution and pitch. The third array print test, using the parameters of Dose test 5 and a LP ranging between 40% and 60%, showed that using a LP of 50 % was suitable for well-defined pillars, when compared to a LP of 40% and 60% (Fig. 5.9). An LP of 60% gave inconsistent results and exhibited defects in several pillars (Fig. 5.9 C). The best printing parameters discerned for the designed pillars on a silicon substrate were: a slice and hatching distance of 0.3  $\mu\text{m}$  and 0.2  $\mu\text{m}$ , respectively; A shell contour count of zero; A LP and SS of 50% and 10 000  $\mu\text{m/s}$ , respectively; Oxygen plasma treatment beforehand; And a galvoacceleration of 10 V/ms<sup>2</sup>, stagevelocity of 200  $\mu\text{m/s}$  and a powerscaling of 1. Therefore, in fabrication of the final array, Array test 4, these parameters were incorporated (Fig. 5.10).

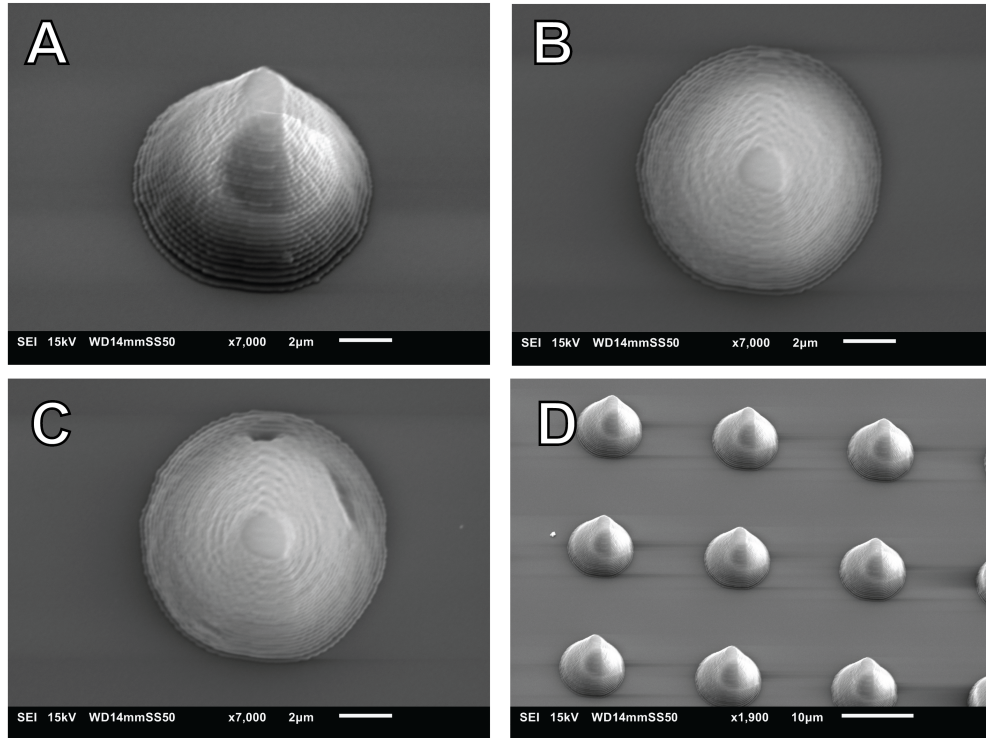


Figure 5.9: SEM images showing pillars created in Array test 3. (A) Pillar created using a LP of 40%. Image taken under an angle of 30°. (B) Top view of a pillar created using a LP of 50%. (C) Pillar created using a LP of 60%. Defects are visible. (D) Side view of the pillars created with a LP of 50%, image taken under an angle of 30°.

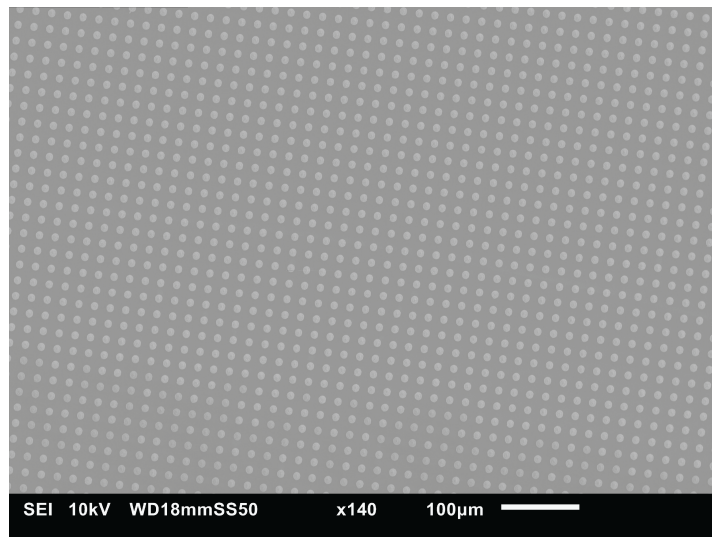


Figure 5.10: SEM image showing an array of conical pillars created in Array test 4.

## 5.5. POMaC stiffness quantification

To obtain the effective Young's modulus of the EPPOMaC samples tested by nanoindentation, the Dataviewer V2 software of Optics11 Life was used to analyse the raw data. The data fit was based on a Hertzian model (Section 4.5). An illustrative load-indentation curve of raw indentation data including a Hertzian fit for a single indentation measurement is shown in Figure 5.11. The red curve indicates the Hertzian fit overlying the blue loading data. The green line indicates the unloading of the indentation [109]. For the Hertzian model a single fit with  $P_{max} = 100\%$  was used, meaning that all measurement data of the indentation loading step are taken into account in the calculation of the effective Young's modulus at each location.

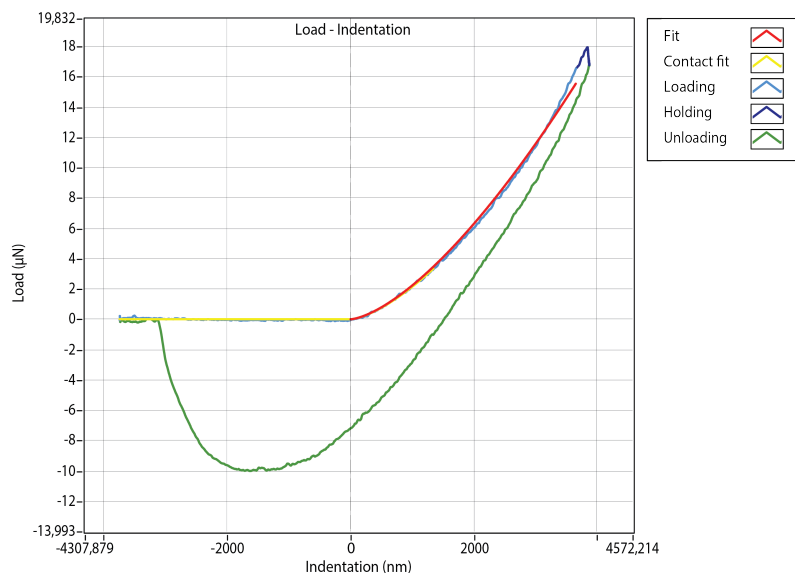


Figure 5.11: An example of a load-indentation graph of a single measurement including a Hertzian fit (red) on raw indentation data (blue).

To analyse the results, the Matlab boxplot function was used. A full overview of the Matlab script and the data can be found in Appendix C.2 and the Supplementary files. The boxplots in Figure 5.12 give an overview of the effective Young's moduli at the tested locations of the various samples. The different location points are indicated in Figure 4.6.

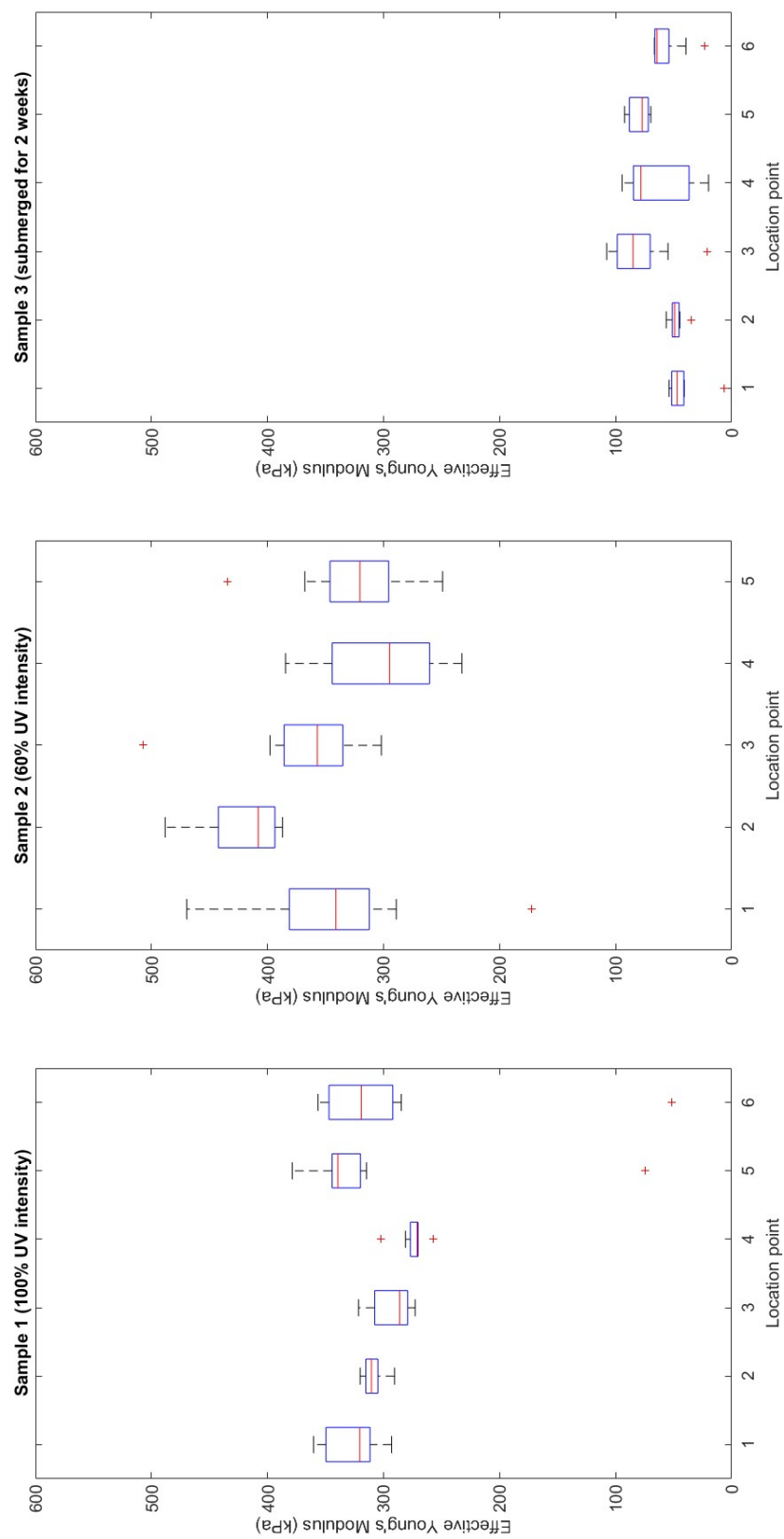


Figure 5.12: The effective Young's moduli of the three samples at various locations on the sample.

The top and bottom of the box indicate the 25<sup>th</sup> and 75<sup>th</sup> percentile of the data set, respectively, and the red midline represents the median. The whiskers indicate the furthest data point within the dataset, excluding outliers. Any outliers, indicated by a red +, are defined as any value more than 1.5 times the interquartile range away from the top or bottom of the box. The interquartile range is the distance between the top and bottom of the box.

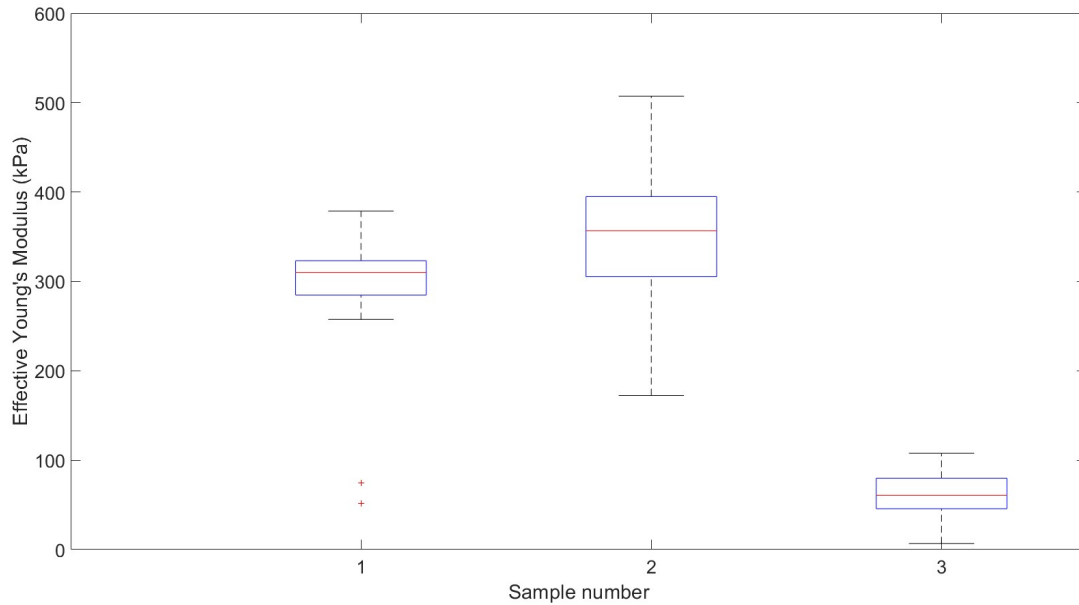


Figure 5.13: An overview of the mean effective Young's modulus of each sample.

A comparison of the mean effective Young's modulus of the samples is given in Figure 5.13. The mean effective Young's modulus and standard deviation of each sample were calculated using Equation 5.3 and Equation 5.4, respectively.

$$\bar{x} = \frac{1}{n} \sum_{i=1}^n x_i \quad (5.3)$$

$$\sigma = \sqrt{\frac{\sum_{i=1}^n (x_i - \bar{x})^2}{n-1}} \quad (5.4)$$

The samples had been submerged for different lengths of time: 2 weeks for Sample 3 versus <1 hour for Sample 1 and 2. From the results it is clear that if POMaC is submerged for a prolonged time the effective Young's modulus becomes significantly lower. Sample 1 and 2 have a mean effective Young's modulus of  $301 \pm 60$  kPa and  $352 \pm 70$  kPa respectively, whereas the longer submerged Sample 3 has a mean effective Young's modulus at the surface of the material of  $62 \pm 20$  kPa. Moreover, there is no significant difference between Sample 1 and Sample 2, which were fabricated using a different UV intensity. The measurement of the second sample does show a higher uncertainty.



## 5.6. Degradation

The results of the degradation test of PPOMaC submerged in DMEM cell culture medium under static conditions are shown in Figure 5.14. At the start of the test, the POMaC is still fully transparent (Fig. 5.14 A). After 2 days submersion in medium, parts of the POMaC have turned opaque and no significant swelling is present (Fig. 5.14 B and C). After 12 days submersion, swelling of the PPOMaC can be observed (Fig. 5.14 E). Moreover, parts of the opaque POMaC are turning transparent again (Fig. 5.14 D). On day 29 of submersion in medium, it can be observed that the opacity is further diminishing. The transparency is located at the shallow regions within the structure, while at the deeper locations opacity is still present (Fig. 5.14 F). Swelling has increased slightly (Fig. 5.14 G). No parts of the 3D printed structures became exposed and free of POMaC during the experiment under static or dynamic flow conditions. Therefore, overall, PPOMaC submerged in DMEM medium under both conditions does not degrade more than 100  $\mu\text{m}$  within 1 month. Furthermore, it was observed that the cell culture medium changes from pink to a light yellow colour after 1 to 2 days of use (Fig. 4.9).

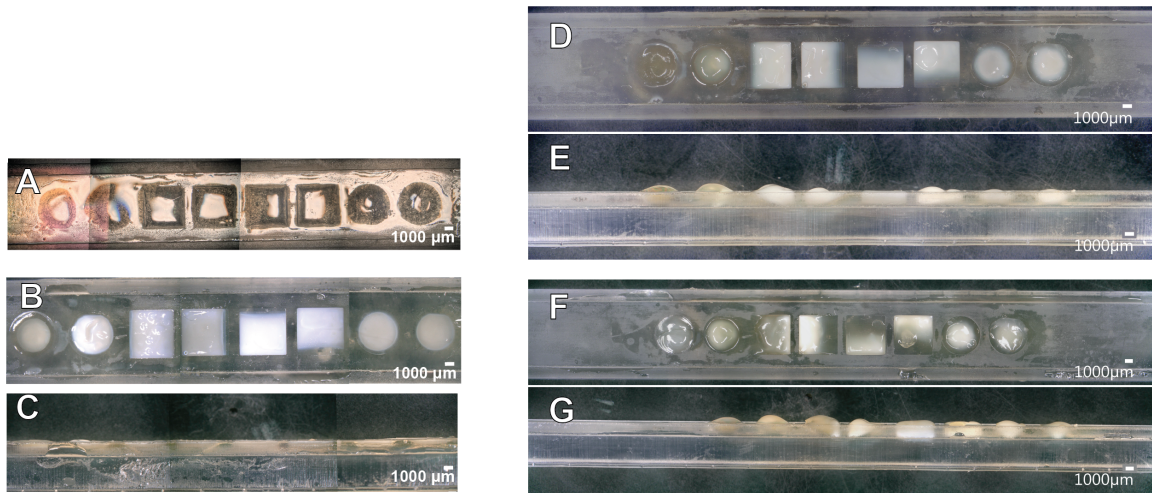


Figure 5.14: Degradation of PPOMaC under static conditions over several days. A) POMaC before degradation, day 0. B) Top view after 2 days submersion in medium. POMaC is turning opaque. C) Side view after 2 days submersion in medium. D) Top view after 12 days submersion. E) Side view after 12 days submersion. Swelling of the POMaC can be observed. F) Top view after 29 days submersion. G) Side view after 29 days submersion.

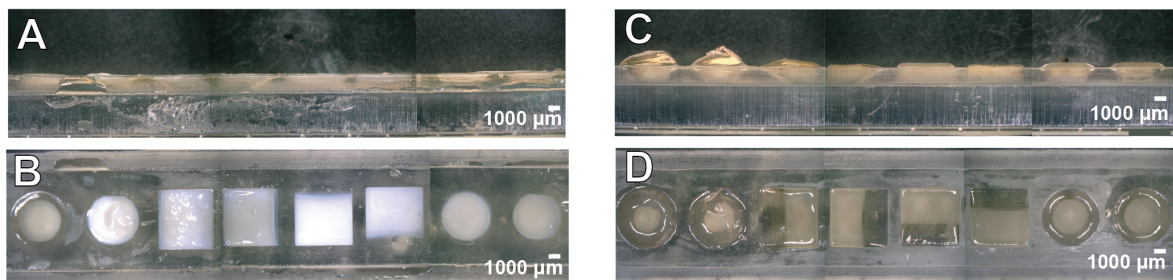


Figure 5.15: Comparison of PPOMaC under static conditions and under dynamic flow conditions after 2 days submersion in DMEM medium. A) Side view of POMaC in static conditions. B) Top view of POMaC in static conditions. C) Side view of POMaC in dynamic flow conditions. D) Top view of POMaC in dynamic flow conditions.

Figure 5.15 shows the difference between PPOMaC under static and under dynamic flow conditions. PPOMaC under a dynamic flow condition where the culture medium is pumped around with 65 ml/min, exhibits more swelling than under static conditions (Fig. 5.15 A and C). Moreover, the opaque layer in PPOMaC under this dynamic flow was diminished by  $29\% \pm 10\%$  with respect to the static condition. The decrease in the opaque

layer was calculated by close visual and pixel measurement of the images. First, the decrease in opaqueness as percentage of the total structure intersection length ( $L_i$ ) was taken, in every structure within the static and dynamic flow samples after 2 days (Fig. 5.16 A and Tab. 5.4). Second, using Equation 5.5 the corresponding depth of the opaque layer was calculated. Here  $L_i$  is the initial length of the structure (2.43 mm and 4.86 mm for the conical and square structures, respectively),  $L_t$  is the length of the transparent material,  $\alpha$  is the angle within the structure (38.6° and 21.8°, resp.), and  $d$  is the depth at which the opaque layer is assumed present (Fig. 5.16 B).

$$d = \tan(\alpha) * L_t \quad (5.5)$$

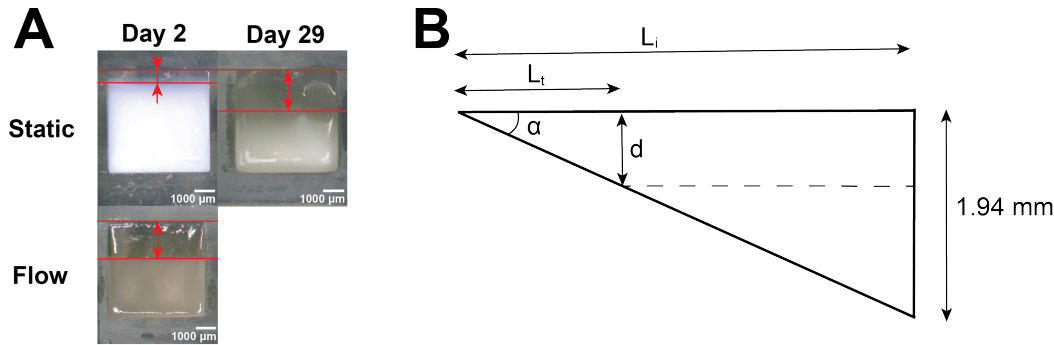


Figure 5.16: (A) Comparison of PPOMaC under static conditions (after 2 and 29 days) and under dynamic flow conditions (after 2 days). For PPOMaC under static conditions after 2 days an opaque layer depth of  $0.31 \pm 0.2$  mm was calculated. PPOMaC under dynamic flow conditions exhibited a degradation boundary depth of  $0.87 \pm 0.2$  mm after two days. Differences in white intensity may be due to light settings, opaque layer depth and dispersity changes. (B) Schematic illustration of the calculation of the opaque layer depth (dashed line).

Table 5.4: Overview of the decrease in opaqueness, as percentage of the total structure intersection length, in every structure within the static and dynamic flow samples after 2 days. The corresponding depth at which this opaque boundary layer is assumed present is included as well.

Structure	Static, day 2		Flow, day 2	
	Decrease of opaqueness	Corresponding layer depth [mm]	Decrease of opaqueness	Corresponding layer depth [mm]
1.	30%	0.58	60%	1.16
2.	20%	0.39	50%	0.97
3.	6%	0.11	45%	0.86
4.	11%	0.22	45%	0.86
5.	11%	0.22	39%	0.76
6.	17%	0.33	39%	0.76
7.	16%	0.31	40%	0.77
8.	18%	0.35	40%	0.77
<b>Average</b>	<b><math>16\% \pm 7\%</math></b>	<b><math>0.31 \pm 0.2</math></b>	<b><math>45\% \pm 7\%</math></b>	<b><math>0.87 \pm 0.2</math></b>

The average depth at which the opaque boundary layer was present after 2 days was  $0.31 \pm 0.2$  mm for the static condition and  $0.87 \pm 0.2$  mm for the dynamic flow condition (Tab. 5.4). This is a difference of roughly 35% between the two conditions. A numerical comparison between day 2 and day 29 for the static condition was not conducted due to the vague opaque layer boundaries after 29 days, impairing accurate measurements. Thus, PPOMaC exhibits opaqueness upon degradation in a layered manner. This opaqueness may decrease over time where the areas close to the material surface are affected first. Moreover, PPOMaC exhibits swelling during degradation. Incorporating a flow rate speeds up this process, presenting an increased degradation rate.

## 5.7. POMaC bonding

A strong bond connecting the POMaC membrane to the PDMS LOC device which remains intact under actuation and membrane stretching is necessary. Moreover, a strong bond between the membrane and an additional structure could also aid in detaching the membrane from the substrate. Both POMaC-POMaC bonding and POMaC-PDMS bonding were evaluated. POMaC-POMaC bonding formed long-term stable bonds. Pulling at each side of the bond with tweezers to detach the POMaC did not undo the bond before general rupture of the POMaC slabs. Thus, POMaC can be bonded well to POMaC by adding and heating uncured POMaC between two cured POMaC slabs.

None of the PDMS-POMaC bonds created using the methods in Section 4.7 showed long-term stability. The direct POMaC-PDMS bond and POMaC-PDMS bond with a liquid POMaC or PDMS layer in between cured the layers were found to loosen immediately when being submerged in DI water (Fig. 5.17). This shows that connecting POMaC to PDMS *via* these methods, does not create a strong bond. Moreover, in both tests incorporating oxygen plasma, no strong bond was created when using oxygen plasma on the POMaC and PDMS layers before placing them together. The samples were detachable from each other easily using negligible force.

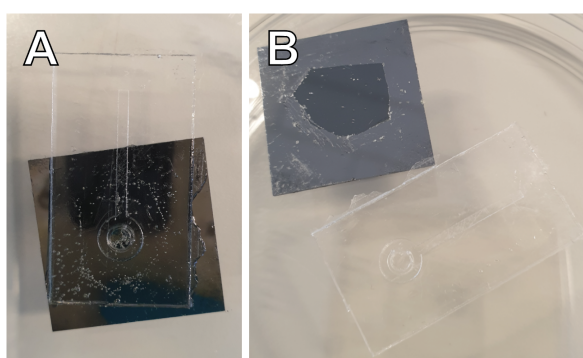


Figure 5.17: The result of POMaC-PDMS direct bonding. A) a PDMS actuator part was directly bonded to a thin POMaC layer on a silicon substrate. B) The two layers were easily detached, leaving both layers unimpaired.

## 5.8. Cytotoxicity of POMaC and photoinitiators

A cytotoxicity assay using eluates was conducted to evaluate the cytotoxicity of POMaC and two photoinitiators, Irgacure 2959 and TPO. Images of the cell culture exposed for one day and five days to the eluates of the T=1 condition are included in Appendix C.3. The cell culture results after two days in contact with the eluates are included in this Section. The T=1 eluate condition has been incubated with POMaC for the shortest time (1 day). The images of the cell cultures with eluates exposed longer to POMaC (T=2 and T=5) are included in the Supplementary files.

Figure 5.18 and 5.19 show the cell culture two days after the POMaC eluates are added. The eluates in these images have been in contact with the POMaC samples for one day (T=1) prior to being added to the cell culture. The control wells containing regular KSFM cell culture medium showed that most cells adhered to the substrate and were spread out. In addition, a large number of cells were present (Fig. 5.18 A). In the EPOMaC sample containing no photoinitiator (Fig. 5.18 B), fewer cells than in the control were present, of which about half adhered well to the substrate. The other half exhibited round cells which were loosely attached, showing moderate cytotoxic reactivity to the eluate. The cytotoxic reactivity of the cell culture is based on the qualitative morphological grading of cytotoxicity of extracts according to ISO10993-5 (Tab. 5.6). A general overview of the reactivity of the various cell culture conditions where the eluate was incubated with POMaC for 24h at 37°C (T=1) is included at the end of this Section in Table 5.5.

Moreover, the cells in culture with eluates from PPOMaC with cured 1 wt% TPO do not exhibit good adherence to the substrate, even at low eluate concentration (T=1), showing severe reactivity to the eluate (Fig. 5.19 A). In addition, cell cultures containing eluate from PPOMaC with cured 5 wt% Irgacure 2959 also showed similar, poor adherence of the cells to the substrate, small round cells and limited cell growth (Fig. 5.18 D). In contrast, the cell culture with eluate from uncured 1 wt% TPO looks more healthy than the cultures with cured 1 wt% TPO when comparing the T=1 eluates, showing a mild reaction to the eluate after one and two



days in cell culture. This cell culture contained better-adhered cells of which not more than 20% showed a rounded morphology and no extensive cell lysis was present. Overall, none of the cell cultures showed as good cell viability as the control. After five days in culture, the control showed a significantly more confluent cell layer than the cultures containing eluate, which showed very little cell viability, extensive cell lysis and a low cell count.

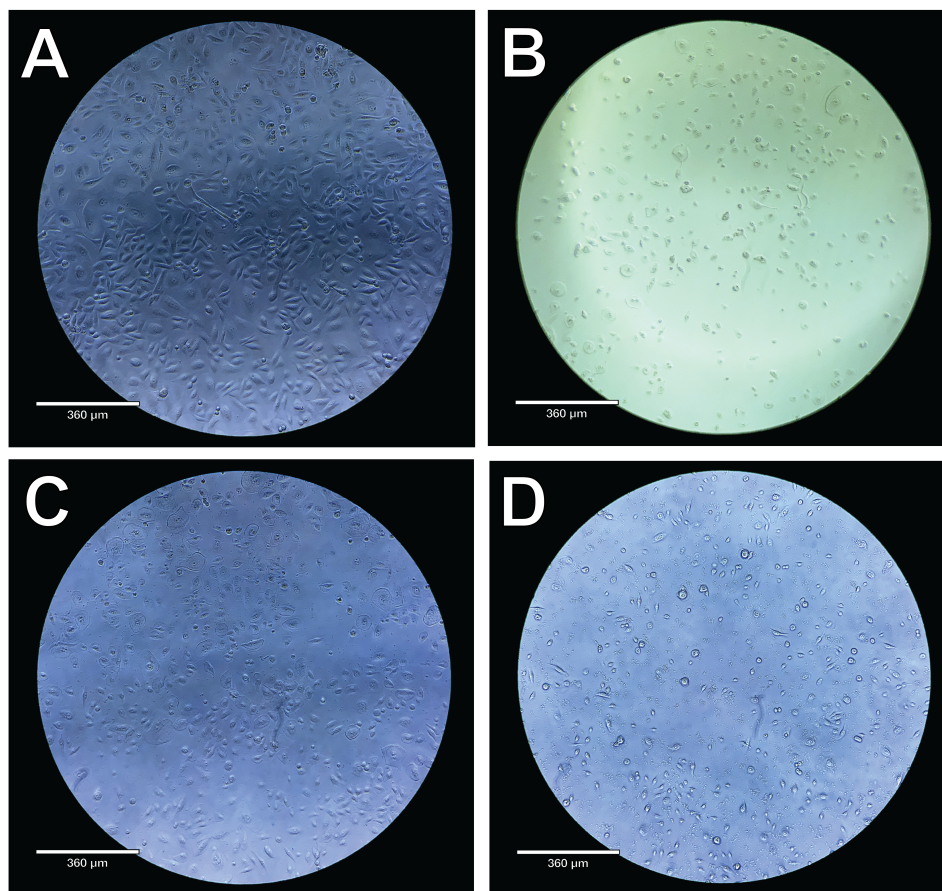


Figure 5.18: Cell culture images after 2 days in culture with the POMaC T=1 eluate. A) Control cell culture. B) EPOMaC with no photoinitiator, T = 1, well A. C) EPOMaC with 1 wt% uncured TPO, T = 1, well B. D) PPOMaC containing 5 wt% Irgacure 2959, T = 1, well B.

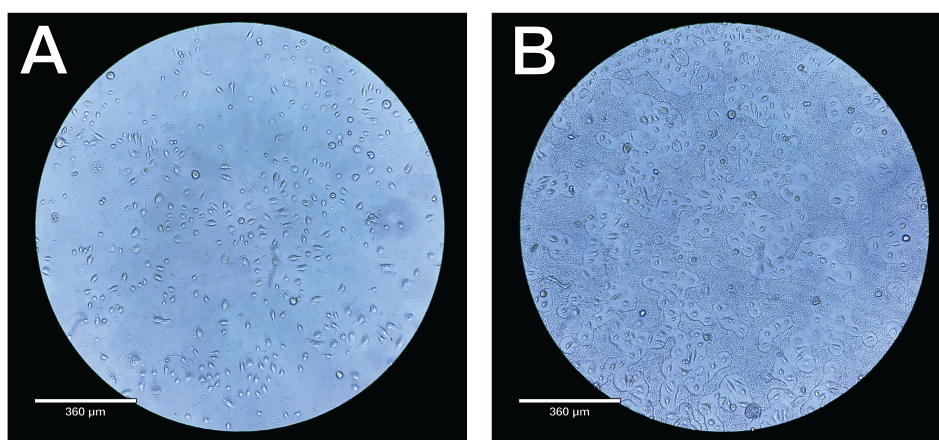


Figure 5.19: Comparison of the cell culture images of two different eluates, after 2 days in culture with the POMaC eluates added. A) PPOMaC containing 1wt% TPO, T = 1, well B. B) PPOMaC containing 1wt% TPO, T = 5, well B.

When the eluates had been in longer contact with the POMaC (T=1 vs. T=5), the cells exhibited a slightly lower adherence to the substrate and their morphology was more round, indicating higher reactivity to the eluate. This phenomenon was observed in the cell cultures containing eluate of the POMaC with uncured TPO and the cell cultures with eluates of POMaC containing no photoinitiator. In the cell cultures containing eluate of PPOMaC with cured TPO and Irgacure 2959, this phenomenon was difficult to establish, since this cell culture already exhibited a severe reactivity to the eluate. Thus, a higher POMaC concentration might have a negative influence on cell viability.

Moreover, little specs of material can be seen throughout the cell cultures imaged after two days in cell culture with the eluates. The amounts differ per sample, eluates from POMaC with no photoinitiator or with cured Irgacure 2959 hardly contain extra material, whereas the one containing PPOMaC with cured TPO contains a lot of precipitated material. Figure 5.19 shows the difference in the amount of material in the cell culture with an eluate that has been in contact with PPOMaC containing cured TPO for one day (T=1) (A) versus for five days (T=5) (B). The number of specs increases with the time the POMaC samples have been in contact with the medium to create the eluate. Therefore, the material specs might be dissolved and settled POMaC within the eluate.

Table 5.5: Qualitative morphological evaluation of cytotoxicity of POMaC eluate, incubated for 24 h at 37°C (T=1), with respect to PBEC reactivity. The various columns indicate the different cell culture durations. The reactivity is graded based on ISO10993-5.

Eluate condition	Cell culture reactivity		
	Day 1	Day 2	Day 5
Control	None	None	Slight
EPOMaC, No photoinitiator	Moderate	Moderate	Severe
EPOMaC, Uncured 1 wt% TPO	Mild	Mild	Severe
PPOMaC, 5 wt% Irgacure 2959	Severe	Severe	Severe
PPOMaC, 1 wt% TPO	Severe	Severe	Severe

Table 5.6: The qualitative morphological grading of cytotoxicity of polymer extracts, as stated in ISO 10993-5:2009(E).

Reactivity	Condition of cell cultures
None	No cell lysis, no reduction of cell growth, discrete intracytoplasmatic granules.
Slight	Not more than 20% of the cells are round, loosely attached and without intracytoplasmatic granules, or show changes in morphology; occasional lysed cells are present; only slight growth inhibition observable.
Mild	Not more than 50% of the cells are round, devoid of intracytoplasmatic granules, no extensive cell lysis; not more than 50% growth inhibition observable.
Moderate	Not more than 70% of the cell layers contain rounded cells or are lysed; cell layers not completely destroyed, but more than 50% growth inhibition observable.
Severe	Nearly complete or complete destruction of the cell layers.

## 5.9. Autofluorescence of POMaC

The results of the 1 mm thick samples showed that pure POMaC exhibits autofluorescence on multiple wavelengths commonly used in fluorescence imaging: CY5, DAPI, FITC, and TXRED (Fig. 5.20). There was no significant difference between POMaC without or with photoinitiator added. The intensity of the autofluorescence depends on the material thickness and the exposure time used when taking the image. To test whether this autofluorescence would limit imaging of fluorescently stained cells on a thin membrane, a ~200  $\mu\text{m}$  thin membrane containing PPOMaC with 1 wt% TPO was tested with a stained cell culture on top using realistic exposure times (Fig. 5.21). It was found that the thin membrane at these exposure times showed little autofluorescence (Fig. 5.21 A), comparable with the autofluorescence of PDMS (Fig. 5.21 B), and did not

limit the imaging of the stained cell culture (Fig. 5.21 C). An overview of the results for all the samples and the exposure times used are included in Appendix C.4 and A.7, respectively.

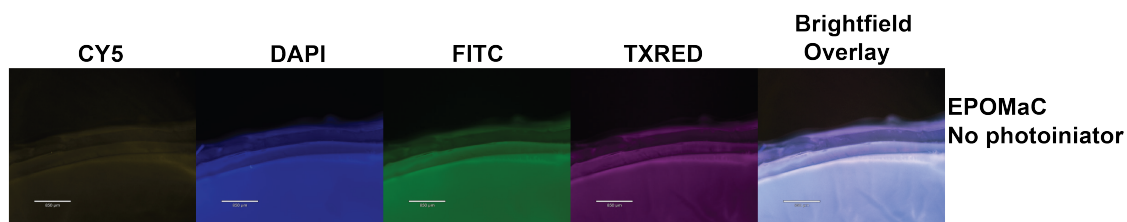


Figure 5.20: Autofluorescence imaging results of a 1 mm EPOMaC sample containing no photoinitiator. Scalebar, 850  $\mu\text{m}$ .

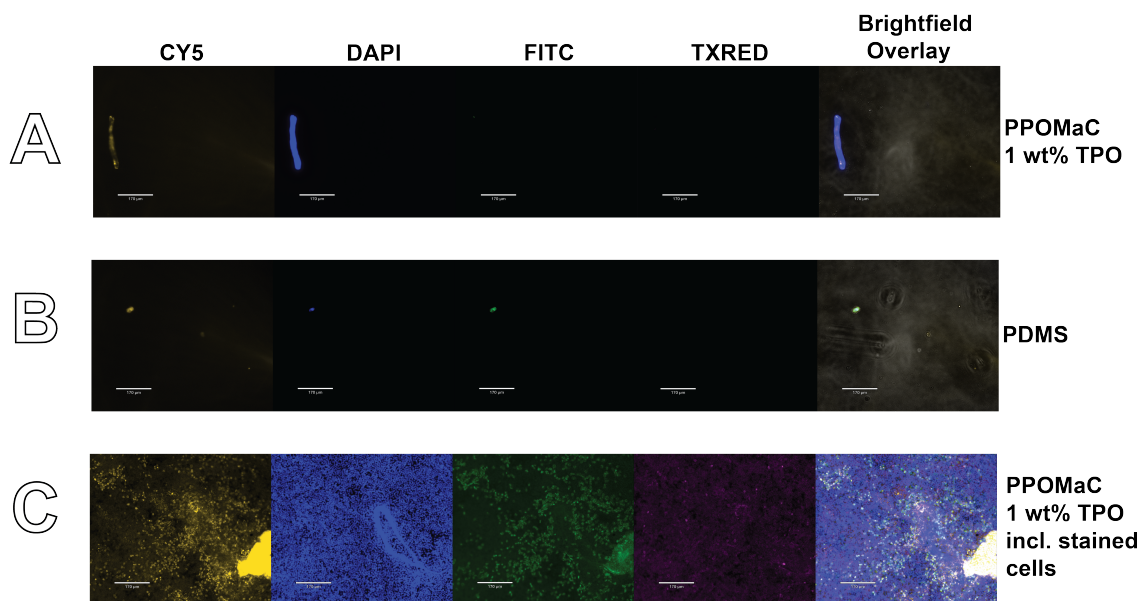


Figure 5.21: Autofluorescence imaging results of a thin PPOMaC and PDMS sample comparing the level fluorescence with the addition of stained cells. A) The autofluorescence measured on a 200  $\mu\text{m}$  thick PPOMaC sample containing 1 wt% TPO. B) The autofluorescence measured on a 200  $\mu\text{m}$  thick PDMS sample, using the same exposure times. C) The autofluorescence measured on a 200  $\mu\text{m}$  thick PPOMaC sample containing 1 wt% TPO with a microscope slide containing a fluorescently stained cell culture on top. Using the same exposure times. Scale bars, 170  $\mu\text{m}$ .



# 6

## Discussion

This study evaluates whether a membrane with a dynamic pore size could be fabricated based on material biodegradability and evaluates POMaC's suitability as a structural membrane material to this end. Part one of this discussion will interpret the obtained results and analyse the methodology used. In part two, the project will be analysed in a broader view and provide alternative approaches that could be followed if the methodology used is to be discarded.

### 6.1. Interpretation of findings

The concept of using biodegradation to create an increasing pore size was studied in closer detail: whether a thin membrane could be spincoated; and whether small pillars could be 2PP-printed as a moulding structure for creating an imprint in the spincoated membrane. Moreover, POMaC with a 5:1:4 monomer ratio (1,8-octanediol: citric acid: maleic acid) was evaluated on several aspects: its mechanical properties; its surface adhesion and bonding to various materials; its degradability; its autofluorescence; and its toxicity. This Section will discuss the results of the studied aspects. Afterwards, an overall analysis will be given.

#### Fabrication differences

The UV lamp used was a point source (Bluepoint 4 Ecocure) with light output dimensions of about 1 cm<sup>2</sup> point diameter, giving a high local intensity within and low intensity outside this area. Therefore, larger areas than the point diameter were more challenging to cure equally, possibly creating polymerization differences within larger POMaC samples due to fabrication. However, care was taken to mitigate this effect as much as possible by, e.g. polymerizing in steps and covering not yet-to-be-cured parts with aluminium foil. Moreover, in a small amount of the experiments, an unreliable UV lamp (Photopol Light-curing unit, Dentalfarm, Italy) was used; the results obtained with this lamp are therefore not included or considered in the conclusions. In future research, local variations can be limited by using a UV flood light instead of a point source.

Several results were obtained regarding the two photoinitiators, 5 wt% Irgacure 2959 and 1 wt% TPO. No significant difference in the cytotoxicity of 5 wt% Irgacure 2959 and 1wt% TPO was found, as both cultures did not exhibit good cell viability. POMaC with 5 wt% Irgacure 2959 exhibited yellowing after curing, whereas POMaC with 1 wt% TPO did not. Although yellow, the POMaC with Irgacure 2959 had similar transparency to POMaC with TPO and can be assumed to provide relatively equal imaging possibilities. Moreover, 5 wt% Irgacure 2959 was found to cure POMaC significantly faster than 1 wt% TPO. Curing POMaC with 1 wt% TPO takes a relatively long time (~ 30 minutes for a thin layer). To speed up the curing process, 5wt% Irgacure 2959 could be used as a photoinitiator, despite the yellowing. A second option is to increase the concentration of 1wt% TPO in future research. The toxicity and stiffness of POMaC, among others, with an adjusted photoinitiator concentration would have to be re-evaluated.

#### Spincoating and pillar moulding

It was evaluated whether spincoating could be a possibility for fabricating a membrane with a thickness of about 10 µm. In order to do this, several spincoating settings were used, and various substrate primers were



tested. HMDS, as a surface primer, provided the best results, providing uniform and stable (thin) spincoated layers after curing. A membrane with a thickness of  $13 \pm 5 \mu\text{m}$  could be fabricated, roughly the desired thickness range for the LOC concept membrane although with still quite some thickness variability. This spincoated thickness was limited mainly by the handleability of the membrane due to membrane detachment difficulties.

Furthermore, it was tested whether a mould containing conical pillars could be fabricated using 2PP-printing. Well-defined pillars could be created in an array spanning 3 mm by 3 mm, with accurate dimensions of the 2PP-prints with respect to the design. The pitch of the pillars used in the dose and array tests was  $20 \mu\text{m}$ , which posed no issues. A larger pitch should, therefore, also not give any challenges. The pitch advised when fabricating the final membrane is about  $35 \mu\text{m}$ , as stated in Section 3. Overall, 2PP-printing is a promising method for fabricating a mould containing conical pillars. To what extent the pillars remain adhered to the substrate during the POMaC membrane demoulding is to be evaluated. A recommended approach for testing this is included in Appendix D.1. Moreover, UV post-polymerization of the pillars post-printing could enhance their stability and prevent shrinkage. In future, this additional step could be tested and incorporated as well.

A thin, uniform and stable POMaC film was thus created and detached. Moreover, an array of well shaped conical pillars was also created, which could be used as a structural mould for imprinting the pore structures within the membrane. A combination of fabricating and detaching a thin membrane while utilizing the cone-shaped pillars still has to be conducted.

### Stiffness quantification

Regarding the present variation within one sample and the variation between samples, these results mainly give a valuable indication of the material's elastic modulus at the surface. There are relatively large deviations between the measurements even though they are taken close together. These deviations can have several reasons: fabrication differences such as UV lamp spot differentiation, irregularities and imperfections in the material, and sample adhesion to the substrate during measurement. Moreover, the second sample was submerged for a shorter time than the first; Sample 1 was submerged for around 20 minutes longer while setting up the experiment, whereas Sample 2 was measured immediately. This time difference might explain the slight difference in standard deviation and mean stiffness between these samples. Note that the effective Young's modulus was measured at the top layer of the sample. This stiffness is experienced by cells located at the surface. The Young's modulus within the bulk of the material may differ. This latter stiffness is critical to the overall strength and elasticity of the membrane. Naturally, the thinner the sample, the less variation there will be in the stiffness throughout the material.

The obtained effective Young's moduli of  $0.30 \pm 0.06 \text{ MPa}$ ,  $0.35 \pm 0.07 \text{ MPa}$  and  $0.06 \pm 0.02 \text{ MPa}$  fit in the  $0.03 \text{ MPa} - 1.54 \text{ MPa}$  stiffness range for POMaC as stated by Tran et al. [67]. Moreover, it corresponds with observations of Boutry et al. [68], who found a tensile modulus of  $0.3 \text{ MPa}$  with slightly different parameters<sup>1</sup>. Moreover, Tran et al. [67] found a Young's modulus of  $0.29 \pm 0.04 \text{ MPa}$ <sup>2</sup>. Both these studies exhibit a similar stiffness range as the EPPOMaC samples with 1 wt% TPO as the photoinitiator tested in this research.

Moreover, the effective Young's modulus, measured at the EPPOMaC surface, is lower after 2 weeks of sample submersion in PBS. This corresponds with the results of Boutry et al. [68], who found that the tensile modulus of both EPPOMaC and EPOMaC diminished the longer the material was incubated in PBS at  $37^\circ\text{C}$ . EPPOMaC exposed to physiological media had a decreasing tensile modulus at a rate of -11% per week [68]. This research found an effective Young's modulus decrease of more than 65% after two weeks, which is significantly higher. This difference could be due to a difference in measurement location. Whereas Boutry et al. [68] measured the bulk properties during tensile tests, this study performed a stiffness measurement solely at the material surface.

Moreover, the type and concentration difference of the photoinitiator used might also play a role. Suppose fewer non-hydrolysable photocrosslinks are generated with 1 wt% TPO than with 5 wt% Irgacure 2959. In that case, POMaC with 1 wt% TPO could have a faster deteriorating mechanical cohesion in the material during degradation, even with a lower citric acid concentration compared to the monomer ratio that Boutry et al.

<sup>1</sup>EPPOMaC with 5 wt% Irgacure 2959 as photoinitiator, UV cured for 20 min. and 48 hours oven post-polymerisation, using a monomer ratio containing a higher citric acid to maleic acid ratio than this project [68].

<sup>2</sup>Using PPOMaC with the same molar ratio as this project, containing 1 wt% Irgacure 2959, UV irradiated for 10 min [67].

[68] used. Therefore, to diminish the stiffness decrease of the membrane within the LOC upon degradation, besides adjusting the monomer ratio, the photoinitiator concentration and type could be adjusted to increase the crosslinking density. Naturally, this also influences the degradation rate, as will be explained later in this Section.

The effective Young's modulus of the POMaC sample submerged for 2 weeks was  $62 \pm 20$  kPa. This is softer than most cell culture scaffolds reported up to now [12, 14, 19, 39, 47]. Moreover, the found stiffness comes close to the stiffness range of native lung tissue (5 - 30 kPa) [67]. Generally, the stiffness of the alveolar-capillary barrier is assumed lower than 10 kPa [4, 30, 36]. Literature has shown that soft and elastic scaffolds provide better angiogenesis than stiff scaffolds [67]. Therefore, POMaC proves to be a very promising material regarding its surface stiffness for lung cell cultures.

Moreover, the LOC device prior designed by the PME Department was designed for a 10  $\mu\text{m}$  thick, 15:1 base: crosslinking agent ratio PDMS membrane [1]. Depending on the curing method, this type of PDMS has a stiffness of  $\sim 400$  kPa when baked at 90  $^{\circ}\text{C}$  for 15 min. The POMaC was found to have a stiffness between roughly 60 and 350 kPa. A lower membrane stiffness would require a lower actuation pressure, which is possible. Lastly, since POMaC degrades layer-by-layer, the measured stiffness measured at the surface after prolonged submersion will be lower than within the centre of the material. How fast the stiffness throughout the whole material is affected and decreases depends on the degradation and water diffusion rate.

### POMaC degradation

A surface erosion rate of 0.5  $\mu\text{m}/\text{week}$  was aimed for to obtain the ideal pore size proposed in the concept ( $3 \geq d \leq 8 \mu\text{m}$ ) by the time flow is introduced in the LOC (Section 3). This means that over 4 weeks, the span of the degradation experiment, a surface erosion of 2  $\mu\text{m}$  is assumed ideal for a purely static condition. However, significant swelling was observed. The PPOMaC was affected by degradation at a depth larger than 2  $\mu\text{m}$  after two days, as indicated by the presence of an opaque layer at these depths (Tab. 5.4). After two days under static conditions, a layer of about  $0.3 \pm 0.1$  mm was affected by degradation. For conditions under dynamic flow, the degradation rate was higher, where the POMaC was affected by degradation to a layer depth of  $0.9 \pm 0.2$  mm (Fig. 5.16).

Since the opaque layer depth progressed layer-by-layer, it was evident that the PPOMaC was affected by degradation in a layered manner. This corresponds with the literature [66–68]. Moreover, regarding the large amount of swelling present, it was observed that the rate at which water penetrates the material significantly exceeds the rate at which the polymer is broken down, a hallmark of bulk degradation [77]. A significant decrease in material strength, but not in volume was observed (Fig. 5.13 and Fig. 5.14). It was also evident that the degradation moved in a layered manner through the material, as the opaque transition layer moved down through the POMaC (Fig. 5.14). Therefore, it can be argued that POMaC does degrade in a layer-by-layer manner. However, the top layer, affected by hydrolysis, exhibits bulk degradation characteristics, where molecular weight decrease and loss of strength precede mass loss (Fig. 2.16). This has several implications: large material swelling and loss of material strength before loss of mass.

A model of the breakdown of POMaC is proposed and illustrated in Figure 6.1. In this model, initially, both hydrolysable ester bonds (blue) and carbon-carbon crosslinks (red) are present in the polymer (Fig. 6.1 A). When water propagates into the polymer, hydrolysis starts, breaking down the ester bonds, shortening the polymer chains and decreasing the molecular weight of the area affected by water propagation. The polymer network structure remains still largely intact, maintaining the network strength. With more polymer bonds broken, this network strength deteriorates. The non-hydrolysable carbon-carbon crosslinks remain, maintaining a network structure which maintains part of the polymer strength. Mass loss is, at this point, limited since polymer chains are still entrapped by or connected to the network by, for example, the non-hydrolysable vinyl crosslinks. The subsequent weakened network structure swells with the encapsulated water (Fig. 6.1 B).

The amount of swelling in photocrosslinked POMaC can be directly correlated to the amount of crosslinking in the polymer. This crosslinking density depends, among others, on the concentration of maleic anhydride in the polymer [67]. Increasing maleic anhydride concentration increases the degree of carbon-carbon crosslinking *via* photopolymerisation, causing a slower degradation rate [67]. Moreover, a higher density of ester bond crosslinking also decreases the biodegradability rate when comparing monomers with equal monomer ratio's [67]. On the other hand, if the citric acid to maleic anhydride ratio is increased, the amount of carbon-carbon crosslinking diminishes, the hydrophilicity increases and the degradation rate increases

under equal curing conditions [67]. It can be assumed that a higher degree of crosslinking prevents the water molecules from penetrating at the same rate through the material, slowing them down. A lower degree of crosslinking or increased hydrophilicity elicits an opposite effect, increasing the water diffusion rate. This means that a trade-off is present between the degradation rate and the amount of swelling observed by adjusting the monomer ratios.

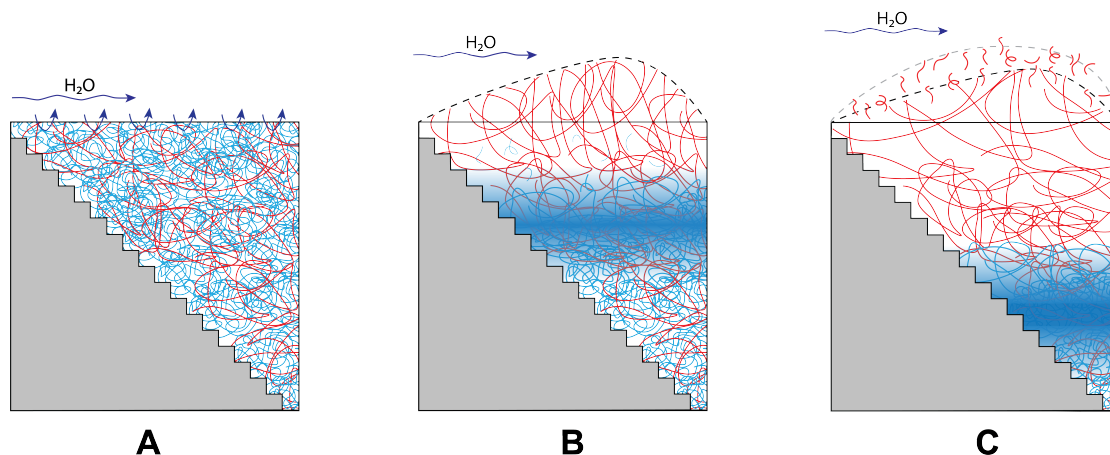


Figure 6.1: A schematic illustration depicting a structure (grey) containing POMaC exposed to water during degradation over time. (A) POMaC containing ester bonds (blue) and carbon-carbon crosslinks (red). (B) Water is seeping into the material breaking the hydrolysable ester bonds. Carbon-carbon crosslinks remain and swelling occurs. (C) The hydrolysis transition layer (blue area) proceeds deeper into the material. Eventually carbon-carbon crosslinks are broken down, causing mass loss.

The material turns opaque (blue layer) when affected by hydrolysis. This increase in opacity is a sign that hydrolytic degradation has started [79]. This loss of transparency indicates a change in the reflective index due to water absorption and the formation of low molecular weight compounds. Crystallinity increases and voids are formed, which also may contribute to an increase in opacity as polymers are usually opaque because of light scattering on the numerous boundaries between the differently organised material regions [79]. For example, crystallinity could occur due to broken-down chains having greater freedom to form regions with more highly organised structures, as is the case for hydrophilised amorphous cellulose and many polymers [77, 79, 122]. The fact that the polymer becomes an opaque white colour is also seen in PLA degradation, which degrades with hydrolysis as well [81].

As water further propagates into the material, causing a hydrolysis reaction further away from the surface, this opaque transition layer also propagates further down into the material (Fig. 6.1 C). This propagation is relatively slow, exhibiting the layer-by-layer degradation of POMaC. Significant mass loss and complete network breakdown are present once the carbon-carbon crosslinks also degrade away, which is at a significantly later stage than the ester bond breakdown.

The first implication of degradation with bulk characteristics is that POMaC exhibits significant swelling as the hydrolysable ester bonds are broken, but the carbon-carbon crosslinks remain. This swelling is decreased from the top side when mass loss kicks in. However, the further down the opaque layer travels, the more swelling will occur. Thus, swelling will be present until the entire device has been broken down. This is different than would occur in pure surface erosion where material breakdown exceeds the rate of water propagation into the material, limiting swelling [77]. Since swelling will be omnipresent during degradation, the pores in the membrane would close up instead of becoming open more during material breakdown.

A second implication is that POMaC exhibits strength loss before mass loss in the area affected by hydrolysis. The breakdown of the hydrolysable ester bonds decreases the material strength of the material within the region affected by water. The deeper into the material POMaC is affected by the penetrating water, the more the mechanical properties will decrease, causing loss of strength before loss of mass. This aspect was also observed in the effective Young's modulus measurements at the surface of submerged POMaC (Fig. 5.13).

The top part of the POMaC basically turns into a hydrogel where water is kept between the polymer network.

For the design of a cell-supporting membrane under strain, the layer-by-layer degradation and penetration of water into the material need to be sufficiently slow so that the internal mechanical strength of the membrane is preserved. The diffusion rate of water into the material is thus a critical parameter. The degradation rate and the amount of swelling can be influenced by the crosslink density, which limits the propagation of water into the material [67, 92]. However, the rate of mass loss should, for the concept tested in this study, be fast enough to enable the opening up of dynamic pore sizes. Significant material loss only starts once the carbon-carbon crosslinks also degrade away, breaking up the remaining polymer network. At this point, the overall dimensions of the material will start to decrease. Figure 6.2 illustrates a model on how POMaC could degrade around a pore based on the model introduced above (Fig. 6.2 A) versus a membrane exhibiting pure surface erosion (Fig 6.2 B). For POMaC, the deeper the degradation boundary reaches into the POMaC, the more pronounced the swelling will become. Due to swelling, the pores in the membrane, instead of opening up, will close up. This would not limit water permeability but might impede signalling molecule and immune cell transmigration.

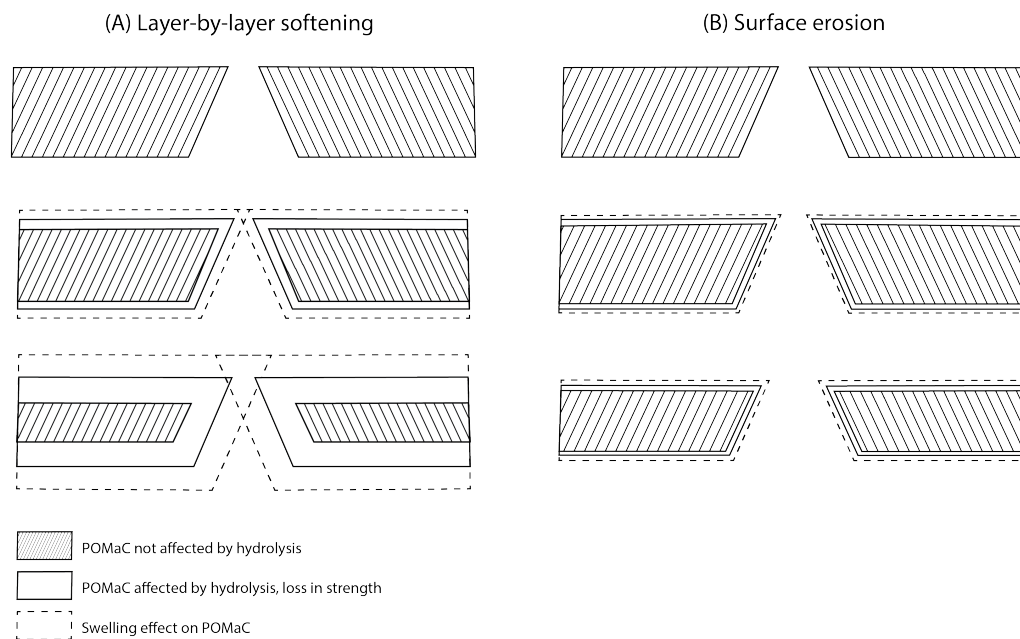


Figure 6.2: Schematic illustration of a pore in the membrane affected by (A) layer-by-layer softening exhibiting bulk degradation characteristics. As POMaC is broken down by hydrolysis, the material decreases in strength, a polymer network remains present and the material exhibits swelling. (B) An illustration of the effect of surface erosion, where the degradation reactions are limited to the surface of the polymer and the rate of hydrolysis of bonds is relatively fast compared to the diffusion rate of water into the bulk material [77]. As such, swelling is limited.

Overall, POMaC degrades layer-by-layer since the water takes time to reach the other side of the sample, possibly due to a large degree of crosslinking. As such, POMaC is a very suitable degradable packaging material, reducing the effect of material breakdown to the surface and limiting it in the area of the material not yet affected by water. This corresponds with Huyer et al. [66], who stated that POMaC maintained its mechanical properties over 2 months in hydrolytic degradation conditions for a  $1.5 \times 0.5 \times 10$  mm sample. Furthermore, POMaC showed no appreciable mass loss over 14 days when exposed to the enzymatic environment of cardiac cells [66]. On the other hand, POMaC is less suitable when a structural geometry at the microscale needs to be maintained within the material, as large amounts of swelling can be observed upon degradation, which does not diminish appreciably over short time spans.

The presence of cells on the material and increased temperature in the incubator might increase the degradation rate. Enzymes might affect the moment when mass loss starts since these might readily break down the carbon-carbon and ester crosslinks. However, it is difficult to establish to what extent enzymatic degra-

dation, also with respect to hydrolysis, plays a role in polymer breakdown due to difficulties in comparing *in vivo* data to *in vitro* data due to the lack of standardisation for *in vivo* studies, and the minimal data on POMaC [81]. Furthermore, it has been reported that POMaC has a degradation mechanism comparable to that of PGS, where both take place *via* hydrolysis [68]. Pomerantseva et al. [83] state that enzymatic digestion played a significant role in the degradation of PGS, indicating that PGS resorption might be primarily due to enzymatic degradation, as observed for other surface eroding polymers, next to slow hydrolytic degradation [83]. Enzymes capable of hydrolysing ester bonds are, for example, lipases [83]. Thus, the cellular effect on degradation is a vital aspect to consider in future studies.

#### Comments on experimental set-up

Since POMaC degrades layer-by-layer, but the material does not degrade away fully simultaneously with polymer bond breakdown, the degradation experiment set-up was too idealistic. This set-up assumed solely surface erosion characteristics and material dissolution roughly at the moment of material degradation and, therefore, utilised geometric structures to evaluate the rate of degradation [77, 81]. However, for reasons described previously, the polymer network exhibits swelling quite a long time after degradation is initiated, limiting the use of geometry to get an indication of the degradation rate.

Furthermore, letting the syringe pump run for multiple days placed considerable wear on the tubing, causing leaks. Subsequently, this wear was diminished by way of lubrication. Additionally, a different pump with a higher flow rate or a lower channel height should ideally be incorporated if a more optimal version of the degradability channel mould is desired to be used, as explained in Section 4.6.

Furthermore, it was observed that the initially pink cell culture medium in the degradability experiment changes to a light yellow colour after 1 to 2 days of use (Fig. 4.9). This DMEM medium obtains its colour from phenol red, which is an indication of the medium pH. Yellowing indicates a reduction in the pH, which can have several causes. A reduction in the pH could be due to the increase in carboxylic acid groups within the POMaC, which act as proton donors (as explained in Section 2.5.2). Another possible reason is the high environmental oxygen concentration during the experiment. Usually, this medium is used in an incubator with an oxygen percentage of about 5%, whereas the experimental environment contains 21% oxygen. Moreover, normal cellular respiration (glycolysis) and the presence of aerobic bacteria also result in medium acidification [123, 124]. Sample contamination can, therefore, also be a source of medium acidification.

The molecular weight decrease, loss in strength and loss in mass for polymer degradation are commonly studied with chromatography, tensile testing (e.g. by DMA) and mass reduction measurements, respectively [81, 87, 124]. Studying the degradation using these techniques could give a better understanding of the exact degradation process and validation of the model introduced above. It might also be interesting to measure the difference in mechanical properties between POMaC already degrading and the part that has not yet been degraded. So, for example, cut a partly affected POMaC sample and measure the stiffness of the polymer on either side. Also, research into the water diffusion rate into the polymer would be very valuable.

Furthermore, a permeability measurement to study the degradation effect on the pores would be interesting. As mentioned, the material swells and expectedly, the pores close up. However, the pores are still present, and the surrounding material becomes softer. Thus the membrane would still be water permeable, though it is as yet unclear how permeable it would be to proteins, signalling molecules and cells. A short and schematic proposal for an experiment is included in Appendix D.2.

Lastly, deviations in swelling and the degree of opaqueness within various sample structures can be due to local differences in the degree of photopolymerisation. This aspect could have been diminished by using a UV floodlight instead of a point source. Moreover, as UV curing was only conducted on one side of the sample, that surface might have absorbed more energy and contain a higher crosslinking density. Naturally, this could affect the rate and characteristics of degradation. This effect would be less present in a thinner sample.

#### Bioimaging

Based on the results, a  $\sim 200\ \mu\text{m}$  thin POMaC membrane showed limited autofluorescence, comparable to PDMS, using realistic exposure times. A stained cell culture placed directly on top of the membrane could be adequately imaged for several commonly used wavelengths. Thus, autofluorescence of POMaC is not a limitation in designing a thin membrane for fluorescent cell culture imaging. Further studies could include the effect of POMaC fluorescence by absorption of fluorescent markers used in cell staining, as this study focused

solely on the intrinsic autofluorescence of the material. Since cells are stained by adding a fluorescent component to the culture that the cells absorb, it is relevant to study to what extent POMaC absorbs these markers and exhibits fluorescence by absorption. Moreover, it was observed that upon degradation, POMaC turns opaque. It would be relevant to study to what extent and for what time this opacity would be present in fully submerged thin POMaC layers and to what extent it would limit confocal microscopy applications and exhibit autofluorescence.

### Membrane integration

None of the PDMS-POMaC bonds created with the methods in Section 4.7 showed long-term stability. Zhang et al. [57] reported weak bonding between PDMS and POMaC when UV curing POMaC directly on PDMS due to inhibition of polymerisation at the PDMS-POMaC surface [57]. This corresponds with the result found when using liquid POMaC. Furthermore, it was found that when using previously cured POMaC and PDMS layers or liquid PDMS, no long-term stable bonds could be formed either. The samples treated with oxygen plasma were left for 30 min. whereas Ramakrishna et al. [114] bound his PDMS samples overnight in an oven at 45 degrees after plasma treatment. Heating could help in initiating and speeding up the polycondensation reaction. A stronger bond between PDMS and POMaC can possibly be achieved if a longer (heating) step and a certain bonding pressure are applied.

Since POMaC bonds well to itself, it could be a possibility to fabricate the whole device out of POMaC. Fabricating the whole device from POMaC would aid membrane integration and minimise the absorption of small molecules throughout the LOC but would also introduce several disadvantages: It would make the LOC actuator and flow channels degradable, and the channels would swell upon exposure to aqueous media, causing varying channel dimensions and limiting LOC durability. Moreover, the LOC actuator dimensions should be adjusted for the stiffness of POMaC, which was found to not be constant throughout degradation and submersion. This would necessitate constant actuation pressure adjustments throughout the LOC lifetime to maintain equal strain on the membrane. Therefore, this is not deemed a suitable solution.

Another promising bonding method could be to use polyurethane since it bonds both to PDMS [113] and to POMaC [93]. Citrate-based elastomers (POC) have been crosslinked previously with polyurethane<sup>3</sup> [65]. Moreover, Domansky et al. [113] and Zhao et al. [93] researched polyurethane elastomers. Zhao et al. [93] used polyurethane as a bonding material to secure POMaC wires to polystyrene microwells, based on the work of Domansky et al. [113], who bonded polyurethane to PDMS. Both studies used the same castable two-component polyurethane (GSP 1552-2, GS polymers, Inc.) to bond the materials. The bonding was conducted with air plasma treatment on PDMS and polyurethane samples before placing them together under pressure, generating a bond strength of  $> 38.1 \pm 1.2$  kPa [113]. Zhao et al. [93] applied a minimal quantity of the castable two-component polyurethane creating a bond between polystyrene and POMaC [93].

Domansky et al. [113] found that the polyurethane used was nontoxic. Moreover, polyurethane has less absorption of small hydrophobic molecules than PDMS, and it is an elastic material [113]. Domansky et al. [113] stretched pure polyurethane at 10% strain for 200 cycles at 0.125 Hz and found that it exhibits similar elastomeric properties to Sylgard 184 PDMS. The Young's modulus of the polyurethane at higher strains (10%-25%) was higher than for 1:10 PDMS,  $\approx 2.56$  MPa versus  $\sim 1.22$  MPa, respectively. This stiffness difference should be considered when determining the actuation pressure within the LOC device. For future studies into the integration of the POMaC membrane into the device, a study into the use of polyurethane as described by Domansky et al. [113] and Zhao et al. [93] is therefore recommended.

### Toxicity and biocompatibility

A difference between the cytotoxicity of photoinitiators was not observed in this cytotoxicity assay. Moreover, POMaC, based on literature, is a very biocompatible material, although currently not yet tested with primary lung cells, to the author's knowledge. However, ideal cytocompatibility was not found. According to ISO10993-5, a material is cytotoxic when its extract induces a moderate to severe reactivity on the cell culture. This definition means that not more than 50% of the cells exhibit a round morphology and that no extensive cell lysis or more than 50% growth inhibition is observable in the cell culture [125]. Based on the results in Section 5.8, it can be concluded that the POMaC eluates are cytotoxic to the PBECs used in this experiment. Overall, none of the cell cultures showed as good cell viability as the control, generally exhibiting severe reactivity to the eluate, indicating cytotoxicity. This cytotoxicity may be attributed to material property

<sup>3</sup>Polyurethane doping *via* 1,6-hexamethylene diisocyanate (HDI) crosslinking [65].

or sterilisation issues.

Generally, unreacted photoinitiators may be a cause of cytotoxicity. For example, Wang et al. [65] state that a photoinitiator concentration of 1.0% of reacted TPO was found to be cytocompatible, whereas the cytocompatible concentration of unreacted TPO is relatively low (<0.01%) [65]. This implies that the cell culture based on 1 wt% uncured TPO photoinitiator was expected to have exhibited higher cytotoxicity than the culture with cured 1 wt% TPO. As evident from the results, this was not the case. The cells in culture with eluates from PPOMaC with cured 1 wt% TPO and cured 5 wt% Irgacure 2959 did not exhibit good adherence to the substrate. In contrast, the cell culture with eluate from uncured 1 wt% TPO looked more healthy than those with cured TPO when comparing the T=1 eluates after two days in cell culture. Therefore, this viability difference might be more due to sample fabrication and sterilisation than a (un)reacted photoinitiator's presence.

In order to eliminate the possibility of sterilisation issues, a more rigorous sterilisation procedure could be carried out. Tran et al. [67] cleaned *in vitro* POMaC samples with 70% ethanol for 3 hours instead of 10 seconds, and applied UV light for 30 min before washing them in PBS [67]. This more rigorous sterilisation method is similar to the one used for *in vivo* sterilisation. A method like this might provide a promising alternative.

The difference between the cytotoxicity of photoinitiators and the cytotoxicity of POMaC for primary lung cells were not conclusively found in the toxicity assay. However, the literature does indicate that POMaC is a very biocompatible material. Therefore, further research on using POMaC for lung cell cultures will remain beneficial to exclude the effect of possible sterilisation issues during fabrication and pre-culture treatment. Lastly, it was observed that precipitation of small particles was present when using eluates of PPOMaC with 1 wt% TPO at higher concentrations (Fig. 5.19 A). Based on the literature, POMaC breakdown products are stated to be fully soluble [67]. The observed precipitation might be due to a high POMaC concentration in the eluate, causing agglomeration of breakdown products. Further research into the chemical build-up of the material and its effect on cells should be conducted.

## Summary

Concerning the membrane concept, POMaC can be spincoated into thin, uniform layers and detached from the substrate. Furthermore, well shaped pillars that could be used as a structural mould can be created. POMaC showed significant material softening when exposed to aqueous media. The stiffness was found to be in the expected range. The degradation behaviour of POMaC was different than hypothesised and showed layer-by-layer softening and swelling. This would impede pore opening. Cured POMaC was found suitable for confocal microscopy and fluorescently staining applications when not yet having been submerged. Overall, POMaC is a promising material so far. However, as previously mentioned, more research needs to be conducted, especially on its cytotoxicity, and possibly a different approach could be taken to implement dynamic pore sizes. This Section provided an overview of the interpretation of the obtained results and incorporated suggestions to improve the methodology used. Part two of the discussion will discuss the project in a broader light and provide some other approaches that could be followed if the methodology used is discarded.

## 6.2. A broader view

This project started with the concept of a membrane for an AOC that could incorporate a dynamical pore size. A material with, among others, degradable properties was chosen: POMaC. As discussed in Section 6.1, creating a dynamic pore size that could increase to a diameter through which immune cells can migrate remains challenging with POMaC. However, the concept of using a dynamical pore size remains promising. Therefore, in this Section, three other approaches are discussed.

The first approach is to mitigate the effect of POMaC swelling by incorporating it into the membrane design and allowing the membrane to swell before implementing it in the cell culture (Fig. 6.3 A). By incorporating a larger initial pore size, the pores will not close up more when submerged. A challenge in this approach is the membrane stiffness of a thin membrane, as the degrading POMaC loses its structural integrity. It might also be challenging to design a suitable initial membrane geometry and accurately determine the effect of swelling.

A second approach is to incorporate two material types. One part of the material maintains its structural integrity, exhibiting a low degradation rate, and limiting swelling behaviour. Another part of the material, filling the pores, degrades away much quicker, opening up the pores (Fig. 6.3 B1). A material with a low

molecular weight (low Dalton number) and a shorter polymer chain could degrade faster and limit swelling behaviour. Materials such as PVA, sugar, collagen or gelatin could be further investigated [7]. This could also be achieved by placing a sacrificial layer on top of the membrane (Fig. 6.3 B2). Both approaches would provide no pores in the first phase of the cell culture. If the underlying pores have a diameter  $> 3 \mu\text{m}$ , this will create a suitable pore size for immune cell transmigration. Next to finding a suitable material, in this approach, it remains a challenge to incorporate a range of pore sizes in the membrane throughout the cell culture.

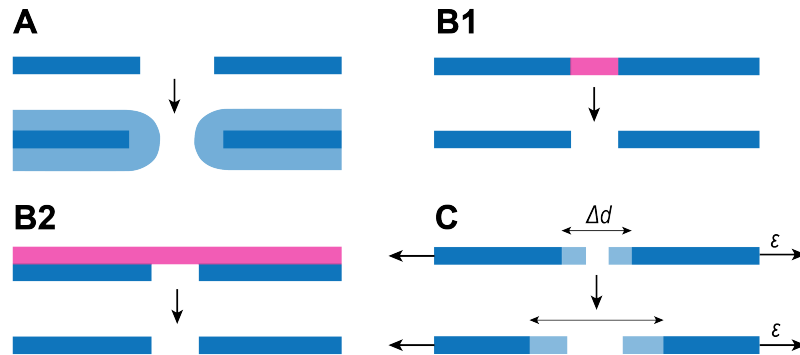


Figure 6.3: Schematic illustrations of alternative design concepts. (A) POMaC membrane, initiating swelling before membrane implementation in the cell culture. (B1) Pore opening by use of a second, faster degrading, material (pink). (B2) Pore opening by use of a sacrificial layer (pink). (C) Increasing pore diameter by increasing the average strain on the membrane.

A third approach could be to increase pore diameter by increasing the overall membrane strain (Fig. 6.3 C). By increasing the average actuation pressure, the base pore size in the membrane could also be increased. It should be investigated how an increase in average strain affects the stress experienced by the cell layer.

The second option, using two material types, is the most likely to succeed in incorporating a dynamical pore size and, therefore, the advised alternative approach. This approach could be expanded by using multiple material types with different degradation rates, as shown in Figure 6.4 (B3). Hereby, various pore sizes could be incorporated within the membrane.



Figure 6.4: Schematic illustrations of alternative design concept using multiple material types with different degradation rates over time, ranging from high (pink) to low (blue) degradation rate.





# 7

## Conclusion

The research question of this thesis is: How to fabricate a LOC membrane containing a dynamic membrane pore size to be able to study the monolayer formation, adherence, and immune cell transmigration. In this research, a new concept of a membrane containing a dynamic pore size was designed, and its viability was tested. A dynamic pore size was proposed to resolve the 'pore size dilemma' (Section 2.4). This project discussed two main focus points: What material should be used within the AOC membrane? Secondly, how to fabricate a thin membrane containing a dynamic pore size? The aspects studied to evaluate the concept viability and material suitability were: the material synthesis; the thin film and pore fabrication possibilities; the effective Young's modulus; the autofluorescence; the toxicity; the biodegradability, and the material bonding.

First, the membrane concept was developed based on the collected requirements for a LOC membrane. The membrane concept allows for introducing an ALI, a physiological fluid flow and cyclic stretch. It was found in the literature that the membrane should ideally be around 10  $\mu\text{m}$  thick, and the pore diameter should start at less than 3  $\mu\text{m}$  and increase to 3  $\mu\text{m}$  to 8  $\mu\text{m}$  [30, 55]. Second, POMaC was selected as a promising PDMS alternative due to its (bio)degradability and considerable allowed strain. On top of the properties also attributed to PDMS, such as relatively simple fabrication, reported biocompatibility, optical transparency and sterilisability, POMaC has minimal small molecule absorption, highly tunable material properties and UV curing possibilities [7, 57, 67, 68, 84].

A fabrication method for creating a membrane with dynamic pore sizes was studied in detail, which involved spincoating the material over a 2PP-printed structure. POMaC was spincoated and detached in  $13 \pm 5 \mu\text{m}$  thin and uniform layers with an area of at least  $3 \times 3 \text{ mm}^2$ . Pre-POMaC with a 5:1:4 monomer ratio (1,8-octanediol: citric acid: maleic acid) heated at 140  $^{\circ}\text{C}$  for 3 hours, provided the best results concerning film uniformity and curing time. The thinness was limited by the handling of the membrane after curing. Substrate priming, spincoating parameters, curing time and temperature of both photopolymerisation and oven curing significantly affected the uniformity and stability of the thin film. The best results regarding these aspects were obtained when spincoating preheated POMaC over an HMDS surface primer on a silicon or glass substrate and using UV curing. Film detachment was possible by placing the structure in DI water for one day.

Moreover, an array of well shaped conical pillars was created using 2PP-printing, which could be used as a structural mould for imprinting the pore structures within the membrane. A combination of fabricating and detaching a thin membrane while utilising the coned pillars still has to be conducted. The structure was developed on the Nanoscribe printer using IP-Dip as resin. A 63x objective was used, allowing for a sub-micron resolution. A silicon substrate, treated with oxygen plasma right before printing, was used to increase the adherence of the cones to the substrate.

Furthermore, two photoinitiators, 5 wt% Irgacure 2959 and 1wt% TPO were tested, where a trade-off was found between curing speed versus material colour. 5 wt% Irgacure 2959 provided faster curing, but probably acceptable yellowing, whereas 1wt% TPO exhibited slower curing. Increasing the photoinitiator concentration might increase curing speed.

Nanoindentation measurements were used to obtain a stiffness indication at the surface of POMaC. An effective Young's modulus between  $301 \pm 60$  kPa and  $352 \pm 70$  kPa was found for EPPOMaC placed for  $<1$  hour in DI water. UV intensity during curing has no significant influence on the stiffness of the material, while submerging EPPOMaC for a prolonged time (2 weeks) significantly lowers the effective Young's modulus. Submersion lowered the mean effective Young's modulus in samples with a similar fabrication from  $352 \pm 70$  kPa to  $62 \pm 20$  kPa, which gives a valuable indication of the stiffness range and the effect of submersion. This stiffness falls within the range set as a requirement for a LOC membrane.

For the integration of the POMaC membrane into the PDMS device, several methods were tested: directly bonding PDMS and POMaC together using UV and heat curing; bonding the two materials together by placing either liquid PDMS or POMaC in between and subsequently UV or heat curing; and using oxygen plasma for surface activation. None of these bonds showed long-term stability. Using polyurethane to bond POMaC and PDMS might be a promising solution.

It was found that POMaC exhibits a small amount of autofluorescence. However, a  $\sim 200$   $\mu\text{m}$  thick POMaC layer did not limit the imaging of fluorescently labelled cells. This implies that autofluorescence interference is likely absent for a thin membrane. Moreover, POMaC, after curing, is transparent. So it is an adequate material for confocal microscopy. However, POMaC turns opaque upon degradation. To what extent this interferes with confocal microscopy needs to be further assessed.

POMaC, based on the literature, is a very biocompatible material, although not yet tested with primary lung cells. In the toxicity assay on primary lung cells, conclusive evidence regarding this (expected) biocompatibility of POMaC was not found. This result may be attributed to material property or sterilisation issues, as all experimental wells were affected similarly, and apoptosis did not happen immediately. Moreover, a clear difference between the two photoinitiators and POMaC without any photoinitiator was also not found.

In order to obtain a membrane with dynamic pore sizes, the estimation and control of the degradation rate of the material are essential. The degradation rate largely depends on the monomer ratio and curing method, therefore it can be tuned in fabrication. During the concept design, it was assumed that POMaC degrades *via* surface erosion. A novel method of measuring the degradation rate was designed, allowing quick and simple fabricated 3D printed mould use. Photopolymerized POMaC was studied in both static and dynamic flow conditions. The flow was designed so that the shear stress exerted at the surface would mimic the shear stress exerted on the membrane in the LOC chip. Based on the results, a degradation model of POMaC was proposed. This model discusses POMaC's layer-by-layer material softening. Due to the significant material swelling, POMaC is a less suitable material when a structural geometry needs to be maintained at the microscale.

Concluding, POMaC can be spincoated into thin, uniform layers and detached from the substrate. Furthermore, well shaped pillars that could be used as a structural mould can be created. A combination of fabricating and detaching a thin membrane while utilising the coned pillars still has to be conducted, but the fabrication concept remains promising. Moreover, the selected material was not optimal for the design concept. Although the stiffness was in the expected range, and the bioimaging properties were found to be suitable so far, the degradation behaviour was different than hypothesised and showed layer-by-layer softening and swelling. This would impede the pore diameter increase necessary for immune cell transmigration. Additionally, more research needs to be conducted, especially on its cytotoxicity, and possibly a different approach could be taken to implement dynamic pore sizes.

## Outlook

A promising concept for fabricating a membrane containing a dynamic pore size has been developed. POMaC as a structural material for a membrane is a promising candidate, although the degradation behaviour was not optimal. Several alternative approaches were proposed in Section 6.2, of which the approach using multiple materials with different degradation rates is the advised alternative approach. If POMaC is to be further investigated, this Section provides an outlook that future research can cover.

**Fabrication:** It has been proven that a  $13 \pm 5$   $\mu\text{m}$  membrane can be spincoated. The Literature Review showed that a membrane of about  $10$   $\mu\text{m}$  was ideal. The main limitation of the membrane thickness was the handleability during the membrane detachment. Thus, the POMaC membrane bonding to a support structure or to the LOC device could be optimised to obtain a thinner membrane. Regarding the integration of the membrane into the LOC device, several bonding options were studied and proven not to be possible. For future

studies into the integration of the POMaC membrane into the device, a promising approach could be using polyurethane as described in Section 6.1. Furthermore, well shaped coned pillars which can serve as moulds were printed using 2PP-printing. The spincoating and 2PP-printed results are yet to be combined to create a thin membrane with dynamic pores. A proposed methodology for this is included in Appendix D.1.

**Material:** It has been found that POMaC, upon degradation, exhibits an opaque colour. In order to determine whether this would limit confocal microscopy, an experiment needs to be conducted where a partly degraded thin membrane is placed under a confocal microscope. Moreover, the cellular effect on degradation is a vital aspect to consider in any future studies. Additionally, since no conclusive evidence regarding POMaC's biocompatibility for primary lung cells was found, which may be attributed to material properties or sterilisation issues, more research on the effect of POMaC on primary lung cells is needed as well as on the sterilisation protocol. In this research a standard sterilisation protocol was used, described in Section 4.8. A protocol used by Tran et al. [67] as described in Chapter 6 might be a more suitable option. Moreover, besides more research on the toxicity of POMaC, long-term biocompatibility studies are needed to evaluate cell behaviour on POMaC. Since cell cultures tend to last 2 to 4 weeks, biocompatibility should last at least this period. Lastly, validation of the proposed POMaC degradation model is required.

**Membrane properties:** In future, the properties of this membrane regarding its elasticity, membrane-specific degradation, the geometric effects of the membrane on cells, long-term actuation and membrane reliability should be evaluated. For example, it should be evaluated whether an in-plane linear cyclic strain between 4% and 20% at a frequency of 0.2 Hz could be applied to the membrane. Moreover, studies into how cells react to a dynamic and increasing pore size are desired.

If a dynamical pore size could successfully be incorporated in a thin membrane on which both epithelial and endothelial cells can be grown, it would be a big step forward in *in vitro* cell culture studies. It would allow the study of the effect of pore size at different stadia of the cell culture, providing more information on the immunology and cell behaviour, and it could, in the ideal case, create an environment that more closely recapitulates the alveolar environment than has been achieved so far. Moreover, a better recapitulated alveolar environment would allow for more accurate cell behaviour and, subsequently, more accurate drug screening results. Although this study did not yet achieve the desired end result, the prize in succeeding certainly warrants further research.



# A

## Methodology

### A.1. Detailed drawing of 3D-printed moulds

#### A.1.1. POMaC and PDMS moulding

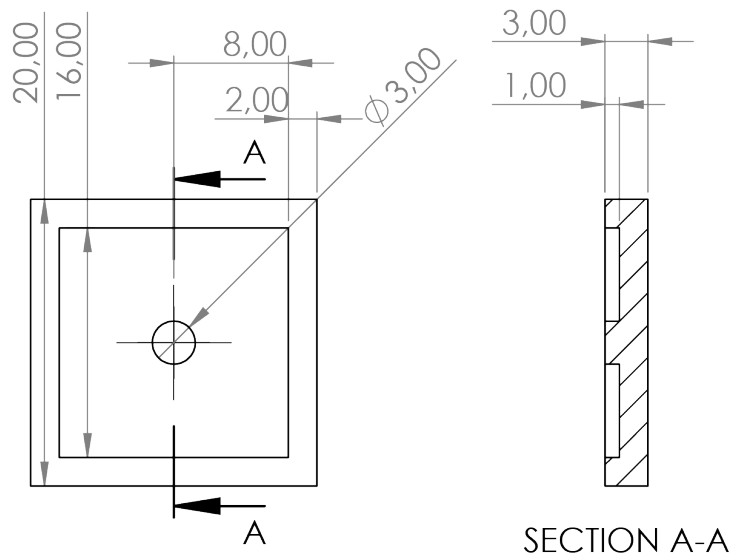


Figure A.1: Drawing of the square mould used for direct POMaC moulding in a 3D printed mould. Dimensions are in millimeters (mm).

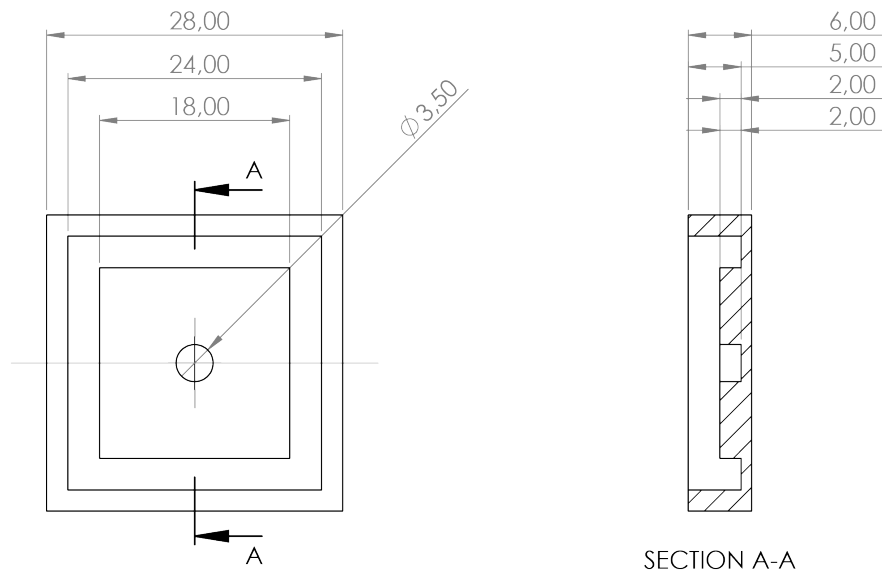


Figure A.2: Drawing of the square mould used for the fabrication of the PDMS moulds. Dimensions are in millimeters (mm).

#### A.1.2. Toxicity assay

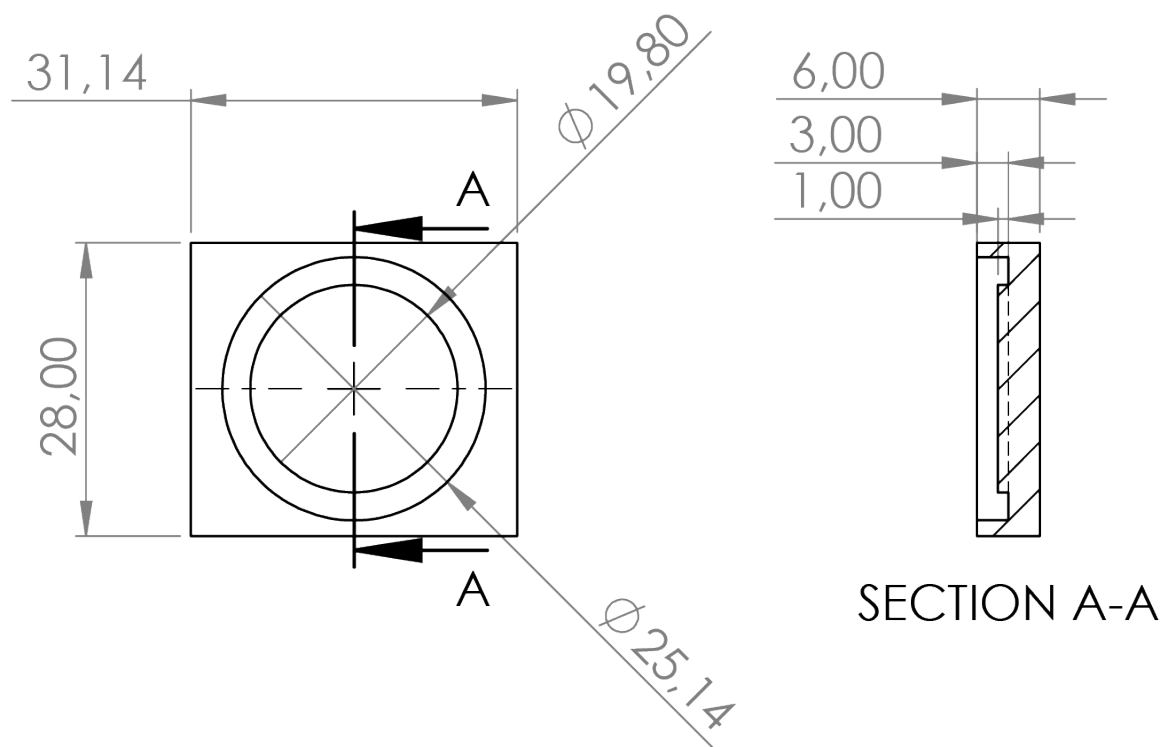


Figure A.3: Drawing of the mould used for fabricating the samples used in the cytotoxicity assay. Dimensions are in millimeters (mm).

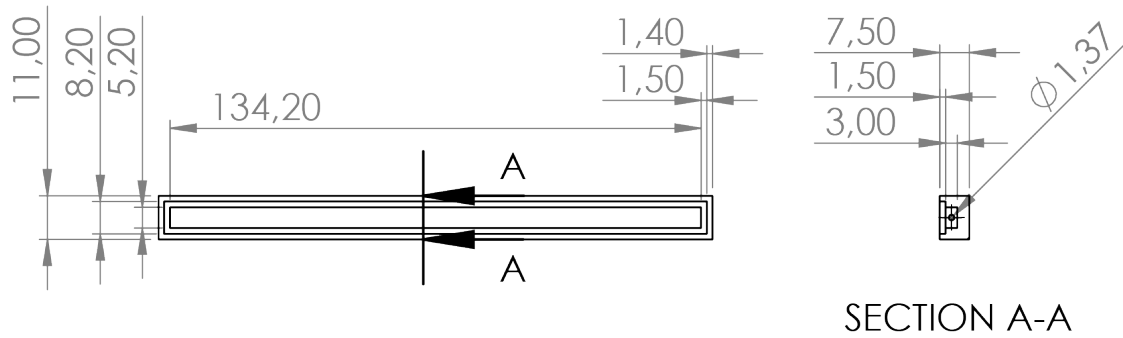
**A.1.3. Degradability assessment****Top part of the degradation experiment channel**

Figure A.4: Drawing of the top part of the mould used in the degradation rate experiment. Dimensions are in millimeters (mm).

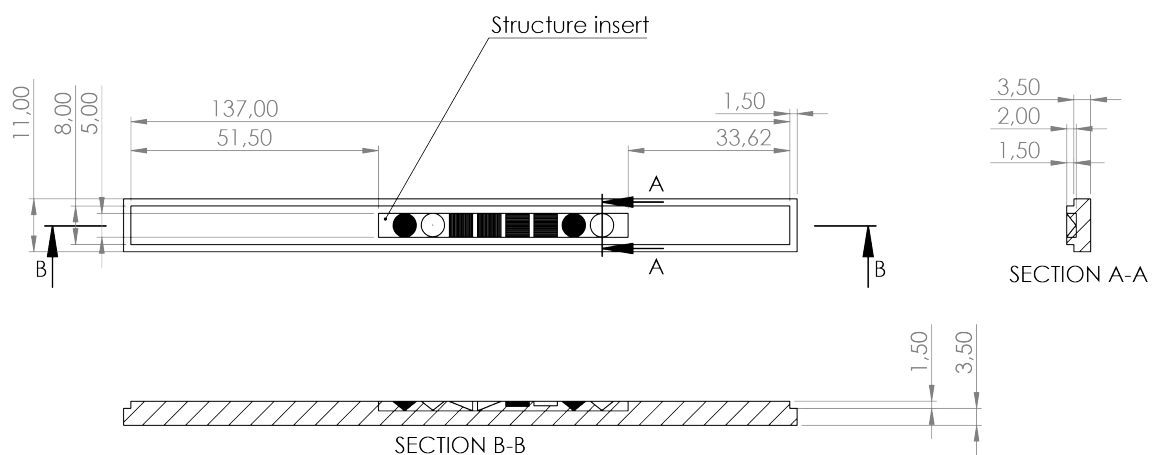
**Bottom part of the degradation experiment channel**

Figure A.5: Drawing of the bottom part of the mould used in the degradation rate experiment, including the structure insert. Dimensions are in millimeters (mm).



### Structural insert of the degradation experiment channel

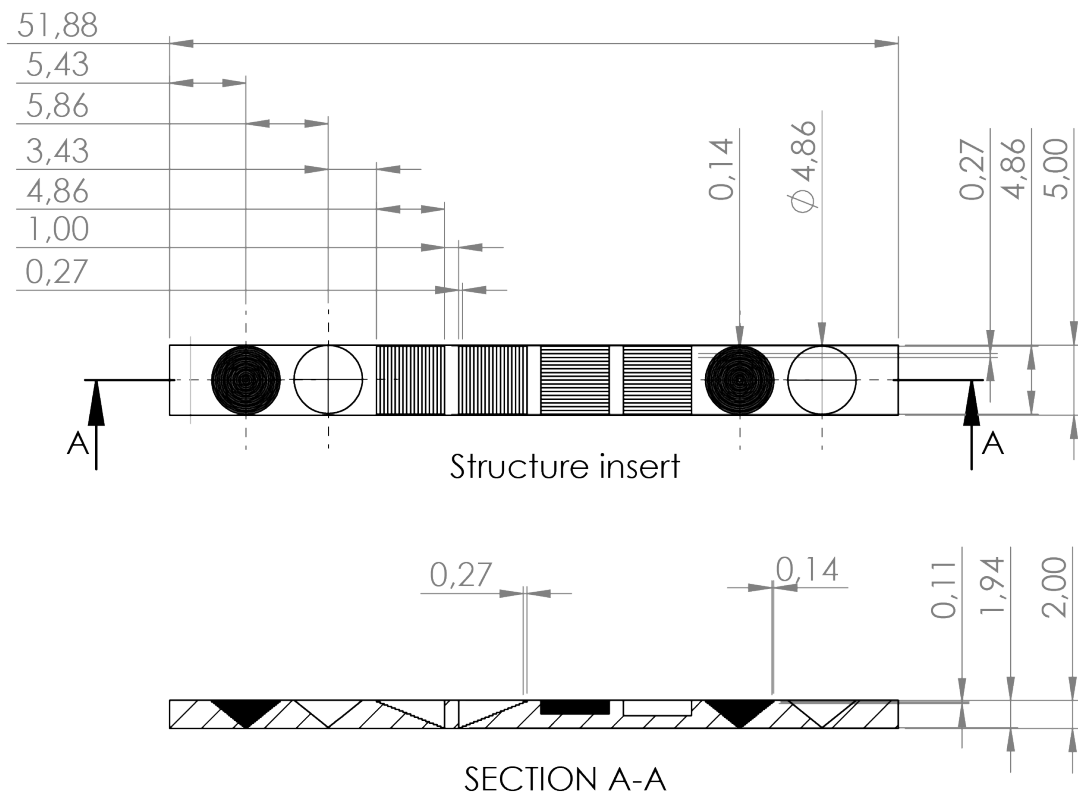


Figure A.6: Drawing of the structure insert placed in the bottom part of the mould used in the degradation experiment. Note that this part was assembled to the bottom mould part within Solidworks, converted to a parasolid and printed together as one structure. Dimensions are in millimeters (mm).

## A.2. Overview of several spincoating experiments

Table A.1: Overview of parameters used in spincoating tests.

Test	Substrate priming	POMaC type	Spincoat parameters	Curing
1.	Silicon, no priming	2.5 h POMaC, 5 wt% Irgacure 2959	1000 rpm/s, 2500 rpm, 5 min.	No UV curing possible*, hot plate 150 °C, 2 hrs.
2.	Glass, no priming	"	"	No UV curing possible*, hot plate slowly increased to 100 °C, 2 hrs.
3.	PTFE	"	Desiccated 20 min. prior at -950 mbar 1000 rpm/s, 2500 rpm, 5 min.	25 min. with Photopol UV source.*
4.	Glass substrate, no priming	3 h POMaC, 5 wt% Irgacure 2959 Heated at 50 °C for 20 min.	No desiccator. 1000 rpm/s, 1000 rpm, 2.5 min.	30 min. (2x15) UV, h = 1.5 cm, I = 100%
5.	Silicon, HMDS	"	"	"
6.	Silicon, HMDS	"	No desiccator. Substrate incl. POMaC 10 min. on hotplate at 100 °C prior to spinning. 1000 rpm/s, 1000 rpm, 2.5 min.	"
7.	Silicon, HMDS and 1 wt% Pluronic F-127	"	No desiccator. 1000 rpm/s, 2500 rpm, 5 min.	15 min. UV, h = 1.5 cm, I=100%
8.	Silicon, HMDS and 1 wt% Pluronic F-127 dried 5 min. on hot plate at 100 °C	"	"	"
9.	Silicon, HMDS	"	No desiccator. 1000 rpm/s, 2500 rpm, 5 min.	30 min. (2x15) UV, h = 2 cm, I = 100%
10.	Silicon, HMDS	"	"	"

\*The Photopol UV light curing unit was broken and the results were, therefore, discarded. The lamp was not used during further experiments. All other measurements were conducted with the Bluepoint UV point source.

### **A.3. Substrate priming methodology**

All substrates were cleaned using acetone, IPA and DI water respectively prior to the priming procedures.

#### **A.3.1. PTFE priming procedure**

As PTFE primer Teflon sheets were attached with doublesided tape (3M) to a glass slide. The Teflon surface was subsequently cleaned with acetone, IPA and DI water and dried before adding POMaC for spincoating.

#### **A.3.2. HMDS priming procedure**

This procedure was followed to add an HMDS primer to the substrate.

1. Place the substrate on a hot plate at 100°C for 20 minutes to prepare it for silanization.
2. Put 2 layers of gloves on, a face-protection mask and a thick nitrile glove on your left hand.
3. Prepare fumehood area. Put a piece of rip-off paper cloth on the surface and place the dessicator in the fumehood. Lay out a small glass Petri dish, a syringe needle, tweezers, a small beaker and the HMDS.
4. Put 0.5 – 1 mL of HMDS in the glass petridish with the syringe. Put the petridish at the bottom part (under the white plate) in the dessicator. Put the white plate with the smooth side down back in the dessicator, and place the warm chips on top. Start dessicator. Leave for 2 hours.
5. Clean up the fumehood area after starting the dessicator. After putting back the HMDS, put acetone in a beaker and rinse the syringe 3x with it. Put the syringe needle in the box for sharp waste. Put the rest of the syringe in the general contaminated waste bin. Clean acetone beaker, by rinsing 3 times with DI water. Throw away the acetone and water into the organics bin.
6. After 2 hours, take out the primed samples and clean up. Put on mask and extra gloves and place paper on the worktable. Clean the Petri dish by rinsing 3 times with acetone, then rinsing 3 times with DI water. Put the acetone and HMDS mixture in the designated waste bottle. Clean the dessicator with acetone and subsequently DI water on a cloth.
7. Keep the pillar mould on a hot plate at 100°C for 20 minutes to activate the bonding of the HMDS coating to the silicon surface. Let the pillar mould cool down to room temperature.

#### **A.3.3. Pluronic F-127 priming procedure for spincoating**

A 10 wt% of Pluronic F-127 solution was initially made, by adding 20 gr. of Pluronic® F-127 powder to 200 mL of DI water. This mixture was stirred for 30 minutes at 40 °C on a hot plate. After all Pluronic F-127 was dissolved, the solution was diluted with DI water to the desired concentration. For substrate priming, the substrate was placed in a 1% solution of Pluronic F-127 for 5 minutes. After 5 minutes, the substrate was removed from the solution and let dry in the fume hood.

## A.4. Overview of dose test parameters

Table A.2: Overview of the parameters used in the dose tests and array tests in fabrication of the micropillar array.

Test	Objective, Resin	Substrate	Oxygen plasma	Size (pillars)	Slice ( $\mu\text{m}$ )	Hatch ( $\mu\text{m}$ )	Shell contour count	Parameters	
								Laser power (LP, %)	Scanning speed (SS, $\mu\text{m/s}$ )
Dose test 1	25x, IP-S	ITO	No	4x4	0.5	0.2	1	contour: 20+i*20, i = 0 to 4 solid: 80+i*20, i = 0 to 4	contour: 5000+j*5000, j = 0 to 4 solid: 10000+j*20000, j = 0 to 4
Dose test 2	25x, IP-S	ITO	No	4x4	0.5	0.2	1	contour: 5+i*5, i = 0 to 4 solid: 20+i*20, i = 0 to 4	contour: 5000+j*5000, j = 0 to 4 solid: 10000+j*20000, j = 0 to 4
Dose test 3	25x, IP-S	Si	No	20x20	0.5	0.2	1	contour, solid: 20+i*4, i = 0 to 19	contour, solid: 10000+j*4000, j = 0 to 19
Dose test 4	25x, IP-S	Si	No	Area 1: 5x5	1	0.5	12	contour, solid: 20+i*16, i = 0 to 5	contour, solid: 10000+j*16000, j = 0 to 5
				Area 2: 5x5	0.5	0.5	2	"	"
				Area 3: 5x5	0.5	0.5	2	"	"
				Area 4: 5x5	1	0.4	2	"	"
Dose test 5	63x, IP-Dip	Si	Yes	Area 1: 4x5	0.3	0.2	0	solid: 20+i*20, i = 0 to 4	solid: 5000+j*5000, j = 0 to 3
				Area 2: 7x2	0.9	0.35	2	contour: 35+i*10, i = 0 to 6 solid: 40+i*10, i = 0 to 6	contour: 25000, solid: 100000, base: 50000
				Area 3: 4x5	0.3	0.2	2	contour, solid: 20+i*20, i = 0 to 4	contour, solid: 5000+j*5000, j = 0 to 3
				Area 4: 7x5	0.9	0.35	2	contour, solid: 40+i*10, i = 0 to 6	contour, solid: 10000+j*25000, j = 0 to 4
Array test 1	25x, IP-S	Si	Yes	80x40	1	0.5	2	50	50000
Array test 2	63x, IP-Dip	Si	Yes	40x40	0.3	0.2	2	52	62000
Array test 3	63x, IP-Dip	Si	Yes	Area 1: 20x10	0.3	0.2	0	40	10000
				Area 2: 20x10	0.3	0.2	0	50	10000
				Area 3: 20x10	0.3	0.2	0	60	10000
Array test 4	63x, IP-Dip	Si	Yes	80x80	0.3	0.2	0	50	10000

## A.5. Calculations of biodegradability mould dimensions

```

1  clc
2  clear all
3  close all
4
5  % Fluid Parameters
6  rho = 993.18 ; % PBS density in kg/m^3 % water 1000, blood 1060 % DMEM 1.00 + 0.1 XG ...
   % dextran 20% w/w =1060
7
8  % Calculation of volumetric flow with respect to width and height of biodegradability ...
   mould
9
10 % Hele-Shaw shear for h<<w
11 %tau = 6*eta*Q/(w*(h^2))% shear in Pa
12 tau = 0.55 ; % [Pa] [kg/(ms^2)] (minimum)
13 eta = 1E-3 ; % [kg/m*s] The viscosity of PBS at 25 deg
14 eta_LOC = 0.6913E-3 ; %viscosity of water/PBS at 37 deg
15
16 Q_LOC = 0.03819E-6 ; % [m^3/s] = 137.5 [ml/h] = 2.6 ml/min. Is volumetric flow ...
   in LOC
17 h_LOC = 0.4E-3 ; % [m]
18 w_LOC = 0.0032 ; % [m] (3.2mm)
19
20 %set:
21 %h_deg = 0.001 ; % [m]
22 h_deg = linspace(0.5E-3, 5E-3) ; %GRAPH ONLY
23 w_deg = 0.005 ; % 5 mm
24
25 A_LOC = h_LOC*w_LOC;
26 v_LOC = Q_LOC/A_LOC;
27
28 v_deg = (h_deg ./eta).* (v_LOC*eta_LOC/h_LOC);
29 Q_deg = w_deg* h_deg.* v_deg; % [m^3/sec]
30 Q_deg_mlmin = Q_deg*6E7 % [milliliter/min]
31
32 %Q_deg_mlmin is set at 135 ml/min. This equals a flow velocity of:
33 Q_final = 135; % [ml/min]
34 h_final = 0.003; % [m]
35 u_deg = (Q_final/6E7)/(w_deg*h_final)
36
37 %% Graph
38 figure
39 hold on
40 plot(h_deg,Q_deg_mlmin)
41
42 %title('Biodegradability mould channel height versus volumetric flow rate for a ...
   constant shear stress')
43 ylabel('Volumetric flow rate [ml/min]')
44 xlabel('Channel height [m]')
45
46
47
48 %L_e = linspace(0, 0.01) ; % entrance length [m] (0 tot 10 mm)
49 d = 0.005; %>w? %diameter of channel = width (larger side) [m]
50 %rho = rho hierboven
51 u = u_deg; %is flow velocity [m/s] (v_deg is set at 135 ml/min )
52 %L =
53 %eta = eta hierboven
54 h = h_final;
55 w = w_deg;
56
57 %EL = L_e./d; %entrance length number [-] = length to fully
58 %developed velocity profile [m]/tube diameter [m]. Calc. zowel uit paper
59 %als online
60
61 %Re = rho*u*L/eta; %Reynolds number
62 d_h = 2*w*h/(w+h); %hydraulic diameter of a rectangular channel
63 Re_dh = rho*u*d_h/eta; %Reynolds number based on the hydraulic diameter (for a ...
   square duct: Re_dh = Re)

```

```

64 AR = h/w; %channel aspect ratio (height/width)
65
66 Re = Re_dh
67
68
69
70 if Re < 2300
71     disp('laminar flow') %is in practice only actual for viscous fluids- oils i.e. ...
72     (and blood? > zie aantekeningen in anatomy schrift)
73     EL = 0.06.*Re
74 end
75 if Re > 2300 & Re< 4000
76     disp('transient flow')
77     EL = 4.4*Re^(1/6)
78 end
79 if Re > 4000
80     disp('turbulent flow')
81 end
82 L_e = EL*d %L_e is dimensional development length (Zie calculation ...
83     hierboven.)
84 %Entrance length for small rectangular channels with laminar flow, based on
85 %German Ferreira (2021)
86
87 C1 = 0.7*AR^(0.25);
88 C2 = (6.8*AR^(3.75))/(1+90*AR^2.8);
89 C3 = 1+AR;
90 L_german = (C1^C3+(C2*Re)^C3)^(1/C3)
91
92 L_e_german = L_german*d;
93
94
95 %For turbulent flow: In most practical engineering applications, this
96 %entrance effect becomes insignificant beyond a pipe length of 10 times the
97 %diameter and hence it is approximated to be:
98 % My design: >50 mm for a width of 5 mm, so this rule applies
99 L_turbulent_approx = 10*d %Zie Cimbala (2006) for source
100 A = h*w;
101 P = 2*w+2*h;
102
103 d_hCimbala = 4*A/P; %is exactly same as d_h hierboven
104 L_turbulent_approx = 10*d_hCimbala %Entrance length with hydraulic diameter and ...
105     turbulent flow.
106
107 %Exit length is much shorter than entrance length and not significant at
108 %moderate to high Re.

```

## A.6. Calculations of toxicology mould dimensions

```

1 %% Calculation of toxicology mould dimensions
2
3 %Volume of POMaC membrane in the LOC
4 Rm_LOC = 0.3/2 %cm radius membrane in chip
5 tm_LOC = 0.006 %cm thickness membrane in chip
6 Vm_LOC = pi*Rm_LOC^2*tm_LOC
7 %AR_LOC = 3: 0.01; %aspect ratio of the membrane
8
9 %Volume of medium in the LOC channel with no flow present
10 %(Total length is 2 cm)
11 length_1 = 1.7; %cm
12 height_1 = 0.02; %cm
13 length_2 = 0.3; %cm
14 height_2 = 0.03; %cm
15 width = 0.32; %cm
16
17 Vc_LOC = (length_1*height_1 + length_2*height_2)*width; %cm^3 = ml
18

```

```

19 %For POMaC volume per 1 ml medium:
20 V_POMaC = Vm_LOC/Vc_LOC; %cm^3 POMaC/ 1 ml medium
21
22 %For 10 ml medium the amount of POMaC needed:
23 V_needed = V_POMaC*10; %cm^3
24
25 %A disc with a thickness of 1 mm then has a radius of:
26 t_disc = 0.1; %cm
27 R_disc = sqrt(V_needed/(pi*t_disc));
28 D_disc = R_disc*2

```

## A.7. Exposure times in autofluorescence testing

Table A.3: Exposure times used during autofluorescence testing

Sample:	Type of POMaC, photoinitiator	Measurement location	Exposure (ms) used for the images:				
			DAPI	FITC	TXRED	CY5	Brightfield images
1.	EPPOMaC, 5% Irgacure 2595	Middle	85	0	1120	565	5
		Edge	85	0	1120	565	5
2.	EPPOMaC, 1 wt% TPO	Middle	170	45	1120	1015	155
		Edge	20	45	1120	1015	45
3.	EPOMaC, No photoinitiator	Middle	170	45	1120	1015	155
		Edge	170	45	1120	1015	1650
4.	EPOMaC, Uncured 1 wt% TPO	Middle	170	45	1120	1015	155
		Edge	170	45	1120	1115	50
5.	PPOMaC, 5% Irgacure 2595	Middle	190	5	1120	1115	50
		Edge	85	5	1120	1115	50
6.	PPOMaC, 1 wt% TPO	Middle	170	45	1120	1115	155
		Edge	170	45	1120	1115	155
7.	PPOMaC, 1 wt% TPO	All locations	95	200	600	600	55

# B

## DeScribe Code

This Appendix contains all DeScribe code used in the dose tests and array printing on the 2PP-printer.

### B.1. singlemouldpillardata.gwl

This file contains the information of the structure and is used in the job files for dose test 1, dose test 2 and dose test 3, included below.

```
1 % File generated by DeScribe 2.7
2 %
3 % Creation time
4 %   2022-04-26T11:22:06+02:00
5 %
6 % Source file
7 %   Type: Mesh
8 %
9 % Volume 2.92x10E-7 mm^3
10 %
11 % Bounding box
12 %   Minimum X: 0.004 Y: -0.496 Z: 0
13 %   Maximum X: 9.996 Y: 9.496 Z: 9
14 %
15 % Transformation
16 %   Scaling X: 0.1 Y: 0.1 Z: 0.1
17 %   Rotation X: 0.5 Y: -0.5 Z: -0.5 W: 0.5
18 %   Translation X: 10 Y: 9.5 Z: 0
19 %
20 % Slicing
21 %   SlicingMode: Fixed
22 %   Distance: 0.5
23 %   SimplificationTolerance: 0
24 %   FixSelfIntersections: on
25 %
26 % Hatching
27 %   ContourCount: 1
28 %   HatchingDistance: 0.2
29 %   HatchingAngle: auto
30 %
31 % Output options
32 %   HatchLines: Alternate
33 %   ZAxis: Piezo
34 %   Exposure: Variable
35 %   InvertZAxis: on
36 %   WritingDirection: Up
37 %   ScanMode: Galvo
38 %   WritingOrder: ContourFirst
39 %   SkipInterfaceFinder: off
40 %
```



```
41
42 MoveStageX 5
43 MoveStageY 4.5
44
45 FindInterfaceAt $interfacePos
46
47 % BLOCK 0|0|0
48 include singlemouldpillar_files\singlemouldpillar_0_0_0.gwlb
```

## B.2. Dose test 1

```
1 % File generated by DeScribe 2.5.5
2
3 % System initialization
4 InvertZAxis 1
5
6 % Writing configuration
7 GalvoScanMode
8 ContinuousMode
9 PiezoSettlingTime 10
10 GalvoAcceleration 10
11 StageVelocity 200
12
13 % Scan field offsets
14 XOffset 0
15 YOffset 0
16 ZOffset 0
17
18 % Writing parameters
19 PowerScaling 1.0
20
21 var $i = 0
22 var $j = 0
23 %var $LP = 0
24 % var $$$ = 0
25 var $contourLaserPower = 0
26 var $contourScanSpeed = 0
27
28 var $solidLaserPower = 0
29 var $solidScanSpeed = 0
30
31 var $interfacePos = 0.6
32
33 WriteText "Dose test"
34
35 MoveStageY 20
36
37 for $i = 0 to 4
38     for $j = 0 to 4
39
40         set $contourLaserPower = 20 + $i * 20
41         set $contourScanSpeed = 5000 + $j * 5000
42
43         set $solidLaserPower = 80 + $i * 20
44         set $solidScanSpeed = 10000 + $j * 20000
45
46
47 % Base writing parameters
48 var $baseLaserPower = $contourLaserPower
49 var $baseScanSpeed = $contourScanSpeed
50
51 % Include slicer output
52 include singlemouldpillar_data.gw1
53
54 Movestagex 20
55
56 end
57
```

```
58 StageGotoX 0
59 Movestagey 20
60
61 end
```

## B.3. Dose test 2

```
1  % File generated by DeScribe 2.5.5
2
3  % System initialization
4  InvertZAxis 1
5
6  % Writing configuration
7  GalvoScanMode
8  ContinuousMode
9  PiezoSettlingTime 10
10 GalvoAcceleration 10
11 StageVelocity 200
12
13 % Scan field offsets
14 XOffset 0
15 YOffset 0
16 ZOffset 0
17
18 % Writing parameters
19 PowerScaling 1.0
20
21 var $i = 0
22 var $j = 0
23 %var $LP = 0
24 % var $SS = 0
25 var $contourLaserPower = 0
26 var $contourScanSpeed = 0
27
28 var $solidLaserPower = 0
29 var $solidScanSpeed = 0
30
31 var $interfacePos = 0.6
32
33 WriteText "Dose test"
34
35 MoveStageY 20
36
37 for $i = 0 to 4
38     for $j = 0 to 4
39
40         set $contourLaserPower = 5 + $i * 5
41         set $contourScanSpeed = 5000 + $j * 5000
42
43         set $solidLaserPower = 20 + $i * 20
44         set $solidScanSpeed = 10000 + $j * 20000
45
46
47 % Base writing parameters
48 var $baseLaserPower = $contourLaserPower
49 var $baseScanSpeed = $contourScanSpeed
50
51 % Include slicer output
52 include singlemouldpillar_data.gwl
53
54 Movestagex 20
55
56 end
57
58 StageGotoX 0
59 Movestagey 20
60
61 end
```

## B.4. Dose test 3

```
1  % File generated by DeScribe 2.5.5
2
3  % System initialization
4  InvertZAxis 1
5
6  % Writing configuration
7  GalvoScanMode
8  ContinuousMode
9  PiezoSettlingTime 10
10 GalvoAcceleration 10
11 StageVelocity 200
12
13 % Scan field offsets
14 XOffset 0
15 YOffset 0
16 ZOffset 0
17
18 % Writing parameters
19 PowerScaling 1.0
20
21 var $i = 0
22 var $j = 0
23 %var $LP = 0
24 % var $SS = 0
25
26
27 var $solidLaserPower = 0
28 var $solidScanSpeed = 0
29 var $contourLaserPower = 0
30 var $contourScanSpeed = 0
31
32
33 var $interfacePos = 0.6
34
35 TextLaserPower 80
36 TextScanSpeed 30000
37
38 WriteText "Dose test"
39
40
41
42 MoveStageY 20
43
44 for $i = 0 to 19
45     if $i == 5
46         MoveStageY 10
47     end
48     if $i == 10
49         MoveStageY 10
50     end
51     if $i == 15
52         MoveStageY 10
53     end
54     if $i == 20
55         MoveStageY 10
56     end
57     if $i == 25
58         MoveStageY 10
59     end
60     if $i == 30
61         MoveStageY 10
62     end
63     if $i == 35
64         MoveStageY 10
65     end
66     if $i == 40
67         MoveStageY 10
68     end
end
```

```

69
70
71     for $j = 0 to 19
72     if $j == 5
73         MoveStageX 10
74     end
75     if $j == 10
76         MoveStageX 10
77     end
78     if $j == 15
79         MoveStageX 10
80     end
81     if $j == 20
82         MoveStageX 10
83     end
84     if $j == 25
85         MoveStageX 10
86     end
87     if $j ==30
88         MoveStageX 10
89     end
90     if $j == 35
91         MoveStageX 10
92     end
93     if $j ==40
94         MoveStageX 10
95     end
96
97
98         set $solidLaserPower = 20 + $i * 4
99         set $solidScanSpeed = 10000 + $j * 4000
100
101     set $contourLaserPower = $solidLaserPower
102     set $contourScanSpeed = $solidScanSpeed
103
104
105
106
107 % Base writing parameters
108 var $baseLaserPower = $contourLaserPower
109 var $baseScanSpeed = $contourScanSpeed
110
111 % Include slicer output
112 include singlemouldpillar_data.gwl
113
114 Movestagex 20
115 %Movestagey -1.4
116 end
117
118 StageGotoX 0
119 Movestagey 20
120
121 end

```

## B.5. Dose test 4

### B.5.1. Main code

```

1 % File generated by DeScribe 2.7
2
3 % System initialization
4 InvertZAxis 1
5
6 % Writing configuration
7 GalvoScanMode
8 ContinuousMode
9 PiezoSettlingTime 10
10 GalvoAcceleration 10
11 StageVelocity 200

```

```
12
13 % Scan field offsets
14 XOffset 0
15 YOffset 0
16 ZOffset 0
17
18 % Include
19 include Square3.gwl
20
21 include Square1.gwl
22
23 MoveStageY -300
24 MoveStageX 200
25
26 include Square2.gwl
27 include Square2.gwl
```

### B.5.2. Additional codes

#### Square1.gwl

```
1 % File generated by DeScribe 2.5.5
2
3 % System initialization
4 InvertZAxis 1
5
6 % Writing configuration
7 GalvoScanMode
8 ContinuousMode
9 PiezoSettlingTime 10
10 GalvoAcceleration 10
11 StageVelocity 200
12
13 % Scan field offsets
14 XOffset 0
15 YOffset 0
16 ZOffset 0
17 LaserPower 100
18 ScanSpeed 100000
19
20 % Writing parameters
21 PowerScaling 1.0
22
23 var $i = 0
24 var $j = 0
25 %var $LP = 0
26 % var $SS = 0
27
28 %var $LaserPower = 50
29 %var $ScanSpeed = 50
30 var $solidLaserPower = 50
31 var $solidScanSpeed = 50
32 var $contourLaserPower = 5
33 var $contourScanSpeed = 50
34
35
36 var $interfacePos = 0.6
37
38
39 WriteText "Dose test Area 1"
40
41
42 MoveStageY 20
43
44 for $i = 0 to 5
45
46 for $j = 0 to 5
47
48
```

```
49
50         LaserPower 20 + $i * 16
51         ScanSpeed 10000 + $j * 16000
52
53
54
55 % Include slicer output
56 include singlemouldpillarcontour_data.gwl
57
58 Movestagex 20
59 %Movestagey -1.4
60
61 end
62 StageGotoX 0
63 Movestagey 20
64
65
66 end
```

## Square2.gwl

```
1 % File generated by DeScribe 2.5.5
2
3 % System initialization
4 InvertZAxis 1
5
6 % Writing configuration
7 GalvoScanMode
8 ContinuousMode
9 PiezoSettlingTime 10
10 GalvoAcceleration 10
11 StageVelocity 200
12
13 % Scan field offsets
14 XOffset 0
15 YOffset 0
16 ZOffset 0
17 LaserPower 100
18 ScanSpeed 100000
19
20 % Writing parameters
21 PowerScaling 1.0
22
23 var $i = 0
24 var $j = 0
25 %var $LP = 0
26 % var $SSS = 0
27
28 %var $LaserPower = 50
29 %var $ScanSpeed = 50
30 var $solidLaserPower = 50
31 var $solidScanSpeed = 50
32 var $contourLaserPower = 5
33 var $contourScanSpeed = 50
34
35
36 var $interfacePos = 0.6
37
38
39 WriteText "Dose test Area 2"
40
41
42 MoveStageY 20
43
44 for $i = 0 to 5
45
46 for $j = 0 to 5
47
48
```

```
49
50         LaserPower 20 + $i * 16
51         ScanSpeed 10000 + $j * 16000
52
53
54
55 % Include slicer output
56 include singlemouldpillar_adjslice_data.gwl
57
58 Movestagex 20
59 %Movestagey -1.4
60
61 end
62 StageGotoX 200
63 Movestagey 20
64
65
66 end
```

## Square3.gwl

```
1 % File generated by DeScribe 2.5.5
2
3 % System initialization
4 InvertZAxis 1
5
6 % Writing configuration
7 GalvoScanMode
8 ContinuousMode
9 PiezoSettlingTime 10
10 GalvoAcceleration 10
11 StageVelocity 200
12
13 % Scan field offsets
14 XOffset 0
15 YOffset 0
16 ZOffset 0
17 LaserPower 100
18 ScanSpeed 100000
19
20 % Writing parameters
21 PowerScaling 1.0
22
23 var $i = 0
24 var $j = 0
25 %var $LP = 0
26 % var $SSS = 0
27
28 %var $LaserPower = 50
29 %var $ScanSpeed = 50
30 var $solidLaserPower = 50
31 var $solidScanSpeed = 50
32 var $contourLaserPower = 5
33 var $contourScanSpeed = 50
34
35
36 var $interfacePos = 0.6
37
38
39 WriteText "Dose test Area 3"
40
41
42 MoveStageY 20
43
44 for $i = 0 to 5
45
46 for $j = 0 to 5
47
48
```

```

49
50         LaserPower 20 + $i * 16
51         ScanSpeed 10000 + $j * 16000
52
53
54
55 % Include slicer output
56 include singlemouldpillar_adjhatch_data.gwl
57
58 Movestagex 20
59 %Movestagey -1.4
60
61 end
62 StageGotoX 0
63 Movestagey 20
64
65
66 end

```

### singlemouldpillarcontour\_data.gwl

```

1 % File generated by DeScribe 2.7
2 %
3 % Creation time
4 %   2022-05-16T13:01:56+02:00
5 %
6 % Source file
7 %   Type: Mesh
8 %
9 %Volume 2.92x10E-7 mm^3
10 %
11 % Bounding box
12 %   Minimum X: 0.004 Y: -0.496 Z: 0
13 %   Maximum X: 9.996 Y: 9.496 Z: 9
14 %
15 % Transformation
16 %   Scaling X: 0.1 Y: 0.1 Z: 0.1
17 %   Rotation X: 0.5 Y: -0.5 Z: -0.5 W: 0.5
18 %   Translation X: 10 Y: 9.5 Z: 0
19 %
20 % Slicing
21 %   SlicingMode: Fixed
22 %   Distance: 1
23 %   SimplificationTolerance: 0.05
24 %   FixSelfIntersections: on
25 %
26 % Hatching
27 %   ContourCount: 12
28 %   ContourDistance: 0.2
29 %   ConcaveCornerMode: Beveled
30 %   HatchingDistance: 0.5
31 %   HatchingAngle: auto
32 %
33 % Output options
34 %   HatchLines: Alternate
35 %   ZAxis: Piezo
36 %   Exposure: Constant
37 %   InvertZAxis: on
38 %   WritingDirection: Up
39 %   ScanMode: Galvo
40 %   WritingOrder: ContourFirst
41 %   SkipInterfaceFinder: off
42 %
43
44 MoveStageX 5
45 MoveStageY 4.5
46
47 FindInterfaceAt $interfacePos
48

```



```

49 % BLOCK 0|0|0
50 include singlemouldpillarcontour_files\singlemouldpillarcontour_0_0_0.gwlb

```

### singlemouldpillar\_adjhatch\_data.gwl

```

1 % File generated by DeScribe 2.7
2 %
3 % Creation time
4 % 2022-05-16T13:05:12+02:00
5 %
6 % Source file
7 % Type: Mesh
8 %
9 %Volume 2.92x10E-7 mm^3
10 %
11 % Bounding box
12 % Minimum X: 0.004 Y: -0.496 Z: 0
13 % Maximum X: 9.996 Y: 9.496 Z: 9
14 %
15 % Transformation
16 % Scaling X: 0.1 Y: 0.1 Z: 0.1
17 % Rotation X: 0.5 Y: -0.5 Z: -0.5 W: 0.5
18 % Translation X: 10 Y: 9.5 Z: 0
19 %
20 % Slicing
21 % SlicingMode: Fixed
22 % Distance: 1
23 % SimplificationTolerance: 0.05
24 % FixSelfIntersections: on
25 %
26 % Hatching
27 % ContourCount: 2
28 % ContourDistance: 0.2
29 % ConcaveCornerMode: Beveled
30 % HatchingDistance: 0.4
31 % HatchingAngle: auto
32 %
33 % Splitting
34 % Mode: Rectangular
35 % BlockSize X: 285 Y: 285 Z: 10
36 % Offset X: 142.5 Y: 142.5 Z: 0
37 % Shear: 15
38 % Overlap: XY: 2 Z: 1
39 % BlockWidth X: 289.947 Y: 289.947 Z: 11
40 % BlockOrder: Lexical
41 % AvoidFlyingBlocks: on
42 % GroupBlocks: on
43 % BacklashCorrection: on
44 %
45 % Output options
46 % HatchLines: Alternate
47 % ZAxis: Piezo
48 % Exposure: Constant
49 % InvertZAxis: on
50 % WritingDirection: Up
51 % ScanMode: Galvo
52 % WritingOrder: ContourFirst
53 % SkipInterfaceFinder: off
54 %
55
56 MoveStageX 5
57 MoveStageY 4.5
58
59 FindInterfaceAt $interfacePos
60
61 MoveStageY -54.5
62 MoveStageX -55
63 MoveStageY 50
64 MoveStageX 50

```

```

65
66 % BLOCK 0|0|0
67 include singlemouldpillar_adjhatch_files\singlemouldpillar_adjhatch_0_0_0.gwlb

```

### singlemouldpillar\_adjslice\_data.gwl

```

1 % File generated by DeScribe 2.7
2 %
3 % Creation time
4 %   2022-05-16T13:06:51+02:00
5 %
6 % Source file
7 %   Type: Mesh
8 %
9 % Volume 2.92x10E-7 mm^3
10 %
11 % Bounding box
12 %   Minimum X: 0.004 Y: -0.496 Z: 0
13 %   Maximum X: 9.996 Y: 9.496 Z: 9
14 %
15 % Transformation
16 %   Scaling X: 0.1 Y: 0.1 Z: 0.1
17 %   Rotation X: 0.5 Y: -0.5 Z: -0.5 W: 0.5
18 %   Translation X: 10 Y: 9.5 Z: 0
19 %
20 % Slicing
21 %   SlicingMode: Fixed
22 %   Distance: 0.5
23 %   SimplificationTolerance: 0.05
24 %   FixSelfIntersections: on
25 %
26 % Hatching
27 %   ContourCount: 2
28 %   ContourDistance: 0.2
29 %   ConcaveCornerMode: Beveled
30 %   HatchingDistance: 0.5
31 %   HatchingAngle: auto
32 %
33 % Splitting
34 %   Mode: Rectangular
35 %   BlockSize X: 285 Y: 285 Z: 10
36 %   Offset X: 142.5 Y: 142.5 Z: 0
37 %   Shear: 15
38 %   Overlap: XY: 2 Z: 1
39 %   BlockWidth X: 289.947 Y: 289.947 Z: 11
40 %   BlockOrder: Lexical
41 %   AvoidFlyingBlocks: on
42 %   GroupBlocks: on
43 %   BacklashCorrection: on
44 %
45 % Output options
46 %   HatchLines: Alternate
47 %   ZAxis: Piezo
48 %   Exposure: Constant
49 %   InvertZAxis: on
50 %   WritingDirection: Up
51 %   ScanMode: Galvo
52 %   WritingOrder: ContourFirst
53 %   SkipInterfaceFinder: off
54 %
55
56 MoveStageX 5
57 MoveStageY 4.5
58
59 FindInterfaceAt $interfacePos
60
61 MoveStageY -54.5
62 MoveStageX -55
63 MoveStageY 50

```

```

64 MoveStageX 50
65
66 % BLOCK 0|0|0
67 include singlemouldpillar_adjslice_files\singlemouldpillar_adjslice_0_0_0.gwlb

```

## B.6. Dose test 5

### B.6.1. Main code

```

1 % File generated by DeScribe 2.7
2
3 % System initialization
4 InvertZAxis 1
5
6 % Writing configuration
7 GalvoScanMode
8 ContinuousMode
9 PiezoSettlingTime 10
10 GalvoAcceleration 10
11 StageVelocity 200
12
13 % Scan field offsets
14 XOffset 0
15 YOffset 0
16 ZOffset 0
17
18 % Include
19
20 %Area 3
21 include singlemouldpillar_ns_c_job.gwl
22
23 %Area 1
24 include singlemouldpillar_ns_nc_job.gwl
25
26 MoveStageY -300
27 MoveStageX 100
28 %Area 4
29 include singlemouldpillar_s_c_job.gwl
30
31 %Area 2
32 include singlemouldpillar_LP_SS_system_job.gwl

```

### B.6.2. Additional codes

#### singlemouldpillar\_ns\_c\_job.gwl

```

1 % File generated by DeScribe 2.7
2
3 % System initialization
4 InvertZAxis 1
5
6 % Writing configuration
7 GalvoScanMode
8 ContinuousMode
9 PiezoSettlingTime 10
10 GalvoAcceleration 10
11 StageVelocity 200
12
13 % Scan field offsets
14 XOffset 0
15 YOffset 0
16 ZOffset 0
17
18 % Writing parameters
19 PowerScaling 1.0
20
21 WriteText "Dose test NSC"

```

```

22
23 var $i = 0
24 var $j = 0
25
26 var $solidLaserPower = 40
27 var $solidScanSpeed = 10000
28 var $contourLaserPower = 40
29 var $contourScanSpeed = 10000
30
31 MoveStageY 20
32
33 % Loop (5X4)
34
35 for $i = 0 to 4
36
37   for $j = 0 to 3
38
39     var $contourLaserPower = 20 + $i * 20
40     var $contourScanSpeed = 5000 + $j * 5000
41     var $solidLaserPower = 20 + $i * 20
42     var $solidScanSpeed = 5000 + $j * 5000
43
44 % Contour writing parameters
45 %var $contourLaserPower = 40
46 %var $contourScanSpeed = 10000
47
48 % Solid hatch lines writing parameters
49 %var $solidLaserPower = 40
50 %var $solidScanSpeed = 10000
51
52 var $interfacePos = 0.5
53
54 % Include slicer output
55 include singlemouldpillar_ns_c_data.gwl
56
57 MoveStageX 20
58
59 end
60 MoveStageY 20
61 MoveStageX -80
62
63 end

```

### singlemouldpillar\_ns\_nc\_job.gwl

```

1 % File generated by DeScribe 2.7
2
3 % System initialization
4 InvertZAxis 1
5
6 % Writing configuration
7 GalvoScanMode
8 ContinuousMode
9 PiezoSettlingTime 10
10 GalvoAcceleration 10
11 StageVelocity 200
12
13 % Scan field offsets
14 XOffset 0
15 YOffset 0
16 ZOffset 0
17
18 % Writing parameters
19 PowerScaling 1.0
20
21 WriteText "Dose test NSNC"
22
23 var $i = 0
24 var $j = 0

```

```
25
26 var $solidLaserPower = 40
27 var $solidScanSpeed = 10000
28
29 MoveStageY 20
30
31 % Loop (5X4)
32
33 for $i = 0 to 4
34
35   for $j = 0 to 3
36
37     var $solidLaserPower = 20 + $i * 20
38     var $solidScanSpeed = 5000 + $j * 5000
39
40     % Solid hatch lines writing parameters
41     %var $solidLaserPower = 40
42     %var $solidScanSpeed = 10000
43
44   var $interfacePos = 0.5
45
46   % Include slicer output
47   include singlemouldpillar_ns_nc_data.gwl
48
49   MoveStageX 20
50
51   end
52 MoveStageY 20
53 MoveStageX -80
54
55 end
```

### singlemouldpillar\_s\_c\_job.gwl

```
1 % File generated by DeScribe 2.7
2
3 % System initialization
4 InvertZAxis 1
5
6 % Writing configuration
7 GalvoScanMode
8 ContinuousMode
9 PiezoSettlingTime 10
10 GalvoAcceleration 10
11 StageVelocity 200
12
13 % Scan field offsets
14 XOffset 0
15 YOffset 0
16 ZOffset 0
17
18 % Writing parameters
19 PowerScaling 1.0
20
21 WriteText "Dose test SC"
22
23 var $i = 0
24 var $j = 0
25
26 var $contourLaserPower = 95
27 var $contourScanSpeed = 25000
28
29 var $solidLaserPower = 100
30 var $solidScanSpeed = 100000
31
32 var $baseLaserPower = 100
33 var $baseScanSpeed = 50000
34
35
```

```
36 MoveStageY 20
37
38 % Loop (7X4)
39
40 for $i = 0 to 6
41
42   for $j = 0 to 4
43
44     var $contourLaserPower = 40 + $i * 10
45     var $contourScanSpeed = 10000 + $j * 25000
46     var $solidLaserPower = 40 + $i * 10
47     var $solidScanSpeed = 10000 + $j * 25000
48     var $baseLaserPower = 40 + $i * 10
49     var $baseScanSpeed = 10000 + $j * 25000
50
51
52 % Contour writing parameters
53 %var $contourLaserPower = 95
54 %var $contourScanSpeed = 25000
55
56 % Solid hatch lines writing parameters
57 %var $solidLaserPower = 100
58 %var $solidScanSpeed = 100000
59
60 % Base writing parameters
61 %var $baseLaserPower = 100
62 %var $baseScanSpeed = 50000
63
64 var $interfacePos = 1
65
66 % Include slicer output
67 include singlemouldpillar_s_c_data.gwl
68
69 MoveStageX 20
70
71 end
72 MoveStageY 20
73 MoveStageX -100
74
75 end
```

### singlemouldpillar\_LP\_SS\_system.job.gwl

```
1 % File generated by DeScribe 2.7
2
3 % System initialization
4 InvertZAxis 1
5
6 % Writing configuration
7 GalvoScanMode
8 ContinuousMode
9 PiezoSettlingTime 10
10 GalvoAcceleration 10
11 StageVelocity 200
12
13 % Scan field offsets
14 XOffset 0
15 YOffset 0
16 ZOffset 0
17
18 % Writing parameters
19 PowerScaling 1.0
20
21 WriteText "Dose test Syst"
22
23 var $i = 0
24 var $j = 0
25
26 % Contour writing parameters
```

```

27 var $contourLaserPower = 95
28 var $contourScanSpeed = 25000
29
30 % Solid hatch lines writing parameters
31 var $solidLaserPower = 100
32 var $solidScanSpeed = 100000
33
34 % Base writing parameters
35 var $baseLaserPower = 100
36 var $baseScanSpeed = 50000
37
38 MoveStageY 20
39
40 % Loop (7X4)
41
42 for $i = 0 to 6
43
44   for $j = 0 to 1
45
46     var $contourLaserPower = 35 + $i * 10
47     var $contourScanSpeed = 25000
48     var $solidLaserPower = 40 + $i * 10
49     var $solidScanSpeed = 100000
50     var $baseLaserPower = 40 + $i * 10
51     var $baseScanSpeed = 50000
52
53     %% Contour writing parameters
54     %var $contourLaserPower = 95
55     %var $contourScanSpeed = 25000
56     %
57     %% Solid hatch lines writing parameters
58     %var $solidLaserPower = 100
59     %var $solidScanSpeed = 100000
60     %
61     %% Base writing parameters
62     %var $baseLaserPower = 100
63     %var $baseScanSpeed = 50000
64
65   var $interfacePos = 1
66
67   % Include slicer output
68   include singlemouldpillar_LP_SS_system_data.gwl
69
70   MoveStageX 20
71
72   end
73   MoveStageY 20
74   MoveStageX -40
75
76   end

```

## singlemouldpillar\_ns\_c\_data.gwl

```

1 % File generated by DeScribe 2.7
2 %
3 % Creation time
4 %   2022-05-18T11:09:07+02:00
5 %
6 % Source file
7 %   Type: Mesh
8 %
9 % Volume 2.92x10E-7 mm^3
10 %
11 % Bounding box
12 %   Minimum X: 0.004 Y: -0.496 Z: 0
13 %   Maximum X: 9.996 Y: 9.496 Z: 8.7
14 %
15 % Transformation
16 %   Scaling X: 0.1 Y: 0.1 Z: 0.1

```

```

17 %   Rotation X: 0.5 Y: -0.5 Z: -0.5 W: 0.5
18 %   Translation X: 10 Y: 9.5 Z: 0
19 %
20 % Slicing
21 %   SlicingMode: Fixed
22 %   Distance: 0.3
23 %   SimplificationTolerance: 0
24 %   FixSelfIntersections: on
25 %
26 % Hatching
27 %   ContourCount: 2
28 %   ContourDistance: 0.2
29 %   ConcaveCornerMode: Beveled
30 %   HatchingDistance: 0.2
31 %   HatchingAngle: 90
32 %   HatchingAngleOffset: 0
33 %
34 % Splitting
35 %   Mode: Rectangular
36 %   BlockSize X: 120 Y: 120 Z: 10
37 %   Offset X: 60 Y: 60 Z: 0
38 %   Shear: 17
39 %   Overlap: XY: 2 Z: 1.8
40 %   BlockWidth X: 125.608 Y: 125.608 Z: 11.8
41 %   BlockOrder: Lexical
42 %   AvoidFlyingBlocks: on
43 %   GroupBlocks: on
44 %   BacklashCorrection: on
45 %
46 % Output options
47 %   HatchLines: OneWay
48 %   ZAxis: Piezo
49 %   Exposure: Variable
50 %   InvertZAxis: on
51 %   WritingDirection: Up
52 %   ScanMode: Galvo
53 %   WritingOrder: ContourFirst
54 %   SkipInterfaceFinder: off
55 %
56
57 MoveStageX 5
58 MoveStageY 4.5
59
60 FindInterfaceAt $interfacePos
61
62 MoveStageY -54.5
63 MoveStageX -55
64 MoveStageY 50
65 MoveStageX 50
66
67 % BLOCK 0|0|0
68 include singlemouldpillar_ns_c_files\singlemouldpillar_ns_c_0_0_0.gwlb

```

## singlemouldpillar\_ns\_nc\_data.gwl

```

1 % File generated by DeScribe 2.7
2 %
3 % Creation time
4 %   2022-05-18T11:07:00+02:00
5 %
6 % Source file
7 %   Type: Mesh
8 %
9 % Volume 2.92x10E-7 mm^3
10 %
11 % Bounding box
12 %   Minimum X: 0.004 Y: -0.496 Z: 0
13 %   Maximum X: 9.996 Y: 9.496 Z: 8.7
14 %

```



```

15 % Transformation
16 %   Scaling X: 0.1 Y: 0.1 Z: 0.1
17 %   Rotation X: 0.5 Y: -0.5 Z: -0.5 W: 0.5
18 %   Translation X: 10 Y: 9.5 Z: 0
19 %
20 % Slicing
21 %   SlicingMode: Fixed
22 %   Distance: 0.3
23 %   SimplificationTolerance: 0
24 %   FixSelfIntersections: on
25 %
26 % Hatching
27 %   HatchingDistance: 0.2
28 %   HatchingAngle: 90
29 %   HatchingAngleOffset: 0
30 %
31 % Splitting
32 %   Mode: Rectangular
33 %   BlockSize X: 120 Y: 120 Z: 10
34 %   Offset X: 60 Y: 60 Z: 0
35 %   Shear: 17
36 %   Overlap: XY: 2 Z: 1.8
37 %   BlockWidth X: 125.608 Y: 125.608 Z: 11.8
38 %   BlockOrder: Lexical
39 %   AvoidFlyingBlocks: on
40 %   GroupBlocks: on
41 %   BacklashCorrection: on
42 %
43 % Output options
44 %   HatchLines: OneWay
45 %   ZAxis: Piezo
46 %   Exposure: Variable
47 %   InvertZAxis: on
48 %   WritingDirection: Up
49 %   ScanMode: Galvo
50 %   WritingOrder: ContourFirst
51 %   SkipInterfaceFinder: off
52 %
53
54 MoveStageX 5
55 MoveStageY 4.5
56
57 FindInterfaceAt $interfacePos
58
59 MoveStageY -54.5
60 MoveStageX -55
61 MoveStageY 50
62 MoveStageX 50
63
64 % BLOCK 0|0|0
65 include singlemouldpillar_ns_nc_files\singlemouldpillar_ns_nc_0_0_0.gwlb

```

### singlemouldpillar\_s\_c\_data.gwl

```

1 % File generated by DeScribe 2.7
2 %
3 % Creation time
4 %   2022-05-18T11:14:01+02:00
5 %
6 % Source file
7 %   Type: Mesh
8 %
9 % Volume 2.92x10E-7 mm^3
10 %
11 % Bounding box
12 %   Minimum X: 0.004 Y: -0.496 Z: 0
13 %   Maximum X: 9.996 Y: 9.496 Z: 9
14 %
15 % Transformation

```

```

16 %   Scaling X: 0.1 Y: 0.1 Z: 0.1
17 %   Rotation X: 0.5 Y: -0.5 Z: -0.5 W: 0.5
18 %   Translation X: 10 Y: 9.5 Z: 0
19 %
20 % Slicing
21 %   SlicingMode: Fixed
22 %   Distance: 0.9
23 %   SimplificationTolerance: 0
24 %   FixSelfIntersections: on
25 %
26 % Hatching
27 %   ContourCount: 2
28 %   ContourDistance: 0.2
29 %   ConcaveCornerMode: Sharp
30 %   HatchingDistance: 0.35
31 %   HatchingAngle: auto
32 %
33 % Splitting
34 %   Mode: Rectangular
35 %   BlockSize X: 120 Y: 120 Z: 10
36 %   Offset X: 60 Y: 60 Z: 0
37 %   Shear: 17
38 %   Overlap: XY: 2 Z: 1.8
39 %   BlockWidth X: 125.608 Y: 125.608 Z: 11.8
40 %   BlockOrder: Lexical
41 %   AvoidFlyingBlocks: on
42 %   GroupBlocks: on
43 %   BacklashCorrection: on
44 %
45 % Output options
46 %   HatchLines: Alternate
47 %   ZAxis: Piezo
48 %   Exposure: Variable
49 %   InvertZAxis: on
50 %   WritingDirection: Up
51 %   ScanMode: Galvo
52 %   WritingOrder: ContourFirst
53 %   SkipInterfaceFinder: off
54 %
55
56 MoveStageX 5
57 MoveStageY 4.5
58
59 FindInterfaceAt $interfacePos
60
61 MoveStageY -54.5
62 MoveStageX -55
63 MoveStageY 50
64 MoveStageX 50
65
66 % BLOCK 0|0|0
67 include singlemouldpillar_s_c_files\singlemouldpillar_s_c_0_0_0.gwlb

```

## singlemouldpillar\_LP\_SS\_system\_data.gwl

```

1 % File generated by DeScribe 2.7
2 %
3 % Creation time
4 %   2022-05-18T11:18:43+02:00
5 %
6 % Source file
7 %   Type: Mesh
8 %
9 % Volume 2.92x10E-7 mm^3
10 %
11 % Bounding box
12 %   Minimum X: 0.004 Y: -0.496 Z: 0
13 %   Maximum X: 9.996 Y: 9.496 Z: 9
14 %

```

```

15 % Transformation
16 %   Scaling X: 0.1 Y: 0.1 Z: 0.1
17 %   Rotation X: 0.5 Y: -0.5 Z: -0.5 W: 0.5
18 %   Translation X: 10 Y: 9.5 Z: 0
19 %
20 % Slicing
21 %   SlicingMode: Fixed
22 %   Distance: 0.9
23 %   SimplificationTolerance: 0
24 %   FixSelfIntersections: on
25 %
26 % Hatching
27 %   ContourCount: 2
28 %   ContourDistance: 0.2
29 %   ConcaveCornerMode: Sharp
30 %   HatchingDistance: 0.35
31 %   HatchingAngle: auto
32 %
33 % Splitting
34 %   Mode: Rectangular
35 %   BlockSize X: 120 Y: 120 Z: 10
36 %   Offset X: 60 Y: 60 Z: 0
37 %   Shear: 17
38 %   Overlap: XY: 2 Z: 1.8
39 %   BlockWidth X: 125.608 Y: 125.608 Z: 11.8
40 %   BlockOrder: Lexical
41 %   AvoidFlyingBlocks: on
42 %   GroupBlocks: on
43 %   BacklashCorrection: on
44 %
45 % Output options
46 %   HatchLines: Alternate
47 %   ZAxis: Piezo
48 %   Exposure: Variable
49 %   InvertZAxis: on
50 %   WritingDirection: Up
51 %   ScanMode: Galvo
52 %   WritingOrder: ContourFirst
53 %   SkipInterfaceFinder: off
54 %
55
56 MoveStageX 5
57 MoveStageY 4.5
58
59 FindInterfaceAt $interfacePos
60
61 MoveStageY -54.5
62 MoveStageX -55
63 MoveStageY 50
64 MoveStageX 50
65
66 % BLOCK 0|0|0
67 include singlemouldpillar_LP_SS_system_files\singlemouldpillar_LP_SS_system_0_0_0.gwlb

```

## B.7. Array test 1

### B.7.1. Main code

```

1 % File generated by DeScribe 2.7
2
3 % System initialization
4 InvertZAxis 1
5
6 % Writing configuration
7 GalvoScanMode
8 ContinuousMode
9 PiezoSettlingTime 10
10 GalvoAcceleration 10
11 StageVelocity 200

```

```

12
13 % Scan field offsets
14 XOffset 0
15 YOffset 0
16 ZOffset 0
17
18 % Writing parameters
19 PowerScaling 1.0
20
21 var $i = 0
22 var $j = 0
23
24 for $i = 0 to 80
25
26   for $j = 0 to 40
27
28     % Contour writing parameters
29     var $contourLaserPower = 50
30     var $contourScanSpeed = 50000
31
32     % Solid hatch lines writing parameters
33     var $solidLaserPower = 50
34     var $solidScanSpeed = 50000
35
36     % Base writing parameters
37     var $baseLaserPower = $contourLaserPower
38     var $baseScanSpeed = $contourScanSpeed
39
40     var $interfacePos = 0.5
41
42     % Include slicer output
43     include singlemouldpillar_2cont_data.gwl
44
45     MoveStageX 30
46
47     end
48     MoveStageY 30
49     MoveStageX -30*41
50
51   end

```

### B.7.2. Additional code singlemouldpillar\_2cont\_data.gwl

```

1 % File generated by DeScribe 2.7
2 %
3 % Creation time
4 %   2022-05-18T12:28:49+02:00
5 %
6 % Source file
7 %   Type: Mesh
8 %
9 % Volume 2.92x10E-7 mm^3
10 %
11 % Bounding box
12 %   Minimum X: 0.004 Y: -0.496 Z: 0
13 %   Maximum X: 9.996 Y: 9.496 Z: 9
14 %
15 % Transformation
16 %   Scaling X: 1 Y: 1 Z: 1
17 %   Rotation X: 0 Y: 0 Z: 0 W: 1
18 %   Translation X: 0 Y: 0 Z: 0
19 %
20 % Slicing
21 %   SlicingMode: Fixed
22 %   Distance: 1
23 %   SimplificationTolerance: 0.05
24 %   FixSelfIntersections: on

```

```

25 %
26 % Hatching
27 %   ContourCount: 2
28 %   ContourDistance: 0.2
29 %   ConcaveCornerMode: Sharp
30 %   HatchingDistance: 0.5
31 %   HatchingAngle: auto
32 %
33 % Splitting
34 %   Mode: Rectangular
35 %   BlockSize X: 285 Y: 285 Z: 10
36 %   Offset X: 142.5 Y: 142.5 Z: 0
37 %   Shear: 15
38 %   Overlap: XY: 2 Z: 1
39 %   BlockWidth X: 289.947 Y: 289.947 Z: 11
40 %   BlockOrder: Lexical
41 %   AvoidFlyingBlocks: on
42 %   GroupBlocks: on
43 %   BacklashCorrection: on
44 %
45 % Output options
46 %   HatchLines: OneWay
47 %   ZAxis: Piezo
48 %   Exposure: Variable
49 %   InvertZAxis: on
50 %   WritingDirection: Up
51 %   ScanMode: Galvo
52 %   WritingOrder: ContourFirst
53 %   SkipInterfaceFinder: off
54 %
55
56 MoveStageX 5
57 MoveStageY 4.5
58
59 FindInterfaceAt $interfacePos
60
61 MoveStageY -54.5
62 MoveStageX -55
63 MoveStageY 50
64 MoveStageX 50
65
66 % BLOCK 0|0|0
67 include singlemouldpillar_2cont_files\singlemouldpillar_2cont_0_0_0.gwlb

```

## B.8. Array test 2

### B.8.1. Main code

```

1 % File generated by DeScribe 2.7
2
3 % System initialization
4 InvertZAxis 1
5
6 % Writing configuration
7 GalvoScanMode
8 ContinuousMode
9 PiezoSettlingTime 10
10 GalvoAcceleration 10
11 StageVelocity 200
12
13 % Scan field offsets
14 XOffset 0
15 YOffset 0
16 ZOffset 0
17
18 % Writing parameters
19 PowerScaling 1.0
20
21 var $i = 0

```

```

22 var $j = 0
23
24 for $i = 0 to 40
25
26 for $j = 0 to 40
27
28 % Contour writing parameters
29 var $contourLaserPower = 52
30 var $contourScanSpeed = 62000
31
32 % Solid hatch lines writing parameters
33 var $solidLaserPower = 52
34 var $solidScanSpeed = 62000
35
36 % Base writing parameters
37 var $baseLaserPower = $contourLaserPower
38 var $baseScanSpeed = $contourScanSpeed
39
40 var $interfacePos = 0.5
41
42 % Include slicer output
43 include singlemouldpillar_3cont_data.gwl
44
45 MoveStageX 30
46
47 end
48 MoveStageY 30
49 MoveStageX -30*41
50
51 end

```

### B.8.2. Additional code singlemouldpillar\_3cont\_data.gwl

```

1 % File generated by DeScribe 2.7
2 %
3 % Creation time
4 % 2022-05-18T12:28:49+02:00
5 %
6 % Source file
7 % Type: Mesh
8 % Volume 2.92x10E-7 mm^3
9 %
10 % Bounding box
11 % Minimum X: 0.004 Y: -0.496 Z: 0
12 % Maximum X: 9.996 Y: 9.496 Z: 9
13 %
14 % Transformation
15 % Scaling X: 1 Y: 1 Z: 1
16 % Rotation X: 0 Y: 0 Z: 0 W: 1
17 % Translation X: 0 Y: 0 Z: 0
18 %
19 % Slicing
20 % SlicingMode: Fixed
21 % Distance: 0.3
22 % SimplificationTolerance: 0.05
23 % FixSelfIntersections: on
24 %
25 % Hatching
26 % ContourCount: 2
27 % ContourDistance: 0.2
28 % ConcaveCornerMode: Sharp
29 % HatchingDistance: 0.2
30 % HatchingAngle: auto
31 %
32 % Splitting
33 % Mode: Rectangular
34 % BlockSize X: 285 Y: 285 Z: 10

```

```

35 %   Offset X: 142.5 Y: 142.5 Z: 0
36 %   Shear: 15
37 %   Overlap: XY: 2 Z: 1
38 %   BlockWidth X: 289.947 Y: 289.947 Z: 11
39 %   BlockOrder: Lexical
40 %   AvoidFlyingBlocks: on
41 %   GroupBlocks: on
42 %   BacklashCorrection: on
43 %
44 % Output options
45 %   HatchLines: OneWay
46 %   ZAxis: Piezo
47 %   Exposure: Variable
48 %   InvertZAxis: on
49 %   WritingDirection: Up
50 %   ScanMode: Galvo
51 %   WritingOrder: ContourFirst
52 %   SkipInterfaceFinder: off
53 %
54
55 MoveStageX 5
56 MoveStageY 4.5
57
58 FindInterfaceAt $interfacePos
59
60 MoveStageY -54.5
61 MoveStageX -55
62 MoveStageY 50
63 MoveStageX 50
64
65 % BLOCK 0|0|0
66 include singlemouldpillar_2cont_files\singlemouldpillar_3cont_0_0_0.gwlb

```

## B.9. Array test 3

The additional code is the *singlemouldpillar\_ns\_nc\_data.gwl* introduced previously.

### Main code

```

1  % File generated by DeScribe 2.7
2
3  % System initialization
4  InvertZAxis 1
5
6  % Writing configuration
7  GalvoScanMode
8  ContinuousMode
9  PiezoSettlingTime 10
10 GalvoAcceleration 10
11 StageVelocity 200
12
13 % Scan field offsets
14 XOffset 0
15 YOffset 0
16 ZOffset 0
17
18 % Writing parameters
19 PowerScaling 1.0
20
21 %WriteText "Dose test NSNC"
22
23 var $i = 0
24 var $j = 0
25
26 var $solidLaserPower = 60
27 var $solidScanSpeed = 10000
28
29 MoveStageY 20

```

```

30
31 % Loop (5X4)
32
33 for $i = 0 to 20
34
35     for $j = 0 to 10
36         % Solid hatch lines writing parameters
37         var $solidLaserPower = 40
38         var $solidScanSpeed = 10000
39         var $interfacePos = 0.5
40         % Include slicer output
41         include singlemouldpillar_ns_nc_data.gwl
42         MoveStageX 20
43     end
44
45     %part 2
46     MoveStageX 20
47     for $j = 0 to 10
48         % Solid hatch lines writing parameters
49         var $solidLaserPower = 50
50         var $solidScanSpeed = 10000
51         var $interfacePos = 0.5
52         % Include slicer output
53         include singlemouldpillar_ns_nc_data.gwl
54         MoveStageX 20
55     end
56
57     %part 3
58     MoveStageX 20
59     for $j = 0 to 10
60         % Solid hatch lines writing parameters
61         var $solidLaserPower = 60
62         var $solidScanSpeed = 10000
63         var $interfacePos = 0.5
64         % Include slicer output
65         include singlemouldpillar_ns_nc_data.gwl
66         MoveStageX 20
67     end
68
69     MoveStageY 20
70     MoveStageX -35*20 %total amount of pillars (=above +1)
71
72 end

```

## B.10. Array test 4

The additional code is the *singlemouldpillar\_ns\_nc\_data.gwl* introduced previously.

### Main code

```

1 % File generated by DeScribe 2.7
2
3 % System initialization
4 InvertZAxis 1
5
6 % Writing configuration
7 GalvoScanMode
8 ContinuousMode
9 PiezoSettlingTime 10
10 GalvoAcceleration 10
11 StageVelocity 200
12
13 % Scan field offsets
14 XOffset 0
15 YOffset 0
16 ZOffset 0
17
18 % Writing parameters

```



```
19 PowerScaling 1.0
20
21 %WriteText "Dose test NSNC"
22
23 var $i = 0
24 var $j = 0
25
26 var $solidLaserPower = 50
27 var $solidScanSpeed = 10000
28
29 MoveStageY 20
30
31 % Loop (5X4)
32
33 for $i = 0 to 80
34
35   for $j = 0 to 80
36
37
38
39     % Solid hatch lines writing parameters
40     %var $solidLaserPower = 40
41     %var $solidScanSpeed = 10000
42
43     var $interfacePos = 0.5
44
45     % Include slicer output
46     include singlemouldpillar_ns_nc_data.gwl
47
48 MoveStageX 20
49
50
51 end
52 MoveStageY 20
53 MoveStageX -81*20 %total amount of pillars (=above +1)
54
55 end
```

# C

## Results

### C.1. Profilometry measurement results

#### C.1.1. Matlab code for mean thickness calculation

This Section contains the Matlab codes used for the mean thickness calculation of the spincoated layer.

##### **importfile.m**

This file was used to read the raw data obtained by the white light interferometry measurement.

```
1 function POMAConnewHMDS2estukje = importfile(filename, dataLines)
2 %IMPORTFILE1 Import data from a text file
3 % POMACONNEWHMDS2ESTUKJE = IMPORTFILE1(FILENAME) reads data from text
4 % file FILENAME for the default selection. Returns the data as a table.
5 %
6 % POMACONNEWHMDS2ESTUKJE = IMPORTFILE1(FILE, DATALINES) reads data for
7 % the specified row interval(s) of text file FILENAME. Specify
8 % DATALINES as a positive scalar integer or a N-by-2 array of positive
9 % scalar integers for dis-contiguous row intervals.
10 %
11 % Example:
12 % POMAConnewHMDS2estukje = importfile1("/home/matthijs/Desktop/sophie/POMAC on new ...
13 % HMDS 2e stukje.ASC", [11, Inf]);
14 % See also READTABLE.
15 %
16 % Auto-generated by MATLAB on 15-Sep-2022 15:08:44
17
18 %% Input handling
19
20 % If dataLines is not specified, define defaults
21 if nargin < 2
22     dataLines = [11, Inf];
23 end
24
25 %% Set up the Import Options and import the data
26 opts = delimitedTextImportOptions("NumVariables", 4);
27
28 % Specify range and delimiter
29 opts.DataLines = dataLines;
30 opts.Delimiter = ",";
31
32 % Specify column names and types
33 opts.VariableNames = ["x", "y", "z", "VarName4"];
34 opts.VariableTypes = ["double", "double", "double", "string"];
35
36 % Specify file level properties
37 opts.ExtraColumnsRule = "ignore";
```

```

38 opts.EmptyLineRule = "read";
39
40 % Specify variable properties
41 opts = setvaropts(opts, "VarName4", "WhitespaceRule", "preserve");
42 opts = setvaropts(opts, "VarName4", "EmptyFieldRule", "auto");
43
44 % Import the data
45 POMACConnewHMDS2estukje = readtable(filename, opts);
46
47 end

```

### process.m

This file was used to fabricate the graphs and calculate the mean and standard deviations of the spincoated POMaC layer thickness.

```

1 files = {
2     'POMAC on new HMDS 2e stukje.ASC',...
3     'POMAC on new HMDS 3e stukje.ASC',...
4     'POMAC on new HMDS 4e stukje.ASC',...
5     'POMAC on new HMDS 5e stukje.ASC',...
6     'POMAC on new HMDS GOED.ASC'
7 };
8 close all;
9 t = tiledlayout(3,2);
10 t1 = nexttile;
11
12 %% Location 1
13 %close all
14 i = 5;
15 filename = files{i};
16 data = importfile(filename);
17
18 % figure();
19 %     hold on;
20 %     title(filename);
21 %     A = [data.x, data.y, data.z];
22 %     surf(A);
23 %     hold off;
24
25 %figure();
26 hold on;
27 histogram(data.z);
28 title('Area 1','FontSize',15);
29 xlabel('Height data (nm)','FontSize',15)
30 ylabel('Number of data points (-)','FontSize',15)
31 xlim([-1.5E4 2.0E4]);
32
33 hold off;
34
35 % Using cropped data of each histogram peak
36 cropped_substrate1 = data.z(data.z(:,1) ≥ -11000 & data.z(:,1) < -6000);
37 cropped_pomac1 = data.z(data.z(:,1) ≥ 0 & data.z(:,1) < 16000);
38
39 mean(cropped_substrate1)
40 mean(cropped_pomac1)
41
42 std(cropped_substrate1)
43 std(cropped_pomac1)
44
45 height_1 = mean(cropped_pomac1) - mean(cropped_substrate1) %subtracting means
46 std_1 = sqrt(std(cropped_substrate1)^2 + std(cropped_pomac1)^2) % correlation ...
    between data points is 0
47
48 %% Location 2
49 %close all
50 t2 = nexttile;
51
52 i = 1;

```

```

53
54 filename = files{i};
55 data = importfile(filename);
56
57 % figure();
58 % hold on;
59 % title(filename);
60 % A = [data.x, data.y, data.z];
61 % surf(A);
62 % hold off;
63
64 %figure();
65 hold on;
66 histogram(data.z);
67 title('Area 2','FontSize',15);
68 xlabel('Height data (nm)','FontSize',15)
69 ylabel('Number of data points (-)','FontSize',15)
70 xlim([-1.5E4 2.0E4]);
71
72 hold off;
73
74 % Using cropped data of each histogram peak
75 cropped_substrate2 = data.z(data.z(:,1) ≥ -11000 & data.z(:,1) < -5000);
76 cropped_pomac2 = data.z(data.z(:,1) ≥ 0 & data.z(:,1) < 16000);
77
78 mean(cropped_substrate2)
79 mean(cropped_pomac2)
80
81 std(cropped_substrate2)
82 std(cropped_pomac2)
83
84 height_2 = mean(cropped_pomac2) - mean(cropped_substrate2) %subtracting means
85 std_2 = sqrt(std(cropped_substrate2)^2 + std(cropped_pomac2)^2) % correlation ...
    between data points is 0
86
87 %% Location 3 %thick edge. No data point
88 % close all
89 t3 = nexttile;
90 i = 2;
91 filename = files{i};
92 data = importfile(filename);
93
94 %figure();
95 hold on;
96 histogram(data.z);
97 title('Area 3','FontSize',15);
98 xlabel('Height data (nm)','FontSize',15)
99 ylabel('Number of data points (-)','FontSize',15)
100 xlim([-1.5E4 2.0E4]);
101
102 hold off;
103
104 % Using cropped data of each histogram peak
105 cropped_substrate3 = data.z(data.z(:,1) ≥ -11000 & data.z(:,1) < 5000);
106 cropped_pomac3 = data.z(data.z(:,1) ≥ 5000 & data.z(:,1) < 16000);
107
108 mean(cropped_substrate3)
109 mean(cropped_pomac3)
110
111 std(cropped_substrate3)
112 std(cropped_pomac3)
113
114 height_3 = mean(cropped_pomac3) - mean(cropped_substrate3) %subtracting means
115 std_3 = sqrt(std(cropped_substrate3)^2 + std(cropped_pomac3)^2) % correlation ...
    between data points is 0
116 %% Location 4
117 t4 = nexttile;
118 %close all
119 i = 3;
120
121 filename = files{i};

```

```

122     data = importfile(filename);
123
124     %figure();
125     hold on;
126     histogram(data.z);
127     title('Area 4','FontSize',15);
128     xlabel('Height data (nm)','FontSize',15)
129     ylabel('Number of data points (-)','FontSize',15)
130     xlim([-1.5E4 2.0E4]);
131
132     hold off;
133
134     % Using cropped data of each histogram peak
135     cropped_substrate4 = data.z(data.z(:,1) ≥ -11000 & data.z(:,1) < 5000);
136     cropped_pomac4 = data.z(data.z(:,1) ≥ 5000 & data.z(:,1) < 16000);
137
138     mean(cropped_substrate4)
139     mean(cropped_pomac4)
140
141     std(cropped_substrate4)
142     std(cropped_pomac4)
143
144     height_4 = mean(cropped_pomac4) - mean(cropped_substrate4) %subtracting means
145     std_4 = sqrt(std(cropped_substrate4)^2 + std(cropped_pomac4)^2) % correlation ...
146     % between data points is 0
147     %% Location 5
148     t5 = nexttile;
149     %close all
150     i = 4;
151
152     filename = files{i};
153     data = importfile(filename);
154
155     %figure();
156     hold on;
157     histogram(data.z);
158     title('Area 5','FontSize',15);
159     xlabel('Height data (nm)','FontSize',15)
160     ylabel('Number of data points (-)','FontSize',15)
161     xlim([-1.5E4 2.0E4]);
162
163     hold off;
164
165     % Using cropped data of each histogram peak
166     cropped_substrate5 = data.z(data.z(:,1) ≥ -11000 & data.z(:,1) < 5000);
167     cropped_pomac5 = data.z(data.z(:,1) ≥ 5000 & data.z(:,1) < 16000);
168
169     mean(cropped_substrate5)
170     mean(cropped_pomac5)
171
172     std(cropped_substrate5)
173     std(cropped_pomac5)
174
175     height_5 = mean(cropped_pomac5) - mean(cropped_substrate5) %subtracting means
176     std_5 = sqrt(std(cropped_substrate5)^2 + std(cropped_pomac5)^2) % correlation ...
177     % between data points is 0
178     %% Overall mean calculation
179     mean = (height_1 + height_2 + height_3 + height_4 + height_5)/5
180     std = sqrt(std_1^2 + std_2^2 + std_3^2 + std_4^2 + std_5^2)

```

## C.1.2. Images of the areas used in the profilometry measurement

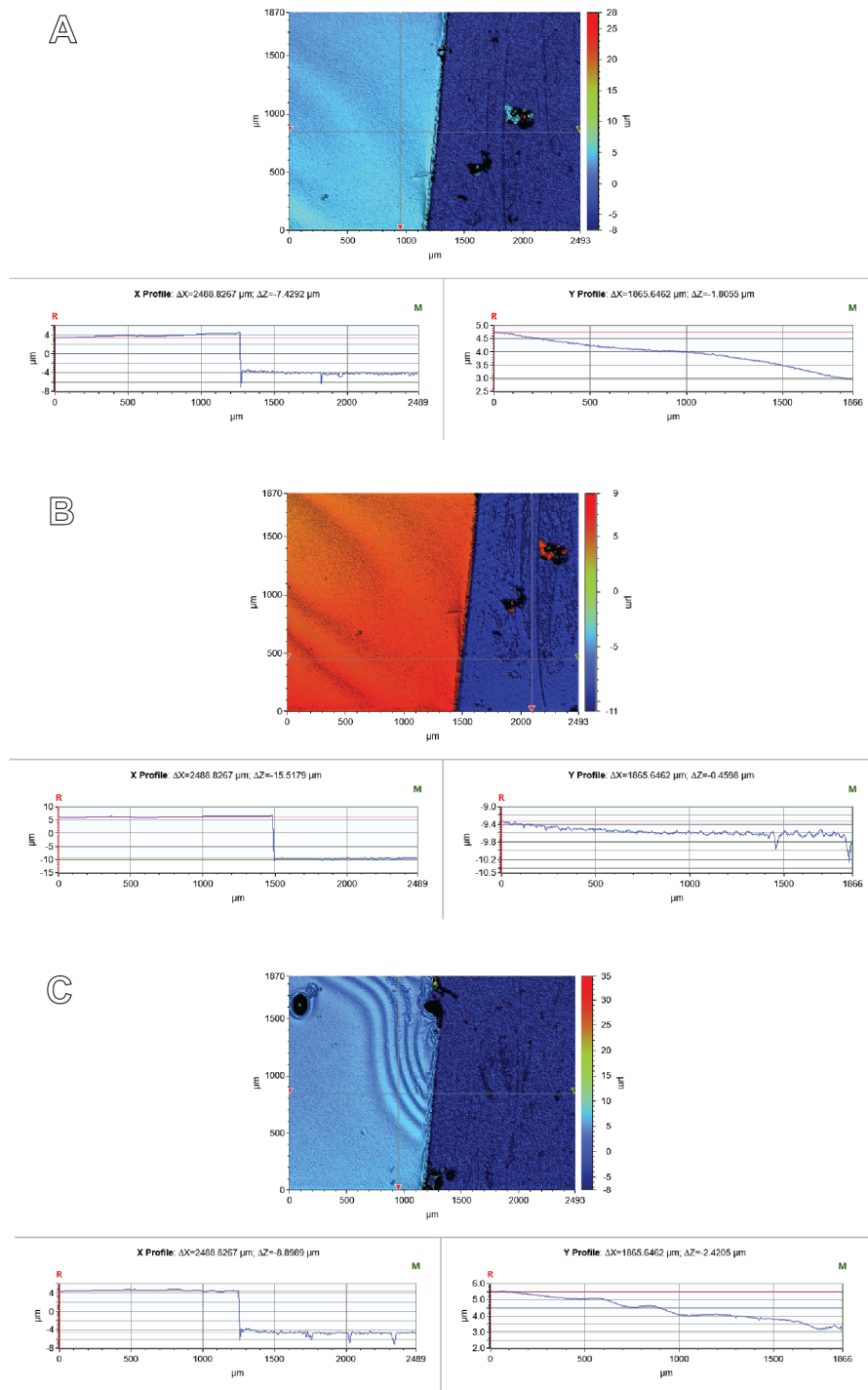


Figure C.1: White light interferometry image along the cut film edge. Letters A to E represent measurements at different locations. F) A 3D side view of the cut thin film on top of the substrate.

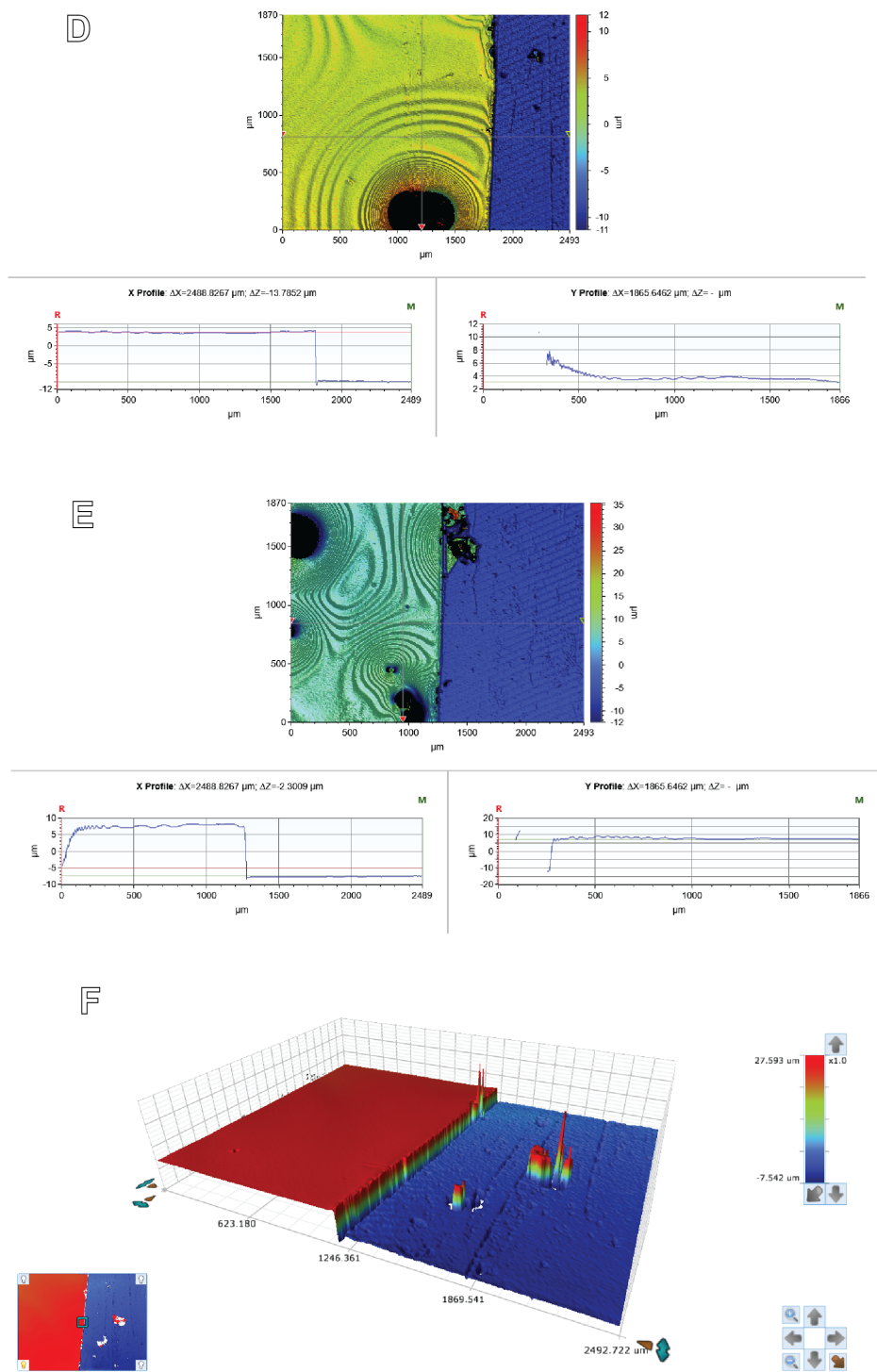


Figure C.2: White light interferometry image along the cut film edge. Letters A to E represent measurements at different locations. F) A 3D side view of the cut thin film on top of the substrate.

## C.2. Matlab code for effective Young's modulus calculation

```

1 clear all
2 close all
3 clc
4
5 datasamples = readtable('sampledata.csv'); %input as csv
6
7 t = tiledlayout(1,3);
8 % sample 1 data boxplot (100% UV intensity)
9
10 t1 = nexttile;
11 boxplot(datasamples.Sample_1_E_eff_kPa, datasamples.Sample_1_location)
12 hold on
13 title('Sample 1 (100% UV intensity)', 'FontSize',15)
14
15 ylim([0 600]);
16 ax = gca
17 ax.XAxis.FontSize = 14;
18 ax.YAxis.FontSize = 14;
19 xlabel('Location point','FontSize',15)
20 ylabel('Effective Young's Modulus (kPa)','FontSize',15)
21 hold off
22
23
24 % sample 2 data boxplot (60% UV intensity)
25
26 t2 = nexttile;
27 boxplot(datasamples.Sample_2_E_eff_kPa, datasamples.Sample_2_location)
28 hold on
29 title('Sample 2 (60% UV intensity)', 'FontSize',15)
30 ax = gca
31 ax.XAxis.FontSize = 14;
32 ax.YAxis.FontSize = 14;
33 xlabel('Location point','FontSize',15)
34 ylabel('Effective Young's Modulus (kPa)','FontSize',15)
35 ylim([0 600]);
36 hold off
37
38
39 % sample 3 data boxplot (submerged in PBS)
40
41 t3 = nexttile;
42 boxplot(datasamples.Sample_3_E_eff_kPa, datasamples.Sample_3_location)
43 hold on
44 title('Sample 3 (submerged for 2 weeks)', 'FontSize',15)
45 ax = gca
46 ax.XAxis.FontSize = 14;
47 ax.YAxis.FontSize = 14;
48 xlabel('Location point', 'FontSize',15)
49 ylabel('Effective Young's Modulus (kPa)','FontSize',15)
50 ylim([0 600]);
51 hold off
52
53
54 linkaxes([t1,t2,t3], 'y')
55
56
57 % Comparison between the three samples boxplot
58
59 figure
60 hold on
61 samplenumber = 1:3;
62 combineddata = [datasamples.Sample_1_E_eff_kPa datasamples.Sample_2_E_eff_kPa ...
63                 datasamples.Sample_3_E_eff_kPa];
64 %table_com_data = array2table(combineddata);
65 boxplot(combineddata)
66
67 %title('A comparison of the effective Young's modulus between samples')
68 ax = gca

```



```
68 ax.XAxis.FontSize = 20;
69 ax.YAxis.FontSize = 20;
70 xlabel('Sample number')
71 ylabel('Effective Young''s Modulus (kPa)')
72 ylim([0 600]);
73 hold off
74
75
76 % Median Effective stiffness data of each sample (in kPa)
77
78 mean_sample_1 = mean(datasamples.Sample_1_E_eff_kPa)
79 mean_sample_2 = mean(datasamples.Sample_2_E_eff_kPa, 'omitnan')
80 mean_sample_3 = mean(datasamples.Sample_3_E_eff_kPa)
81 % standard deviation:
82 std_sample_1 = std(datasamples.Sample_1_E_eff_kPa)
83 std_sample_2 = std(datasamples.Sample_2_E_eff_kPa, 'omitnan')
84 std_sample_3 = std(datasamples.Sample_3_E_eff_kPa)
```

### C.3. Toxicology cell culture results

In this appendix an overview is included of all cell cultures with eluates that had been in contact with POMaC for 1 day (T=1). The additional images can be found in the Supplementary files.

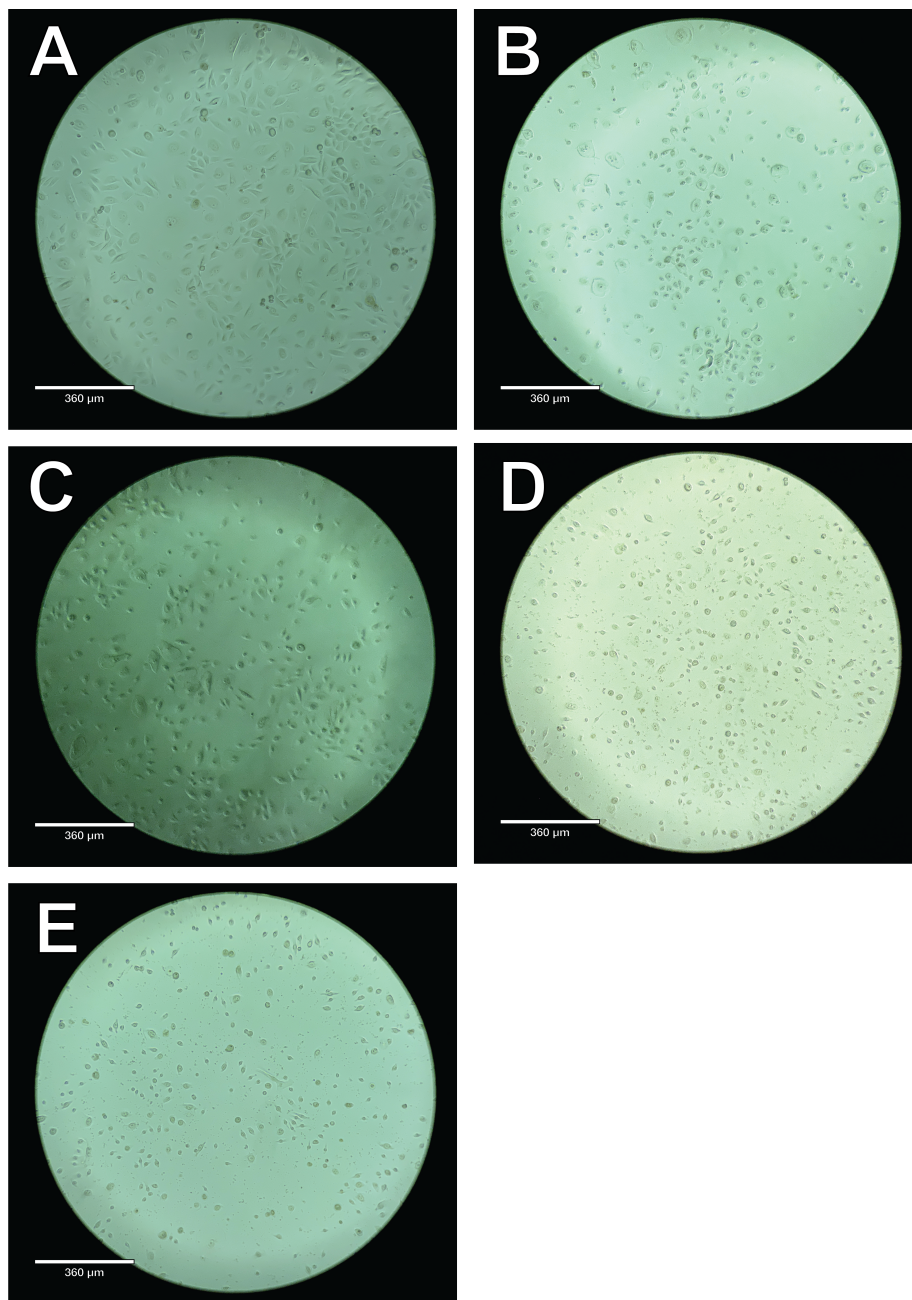


Figure C.3: Cell culture images after 1 day in culture with the POMaC eluates. (A) Control cell culture. (B) EPOMaC with no photoinitiator, T = 1, well A. (C) EPOMaC with 1 wt% uncured TPO, T = 1, well B. (D) PPOMaC containing 5 wt% Irgacure 2959, T = 1, well B. (E) PPOMaC containing 1 wt% TPO, T = 1, well B.

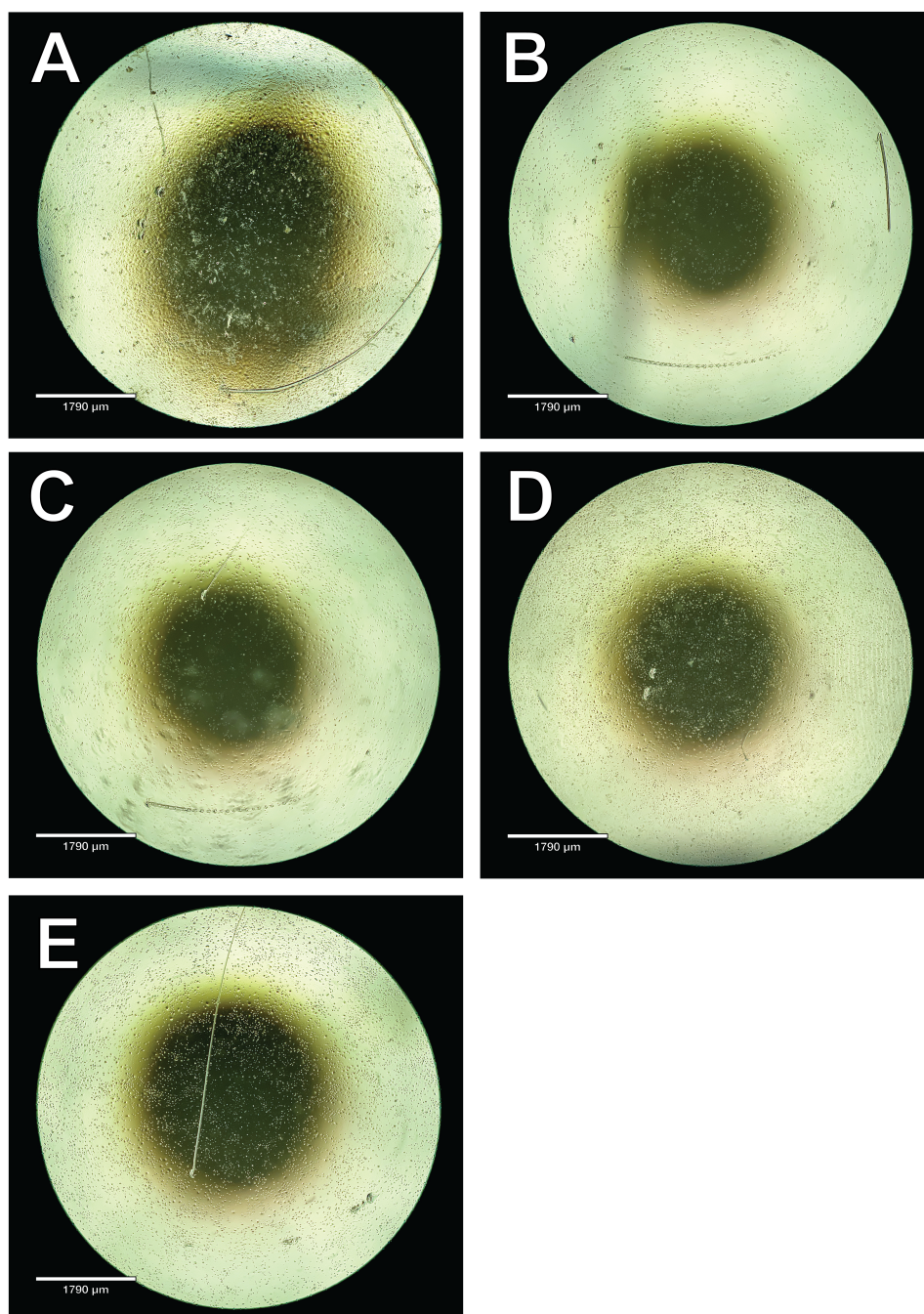


Figure C.4: Cell culture images after 5 days in culture with the POMaC eluates. (A) Control cell culture. (B) EPOMaC with no photoinitiator, T = 1, well A. (C) EPOMaC with 1 wt% uncured TPO, T = 1, well B. (D) PPOMaC containing 5 wt% Irgacure 2959, T = 1, well B. (E) PPOMaC containing 1 wt% TPO, T = 1, well B.

## C.4. Autofluorescence results for the 1 mm thick samples

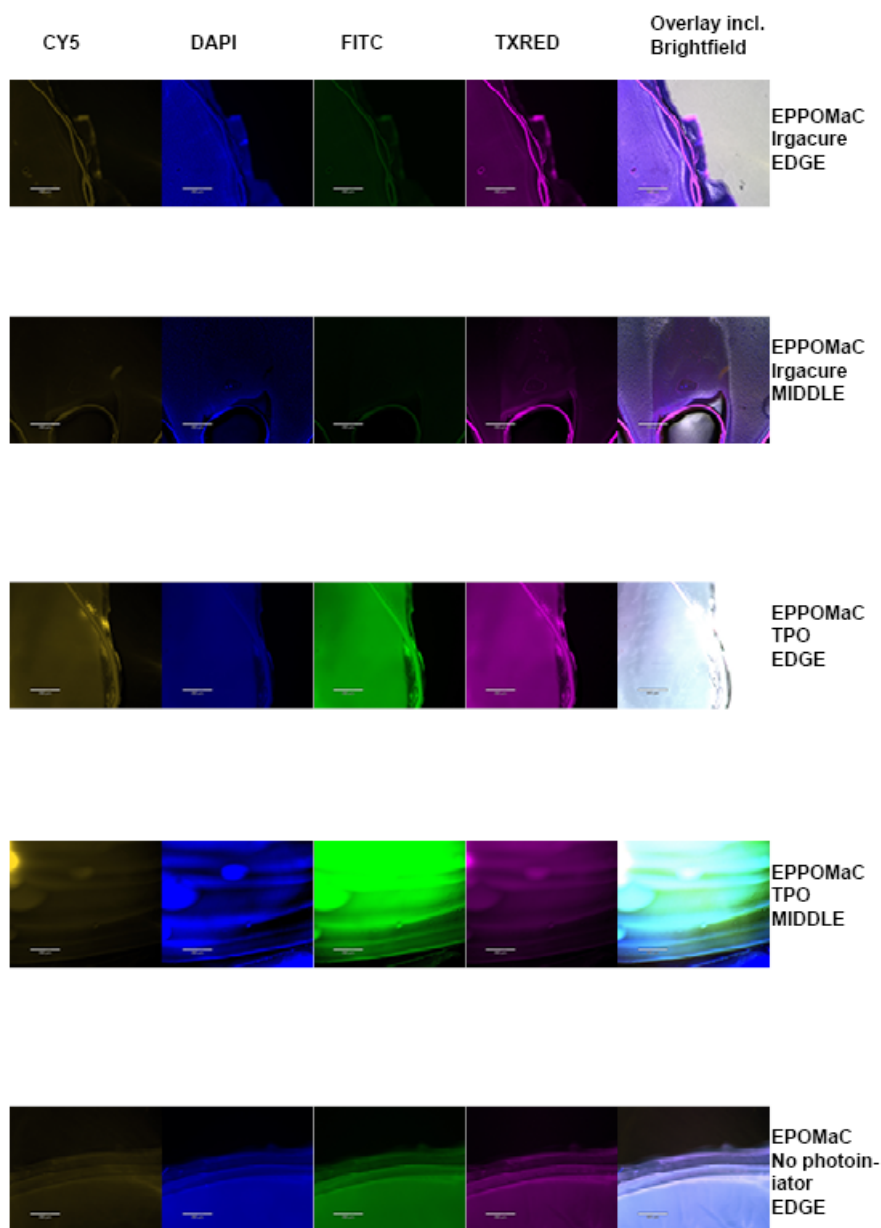


Figure C.5: Results of the autofluorescence test. Results for wavelengths for four different commonly used stains indicated in the top are shown. Page 1.

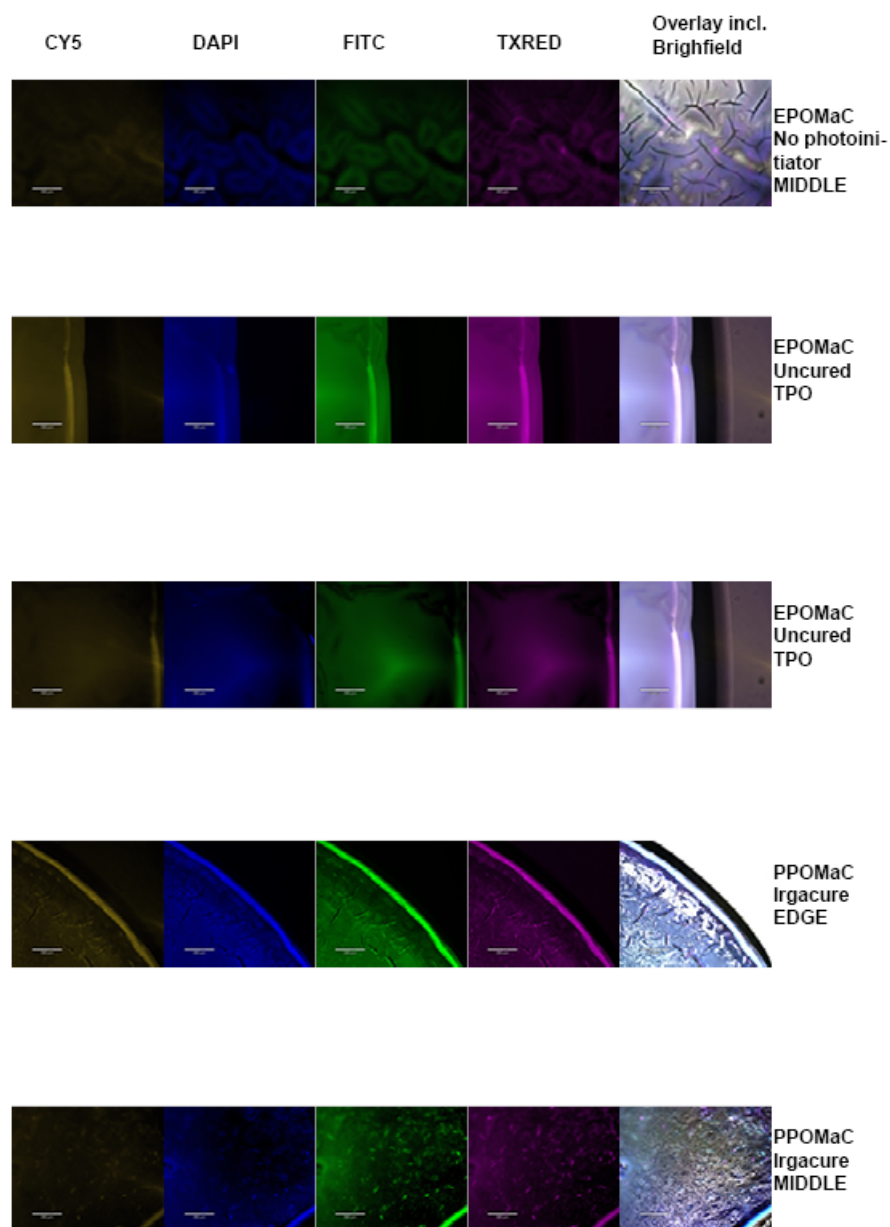


Figure C.6: Results of the autofluorescence test. Results for wavelengths for four different commonly used stains indicated in the top are shown. Page 2.

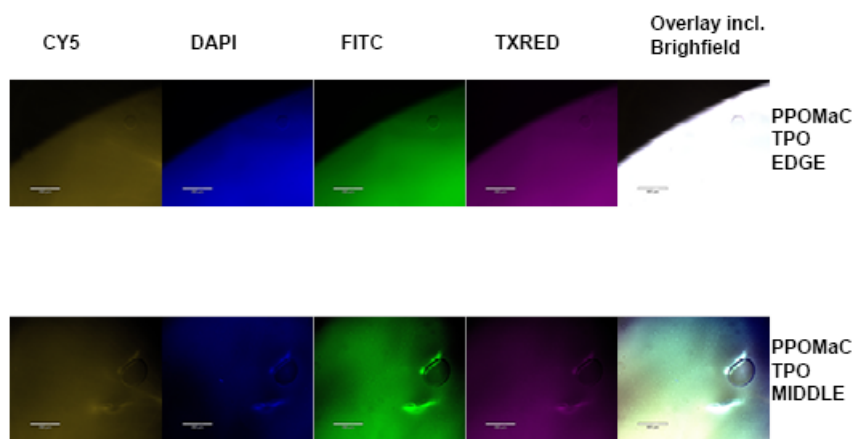


Figure C.7: Results of the autofluorescence test. Results for wavelengths for four different commonly used stains indicated in the top are shown. Page 3.





# D

## Future research

### D.1. Fabrication of a membrane containing a pillar imprint

This Appendix lists the recommended approach for spincoating a membrane on top of a 2PP-printed mould, to obtain a membrane containing an imprinted structure.

1. Clean a silicon substrate with acetone, IPA en demiwater, before drying it with an airgun. Conduct a plasma cleaning step for 15 min at 0.14 mbar at an 80% power equivalent. Afterwards, place a droplet of IP-Dip and place the substrate in the Nanoscribe.
2. Print a 86 x 86 pillar array in the middle of the substrate, with pillar dimensions as explained in the concept introduction and a pitch of 35  $\mu\text{m}$ . Printing parameters should be similar to the ones listed in Array test 4 in Table A.2 in Appendix A.4. A post-curing step could be evaluated.
3. Follow the HMDS surface priming procedure listed in Appendix A.3. An oxygen plasma step could be conducted beforehand to increase the surface roughness and HMDS adherence. A subsequent Pluronic F-127 priming step could be evaluated to diminish POMaC adherence to the pillars.
4. Warm up POMaC containing 5 wt% Irgacure 2959 (or 1 wt% TPO) at 50 °C for 20 minutes, to decrease the viscosity. Place a droplet of around 2 ml in the middle of the substrate and align it with the spincoater centerpoint. Spincoat the POMaC at a spinning speed of 2500 r.p.m. and a spinning acceleration of 1000 r.p.m./s for 5 minutes.
5. Afterwards, UV cure the thin layer for 30 minutes, at a point source intensity of 100 % and a height of 2 cm. Oven post-polymerization could be evaluated.
6. For detachment, attach a detachment structure, e.g. a POMaC slab containing a hole, tape or a LOC component. Subsequently, place the layer in DI water until detached.

Evaluating the membrane and the remaining substrate can be done using an optical or digital microscope, or if higher resolution is needed, using a SEM.



## D.2. Permeability measurement

With this proposed permeability experiment, the permeability of a membrane to liquid and particles of various sizes can be evaluated. This can provide an indication whether liquid, proteins and signalling molecules with various sizes and immune cells can pass through a membrane. The basic set-up includes two channel parts, between which a porous membrane is attached. Figure D.1 shows a schematic image of this set-up. Liquid containing small beads with a known diameter is present on one side of the membrane. This side can be connected to a pressure head, to create a slight constant overpressure. On the other side of the membrane, any liquid containing beads that has passed through is collected. The diameter of these beads indicates what dimension particles might travel through the membrane. The fluid permeability can be calculated by measuring the rate of the flow and Darcy's Law, which is only valid for slow and viscous flow (Eq. D.1) [126]. An example of a permeability measurement is given by Agrawal et al. [126]. The collected beads can be imaged by, for example, X-ray microtomography, after the liquid has evaporated.

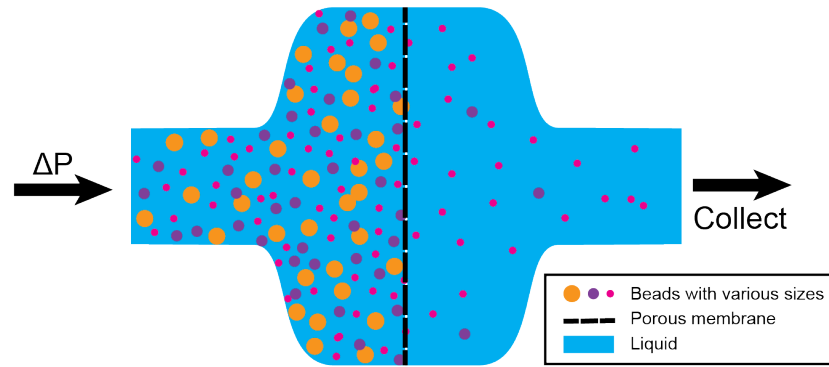


Figure D.1: Schematic of the proposed permeability measurement.

$$q = -\frac{k}{\mu L} \Delta p \quad (\text{D.1})$$

Where:  $q$  = the discharge per unit area (m/s)  
 $k$  = the permeability (m<sup>2</sup>)  
 $\mu$  = the dynamic viscosity (Pa·s)  
 $L$  = sample thickness (m)  
 $\Delta p$  = the pressure drop (Pa)

# Bibliography

- [1] Z. Nissar, "Lung-on-a-chip. Design and Manufacture of a Resealable Device for Recreating the Alveolar-Capillary Barrier in Vitro," Delft University of Technology, Tech. Rep. September, 2021. [Online]. Available: <https://repository.tudelft.nl/>
- [2] D. Huh, "A human breathing lung-on-a-chip," *Annals of the American Thoracic Society*, vol. 12, no. March, pp. S42–S44, 2015.
- [3] A. Laniece, "Alveoli-on-a-chip: A close-contact dynamic model of the alveolar capillary barrier: micro-engineering, microfluidics and induced pluripotent stem cells." Ph.D. dissertation, L'Université Sorbonne Paris Cité, 2019.
- [4] T. Pasman, D. Baptista, S. van Riet, R. K. Truckenmüller, P. S. Hiemstra, R. J. Rottier, N. M. Hamelmann, J. M. Paulusse, D. Stamatialis, and A. A. Poot, "Development of an in vitro airway epithelial–endothelial cell culture model on a flexible porous poly(trimethylene carbonate) membrane based on calu-3 airway epithelial cells and lung microvascular endothelial cells," *Membranes*, vol. 11, no. 197, pp. 1–20, 2021.
- [5] P. Zampugno, S. Wüthrich, S. Achenbach, G. Thoma, J. D. Stucki, N. Hobi, N. Schneider-Daum, C. M. Lehr, H. Huwer, T. Geiser, R. A. Schmid, and O. T. Guenat, "Second-generation lung-on-a-chip with an array of stretchable alveoli made with a biological membrane," *Communications Biology*, vol. 4, no. 168, pp. 1–10, 2021. [Online]. Available: <http://dx.doi.org/10.1038/s42003-021-01695-0>
- [6] D. Huh, D. C. Leslie, B. D. Matthews, J. P. Fraser, S. Jurek, G. A. Hamilton, K. Thorneloe, M. Allen McAlexander, and D. E. Ingber, "A human disease model of drug toxicity-induced pulmonary edema in a lung-on-a-chip microdevice," *Sci Transl Med.*, vol. 4, no. 159, p. 159ra147, 2012.
- [7] S. B. Campbell, Q. Wu, J. Yazbeck, C. Liu, S. Okhovatian, and M. Radisic, "Beyond Polydimethylsiloxane: Alternative Materials for Fabrication of Organ-on-a-Chip Devices and Microphysiological Systems," *ACS Biomaterials Science and Engineering*, vol. 7, no. 7, pp. 2880–2899, 2021.
- [8] K. Domansky, J. D. Sliz, N. Wen, C. Hinojosa, G. Thompson, J. P. Fraser, T. Hamkins-Indik, G. A. Hamilton, D. Levner, and D. E. Ingber, "SEBS elastomers for fabrication of microfluidic devices with reduced drug absorption by injection molding and extrusion," *Microfluidics and Nanofluidics*, vol. 21, no. 6, pp. 1–12, 2017.
- [9] D. Konar, M. Devarasetty, D. V. Yildiz, A. Atala, and S. V. Murphy, "Lung-On-A-Chip Technologies for Disease Modeling and Drug Development," *Biomedical Engineering and Computational Biology*, vol. 7, no. S1, pp. 17–27, 2016.
- [10] J. Shrestha, S. Razavi Bazaz, H. Aboulkheyr Es, D. Yaghobian Azari, B. Thierry, M. Ebrahimi Warkiani, and M. Ghadiri, "Lung-on-a-chip: the future of respiratory disease models and pharmacological studies," *Critical Reviews in Biotechnology*, vol. 40, no. 2, pp. 213–230, 2020. [Online]. Available: <https://doi.org/10.1080/07388551.2019.1710458>
- [11] J. Tenenbaum-Katan, A. Artzy-Schnirman, R. Fishler, N. Korin, and J. Sznitman, "Biomimetics of the pulmonary environment in vitro: A microfluidics perspective," *Biomicrofluidics*, vol. 12, no. 042209, pp. 1–15, 2018.
- [12] K. H. Benam, R. Villenave, C. Lucchesi, A. Varone, C. Hubeau, H. H. Lee, S. E. Alves, M. Salmon, T. C. Ferrante, J. C. Weaver, A. Bahinski, G. A. Hamilton, and D. E. Ingber, "Small airway-on-a-chip enables analysis of human lung inflammation and drug responses in vitro," *Nature Methods*, vol. 13, no. 2, pp. 151–157, 2016.

- [13] D. Huang, T. Liu, J. Liao, S. Maharjan, X. Xie, M. Pérez, I. Anaya, S. Wang, A. T. Mayer, Z. Kang, W. Kong, V. L. Mainardi, C. E. Garciamendez-Mijares, G. G. Martínez, M. Moretti, W. Zhang, Z. Gu, A. M. Ghaemmaghami, and Y. S. Zhang, "Reversed-engineered human alveolar lung-on-a-chip model," *Proceedings of the National Academy of Sciences of the United States of America*, vol. 118, no. 19, pp. 1–10, 2021.
- [14] T. H. Punde, W. H. Wu, P. C. Lien, Y. L. Chang, P. H. Kuo, M. D. T. Chang, K. Y. Lee, C. D. Huang, H. P. Kuo, Y. F. Chan, P. C. Shih, and C. H. Liu, "A biologically inspired lung-on-a-chip device for the study of protein-induced lung inflammation," *Integrative Biology (United Kingdom)*, vol. 7, no. 2, pp. 162–169, 2015.
- [15] D. Huh, B. D. Matthews, A. Mammoto, M. Montoya-Zavala, H. Yuan Hsin, and D. E. Ingber, "Reconstituting organ-level lung functions on a chip," *Science*, vol. 328, no. 5986, pp. 1662–1668, 2010.
- [16] C. Chen, B. T. Mehl, S. A. Sell, and R. S. Martin, "Use of electrospinning and dynamic air focusing to create three-dimensional cell culture scaffolds in microfluidic devices," *Analyst*, vol. 141, pp. 5311–5320, 2016.
- [17] J. C. Mejías, M. R. Nelson, O. Liseth, and K. Roy, "A 96-well format microvascularized human lung-on-a-chip platform for microphysiological modeling of fibrotic diseases," *Lab on a Chip*, vol. 20, no. 19, pp. 3601–3611, 2020.
- [18] T. J. Bennet, A. Randhawa, J. Hua, and K. C. Cheung, "Airway-on-a-chip: Designs and Applications for Lung Repair and Disease," *Cells*, vol. 10, no. 1062, 2021.
- [19] M. Humayun, C. W. Chow, and E. W. Young, "Microfluidic lung airway-on-a-chip with arrayable suspended gels for studying epithelial and smooth muscle cell interactions," *Lab on a Chip*, vol. 18, no. 9, pp. 1298–1309, 2018.
- [20] A. Doryab, S. Tas, M. B. Taskin, L. Yang, A. Hilgendorff, J. Groll, D. E. Wagner, and O. Schmid, "Evolution of Bioengineered Lung Models: Recent Advances and Challenges in Tissue Mimicry for Studying the Role of Mechanical Forces in Cell Biology," *Advanced Functional Materials*, vol. 29, no. 1903114, pp. 1–20, 2019.
- [21] S. R. Polio, A. N. Kundu, C. E. Dougan, N. P. Birch, E. Aurian-blajeni, J. D. Schiffman, A. J. Crosby, and S. R. Peyton, "Cross-platform mechanical characterization of lung tissue," *PLOS ONE*, vol. 13, no. 10, pp. 1–17, 2018.
- [22] A. Stucki, G. Raggi, S. Sigrist, P. Zamprogno, N. Schneider-Daum, C.-M. Lehr, H. Huwer, J. Stucki, N. Hobi, and O. Guenat, "Lung-on-a-Chip: The interplay of primary human epithelial and endothelial cells improves the alveolar barrier function," *Toxicology Letters*, vol. 295, no. 2018, pp. S67–S68, 2018.
- [23] L. Knudsen and M. Ochs, "The micromechanics of lung alveoli: structure and function of surfactant and tissue components," *Histochemistry and Cell Biology*, vol. 150, no. 6, pp. 661–676, 2018. [Online]. Available: <http://dx.doi.org/10.1007/s00418-018-1747-9>
- [24] E. N. Marieb and K. Hoehn, *Human Anatomy & Physiology*, 10th ed. San Francisco: Pearson Education, 2015.
- [25] "Medical Illustration Copyright," 2022. [Online]. Available: <https://catalog.nucleusmedicalmedia.com/>
- [26] P. N. Nonaka, J. J. Uriarte, N. Campillo, V. R. Oliveira, D. Navajas, and R. Farré, "Lung bioengineering: Physical stimuli and stem/progenitor cell biology interplay towards biofabricating a functional organ," *Respiratory Research*, vol. 17, no. 1, pp. 1–10, 2016. [Online]. Available: <http://dx.doi.org/10.1186/s12931-016-0477-6>
- [27] X. Yang, K. Li, X. Zhang, C. Liu, B. Guo, W. Wen, and X. Gao, "Nanofiber membrane supported lung-on-a-chip microdevice for anti-cancer drug testing," *Lab on a Chip*, vol. 18, no. 3, pp. 486–495, 2018.
- [28] A. G. Koutsiaris, S. V. Tachmitzi, N. Batis, and M. G. Kotoula, "Volume flow and wall shear stress quantification in the human conjunctival capillaries and post-capillary venules in vivo," *Biorheology*, vol. 44, no. 5-6, pp. 375–386, 2007.

- [29] M. Radiom, Y. He, J. Peng-Wang, A. Baeza-Squiban, J. F. Berret, and Y. Chen, "Alveolar mimics with periodic strain and its effect on the cell layer formation," *Biotechnology and Bioengineering*, vol. 117, no. 9, pp. 2827–2841, 2020.
- [30] A. Doryab, M. B. Taskin, P. Stahlhut, A. Schröppel, D. E. Wagner, J. Groll, and O. Schmid, "A Biomimetic, Copolymeric Membrane for Cell-Stretch Experiments with Pulmonary Epithelial Cells at the Air-Liquid Interface," *Advanced Functional Materials*, vol. 31, no. 2004707, pp. 1–18, 2021.
- [31] X. Wang, B. Ding, and B. Li, "Biomimetic electrospun nanofibrous structures for tissue engineering," *Materials Today*, vol. 16, no. 6, pp. 229–241, 2013. [Online]. Available: <http://dx.doi.org/10.1016/j.mattod.2013.06.005>
- [32] E. D. Crandall and M. A. Matthay, "NHLBI Workshop Summary - Alveolar Epithelial Transport Basic Science to Clinical Medicine," *Crit. Care Med.*, vol. 162, pp. 1021–1029, 2001. [Online]. Available: <http://ajrccm.atsjournals.org/cgi/content/full/163/4/1021>
- [33] S. Ahadian, R. Civitarese, D. Bannerman, M. H. Mohammadi, R. Lu, E. Wang, L. Davenport-Huyer, B. Lai, B. Zhang, Y. Zhao, S. Mandla, A. Korolj, and M. Radisic, "Organ-On-A-Chip Platforms: A Convergence of Advanced Materials, Cells, and Microscale Technologies," *Advanced Healthcare Materials*, vol. 7, no. 2, pp. 1–53, 2018.
- [34] S. Tas, E. Rehnberg, D. A. Bölükbas, J. P. Beech, L. N. Kazado, I. Svenningsson, M. Arvidsson, A. Sandberg, K. A. Dahlgren, A. Edthofer, A. Gustafsson, H. Isaksson, J. A. Wood, J. O. Tegenfeldt, and D. E. Wagner, "3D printed lung on a chip device with a stretchable nanofibrous membrane for modeling ventilator induced lung injury," *bioRxiv*, p. 450873, 2021. [Online]. Available: <https://www.biorxiv.org/content/10.1101/2021.07.02.450873v1%0Ahttps://www.biorxiv.org/content/10.1101/2021.07.02.450873v1.abstract>
- [35] K. G. Birukov, J. R. Jacobson, A. A. Flores, S. Q. Ye, A. A. Birukova, A. D. Verin, and J. G. Garcia, "Magnitude-dependent regulation of pulmonary endothelial cell barrier function by cyclic stretch," *American Journal of Physiology - Lung Cellular and Molecular Physiology*, vol. 285, pp. 785–797, 2003.
- [36] F. S. A. Cavalcante, S. Ito, K. Brewer, H. Sakai, A. M. Alencar, M. P. Almeida, S. Andrade, A. Majumdar, E. P. Ingenito, S. A. Francisco, S. Ito, and S. Me, "Mechanical interactions between collagen and proteoglycans: implications for the stability of lung tissue," *J Appl Physiol*, vol. 98, pp. 672–679, 2005.
- [37] M. Akashi, T. Akagi, and M. Matsusaki, *Engineered Cell Manipulation for Biomedical Application*, 1st ed., V. Zucolotto, Ed. Tokyo: Springer, 2014. [Online]. Available: <https://link.springer.com/content/pdf/10.1007%2F978-4-431-55139-3.pdf>
- [38] K. L. Sellgren, E. J. Butala, B. P. Gilmour, S. H. Randell, and S. Grego, "A biomimetic multicellular model of the airways using primary human cells," *Lab on a Chip*, vol. 14, pp. 3349–3358, 2014.
- [39] R. Rimsa, A. Galvanovskis, J. Plume, F. Rumnieks, K. Grindulis, G. Paidere, S. Erentraute, G. Mozolevskis, and A. Abols, "Lung on a chip development from off-stoichiometry thiol-ene polymer," *Micromachines*, vol. 12, no. 546, pp. 1–17, 2021.
- [40] E. Sano, C. Mori, N. Matsuoka, Y. Ozaki, K. Yagi, A. Wada, K. Tashima, S. Yamasaki, K. Tanabe, K. Yano, and Y. S. Torisawa, "Tetrafluoroethylene-propylene elastomer for fabrication of microfluidic organs-on-chips resistant to drug absorption," *Micromachines*, vol. 10, no. 793, 2019.
- [41] A. O. Stucki, J. D. Stucki, S. R. Hall, M. Felder, Y. Mermoud, R. A. Schmid, T. Geiser, and O. T. Guenat, "A lung-on-a-chip array with an integrated bio-inspired respiration mechanism," *Lab on a Chip*, vol. 15, no. 5, pp. 1302–1310, 2015.
- [42] Z. Xu, E. Li, Z. Guo, R. Yu, H. Hao, Y. Xu, Z. Sun, X. Li, J. Lyu, and Q. Wang, "Design and Construction of a Multi-Organ Microfluidic Chip Mimicking the in vivo Microenvironment of Lung Cancer Metastasis," *ACS Applied Materials and Interfaces*, vol. 8, no. 39, pp. 25 840–25 847, 2016.

- [43] A. Jain, R. Barrile, A. D. van der Meer, A. Mammoto, T. Mammoto, K. De Ceunynck, O. Aisiku, M. A. Otieno, C. S. Loudon, G. A. Hamilton, R. Flaumenhaft, and D. E. Ingber, "Primary Human Lung Alveolus-on-a-chip Model of Intravascular Thrombosis for Assessment of Therapeutics," *Clinical Pharmacology and Therapeutics*, vol. 103, no. 2, pp. 332–340, 2018.
- [44] M. A. U. Khalid, Y. S. Kim, M. Ali, B. G. Lee, Y. J. Cho, and K. H. Choi, "A lung cancer-on-chip platform with integrated biosensors for physiological monitoring and toxicity assessment," *Biochemical Engineering Journal*, vol. 155, no. 107469, pp. 1–11, 2020. [Online]. Available: <https://doi.org/10.1016/j.bej.2019.107469>
- [45] J. Shrestha, M. Ghadiri, M. Shanmugavel, S. Razavi Bazaz, S. Vasilescu, L. Ding, and M. Ebrahimi Warkiani, "A rapidly prototyped lung-on-a-chip model using 3D-printed molds," *Organs-on-a-Chip*, vol. 1, no. 100001, 2019. [Online]. Available: <https://doi.org/10.1016/j.ooc.2020.100001>
- [46] N. J. Douville, P. Zamankhan, Y. C. Tung, R. Li, B. L. Vaughan, C. F. Tai, J. White, P. J. Christensen, J. B. Grotberg, and S. Takayama, "Combination of fluid and solid mechanical stresses contribute to cell death and detachment in a microfluidic alveolar model," *Lab on a Chip*, vol. 11, no. 4, pp. 609–619, 2011.
- [47] D. D. Nalayanda, C. Puleo, W. B. Fulton, L. M. Sharpe, T. H. Wang, and F. Abdullah, "An open-access microfluidic model for lung-specific functional studies at an air-liquid interface," *Biomedical Microdevices*, vol. 11, no. 5, pp. 1081–1089, 2009.
- [48] W. Hou, S. Hu, Y. Jie, and Z. Hanbin, "Cigarette smoke-induced malignant transformation via STAT3 signalling in pulmonary epithelial cells in a lung-on-a-chip model," *Bio-Design and Manufacturing*, vol. 3, no. 4, pp. 383–395, 2020. [Online]. Available: <https://doi.org/10.1007/s42242-020-00092-6>
- [49] S. Hassan, M. Heinrich, B. Cecen, J. Prakash, and Y. S. Zhang, "Biomaterials for on-chip organ systems," in *Biomaterials for Organ and Tissue Regeneration*. Elsevier Ltd., 2020, ch. 26, pp. 669–707.
- [50] O. T. Guenat and F. Berthiaume, "Incorporating mechanical strain in organs-on-a-chip: Lung and skin," *Biomicrofluidics*, vol. 12, no. 42207, pp. 1–11, 2018. [Online]. Available: <https://doi.org/10.1063/1.5024895>
- [51] F. S. Rezaei, A. Khorshidian, F. M. Beram, A. Derakhshani, J. Esmaeili, and A. Barati, "3D printed chitosan/polycaprolactone scaffold for lung tissue engineering: hope to be useful for COVID-19 studies," *RSC Advances*, vol. 11, no. 32, pp. 19 508–19 520, 2021.
- [52] B. Zhang, M. Montgomery, M. D. Chamberlain, S. Ogawa, A. Korolj, A. Pahnke, L. A. Wells, S. Massé, J. Kim, A. Momen, S. S. Nunes, A. Wheeler, K. Nanthakumar, G. Keller, M. V. Sefton, and M. Radisic, "Biodegradable scaffold with built-in vasculature for organ-on-a-chip engineering and direct surgical anastomosis," *Nat Mater.*, vol. 15, no. 6, pp. 669–678, 2016.
- [53] S. Jin, T.-M. Park, K. Cho-Hee, and K. Jin-Soo, "Three-dimensional migration of neutrophils through an electrospun nanofibrous membrane," *BioTechniques*, vol. 58, no. 6, pp. 285–292, 2015.
- [54] C. Xu, M. Zhang, W. Chen, L. Jiang, C. Chen, and J. Qin, "Assessment of Air Pollutant PM2.5 Pulmonary Exposure Using a 3D Lung-on-Chip Model," *ACS Biomaterials Science and Engineering*, vol. 6, no. 5, pp. 3081–3090, 2020.
- [55] F. Zhang and M. W. King, "Biodegradable Polymers as the Pivotal Player in the Design of Tissue Engineering Scaffolds," *Advanced Healthcare Materials*, vol. 9, no. 13, pp. 1–22, 2020.
- [56] K. Wolf, M. te Lindert, M. Krause, S. Alexander, J. te Riet, A. L. Willis, R. M. Hoffman, C. G. Figdor, S. J. Weiss, and P. Friedl, "Physical limits of cell migration: Control by ECM space and nuclear deformation and tuning by proteolysis and traction force," *Journal of Cell Biology*, vol. 201, no. 7, pp. 1069–1084, 2013.
- [57] B. Zhang, M. Montgomery, M. D. Chamberlain, S. Ogawa, A. Korolj, A. Pahnke, L. A. Wells, S. Masse, J. Kim, L. Reis, A. Momen, S. S. Nunes, A. R. Wheeler, K. Nanthakumar, G. Keller, M. V. Sefton, and M. Radisic, "Biodegradable scaffold with built-in vasculature for organ-on-a-chip engineering and direct surgical anastomosis," *Nature Materials*, vol. 15, no. 6, pp. 669–678, 2016.

- [58] L. Fusaro, C. Gualandi, D. Antonioli, M. Soccio, A. Liguori, M. Laus, N. Lotti, F. Boccafocchi, and M. L. Focarete, "Elastomeric electrospun scaffolds of a biodegradable aliphatic copolyester containing PEG-like sequences for dynamic culture of human endothelial cells," *Biomolecules*, vol. 10, no. 12, pp. 1–16, 2020.
- [59] A. M. Handorf, Y. Zhou, M. A. Halanski, and W. J. Li, "Tissue stiffness dictates development, homeostasis, and disease progression," *Organogenesis*, vol. 11, no. 1, pp. 1–15, 2015.
- [60] P. Zamprogno, G. Thoma, V. Cencen, D. Ferrari, B. Putz, J. Michler, G. E. Fantner, and O. T. Guenat, "Mechanical Properties of Soft Biological Membranes for Organ-on-a-Chip Assessed by Bulge Test and AFM," *ACS Biomaterials Science and Engineering*, 2021.
- [61] L. A. Osório, E. Silva, and R. E. Mackay, "A Review of Biomaterials and Scaffold Fabrication for Organ-on-a-Chip (OOAC) Systems," *Bioengineering*, vol. 8, no. 113, pp. 1–31, 2021.
- [62] L. E. Freed, G. Vunjak-Novakovic, R. J. Biron, D. B. Eagles, D. C. Lesnoy, S. K. Barlow, and R. Langer, "Biodegradable polymer scaffold for tissue engineering," *Nature Structural Biology*, vol. 1, no. 4, pp. 259–263, 1994.
- [63] Y. L. Qiu, X. Chen, Y. L. Hou, Y. J. Hou, S. B. Tian, Y. H. Chen, L. Yu, M. H. Nie, and X. Q. Liu, "Characterization of different biodegradable scaffolds in tissue engineering," *Molecular Medicine Reports*, vol. 49, no. 5, pp. 4043–4056, 2019.
- [64] R. Seghir and S. Arscott, "Extended PDMS stiffness range for flexible systems," *Sensors and Actuators, A: Physical*, vol. 230, pp. 33–39, 2015. [Online]. Available: <http://dx.doi.org/10.1016/j.sna.2015.04.011>
- [65] M. Wang, P. Xu, and B. Lei, "Engineering multifunctional bioactive citrate-based biomaterials for tissue engineering," *Bioactive Materials*, vol. 19, pp. 511–537, 2023. [Online]. Available: <https://doi.org/10.1016/j.bioactmat.2022.04.027>
- [66] L. Davenport Huyer, B. Zhang, A. Korolj, M. Montgomery, S. Drecun, G. Conant, Y. Zhao, L. Reis, and M. Radisic, "Highly Elastic and Moldable Polyester Biomaterial for Cardiac Tissue Engineering Applications," *ACS Biomaterials Science and Engineering*, no. 2, pp. 780–788, 2016.
- [67] R. T. Tran, P. Thevenot, D. Gyawali, J. C. Chiao, L. Tang, and J. Yang, "Synthesis and characterization of a biodegradable elastomer featuring a dual crosslinking mechanism," *Soft Matter*, vol. 6, no. 11, pp. 2449–2461, 2010.
- [68] C. M. Boutry, Y. Kaizawa, B. C. Schroeder, A. Chortos, A. Legrand, Z. Wang, J. Chang, P. Fox, and Z. Bao, "A stretchable and biodegradable strain and pressure sensor for orthopaedic application," *Nature Electronics*, vol. 1, no. 5, pp. 314–321, 2018. [Online]. Available: <http://dx.doi.org/10.1038/s41928-018-0071-7>
- [69] R. T. Tran, J. Yang, and G. A. Ameer, "Citrate-Based Biomaterials and Their Applications in Regenerative Engineering," *Annual Review of Materials Research*, vol. 45, pp. 277–310, 2015.
- [70] H. Zhang, C. Li, J. Guo, L. Zang, and J. Luo, "In situ synthesis of poly(methyl methacrylate)/SiO<sub>2</sub> hybrid nanocomposites via grafting onto strategy based on UV irradiation in the presence of iron aqueous solution," *Journal of Nanomaterials*, no. 217412, pp. 1–9, 2012.
- [71] K. Ruhland, F. Habibollahi, and R. Horny, "Quantification and elucidation of the UV-light triggered initiation kinetics of TPO and BAPO in liquid acrylate monomer," *Journal of Applied Polymer Science*, vol. 137, no. 6, pp. 1–16, 2020.
- [72] Y. T. N. Liang, "Synthesis of Crosslinkable Poly (ester amide)s for Cell Encapsulation and Delivery," Western University, Ontario, Tech. Rep., 2019. [Online]. Available: <https://ir.lib.uwo.ca/etd/6539/>
- [73] M. Zhang, C. Xu, L. Jiang, and J. Qin, "A 3D human lung-on-a-chip model for nanotoxicity testing," *Toxicology Research*, vol. 7, pp. 1048–1060, 2018. [Online]. Available: <http://dx.doi.org/10.1039/c8tx00156a>

- [74] M. Montgomery, L. Davenport Huyer, D. Bannerman, M. H. Mohammadi, G. Conant, and M. Radisic, "Method for the Fabrication of Elastomeric Polyester Scaffolds for Tissue Engineering and Minimally Invasive Delivery," *ACS Biomaterials Science and Engineering*, vol. 4, no. 11, pp. 3691–3703, 2018.
- [75] C. C. Wang, J. Y. Chen, and J. Wang, "The selection of photoinitiators for photopolymerization of biodegradable polymers and its application in digital light processing additive manufacturing," *Journal of Biomedical Materials Research*, vol. 110, no. 1, pp. 204–216, 2022.
- [76] A. Sabnis, M. Rahimi, C. Chapman, and K. T. Nguyen, "Cytocompatibility studies of an in situ photopolymerized thermoresponsive hydrogel nanoparticle system using human aortic smooth muscle cells." *Journal of biomedical materials research (Part A)*, vol. 91, no. 1, pp. 52–59, 2009.
- [77] N. L. Davison, F. Barrère-de Groot, and D. W. Grijpma, "CH:6 Degradation of Biomaterials," in *Tissue Engineering*, 2nd ed. Amsterdam: Elsevier Inc., 2014, ch. 6, pp. 177–215. [Online]. Available: <http://dx.doi.org/10.1016/B978-0-12-420145-3.00006-7>
- [78] J. C. Middleton and A. J. Tipton, "Synthetic biodegradable polymers as orthopedic devices," *Biomaterials*, vol. 21, no. 23, pp. 2335–2346, 2000.
- [79] L. Urbina, I. Algar, C. García-Astrain, N. Gabilondo, A. González, M. Corcuera, A. Eceiza, and A. Retegi, "Biodegradable composites with improved barrier properties and transparency from the impregnation of PLA to bacterial cellulose membranes," *Journal of Applied Polymer Science*, vol. 133, no. 28, pp. 1–10, 2016.
- [80] R. Rai, M. Tallawi, A. Grigore, and A. R. Boccaccini, "Synthesis, properties and biomedical applications of poly (glycerol sebacate) (PGS): A review," *Progress in Polymer Science*, vol. 37, no. 8, pp. 1051–1078, 2012. [Online]. Available: <http://dx.doi.org/10.1016/j.progpolymsci.2012.02.001>
- [81] F. Alexis, "Factors affecting the degradation and drug-release mechanism of poly(lactic acid) and poly[(lactic acid)-co-(glycolic acid)]," *Polymer International*, vol. 54, no. 1, pp. 36–46, 2005.
- [82] T. Casalini and G. Perale, "Types of bioresorbable polymers for medical applications," in *Woodhead Publishing Series in Biomaterials, Durability and Reliability of Medical Polymers*, M. Jenkins and A. Stamboulis, Eds. Woodhead Publishing, 2012, ch. 1, pp. 3–29.
- [83] I. Pomerantseva, N. Krebs, A. Hart, C. M. Neville, A. Y. Huang, and C. A. Sundback, "Degradation behavior of poly ( glycerol sebacate )," *Journal of Biomedical Materials Research Part A*, vol. 91A, no. 4, pp. 1038–1047, 2008.
- [84] B. Turner, S. Ramesh, M. Daniele, and S. Menegatti, "Resorbable elastomers for implantable medical devices : highlights and applications," *Polym Int*, vol. 71, pp. 552–561, 2022.
- [85] M. Daniele, B. Turner, J. Twiddy, M. Wilkins, and K. Kilgour, "Biodegradable Elastomeric Circuit Boards from Citric Acid-based Polyesters," *Preprint*, pp. 0–29, 2022.
- [86] Wikipedia, "Carboxylic acid," 9 2022. [Online]. Available: [https://en.wikipedia.org/wiki/Carboxylic\\_acid](https://en.wikipedia.org/wiki/Carboxylic_acid)
- [87] OECD, "Hydrolysis as a Function of pH," *OECD guideline for testing of chemicals*, no. May, 1981. [Online]. Available: <http://www.oecd.org/chemicalsafety/risk-assessment/1948201.pdf>
- [88] Wikipedia, "Bronsted-Lowry acid-base theory," 8 2022. [Online]. Available: [https://en.wikipedia.org/wiki/Bronsted-Lowry\\_acid-base\\_theory](https://en.wikipedia.org/wiki/Bronsted-Lowry_acid-base_theory)
- [89] A. N. Ford, D. W. Pack, and R. D. Braatz, "Multi-Scale Modeling of PLGA Microparticle Drug Delivery Systems," in *Computer Aided Chemical Engineering*, vol. 29, no. 2. Elsevier, 2011, pp. 1475–1479. [Online]. Available: <http://dx.doi.org/10.1016/B978-0-444-54298-4.50074-X>
- [90] M. Miyajima, A. Koshika, J. Okada, and M. Ikeda, "Effect of polymer/basic drug interactions on the two-stage diffusion-controlled release from a poly(L-lactic acid) matrix," *Journal of Controlled Release*, vol. 61, no. 3, pp. 295–304, 1999.

- [91] M. Tracy, L. Firouzabadian, and Y. Zhang, "Effects of PLGA end groups on degradation." in *the International Symposium on Controlled and Related Bioactive Materials*, vol. 22, 1995, pp. 786–787.
- [92] E. Andrzejewska, "Chapter 2 - Free Radical Photopolymerization of Multifunctional Monomers," in *Three-Dimensional Microfabrication Using Two-photon Polymerization*. Elsevier Inc., 2016, ch. 2, pp. 62–81. [Online]. Available: <https://www.sciencedirect.com/science/article/pii/B9780323353212000042>
- [93] Y. Zhao, N. Rafatian, N. T. Feric, B. J. Cox, R. Aschar-Sobbi, E. Y. Wang, P. Aggarwal, B. Zhang, G. Conant, K. Ronaldson-Bouchard, A. Pahnke, S. Protze, J. H. Lee, L. Davenport Huyer, D. Jekic, A. Wickeler, H. E. Naguib, G. M. Keller, G. Vunjak-Novakovic, U. Broeckel, P. H. Backx, and M. Radisic, "A Platform for Generation of Chamber-Specific Cardiac Tissues and Disease Modeling," *Cell*, vol. 176, pp. 913–927, 2019.
- [94] J. R. Oh, J. H. Moon, H. K. Park, J. H. Park, H. Chung, J. Jeong, W. Kim, and Y. R. Do, "Wafer-scale colloidal lithography based on self-assembly of polystyrene nanospheres and atomic layer deposition," *Journal of Materials Chemistry*, vol. 20, no. 24, pp. 5025–5029, 2010.
- [95] C. M. Boutry, L. Beker, Y. Kaizawa, C. Vassos, H. Tran, A. C. Hinckley, R. Pfattner, S. Niu, J. Li, J. Claverie, Z. Wang, J. Chang, P. M. Fox, and Z. Bao, "Biodegradable and flexible arterial-pulse sensor for the wireless monitoring of blood flow," *Nature Biomedical Engineering*, vol. 3, pp. 47–57, 2019. [Online]. Available: <http://dx.doi.org/10.1038/s41551-018-0336-5>
- [96] P. Apel, "Track etching technique in membrane technology," *Radiation Measurements*, vol. 34, pp. 559–566, 2001.
- [97] L. Ivancevic, "OoC-integrated impedance spectroscopy for blood-brain barrier integrity analysis," Delft University of Technology, Delft, Tech. Rep., 2021. [Online]. Available: <https://repository.tudelft.nl/>
- [98] M. Seo and M. A. Hillmyer, "Reticulated Nanoporous Polymers by Controlled Polymerization-Induced Microphase Separation," *Science*, vol. 336, pp. 1422–1425, 2012.
- [99] L. Li, "Nanoporous Polymers for Membrane Applications," Ph.D. dissertation, DTU Chemical Engineering (Copenhagen), 2012.
- [100] J. R. Brownson, "CH. 3- Laws of Light," in *Solar Energy Conversion Systems*, J. R. Brownson, Ed. Academic Press, 2014, pp. 41–66.
- [101] R. Suntornnond, E. Y. S. Tan, J. An, and C. K. Chua, "A highly printable and biocompatible hydrogel composite for direct printing of soft and perfusable vasculature-like structures," *Scientific Reports*, vol. 7, no. 1, pp. 1–11, 2017. [Online]. Available: <http://dx.doi.org/10.1038/s41598-017-17198-0>
- [102] Y. Didane, C. Vidlot-Ackermann, H. Brisset, J. Ackermann, P. Raynal, F. Fages, and G. H. Mehl, "Liquid crystal  $\alpha,\omega$ -hexyl-distyryl-bithiophene: Morphology and charge transport properties in organic thin film transistors," *Molecular Crystals and Liquid Crystals*, vol. 507, no. September, pp. 178–187, 2009.
- [103] L. Radulovic, "PTFE (Polytetrafluoroethylene; Teflon®)," in *Encyclopedia of Toxicology*, 2014, pp. 1133–1136.
- [104] "Photonic Professional (GT) User Manual," Eggenstein-Leopoldshafen, Germany, 7 2015. [Online]. Available: <http://www.nanoscribe.de/en/products/photonic-professional-gt/>
- [105] M. Pawlicki, H. A. Collins, R. G. Denning, and H. L. Anderson, "Two-photon absorption and the design of two-photon dyes," *Angewandte Chemie - International Edition*, vol. 48, no. 18, pp. 3244–3266, 2009.
- [106] H. Anderson, "Two-Photon Absorption and the Design of Two-Photon Dyes," *Angew. Chem. Int. Ed.*, vol. 48, pp. 3244–3266, 2009.
- [107] M. Zhang, Y. P. Zheng, and A. F. T. Mak, "Estimating the effective Young's modulus of soft tissues from indentation tests — nonlinear finite element analysis of effects of friction and large deformation," *Med. Eng. Phys.*, vol. 19, no. 6, pp. 512–517, 1997.



- [108] M. Vanlandingham, J. S. Villarrubia, W. F. Guthrie, G. Meyers, and D. C. Company, "Nanoindentation of Polymers: An Overview," *Macromolecular Symposia*, vol. 167, no. 1, pp. 15–44, 2001.
- [109] N. Antonovaite and E. Labordus, "Optics11 - Dataviewer V2 User Manual," Amsterdam, 2019.
- [110] E. Yeom, Y. J. Kang, and S. J. Lee, "Changes in velocity profile according to blood viscosity in a microchannel," *Biomicrofluidics*, vol. 8, no. 034110, pp. 1–10, 2014.
- [111] Y. A. Cimbala and J. M. Çengel, *Fluid mechanics : fundamentals and applications*, 1st ed. Boston: McGraw-Hill Higher Education, 2006.
- [112] Wikipedia, "Entrance length (fluid dynamics)," 3 2022. [Online]. Available: [https://en.wikipedia.org/wiki/Entrance\\_length\\_\(fluid\\_dynamics\)](https://en.wikipedia.org/wiki/Entrance_length_(fluid_dynamics))
- [113] K. Domansky, D. C. Leslie, J. McKinney, J. P. Fraser, J. D. Sliz, T. Hamkins-Indik, G. A. Hamilton, A. Bahinski, and D. E. Ingber, "Clear castable polyurethane elastomer for fabrication of microfluidic devices," *Lab on a Chip*, vol. 13, no. 19, pp. 3956–3964, 2013.
- [114] V. Ramakrishna, "Fabrication of Novel Microfluidic Devices for Investigating Ultrafast Structural Dynamics," Ph.D. dissertation, University of Hamburg, 2019.
- [115] C. M. Boutry, I. Gerber-Hörler, and C. Hierold, "Electrically conducting biodegradable polymer composites (polylactide-polypyrrole and polycaprolactone-polypyrrole) for passive resonant circuits," *Polymer Engineering and Science*, vol. 53, no. 6, pp. 1196–1208, 6 2013.
- [116] A. C. Hänzi, I. Gerber, M. Schinhammer, J. F. Löffler, and P. J. Uggowitzer, "On the in vitro and in vivo degradation performance and biological response of new biodegradable Mg-Y-Zn alloys," *Acta Biomaterialia*, vol. 6, no. 5, pp. 1824–1833, 2010.
- [117] Formlabs, "Materials for rapid prototyping -Material data sheet," pp. 4–6, 2017.
- [118] ThermoFisher, "DAPI (4,6-diamidino-2-phenylindole)," 2022. [Online]. Available: <https://www.thermofisher.com/nl/en/home/life-science/cell-analysis/fluorophores/dapi-stain.html>
- [119] Merck, "Fluorescein-5-isothiocyanate (FITC)," Darmstadt, 9 2017. [Online]. Available: <https://www.sigmaaldrich.com/deepweb/assets/sigmaaldrich/product/documents/467/490/124546e.pdf>
- [120] ThermoFisher, "Texas Red (and Texas Red-X) Dye," 2022. [Online]. Available: <https://www.thermofisher.com/nl/en/home/life-science/cell-analysis/fluorophores/texas-red.html>
- [121] —, "Cy5 dye," 2022. [Online]. Available: <https://www.thermofisher.com/nl/en/home/life-science/cell-analysis/fluorophores/cy5-dye.html>
- [122] I. Goldstein and J. Burley, "Wood formation and properties | Chemical Properties of Wood," in *Encyclopedia of Forest Sciences*. Elsevier, 2004, pp. 1835–1839.
- [123] R. Sánchez-Clemente, M. I. Igeño, A. G. Población, M. I. Guijo, F. Merchán, and R. Blasco, "Study of pH Changes in Media during Bacterial Growth of Several Environmental Strains," in *MDPI*, 2018, p. 1297.
- [124] R. Yang, "Polymer degradation and stability," in *Polymer Science and Nanotechnology: Fundamentals and Applications*, 2020, ch. 7, pp. 125–148.
- [125] International Organization for Standardization, "ISO 10993-5:2009(E)," 2009.
- [126] C. M. Agrawal, J. S. McKinney, D. Lanctot, and K. A. Athanasiou, "Effects of fluid flow on the in vitro degradation kinetics of biodegradable scaffolds for tissue engineering," *Biomaterials*, vol. 21, no. 23, pp. 2443–2452, 2000.

# Design of a membrane for a lung-on-a-chip device

## Literature Review

S.A.M. den Boer



# Design of a membrane for a lung-on-a-chip device

Literature Review

by

S.A.M. den Boer

in partial fulfillment of the requirements of the degree of Master of Science  
at the Delft University of Technology,  
to be defended publicly on Friday February 4, 2022 at 11:30 AM.

Student number:	4469178
Project duration:	September 15, 2021 – February 4, 2022
Thesis committee:	Prof. dr. U. Staufer, TU Delft, First supervisor
	Dr. M. Mastrangeli, TU Delft, Second supervisor
	Dr. R. Rottier, Erasmus Medical Center, External supervisor

An electronic version of this thesis is available at <http://repository.tudelft.nl/>.



# Acknowledgements

I would like to thank my supervisors, Prof. Urs Staufer, Dr. Massimo Mastrangeli, and Dr. Robbert Rottier, for their support and weekly meetings during the process of undertaking this literature review.

*S.A.M. den Boer  
Delft, January 2022*



# Abstract

This literature review discusses membrane design for an alveoli-on-a-chip (AOC) device. An AOC device is a device that allows for precise mimicking of the lungs' dynamic alveolar micro-environment by incorporating microfluidics, living cells, and dynamical cues. The subject of organ-on-a-chip (OOC) devices has been broadly studied in the past decades since they are promising alternatives to animal and traditional in-vitro models. However, there are still many future improvements to be made in AOCs and their membrane design. This review undertakes an in-depth review of the state-of-the-art AOC devices designed to date, specifically by considering their membrane dimensions and whether they contain a cyclic strain, air-liquid interface (ALI), and media flow. Furthermore, it gives a clear overview of the requirements that an AOC membrane should exhibit.

The use of poly(dimethylsiloxane) (PDMS) as an OOC material is undesired due to its high ad- and absorption of small molecules. To find alternative materials and the limits in the design of AOC membranes, various materials and manufacturing methods were thoroughly studied. Also membranes that have changing characteristics throughout a cell culture were discussed.

In conclusion, the need for a novel membrane for AOC devices became clear in this review. An adequate membrane should sustain a cyclic in-plane stretch of at least 20%, an ALI along with a physiological fluid flow, and it should have a thickness of 10  $\mu\text{m}$  or less. Furthermore, it should have an adequate pore size, be made of a material that has better ad- and absorption properties than the conventionally used PDMS, and it should be possible to culture cells up to two to four weeks. Moreover, more research on the effect of pore size and porosity throughout the cell culture needs to be undertaken.

Based on that, the research question for the next part of this thesis project is: 'What is the effect of a dynamic membrane pore size on the formation of a confluent alveolar epithelial and endothelial monolayer throughout the cell culture duration, under an ALI, physiological fluid flow and cyclic stretch?'





# Contents

1	Introduction	1
1.1	LOC requirements	2
1.2	Review structure	3
2	Lung-on-a-chip devices: background and state-of-the-art	5
2.1	Lung physiology	5
2.2	Cell types used for in-vitro modelling	8
2.3	Current in-vitro lung models	9
2.4	State-of-the-art LOC devices	10
2.4.1	Overview of LOC characteristics	10
2.4.2	Device layout	11
2.4.3	Representative LOC devices	14
2.5	Conclusions and remarks on current LOC devices	22
3	Materials and manufacturing methods for LOC devices	25
3.1	Materials used for LOC devices	25
3.1.1	The downside of PDMS membranes	25
3.1.2	Alternative materials	27
3.1.3	Biodegradability of materials	30
3.2	Manufacturing methods for LOC devices	31
3.2.1	Soft-lithography based fabrication techniques	31
3.2.2	3D (bio)printing	31
3.2.3	Electrospinning	33
3.2.4	Alginate bead moulding	36
3.2.5	Creating pores in LOC membranes	37
3.3	Membrane integration methods	38
4	Membrane requirements	41
5	Conclusion	47
5.1	Overall aim and research question	48
5.2	Design plan	49
A	Appendix A	51
	Bibliography	59



# Introduction

In-vitro models are fundamental in the study of cell behaviour, the physiological function of organs and their response to drugs and toxins [46][27][40]. These physiological functions are often hard to determine since there is a shortage of accurate and reliable in-vitro models [27]. Furthermore, animal models used in pre-clinical drug development regularly have inadequate predictive power [29][64]. One of the main reasons is because animal tissues vary greatly from human tissues concerning their anatomy, immune system, and inflammatory response [5]. Moreover, 90% of the preclinical studies in animals do not accurately predict the outcome of human clinical trials [26]. Furthermore, the success rate in the clinical phase generally is only about 10% to 20% [40]. This low success rate leads to the disregard of unsuccessful drugs in a late stage of their development, as promising results in these models do not ensure equally successful results in humans [29][64]. When considering the immense expense of drug development and the long development time required, the pressing need for means to quickly and reliably assess drug efficacy and safety at an early stage becomes apparent [29][52].

Traditionally, in-vitro models are organized mostly as 2D cell cultures, on, for example, Petri dishes or well plates [46][38]. These cell cultures lack dynamical cues and fail to mimic the complex nature of tissues, as well as the structural, mechanical, and functional properties that this complex nature entails [64][38]. Furthermore, 2D in-vitro cultures are generally monocultures [64]. A disadvantage of using a monoculture is that it affects, among others, cell morphology, cell division, cell secretion and physiological functions [64]. Apart from 2D cell cultures, also 3D cell cultures have been created with cells that are grown in an extracellular matrix (ECM) gel in order to include more tissue-specific functions [29]. However, these 3D models often fail to accurately capture the functional and structural complexity that in-vivo tissues exhibit [27][29]. The architecture and spatial design of 3D models have been limited, and dynamic mechanical and biochemical cues, which are fundamental in organ function and development, are generally not incorporated either [28].

Organ-on-a-chip (OOC) models pose as promising alternatives for animal models and traditional in-vitro models [78][29][8][14][38][64]. OOC models are micro-engineered microfluidic devices combined with cultured living cells, which create a precisely controlled and dynamic microphysiological environment [64]. These models allow for closer mimicking of the physiological and mechanical microenvironment within organs, thus facilitating a more accurate prediction of cell behaviour. For example, they allow for mimicking the circulation in the body by allowing continuous perfusion of the cells [38]. So far, various barrier tissue interfaces have been recapitulated by microfluidic models, e.g. the blood-brain barrier, the gut, and the lungs' blood-air barrier [78]. To date, OOC models, and more specifically lung-on-a-chip (LOC) models, that precisely and effectively reproduce complete drug responses and disease mechanisms, have not been developed [29].

Therefore, this thesis project aims to design a novel LOC model, focusing on the membrane, and in this literature review, the current advances in LOC models are reviewed. The membrane for this LOC device recapitulates the pulmonary alveolar-capillary barrier. This barrier is the blood-air barrier in the lungs' gas exchanging region. LOC models are currently being used for lung disease modelling, cytotoxicity studies, cancer diagnosis and drug screening assays [69]. Various respiratory diseases that are studied using LOC devices include:

lung cancer, pulmonary oedema, pulmonary thrombosis, asthma, chronic obstructive pulmonary disease (COPD), cystic and pulmonary fibrosis, and pulmonary hypertension [64][44][6]. LOC models are also used to study the effect of air pollution [40], and emergent respiratory viruses, such as SARS-CoV-2, which can have a significant impact on society [26][50]. Although, at this point, the main focus of LOC models still seems to be the study of the lung physiology [40]. A lot of the mechanisms present in the lung are still not well understood, and LOC devices can play a prominent role in helping to discover these mechanisms [40].

### 1.1. LOC requirements

In-vitro models need to mimic the in-vivo environment and its extracellular matrix (ECM) as closely as possible. The effect of breathing, by which a periodic strain is applied to the cells, is deemed to be vital in regulating lung functions [67]. Such a strain can be mimicked by incorporating a flexible polymeric membrane in the LOC and cyclically stretching it [78]. However, so far, this effect has not been intensively modelled [67]. Three-dimensional ECMs have been used to create tissue-specific phenotypes, but their architecture and spatial design have been limited [27]. Dynamic mechanical and biochemical cues fundamental in organ function and development are minimally incorporated as well [27].

The blood-air barrier contains more than 40 different cell types [67][36]. Facing the capillary lumen, it consists of endothelial cells, and facing the alveolar lumen, it consists of epithelial cells with a surfactant layer [36]. Between these two cell layers is the interstitium. This space is made up of various cells, particularly fibroblasts, and an ECM containing elastic fibres, collagen fibrils, and laminin, which provides mechanical integrity [51]. Myofibroblasts span the inter-alveolar septum through pores connecting both sides of this septum, which contributes to the mechanical stability [36]. Lung tissue is subjected to enormous expansions, undergoing strains of 10% to 20% [51].

Knudsen et al. state that various structural requirements must be met to create efficient oxygen and carbon dioxide diffusion through the barrier. First, a large surface area must be present. Second, the diffusion barrier must be thin. In-vivo, the alveolar-capillary barrier is about 1  $\mu\text{m}$  thick [76][36]. Third, the membrane must be stable, which is maintained by the surfactant layer and the connective tissue within the lung. Last, in order to recreate breathing movements, the barrier must be flexible and elastic [36].

To date, most membranes used in LOC models are made of poly(dimethylsiloxane) (PDMS) [27][78]. PDMS is elastic, optically transparent and biocompatible [78]. However, it has high adsorption and absorption of small hydrophobic molecules, which limits its application in drug evaluation studies [78] [14]. Moreover, its intrinsic stiffness and molecular composition are distinctly different from alveolar lung tissue [78]. It also has a high water vapour permeability, which causes osmolarity shifts and thus influences homeostasis [14]. Therefore, other materials than PDMS will be analysed to create a new membrane design. Possible alternative material groups include, for example, thermoplastic polymers, hydrogels and thermoplastic elastomers.

Based on these findings, the following three aspects are considered most important, and these will therefore be the focus of the literature review: (1) a breathing motion by using a stretchable membrane, (2) recapitulation of the ECM structure, and (3) inclusion of an air and media flow.

Several additional requirements need to be met. A simple schematic of an intersection of the membrane environment is shown in Figure 1.1. As stated previously, a cyclic stretch needs to be applied. This stretch should be applied with a frequency of 0.2 Hz, and should exert a strain on the membrane (orange) of 10% to 20%. On the side of the capillary lumen, a continuous media flow that simulates the blood flow should be present. Whereas, on the side of the alveolar lumen, a constant gas flow, simulating airflow, should be present. Both flows exercise a shear stress on the cells seeded on the membrane. The mean wall shear stress on endothelial cells in microvessels in-vivo was found to be 1.54  $\text{N/m}^2$  by Koutsiaris et al. [39].

The material included should be sterilizable and biocompatible to enhance cell viability. Besides that, the membrane material used should be optically transparent to facilitate high-resolution microscopic analyses for reliable cell characterization and assessment [14][8]. The device should also allow for cell culture experiments having a duration of minimally two weeks, up to four weeks. Lastly, it should also be possible to

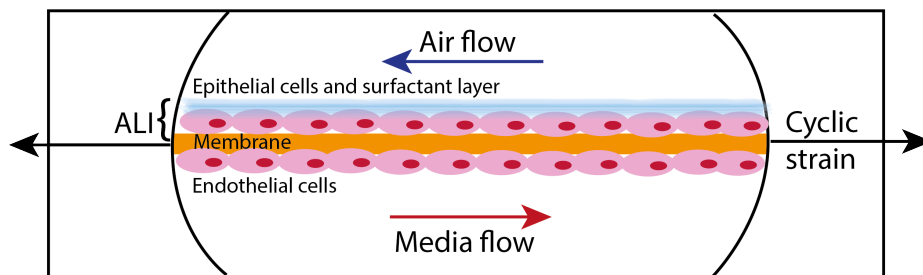


Figure 1.1: Schematic side view of a lung-on-a-chip device.

recover the used membrane to allow for additional testing of the cultured cells. A LOC device designed prior by the Precision and Microsystems Engineering (PME) Department at the Delft University of Technology will be used as a basis for testing the membrane [46]. In conclusion, all these requirements will be considered in this literature review.

## 1.2. Review structure

This literature review first elaborates on lung physiology and the relevant parameters that need to be considered in the design of a lung-on-a-chip. Secondly, the various cell types used in cell cultures are discussed. Subsequently, the various in-vitro models to date will be analyzed, and the state-of-the-art for LOC devices is discussed. This last section provides information about the various characteristics of a LOC model, its general layout, and an overview of the various devices found in the literature. Special attention will be given to the LOC membranes since this literature review aims at designing a novel membrane for the LOC device designed prior by Nissar in the PME Department [46].

Continuing, in the third chapter, a more detailed overview is given on the materials and manufacturing methods that are used to create and integrate LOC membranes. Next, based on the previously discussed literature, the membrane requirements for an alveoli-on-a-chip are detailed. Finally, a conclusion on this literature review is given. Also, a detailed research question and design plan for future research within this thesis project are presented.



# 2

## Lung-on-a-chip devices: background and state-of-the-art

This chapter first focuses on the lung physiology, discussing the characteristics of the alveoli. Secondly, it covers the various cell types used for in-vitro modelling. Subsequently, the various in-vitro models to date are discussed. After which, state-of-the-art LOC devices found in the literature are studied. This section also includes the characteristics and the layout that these devices exhibit. Also, the previous work done by the Department of Precision and Microsystems Engineering at the Delft University of Technology is briefly discussed. Last, a conclusion is given.

### 2.1. Lung physiology

The human respiratory system allows for gas exchange between blood circulating in the body and the external environment [30]. The lungs are the primary organ within this respiratory system, and it allows the exchange of oxygen and carbon dioxide [40]. This system exists of the conducting zone, and the respiratory zone [30]. The conducting zone is merely the region where air is transported to and from the gas exchanging region [30]. Whereas the respiratory zone is the region where the gas exchange actually takes place, and it starts where the terminal bronchioles turn in the respiratory bronchioles (Figure 2.1) [42]. This region is where the acini are located, which consist of bronchioles, alveolar ducts, and alveoli [30]. There are over 30 000 acini present in the adult human lung, and each acinus holds roughly 10 000 alveoli [69]. Overall, this accounts for about 300 million alveoli, which make up most of the human lung volume [42]. Around every alveolus, a dense network of pulmonary capillaries is present.

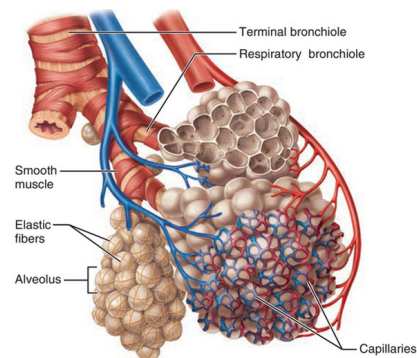


Figure 2.1: View of capillary-alveolar relationships [42].

The gas exchange itself happens via diffusion through the respiratory membrane, also called the alveolar-capillary barrier (ACB) (Figure 2.2) [42]. This thin membrane spans between the alveolar lumen and the capillary lumen. This membrane is so thin that a single sheet of tissue paper is about 15 times thicker [42]. It is comprised of epithelial and endothelial cells, which are located on different sides of a fused basement membrane. Between the alveoli, there is also a membrane, the inter-alveolar membrane, containing pores of Kohn with a diameter of about 10  $\mu\text{m}$  to 15  $\mu\text{m}$  [40]. These alveolar pores equalize the air pressure throughout the alveoli and provide secondary air routes to alveoli otherwise unreachable due to disease [42].

The alveoli are roughly ordered in a honeycomb structure with polyhedral-shaped cavities [69]. This causes the general morphology of the alveolar blasts to be hexagonal [54]. The diameter of the individual alveoli ranges from 200 to 300  $\mu\text{m}$  [54][40].



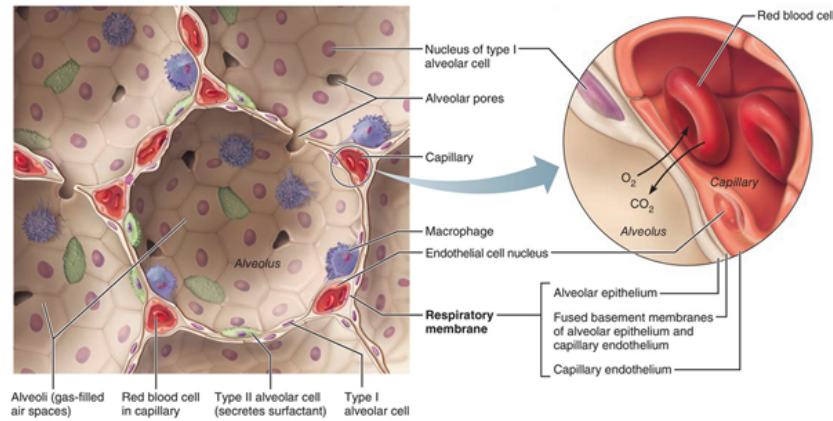


Figure 2.2: Detailed anatomy of the alveolar membranes [42].

On the side of the capillary lumen, endothelial cells are present, creating a monolayer called the endothelium [40]. Whereas, on the side of the alveolar lumen, the alveolar-capillary barrier consists of a single layer of epithelial cells covered by a thin layer of liquid surfactant. The surfactant forms the barrier between the air and the tissue, also called the air-liquid interface (ALI) [15][30]. The epithelial cell layer secretes the surfactant, which consists of alveolar lining fluid [15] [40]. This layer of about  $0.1\text{--}0.2\ \mu\text{m}$  thick protects the epithelial cells from being exposed directly to the air and plays a significant role in the immune defence of the alveoli [40][69]. The surfactant layer also decreases the air-liquid surface tension, which promotes molecule diffusion across the membrane [54]. Upon film compression, which happens during exhalation, the surface tension is almost equal to zero [69]. Along the alveolar lumen, alveolar macrophages transit around freely, which continuously respond to infectious microorganisms that are breathed in [42].

Both the capillary endothelial and alveolar epithelial cell layers have a basement membrane, which poses as a structural support and bonding site for the adjacent cells [16]. Each basement membrane has a thickness of about  $50\ \text{nm}$ . They are fused together to create the alveolar interstitium [15]. This barrier forms the connective tissue between the alveoli and the blood vessel. The thickness of the interstitium itself ranges from  $0.2\ \mu\text{m}$  to  $0.5\ \mu\text{m}$  [40]. The complete alveolar-capillary barrier, including the cell monolayers, has a mean thickness of  $1.1\ \mu\text{m}$  [76][40][15]. But at the gas exchange location, where the membrane is thinnest in order to allow for efficient gas, solutes and protein diffusion, it has a thickness of  $0.62\ \mu\text{m}$  [54][15].

The ECM, of which the interstitium consists, provides the lung with its most vital functionality [15]. The ECM contains roughly 60 different cell types [15], among which elastin and collagen IV fibrils are abundantly present. These fibers have a diameter ranging from  $10$  to  $100\ \text{nm}$  [71][54][40]. Cells present in the lungs include, for example, epithelial cells, smooth muscle cells, endothelial cells, and a specific set of fibroblasts [30][15]. The fibroblasts produce elastin that composes a third of the total lung dry mass [76][40]. It creates a highly elastic intricate woven network of nanofibers, which supports cells [71]. Furthermore, the basement membrane is porous, and it contains two types of pores [15]. The specific pore sizes are still undetermined, but it is suggested that one pore type has a size smaller than  $2.5\ \text{nm}$  and a less common second pore type has a diameter of less than  $400\ \text{nm}$  [15].

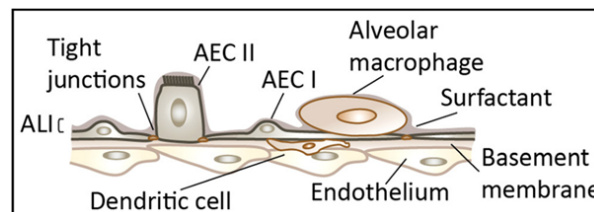


Figure 2.3: Schematic of the alveolar-capillary barrier, showing the cellular composition and the ALI [69].

The epithelial layer consists mainly of squamous type I (AET I) and to a lesser degree cuboidal type II (AET II) alveolar cells (Figure 2.3) [54][40][42]. AET I cells make up about 95% of the alveolar wall. They maintain homeostasis and contribute to particle transport, and gas exchange [54][40]. They are also connected through the basement membrane's ECM to the capillary endothelial cells [54]. AET II cells secrete the surfactant layer, stimulated by cell stretching [54][40]. This surfactant is constantly produced and subsequently broken down and reabsorbed by macrophages [40]. The half-life time of surfactant is 5 to 10 hours [40]. AET II cells also play a prominent role in the immune system by producing antimicrobial proteins [42]. The size of an epithelial cell ranges between 10  $\mu\text{m}$  for AET II cells and 50- 100  $\mu\text{m}$  for AET I cells [12].

The AET I cells form a continuous layer with tight junctions, showing little leakage of particles [40]. Tight junctions are cell-cell adhesions, which tightly connect cells, allowing for paracellular and transcellular transport. Besides that, these junctions play a significant role in controlling intracellular signals, and cellular polarity [16]. The AET I cells are only replaced by differentiated AET II cells, which constantly renew [40].

The endothelial cell layer is a semi-selective barrier, managing the transport of particles and migration of white blood cells between the capillary lumen and the neighbouring alveolar tissue [40]. It has been shown by transmission electron microscopy that alveolar fibroblasts are connected to AET I and AET II cells through basement membrane apertures. Furthermore, the same may be possible with endothelial cells, and thus the endothelium may also be directly connected to the epithelium via fibroblasts [16].

The dynamical aspects will be covered now that the alveoli's anatomical structure and dimensions have been discussed. Firstly, the lung displays unique mechanical forces: every respiratory cycle, a periodic mechanical force is exerted on the alveolar membrane. This dynamical force makes the lung a challenging tissue to mimic in-vivo [1]. Furthermore, Knudsen et al. state that various structural requirements must be met to create efficient oxygen and carbon dioxide diffusion through the septum. First, a large surface area must be present. Second, the diffusion barrier must be thin. Third, the membrane must be stable, which is maintained by the surfactant layer that minimizes the surface tension at the ALI, and the connective tissue within the lung [36][40]. Fourth, in order to recreate breathing movements, the membrane must be flexible and elastic [36].

Physiological stretching of the alveoli is vital in tissue and cell development and in maintaining homeostasis [68]. The alveoli are inflated and stretched during inspiration and deflated during expiration. At rest, both phases are around 1.5 to 2 seconds, with a 1-second pause in between [40]. This results in a regular breathing frequency of around 0.20 Hz [15]. The alveolar basement membrane generally undergoes a linear strain of 4% during this rest condition [15]. During exercise and deep breathing, the respiratory frequency can rise 3 to 5 fold [15][40]. The corresponding linear strain roughly goes up to 12%. This strain range is the physiological strain range [54]. Birukov et al. [7] state, based on clinical observations and models, that a linear mechanical strain greater than 15% may be marked as pathophysiological. In comparison, Tas et al. [68] state that overdistension of the lung happens when the strain goes over 20%. Doryab et al. [15] also state that in a pathological condition, strains up to 20% have been observed.

Table 2.1: Characteristics of the alveoli.

Feature	Value
Thickness basement membrane	~50 nm
Total ACB thickness	~0.6 $\mu\text{m}$
Pore size	< 2.5 nm and < 400 nm
Breathing frequency	0.2 Hz
Physiological linear strain range	4% -12%
Elasticity	1-2 kPa

Regarding tissue stiffness, Pasman et al. [50] state that lung tissue has a Young's modulus of 400 Pa. According to Doryab et al. [15], the alveolar tissue has a Young's modulus of around 1-2 kPa. Furthermore, the Young's modulus of an alveolar wall is roughly 5 kPa, for a wall with an average thickness of 8  $\mu\text{m}$ . However, this is a gross oversimplification by Cavalcante et al. due to not taking into account the wall structure [10]. Generally, the stiffness of the alveolar-capillary barrier is assumed to be in the range of less than 10 kPa.

To date, it has not been possible to exactly recapitulate these variables and the alveolar barrier structure within a LOC membrane simultaneously. Moreover, the obtainable stretch, membrane porosity and stability depend on, for example, the membrane thickness, structural design and the type of materials chosen for the membrane. As such, it might not be possible or necessary to fully mimic every variable exactly, as long as the LOC membrane simulate the native environment adequately enough. An overview of characteristics that the alveoli exhibit is shown in Table 2.1.

## 2.2. Cell types used for in-vitro modelling

For in-vitro cell cultures, various cell types can be chosen. The leading choice is between primary cells and immortalized cell lines, but also induced pluripotent stem cells (iPSC) have recently been tried to culture [40]. The following section is an overview of these cell types. Table 2.2 gives a summary of the advantages and disadvantages of each cell type that is discussed in this section.

**Human primary cells:** Primary cells are directly derived from donor tissue, using specific enzymes [40][46]. Ideally, primary cells are used for cell cultures since they more closely resemble the in-vivo cell properties [50]. However, this is often challenging since primary cells are more costly, more challenging to culture and have a limited life-span [40][46][50].

**Primary epithelial cell types include:** Primary human pulmonary alveolar epithelial cells (pH-PAEC), primary human bronchial epithelial cells (pHBEC), primary human airway epithelial cells (hAECs) [5][26][2], and tracheo-bronchial epithelial cells (AE) [61][46]. hAECs have the best characteristics that simulate in-vivo behaviour [40].

**Primary endothelial cell types include:** primary human umbilical vein endothelial cells (HUVEC) [76][56][58][66][75], human pulmonary microvascular endothelial cells (HPMEC) and primary human lung microvascular endothelial cells (HMVEC-L) [33][67][15][40][46][50]. Besides the frequently applied HPMEC lines, also HUVECs are a non cancerous, and a very commonly used cell line [40].

Table 2.2: Overview of the advantages and disadvantages of the various cell types.

Cell type	Advantages	Disadvantages
<b>Human primary cells</b>	Close resemblance to in-vivo cell properties	Costly Challenging to culture Limited life-span
<b>Immortalized cell lines</b>	Increased life-span Easier to culture	Less resemblance to in-vivo properties
<b>iPSCs</b>	Differentiable into various tissues Increased biological accuracy	No clear differentiation protocol

**Immortalized cell lines:** Since primary cells prove more challenging to use in cell cultures, for the reasons mentioned previously, often immortalized cell lines are used [50]. The lifespan of cells is increased in immortalized cell lines, which are derived from primary cell lines. In order to make them immortalized, a mutation can be induced, by which they keep dividing [40]. Thus, they keep proliferating, and they subsequently can be grown in-vitro long-term [40]. However, due to the changes they undergo, they often do not exhibit the same phenotypes as native cells [40].

**Immortalized epithelial cell types include:** Lung cancer cells (NCI-H1437) [35], pulmonary alveolar epithelial cells (NCI-H441) [15][29], human airway epithelial cells line (Calu-3) [63][30], adenocarcinomic human alveolar basal epithelial cells (A549) [76][56][75][17],[45][54], human bronchial epithelium cells (BEAS-2B) [52][25][46]. A commonly used and thoroughly characterized epithelial cell line is the A549 cell line, although these have been found to form weak junctions. [40]. Since the A549 cell line barely exhibits barrier function, they are less suitable for lung barrier modelling [50]. The NCI-H441 cell line particularly allows for a tight epithelium layer and the generation of surfactant [40]. Also, Calu-3 cell lines have been extensively used to model lung barriers since they have proper barrier function, have good availability and are relatively easy to culture [50].

**Immortalized endothelial cell types include:** Lung cancer cells (NCI-H1237) [46].

**Induced pluripotent stem cell lines:** Induced pluripotent stem cell (iPSC) lines are donor cells reprogrammed into stem cells [38]. These stem cells can subsequently be differentiated into any kind of tissue [40][46]. iPSCs have the ability to replace primary or immortalized cell lines, and they can increase the biological accuracy by permitting experiments on cells from multiple sources [40]. iPSCs have already been used in lung organoids [38], kidney-on-a-chip [23] and in mimicking the blood-brain barrier [64]. However, the differentiation protocols for lung tissue are not adequate yet, and they need further research [40][64].

**Other cell types:** Other cell types have also been included in various research on the alveolar-capillary barrier. These include, but are not limited to, fibroblasts (primary human lung fibroblasts), dendritic cells, human bronchial smooth muscle cells (hBSMCs), or pulmonary macrophages [40][46].

Pasman et al. [50] demonstrated that when compared to monocultures, implementing a coculture with both endothelial and epithelial cells exhibited various benefits. This includes, for example, improved barrier function [50]. Nevertheless, many studies still apply monocultures. For each cell culture study, an adequate cell type must be chosen by taking the aforementioned advantages and disadvantages into account.

## 2.3. Current in-vitro lung models

Cell cultures are typically two-dimensional. For example, they are cultured on plastic or glass culture dishes or well plates [38][76]. 2D cell cultures have been a broadly used method due to their low cost and their ability to provide a means for standardized and consistent studies [38]. However, they generally have various drawbacks when compared to animal models: a simple cell culture does not contain the complex functionality, and physiological/pathological conditions found in-vivo [64][76]. Multiple cell types are present in-vivo, and they continuously give and receive signals and cues from each other [38]. Typically a single cell type is studied in these cell cultures, failing to capture the interaction between various cell types with different phenotypes [38][64].

Transwell inserts are a popular choice and have been used to recreate an ALI with a coculture and a permeable membrane, often between smooth muscle cells and epithelial cells [30][40][69]. However, generally rigid, bioinert membrane materials such as polyethylene terephthalate (PET) are used. These have high stiffness and do not mimic the ECM, both chemically and structurally [30]. Furthermore, these are usually 10  $\mu\text{m}$  thick, which is much thicker than the membrane found in-vivo (of which the fused basement membrane is about 0.2  $\mu\text{m}$ ) [40]. Most importantly, these 2D cell cultures fail to provide dynamical and mechanical cues, which include strain, compression and tension, shear stresses, and the various tissue-specific dimensions and geometrical structures [64]. These cues affect cell behaviour by influencing cell differentiation, proliferation, contractility motility, and organ development [64]. The dynamic shear stress-dependent response also influences the progression of several diseases such as COPD and asthma, and it should be included if diseases such as these are studied [5].

The limitations in two-dimensional cell cultures (and in animal models) caused a shift in research to more extended three-dimensional models, such as organoids [64][76]. Organoids are multicellular 3D cultures containing clusters of cells, set up using stem cells or tumour cells [64]. 3D models generally use biocompatible polymers or natural materials as a scaffold for three-dimensional growth of tissue [76]. More complex 3D cell cultures can provide longer incubation times and an ECM or scaffolding in which multiple cell types can grow, allowing for a more biomimetic environment [56][15]. Also, the tissue-specific structure and shape, and cell-cell or cell-matrix interactions, which influence physiological functions, can be more closely mimicked [76][40]. Therefore, these are proving to be better models for cell migration, differentiation, growth, and general cell survival [40]. Multicell cocultures with up to 5 different cell types have been achieved [15]. Nonetheless, these models, being static cultures, generally fail to provide an air-liquid interface (ALI), and they omit the dynamics to mimic the breathing mechanisms [56].

Current developments in microfabrication techniques have caused an advancement in the possibilities of cell culture constructs. These developments have allowed for the incorporation of various biomechanical characteristics into the in-vivo models, such as its 3D microarchitecture, dynamical cues, or chemical properties [40]. For example, mechanical stimuli, such as the breathing movement, influence not only cell development

and tissue regeneration, but they also influence disease onset, and advancement [15]. Besides that, adding microfluidics to the design, as in organ-on-a-chip (OOC) devices, allows for continuous perfusion of cells. Adding microfluidics not only allows for more extended study durations by continuously providing nutrients, but it also allows for the incorporation of fluid shear effects and the effects of physical, chemical and electrical stimuli [38]. Thus, OOCs allow for precise mimicking of the dynamic micro-environment by incorporating microfluidics, living cells, and dynamical cues. Thereby better replicating the tissue-tissue interfaces, the microarchitectures and environments than traditional cell culture systems [64].

## 2.4. State-of-the-art LOC devices

The first OOC device mimicking the alveolar-capillary barrier was the device designed by Huh et al. in 2010 [28]. They defined OOCs as "microfluidic cell cultures with continuously perfused chambers inhabited by living cells arranged to simulate tissue- and organ-level physiology, created with microchip manufacturing" [28][11]. OOCs provide an accurate in-vitro model of the in-vivo environment while allowing for advantages in laboratory use, such as live imaging and in-vitro analyses of cell activities at a tissue-scale [40]. Since Huh et al. [28], various alterations and designs have been proposed to recreate the alveoli-on-a-chip. Although, not all of them contain both an ALI and a breathing motion.

A lung-on-a-chip (LOC) indicates any organ-on-a-chip that recapitulates a part of the lung. This review is conducted to study ways of recapitulating the alveolar-capillary barrier. Therefore, mostly alveoli-on-a-chip (AOC) devices are reviewed. Nevertheless, some LOC devices that cover other parts of the lung or capillaries are also included since they still provide insight into the manufacturing techniques and materials, breathing movement, and membrane dimension. Moreover, special attention is given to AOC membranes, since in this thesis, a novel and adequate membrane is sought for the AOC device prior designed in the PME Department by Nissar [46].

In the following subsections, an overview is given on the various LOC devices found in the literature. First, an overview of specific characteristics generally present in LOC devices is given. Next, an overview of the various basic device layouts that researchers have proposed to date is given. Last, a more specific and detailed overview of the LOCs present in the literature is provided. Furthermore, the prior work by the PME Department will also be discussed. Finally, a conclusion of the evaluation of the LOC devices is given.

### 2.4.1. Overview of LOC characteristics

In order to mimic the alveolar-capillary barrier, various characteristics are desired to be present in LOC devices (Figure 1.1). Firstly, an air-liquid interface (ALI) and a gas and media flow that simulates the air and blood flow, respectively, must be present. This ALI and media flow is essential to ensure that the in-vivo microenvironment of endothelial and epithelial cells can be simulated [40][69][64]. Secondly, the breathing movement is essential since strain has a significant effect on cell behaviour [28][15][1]. Thirdly, to closely mimic the alveolar-capillary barrier, the thickness of the membrane is essential. The native ACB is a very thin membrane, and the in-vitro membrane must therefore also be adequately thin [15]. Therefore, this review will study the membrane thickness and the driver for this designed thickness. Furthermore, a biodegradable membrane changes the membrane properties over time. This biodegradability can have a beneficial effect on cell cultures, as will be explained later [80][16]. Therefore, whether membranes incorporate this property will also be taken into account.

The inclusion of an ALI is relevant due to several factors. It increases monolayer integrity, allows primary cells to differentiate to epithelial cells, and the addition of air provides an increase in surfactant secretion [69][28]. The inclusion of an ALI also improves the molecular barrier function, compared to submerged conditions [28]. It reasonably also produces stronger tight junctions since Huh et al. [28] found an increased electrical resistance over the cell layer under ALI conditions in their study. The inclusion of a medium flow in the device is also essential since the subsequent shear stress exerts several effects on endothelial cells: endothelial cells align along the flow direction; it influences the permeability of the cell layer, and it has an influence on cell morphology [40]. Besides that, the shear stress also has an influence on inflammation and protein expression, and most critically, it influences the cells' ability to form a tight monolayer [40]. In contrast, the shear stresses can also injure the endothelial cells that are underlying when the stresses become too large [17]. The flow is usually induced with a peristaltic or syringe pump [40].

The simulation of a breathing movement by including a cyclic stretch on the cells is relevant because it affects multiple cellular behaviours [28]. These include, but are not limited to, tight junction formation, cell proliferation, migration and differentiation, and surfactant secretion [15][16]. For example, Stucki et al. [66] showed that cyclic stretching of the membrane has an effect on barrier permeability of the epithelial layer, and Huh et al. [28] found that applying a realistic cyclic stretch enhances nanoparticle transport through the alveolar-capillary barrier. Furthermore, also the metabolic activity of dynamically stretched cells was found to be higher than that of static cells [64]. Besides that, endothelial cells align perpendicular to the straining direction [40] and cyclic (over)stretching also influences the onset and development of various diseases, such as ARDS-like cell injury [17]. Since strain has a significant effect on cellular behaviours, mechanical stimuli are vital in simulating the native (patho)physiological cell environment [15].

Membranes currently used are often about 10  $\mu\text{m}$  thick. This thickness is a factor 20 to 50 thicker than the in-vivo counterpart. Consequently, inter-cellular exchanges, such as translocation and diffusion, which are vital aspects in simulating the native environment, can not be accurately represented [69][40]. Thus, the membrane must be significantly thin enough. Besides that, most devices and their membranes are made with PDMS [56], which has several disadvantages such as ab- and adsorption of hydrophobic molecules, which will be further explained in Section 3.1.1. As such, membranes should ideally be designed using other materials than PDMS. Currently, membranes generally mainly focus on structurally supporting the cells placed on the membrane. However, compared to in-vivo basement membranes, they are too thick and not elastic enough [16].

Thus, as Douville et al. [17] state, in the modelling of an alveolus, both solid and fluid mechanical stresses have a significant influence. Therefore, both kinds of stresses should be incorporated with A: a breathing motion and B: a fluid flow. Furthermore, an ALI and a thin membrane are essential. Besides that, a membrane that changes over time might be beneficial for long-time cell cultures.

### 2.4.2. Device layout

There are various layouts in LOC devices. In order to mimic the in-vivo gas exchange, there needs to be a thin membrane with a large surface area on which the endothelial and epithelial cells are cultured. This membrane simulates the ECM. The various AOC layouts seen in the literature can be ordered in three configurations as follows:

1. Stacked channels
2. Open-air chamber on top of channel or reservoir
3. Single channel or reservoir

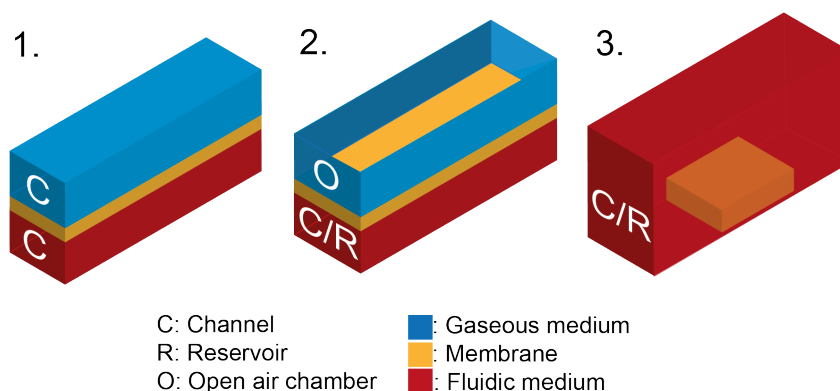


Figure 2.4: Schematic view of three LOC device lay-outs. 1) Stacked channels, 2) Open-air chamber on top of channel or reservoir and 3) Single channel or reservoir. C: channel, R: reservoir and O: open air chamber.

Figure 2.4 shows a schematic visualization of the several LOC device layouts. The cell supporting membrane or scaffold is indicated in yellow. The channel (C) or reservoir (R) containing a fluidic medium is indicated in red. Channels or open-air chambers (O) that contain a gaseous medium are shown in blue.

The first configuration, the stacked channels, consists of two closed off microchannels, perfused with air or fluidic medium, with a membrane in between [56]. Endothelial cells can be cultured on one side of the membrane, and epithelial cells on the other, thereby mimicking the alveolar-capillary barrier. This device layout generally includes an ALI and media flow. Alongside the membrane is often a vacuum chamber, by which a cyclic strain can be applied to the membrane [56]. This layout is the most common type for AOC devices. This configuration was also used by Huh et al. [28] (Figure 2.5 1.) and Jain et al. [33].

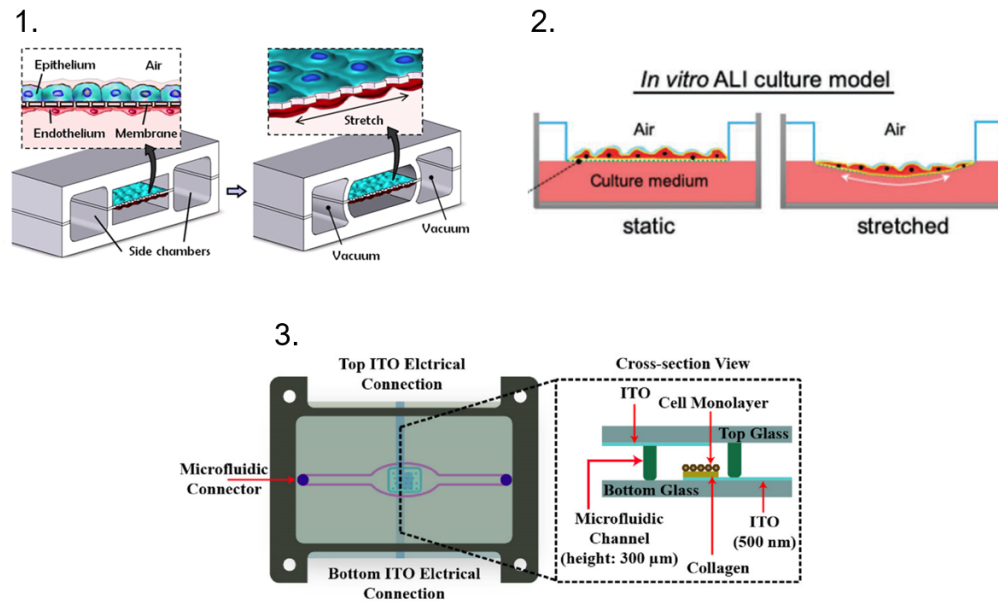


Figure 2.5: Several LOC lay-outs found in literature. 1) LOC by Huh et al. [28], 2) LOC by Doryab et al. [15] and 3) LOC by Khalid et al. [35].

The stacked channels can be located on top of each other or side-by-side. Configurations with multiple stacked channels are also possible. For example, Xu et al. [75], and Sellgren et al. [61] included a triple channel configuration. Both designs subsequently also included two membranes between the three channels (Figure 2.6). A triple channel configuration can, for example, be used to include additional cells types present in the interstitium, such as fibroblasts.

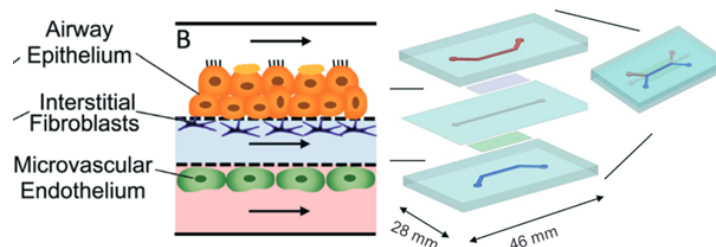


Figure 2.6: Double membrane configuration as designed by Sellgren et al. [61].

The second configuration is an open-air chamber on top of a channel or a reservoir. In this layout, there is a presence of an ALI. Like a culture well, this open-air chamber is not closed-off. An open-air chamber allows

for easy access to the membrane, but the air present in the chamber, which equals the air in the surrounding environment, borders immediately on the cell culture. This creates a challenge if gas with the same composition as the air in the alveoli is to be recapitulated since the air within the alveoli differs from the environmental air in the fact that it has a higher water vapour percentage [45][46]. On the endothelial side of the membrane is a media reservoir or a channel with media flow to provide nutrients [45] and possibly induce shear stresses on endothelial cells. This layout also allows for the stretching of the membrane. Doryab et al. [15] (Figure 2.5 2.) and also, for example, Huang et al. [26], Nayalanda et al. [45] and Stucki et al. [67] implemented this configuration.

The third layout consists of a single channel or reservoir in which a membrane or cell scaffold is present. The cells are entirely submerged, and no ALI is introduced. The cell supporting structure can be a scaffold instead of a thin and flat membrane, as is seen in the research of Rezaei et al. [55]. Generally, no strain is exerted on the membrane. This layout can also be seen in the design by Khalid et al. [35] who cultured a lung cancer cell monolayer on a thin collagen base within a single media perfused channel (Figure 2.5 3.).

### Strain types

In general, various types of strain can be applied to the membrane. As stated previously, strain exerts a significant effect on cells by inducing morphological, biochemical, metabolic and genetic changes in the cells [21]. Due to the strain, cells experience the mechanical forces at their focal adhesions. From there on, this signal is transmitted to the cytoskeleton, which remodels accordingly. The type of strain (1D, 2D or 3D), its magnitude and frequency all have a significant influence on cell behaviour [21].

In-vivo the cells experience triaxial strain, resembling a balloon inflating and deflating. The diameter of the alveoli is between 200 and 500  $\mu\text{m}$  and the surface area of a single alveolar type 1 and type 2 cell is about 5000  $\mu\text{m}^2$  and 250  $\mu\text{m}^2$  respectively [65][43]. These dimensions are roughly in the same order of magnitude, causing the individual cells to undergo significant out-of-plane strain [46].

Different types of strains are present in LOC devices: uni-, bi-, or triaxial strain. Biaxial strain can be in-plane (XY) or out-of-plane (XZ). This strain can be expressed in linear elongation and surface area strain (surface expansion) [21]. A uniaxial isotropic strain can be correlated with a biaxial strain to calculate its corresponding surface expansion. An example for a 10% linear strain by Guenat et al. [21] can be seen in Figure 2.7. This review showed that an out-of-plane biaxial deformation and a triaxial deformation have a similar surface expansion to a uniaxial and a biaxial in-plane straining [21].

This surface expansion is because the out-of-plane deflection of a membrane is negligible on the single-cell scale. A single cell has a length scale of about 20  $\mu\text{m}$ , whereas the substrate membrane typically has a diameter ranging from 500  $\mu\text{m}$  to several millimetres [21]. Thus, although cells in-vivo undergo triaxial strain, on a membrane with a relatively large diameter, in-plane biaxial strain can also be incorporated instead since this lets the cells experience about the same surface expansion.

A smaller membrane could be incorporated if a triaxial strain is applied to the cells. Zamprogno et al. [78], Laniece [40] and Radiom et al. [54] did mimic the out-of-plane triaxial strain exerted on alveolar cells in-vivo by mimicking the alveolar dimensions. They divided the larger membrane into smaller membranes with alveolar dimensions by including a support structure. Only the smaller membranes were stretched, whereas the support structure remained rigid. Therefore, the order of magnitude of the cells and the stretched membrane lie more closely together, such that the cells still experience considerable out-of-plane strain.

There are several different techniques to stretch the membrane. The membrane can be mechanically stretched using vacuum chambers as shown in the device by Huh et al. [28], who stretched the membrane unidirectionally. The walls are pulled together by applying a negative pressure in the vacuum chambers, stretching the membrane. This type of stretching creates an in-plane strain. Stretching can also be done indirectly by pneumatic or hydrodynamic actuation, in which positive or negative pressure is applied to the membrane, by pressurizing a channel filled either with a gas or a liquid, which borders directly on the membrane surface [40] [21]. This type of stretching creates an out-of-plane strain. Such a method can be seen in the devices by Doryab et al. [16], and Stucki et al. [67].



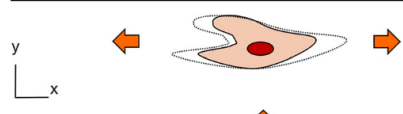
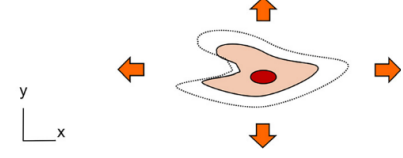
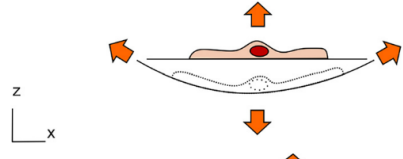
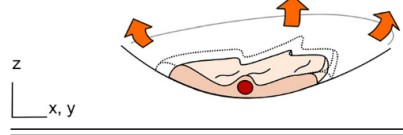
Type of mechanical strain (illustration of a stretched cell)	Type of mechanical strain	Linear strain (num. example)	Surface area strain
	Uniaxial strain (x)	10%	10%
	Bi-axial strain (xy)	10%	21%
	Bi-axial strain (xz)	10%	$\approx 10\%$
	Tri-axial strain (xyz)	10%	$\approx 21\%$

Figure 2.7: The different strain types of thin membranes in microfluidic devices [21].

Furthermore, in-plane stretch and out-of-plane stretch have different effects on the shear stress exerted on the cells by a media flow. During in-plane stretching of the cells, the media flow is parallel to the membranes surface, and the shear force will be uniform on all cells. In a device where the membrane is stretched out-of-plane, the media flow generally does not flow parallel to the membrane at all times. This unparallel flow creates a variation in shear stress at different locations on the membrane.

The wave type of cyclic strain also differs. Some studies use a triangular wave cycle [67][46], whereas other use a sinusoidal wave cycle [54][66][16]. Also, an array of various chips have been established to increase the number of experiments that can be conducted simultaneously [21][30][66][52].

### Membrane types

There are various types of cell supporting membranes. The membrane is usually a thin porous membrane [56]. The general membrane thickness is around  $10\ \mu\text{m}$ . Pores present in the membrane range between  $0.4\ \mu\text{m}$  and  $50\ \mu\text{m}$ , with most pore sizes below  $10\ \mu\text{m}$ . However, also membranes with no pores are used [17][35]. The membrane topology ranges from smooth, textureless membranes to 2.5D/3D membranes such as electrospun membranes, which contain a distinct fibrous texture. A materials that is often used as a membrane material is PDMS, but also various synthetic polymers and hydrogels have recently been researched. When designing a LOC device, great care should be taken in ensuring that the device layout, type of strain, and membrane type correspond with the desired functionality of the device.

### 2.4.3. Representative LOC devices

After discussing the basic LOC layouts, in this section a more detailed overview is given of the devices found in the literature. It was determined whether these devices contain a cyclic stretch, an ALI, a gas or media flow and whether they contain a membrane conversion. A membrane conversion means that a membrane has changing properties over time, for example, due to biodegradable materials. On top of this, the materials used in the devices and the manufacturing methods are summarized. Furthermore, the membrane thickness is reviewed, and it is determined whether this thickness was chosen due to manufacturing possibilities or a biological factor. Also, the pore size and the porosity were studied. Figure A.1 in Appendix A shows an overview of the various LOC devices studied. It should be noted that many devices that are designed to have both an ALI and a cyclic stretch are not necessarily designed to have those characteristics active at the same time [40].

A material that is often utilized in LOC devices is PDMS, both for the membrane and the rest of the device. Multiple devices have sought to replace PDMS as a membrane material, but still use PDMS in the rest of the device. On the membranes with an alternative material often no cyclic stretch is applied. Membrane materials that replace PDMS but do not include a cyclic stretch on the membrane include polytetrafluoroethylene (PTFE) [61], Matrigel [30][74], silicon [52], poly(lactic-co-glycolic acid) (PLGA) [76], polyester [5], polyethylene terephthalate (PET) [45], polycarbonate (PC) [56] and various other hydrogels [44][4]. Materials that are used in combination with a cyclic stretch are various hydrogels and electrospun fibers, consisting of e.g. collagen elastin (CE) -hydrogel [78], gelatin [54][40][16], GelMA [26], and polycaprolactone (PCL) [68][16].

### The first LOC devices

The first LOC device contained a device layout and materials that are still inspiring researchers to date. This device was designed by Huh et al. [28] and is shown in Figure 2.5 1. Huh et al. recreated the cyclic breathing motion using vacuum chambers, which stretched the intermediate membrane when applying negative pressure. They used a 10  $\mu\text{m}$  thick porous PDMS membrane. This membrane was coated with fibronectin or collagen ECM to increase cell viability [28]. Also, the air-liquid interface was recreated after the alveolar cells had become confluent [64]. The strain applied on the membrane was a uniaxial in-plane strain. The device was made using soft-lithography, and it was an influential addition to the study of lung inflammation [28]. Huh et al. [29] later also used this device design to study lung oedema.

The double channel configuration is an often-used device layout in LOC devices. However, other layouts have also been proposed. For example, Stucki et al. [67], and Douville et al. [17] also used PDMS for their membranes, but they created a bulging membrane to apply a three-dimensional out-of-plane strain on the cells (Figure 2.8). Furthermore, PDMS is widely applied, generally in combination with soft-lithography. PDMS has several advantages: elasticity, optical transparency, low fabrication costs and biocompatibility [60][8][14]. However, it also suffers from small molecule ab- and adsorption, making it less suitable in drug screening studies [78][14]. Therefore, many papers looked into the use of other materials. Generally, researchers replaced the membrane, since this is the part that is most in contact with the cells, and left the rest of the device still made of PDMS.

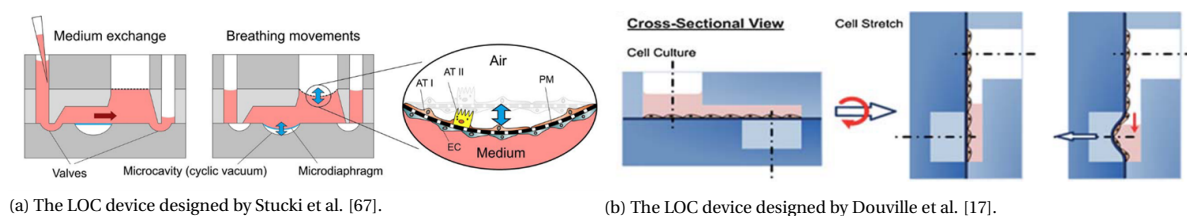


Figure 2.8: Two LOC devices with a PDMS membrane and an out-of-plane strain.

For example, Sellgren et al. [61] also used soft-lithography for their device, but they ventured into using different materials than PDMS. What is remarkable in this device is that they used a double membrane configuration (Figure 2.6). They recreated the air-liquid interface using a triple cell co-culture of primary airway epithelial cells, lung fibroblasts, and microvascular endothelial cells.

This LOC device consists of three compartments containing stiff nanoporous membranes. In the top compartment, epithelial cells are grown and airflow is present. In the middle compartment, interstitial fibroblasts are grown. In the bottom compartment, endothelial cells and the fluid flow are present. The middle compartment with the fibroblasts was included to more closely resemble the microarchitecture in the airway mucosa and to incorporate a geometrical division between cell types [61]. This separation is physiologically relevant since it allows for heterotypic cell interaction over their respective membranes, giving it a more biomimetic structure.

However, this device does not simulate a breathing motion. The membranes were made of PET, PTFE, and PC, which are rigid materials that do not allow for a cyclic stretch. The overall barrier thickness was about

200  $\mu\text{m}$  [61]. Such rigid membranes could also be seen in the research of Punde et al. [52], who designed a microporous silicon basement membrane (Figure 2.9). Other double channel configurations with a rigid membrane have been designed by Benam et al. (polyester) [5], Nalayanda et al. (PET) [45] and Rimsa et al. (PC) [56].

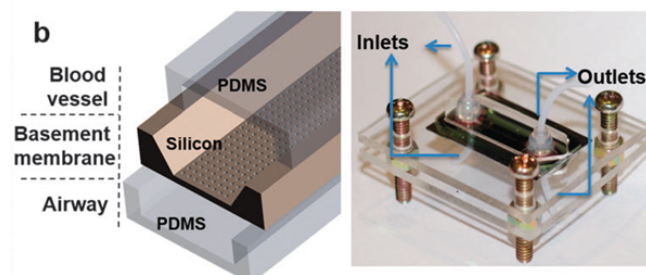
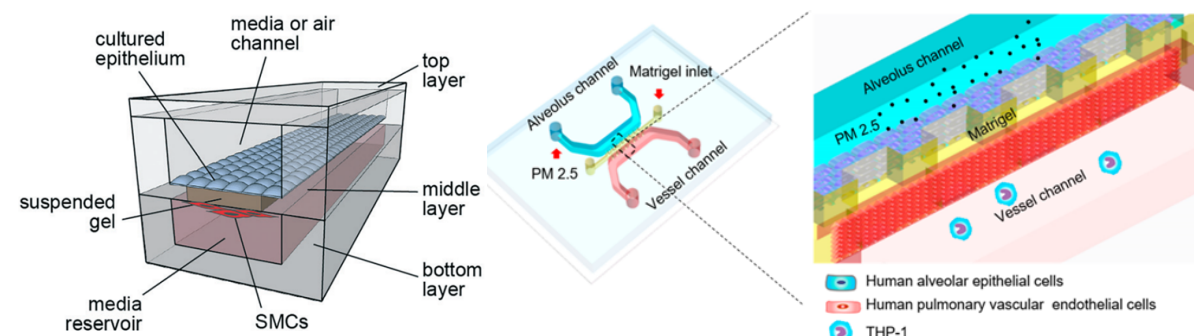


Figure 2.9: The LOC device designed by Punde et al. [52].

### Hydrogel membranes

Other device designs based on the double channel configuration have been designed by Humayun et al. [30], Xu et al. [74], Huang et al. [26] and Zamprogno et al. [78], who all changed the PDMS membrane to a hydrogel membrane. Hydrogels are promising to replace PDMS as a membrane material due to their intrinsic characteristics such as their lower stiffness, chemical composition, and porosity [78]. However, generally, these hydrogel membranes have poor mechanical properties. Consequently, these membranes usually have a thick design or no cyclic stretch is applied. This generates a lack of dynamical cues or an overscaled membrane thickness, as can be seen in the AOC by Xu et al. [74]. Zamprogno et al. [78] circumvented this problem by including a support structure within the membrane.

Humayun et al. [30] focused on the epithelial-smooth muscle cell (SMC) interaction in the upper airways instead of on the gas exchange in the alveoli, which might explain why the membrane they used was designed substantially thicker than the mean thickness of AOC membranes. They used a suspended hydrogel with a thickness of 0.65 mm as a membrane, and they did mimic the ALI. No strain was applied, however. The hydrogel they used was Matrigel in combination with collagen, and the rest of the device was made with PMMA (Figure 2.10a). They were able to set up a coculture for more than 31 days.



(a) The LOC device designed by Humayun et al. [30].

(b) The LOC device designed by Xu et al. [74].

Figure 2.10: Two LOC devices with a hydrogel membrane.

Xu et al. [74] did mimic the alveolar-capillary barrier, with a LOC device based on Zhang et al. [81] (Figure 2.10b). They had an 80  $\mu\text{m}$  thick coagulated Matrigel membrane on which no stretch was applied. No ALI was incorporated, and the media in the alveolar channel was exchanged daily. In the capillary channel, a continuous flow was present [81]. Confluent monolayers could be formed for both endothelial and epithelial cells, on which subsequently the effect of nanoparticles was studied [74].

Huang et al. [26] used a different approach and was able to include a biaxial in-plane cyclic stretch up to 15%, an ALI and a media flow. They developed an AOC by using a 3D porous GelMA membrane to simulate better the composition of the ECM and the physiological stiffness (Figure 2.11). They also state that the topography and composition of the ECM significantly influence the cell functions, and therefore, these characteristics should be incorporated in the design.

They created an inverse opal structure, recapitulating the in-vivo alveolar sac dimensions and the interconnecting windows. Each alveoli pore had a diameter of  $200\ \mu\text{m}$ , and within their design, they were able to recreate about 7050 alveoli. The total membrane thickness was less than 3 mm, and the scaffold structure itself had a thickness of  $546.4\ \mu\text{m}$ , which consisted of about three stacked layers of simulated alveoli. Overall, this is a relatively thick membrane. Although a media flow was present underneath the membrane, the device only contained the epithelial cell layer. A confluent epithelial monolayer could be created. Furthermore, they found that 3D scaffolds present a more optimal geometry and microarchitecture than a 2D, planar structure regarding cell adhesion, proliferation, and migration. They also observed that a cyclic mechanical strain seemed to promote tight junction formation in the epithelial layer [26].

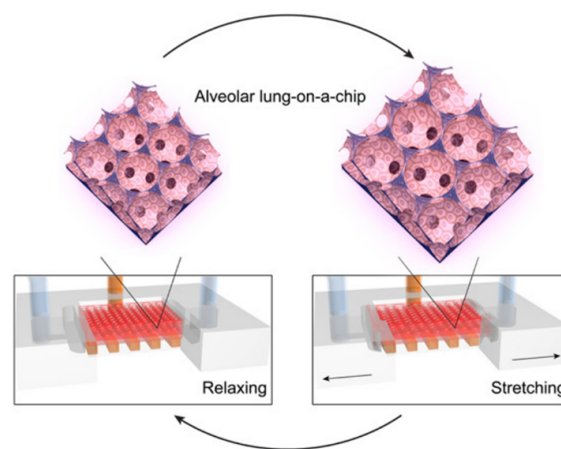


Figure 2.11: The LOC device designed by Huang et al. [26].

Like the design by Huang et al. [26], there have been other studies into creating a three-dimensional hydrogel scaffold for lung cells [26][55][35]. However, it remains an issue that a three-dimensional scaffold does not directly resemble a membrane. The human body contains a dense network of capillaries encapsulating and wrapping around the alveoli. If a three-dimensional scaffold is created, a designer needs to ensure that the scaffold is not too porous or too thick. Simultaneously, thin barriers need to exist between the endothelial and epithelial cells, while nutrients should reach all the cultured cells. This means that a barrier or membrane with limited porosity and thickness should always be present.

### Electrospun membranes

Another type of LOC device is one that uses an electrospun porous nanofiber membrane without a support structure. These membranes are used in the devices by Yang et al. [76], Tas et al. [68] and Jin et al. [34]. An electrospun membrane has several advantages, mainly because its fibres mimic the microarchitecture and anisotropy of the ECM [76]. Besides that, they allow for specific tailoring of characteristics: porosity, mechanical strength, stretchability, thickness, fibre diameter, and fibre orientation can all be adjusted [68]. Also, in-vivo, collagen and elastin fibre networks reorient themselves by deforming irreversibly along the direction of macroscopic strain [68]. Tas et al. [68] found that their fibrous PCL membrane also exhibited this fibre aligning behaviour.

However, electrospun membranes are generally thick membranes. Research has not shown an electrospun membrane for long-term cell cultures without a support structure that is thinner than the widely used PDMS membrane ( $10\ \mu\text{m}$ ). A solution to obtain thinner membranes could be to include a support structure in the membrane. Furthermore, electrospun membranes contain a wide distribution of pore sizes. For example,

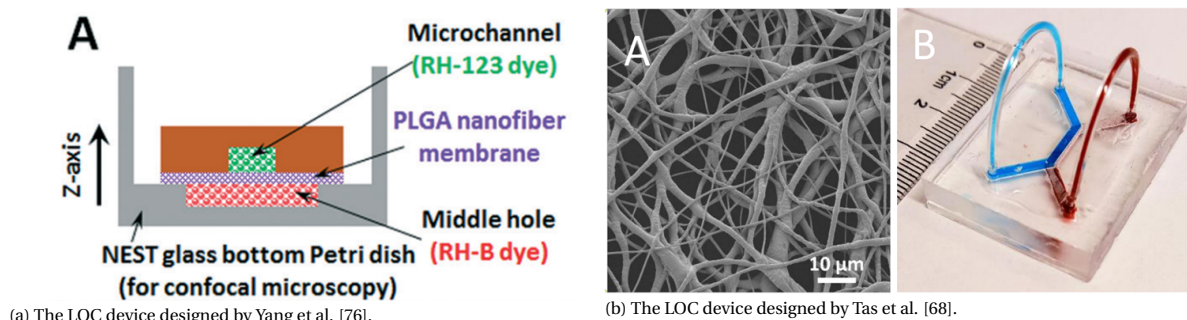


Figure 2.12: Two LOC devices with electrospun membranes.

Jin et al. [34], who created a  $\sim 70 \mu\text{m}$  thick PCL membrane, had a pore size range, where 77% of pores were between 1 and  $10 \mu\text{m}$ . Due to the random nature of electrospinning, it is difficult to create a uniform porosity and homogeneous pore distribution over the membrane.

Yang et al. [76] designed a porous nanofiber membrane in order to mimic the alveolar barrier for anti-cancer drug testing. The device they designed had a cell scaffold with PLGA electrospun nanofibers, placed over PDMS channels (Figure 2.12a). The diameter of the fibres was  $3 \mu\text{m}$ , and the membrane thickness was several microns. The PLGA is biocompatible and biodegradable, although their experiment duration was too short (5 days) to observe degradation. They achieved a co-culture of three cell types and did not observe any significant leakage through the electrospun membrane. Diffusion of rhodamine-B was present through the membrane, indicating the presence of an adequate permeability for molecules. Yang et al. [76] designed a membrane that was thinner than the widely used  $10 \mu\text{m}$ , but no long-term cultures, cyclic stretching or media flow have been studied on this membrane.

Tas et al. [68], although not yet peer-reviewed, designed a  $20 \mu\text{m}$  nanofibrous PCL membrane, between PDMS channels, to model ventilator-induced lung injuries (Figure 2.12b). This membrane was selected to model the 3D nanofibrous structure of the alveolar basement membrane. A cyclic stretch, ALI and media flow were also incorporated into the device. For the breathing motion, a strain of 25% at 0.1Hz was applied for 2 hours to simulate overstretching of the alveoli. The membrane used is commercially available (Cellestave AB, Sweden, 3D Nanomatrix). Moreover, the PCL membranes do not significantly leach cytotoxic materials into the cell culture medium. Tas et al. [68] state that, besides mimicking the mechanical stretch, also the in-vivo nanofibrous topography must be recapitulated in order to support cell growth. No long-term cell cultures have been constructed on this membrane yet.

### Support structures

Various materials use a support structure, especially when the membrane material or its structure has weak mechanical properties. When a support structure is implemented in combination with a strain, the type of strain has so far been a bulging strain in combination with a honeycomb support structure. This type of structure is seen in the research of Laniece [40], Zamprogno et al. [78] and Radiom et al. [54]. Zamprogno et al. [78] designed a hydrogel membrane over this structure, whereas Radiom et al. [54] and Laniece [40] used an electrospun membrane.

Zamprogno et al. [78] designed a LOC model that mimicked the physiological in-vivo dimensions of the alveoli (Figure 2.13a). That means each hexagon diameter in the gold support structure is based on the diameter of a single alveolus. Over this gold support structure, a collagen-elastic (CE) hydrogel is placed. The membrane allows for cyclic stretching to simulate breathing motions and incorporates an ALI. Furthermore, the membrane is partly biodegradable.

They used a biological collagen-elastin (CE) membrane, which was structurally stable and elastic. Vitrifying the membrane allowed the membrane thickness to be decreased to  $5 - 10 \mu\text{m}$ . The hexagonal support structure had a thickness of  $18 \mu\text{m}$ . The CE membrane had reduced resorption of hydrophobic molecules compared to PDMS and could be deposited on the hexagonal structure by drop-casting, using the hydrogels



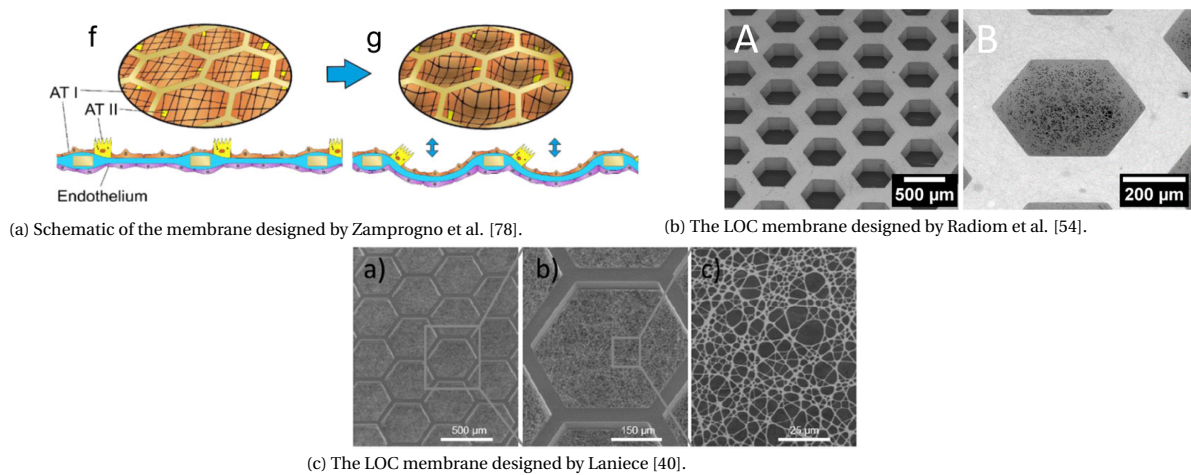


Figure 2.13: LOC devices using a honeycomb support structure.

surface tension. Inside the membrane, collagen molecules are assembled into fibrils, which provide structural support. The membrane's stiffness was between 1Pa and 1kPa, having a Young's modulus lower than that of PDMS. [78]

Zamprogno et al. [78] obtained cell-cell contact after two weeks with primary human lung alveolar epithelial cells, and cultures lasted at least three weeks. A strain of up to 10% was obtained, although not in long-term cultures. Furthermore, no media flow was included, and the membrane's porosity was not defined. When a solution of MMP-8, a neutrophils collagenase, was introduced, the CE membrane would degrade completely. The slowest degradation time they used was about 6 hours. The degradation was tested without cells present on the membrane, so no effect on cells has been studied yet. A biodegradable membrane can aid in investigating alveolar barrier remodelling, which occurs in various lung diseases.

Overall, a CE-membrane is a promising biodegradable material to design a lung alveolar membrane that fits requirements such as: optical transparency, stretchability, low ad- and absorption of molecules, biophysical, good mechanical microstructural properties and biodegradability. However, more long-term studies on, e.g. the long-term strain, porosity, inclusion of a media flow and the rate of degradation should be done.

Radiom et al. [54] and Laniece [40] used a similar hexagonal design, although with an electrospun membrane made of gelatin nanofibers (resp. Figure 2.13c and Figure 2.13b). Their support structure was made of PEGDA and Ormostamp, respectively, and gold coated. Both electrospun membranes had a thickness of around 1 μm, and their pore sizes were approximately comparable. This membrane thickness is comparable to the in-vivo thickness of the interstitium. Unlike Zamprogno et al. [78], they included a media flow, besides incorporating a cyclic stretch and an ALI. Radiom et al. created an ALI by placing the membrane in the microfluidic chip manufactured by MesoBioTech.

Both designs had a hexagonal diameter mimicking the alveolar diameter, although being somewhat larger than an alveolar diameter and the diameter of Zamprogno et al.[78]. An alveolus has a diameter of about 200 to 300 μm, whereas Laniece et al. used a diameter of 400 μm and Radiom et al. of 500 μm [40][54].

Gelatin was used because it is a natural polymer derived from collagen [54]. Radiom et al. found that the elastic modulus of their membrane was  $4.0 \pm 1.0$  MPa, which is in roughly the same order as PDMS [54]. Laniece [40] also observed that HUVEC cells degrade the gelatin membrane, thereby creating unwanted holes in the membrane. So on the membrane, only a combination of cells could be cultured, where no HUVECs were present or where HUVECs could grow on top of other cells.

The cyclic three-dimensional out-of-plane strain that they could achieve with these membranes was for Laniece [40] maximally 6.2% due to the rigidity of their honeycomb and nanofiber structure, which is too low to mimic the complete physiological strain range. Moreover, this was not yet tested on live cells for the

long-term [40]. Secondly, Radiom et al. [54] applied a strain of 5% to the cells at 0.2 Hz for 1 hour. Also, the displacements of the membrane were not constant ( $>10\%$  standard deviation), possibly due to the random deposition process of the electrospinning causing variations in the nanofiber density [54].

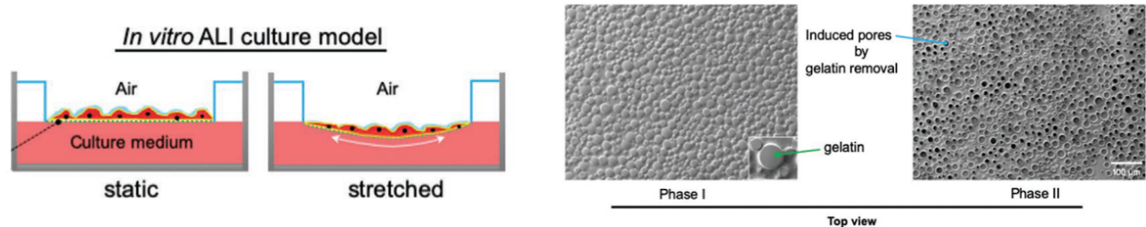
Besides the low strain values, the duration of the experiments in these studies is also too short for the experiments that this current review focuses on. So even though they were able to use a very thin membrane, extended experiment durations would still need to be conducted to study the effect of more prolonged and higher cyclic strain on such a thin membrane. Although the support structure allows thinner membranes to be used, the drawback of these rigid honeycomb structures is that no in-plane stretch is possible. This also limits the possibility of introducing a media flow that remains parallel to the membrane.

### Membranes changing over time

Several studies utilize LOC devices with membranes that change over time, i.e., containing a membrane conversion. Some of which have already been discussed previously, such as Zamprognio et al. [78] and Fusaro et al. [20], who used biodegradable membranes. Moreover, also various scaffolds are designed with biodegradable materials [79][55]. A notable study that uses biodegradable materials to adjust pore size is the study by Doryab et al. [16].

Pores on LOC devices are generally  $1\text{--}3\text{ }\mu\text{m}$  [16]. However, these pores are too small to permit cell migration, which is crucial in, for example, observing neutrophil migration in inflammatory conditions. Doryab et al. [16] state that at the start of a cell culture, no pores are necessary yet. They designed a hybrid AOC membrane that was non-porous during cell seeding and the initial growth phase. When cell stretching and an ALI were introduced, the membrane became porous to allow for cell migration and nutrient exchange in a later stage of the cell culture.

The membrane used by Doryab et al. [16] was thinner than  $5\text{ }\mu\text{m}$  and made of gelatin and poly( $\epsilon$ )-caprolactone (PCL). This Biphasic Elastic Thin for Air-liquid culture conditions (BETA) membrane is stretchable up to 25% linear strain, and the type of strain was a three-dimensional out-of-plane bulging (Figure 2.14a). The design has fitting surface wettability and good porosity for an ALI with lung epithelial cells, besides having a biomimetic elasticity and good optical transparency. No pretreatment was needed to enhance cell adhesion, and proliferation [16].



(a) Schematic of the LOC device designed by Doryab et al. [16].

(b) The membrane designed by Doryab et al. [16].

Figure 2.14: Two LOC devices with electrospun membranes.

The membrane was fabricated by spin coating a PCL and gelatin emulsion. The gelatin bubbles present in the PCL membrane initially provide increased wettability, which is favourable in cell adherence and growth. When cells grow and proliferate, they will secrete their own ECM. This ECM will allow the cells to migrate to less wettable materials, in this case, the PCL. Subsequently, they will form a continuous monolayer spanning both the gelatin and the PCL regions. Eventually, the gelatin will gradually degrade, leaving pores in the PCL membrane. This degradation also increases the elasticity since the more elastic PCL will remain, and the stiffer gelatin will dissolve. The 3D Young's modulus of the membrane during cell culture decreased from  $1.33 \pm 0.14\text{ MPa}$  to  $0.78 \pm 0.24\text{ MPa}$  from day one to day six due to the gelatin dissolving. [16]

They found that on their membranes, the cells only formed a monolayer when the pore size was smaller than the size of an individual cell, which is roughly between  $10\text{ and }50\text{ }\mu\text{m}$ . The pore size ranged between  $1.1\text{ and }7.9\text{ }\mu\text{m}$  and had a mean of  $4.5 \pm 1.7\text{ }\mu\text{m}$ . They noticed ECM formation within pores, and most notably cell-cell

interaction through pores. [16]

The membrane is suitable for experiments up to at least 48 h of cyclic stretching [16]. However, this duration is shorter than the experiments of 2 to 4 weeks that are desired in this project. Also, no endothelial cells have been cultured on this membrane. Nevertheless, this membrane poses a very interesting and promising approach to the use of biodegradable membranes.

### Prior work in the PME group

In order to recapitulate the alveolar-capillary barrier, the Department of Precision and Microsystems Engineering (PME) group at the Delft University of Technology also designed a LOC device [46]. This design is a resealable LOC device, which incorporates biaxial stretch (up to 20% linear strain). Besides that, the device provides an ALI with both a gas and media flow. The media flow in the basal chamber exerted a shear stress of 0.55 Pa on the endothelial cells at a 2.6 ml/min flow rate. The cells can be seeded on the membrane by direct pipetting, and they can be retrieved after the experiment for additional analyses. Furthermore, the LOC is compatible with confocal microscopy and optical sensors to measure pH and  $O_2$  and  $CO_2$  concentrations. It is also possible to include transepithelial electrical resistance (TEER) and temperature sensors. All the materials used (PDMS, glass) have good optical transparency allowing live imaging of the cells. [46]

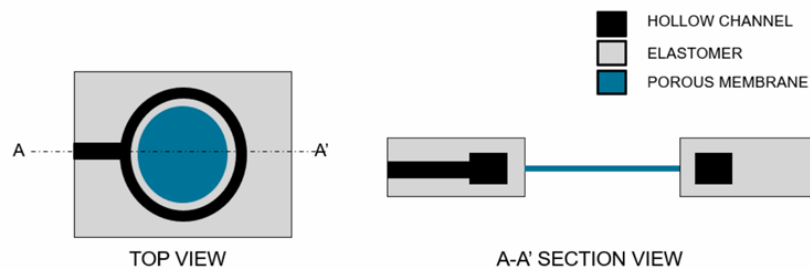


Figure 2.15: Schematic of the LOC device designed by Nissar [46].

The device (Figure 2.15) uses a hollow actuation ring (black), which bends the PDMS elastomeric wall inwards when negative pressure is applied. This inward bending stretches the membrane (blue) biaxially. The PDMS channels were fabricated using soft-lithography, and they were sandwiched between glass layers (Figure 2.16). Plasma bonding was used to bond the channels to the actuator. [46]

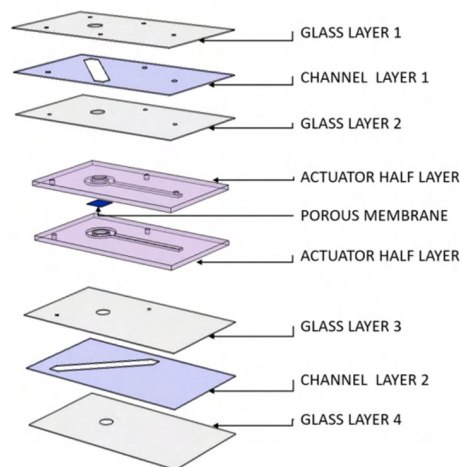


Figure 2.16: Layered view of the device by Nissar [46].



The membrane designed for this device is a porous PDMS membrane coated with type 1 rat tail collagen to adjust its hydrophobic surface properties. The membrane had a thickness of 10  $\mu\text{m}$  and pores with a diameter of 8  $\mu\text{m}$ . The overall porosity was 2.1%. The central membrane hole had a diameter of 3.1 mm, and the porous membrane itself had a diameter of 3 mm. [46]

Human primary bronchial epithelial cells (PBECS) remained viable for at least 16 days in culture on the membrane, and they formed a monolayer after five days. This device is designed for an endothelial and epithelial cell coculture, providing cyclic strain and shear stress. However, the membrane is made of PDMS, which has several disadvantages that will be further explained in Section 3.1.1. Nissar states that, for example, SEBS or cyclo-olefin copolymer (COC) could be used to replace the PDMS and glass, respectively, to make the device better suited for OOC applications and large scale production. The design also allows for scale-up by manufacturing an array of LOCs next to each other so that multiple cell cultures can be performed simultaneously. [46]

## 2.5. Conclusions and remarks on current LOC devices

Even though significant advancement in the design of LOC devices has been made in the past two decades, there are still many limitations in the current designs. Several conclusions can be drawn from the literature. First, only a limited number of studies were able to include a thin membrane ( $<10\ \mu\text{m}$ ), and only two had a membrane equal or thinner than 1  $\mu\text{m}$  to my knowledge [40][54]. Moreover, when a thin membrane was incorporated, it was generally static or not yet tested for long-term cell cultures. No thin membranes made of a different material than PDMS had a cell culture containing a cyclic stretch for longer than 48 hours. However, this review already concluded the importance of a dynamic membrane that can remain functional for multiple weeks. The studies that did include a thin membrane with the possibility of short-term stretching include the design by Laniece [40], Stucki et al. [66], Doryab et al. [16] and Zamprogno et al. [78]. All four studies incorporated a triaxial, out-of-plane stretch (bulging).

Second, many devices had both an ALI, a media flow, and a cyclic stretch incorporated in their devices. Although not all studies were able to apply the cyclic stretch and the media flow or ALI at the same time [40][67]. This means that these LOCs do not simulate a shear stress on the cells, while the cells are also subjected to a strain, as displayed in-vivo. There are also differences present in the type of stretch that was applied. One of the more common stretching types is the bulging stretch. Nonetheless, in-plane stretch was also widely present in literature, although often in combination with thicker membranes.

Third, as explained by Doryab et al. [16] different phases of the cell culture may necessitate for or benefit of diverse membrane requirements. Therefore, research containing changing membranes throughout the cell culture were studied. These include membranes that are (partly) biodegradable. Rezaei et al. [55] designed a biodegradable scaffold not suitable for stretching or an ALI. Also, Zhang et al. [79] made a POMaC scaffold, which could contain an ALI, but no strain was applied to the membrane. Doryab et al. [16] made a promising membrane with varying pore size. Zamprogno et al. [78] designed a promising biological and biodegradable membrane. As such, inspiration can be taken from these designs.

Fourth, there are various promising material alternatives proposed for PDMS. Alternative materials also allow for alternative manufacturing methods and membrane structures, such as electrospun fibres or a rigid support structure. Support structures generally contain a hexagonal shape. Most alternative materials were still incorporated in devices that did not mimic the breathing motion, often due to the rigidity or the limited mechanical strength of the used material. For example, glass [35], PET, PC, PTFE [45][61], polyester [5] and silicon [52] were incorporated as a rigid substitute. Promising materials replacing PDMS that were subjected to a strain include; gelatin [54][40], PLGA [76] and PCL [16][34] in the case of electrospinning. Furthermore, GelMa [26] and CE-hydrogel [78] were proposed as hydrogel alternatives for membranes. The following chapters will take a closer look at several promising materials and manufacturing methods for membranes.

In conclusion, several designs of LOC devices have incorporated a combination of breathing movements, biodegradability, media and airflow while closely mimicking the lungs' ECM. However, there are still no AOC devices to my knowledge that do not use PDMS, and which contain simultaneously: an ALI, media flow, cyclic in-plane physiological stretching, and a membrane with a thickness under 10  $\mu\text{m}$  that allows for both

endothelial and epithelial cell studies spanning multiple weeks. Besides that, generally, little information is present on the motivation of the chosen pore size and its effect on the cell culture. Furthermore, few studies consider that adjusting membranes could have a beneficial effect on cells in different phases of the cell culture. The possibilities of filling this knowledge gap need to be researched for the reasons stated previously, will be further explored in the coming chapters. Future research into an adequate membrane will be conducted using the device designed by Nissar [46] in the Department of Precision and Microsystems Engineering due to its availability and previous promising results.



# 3

## Materials and manufacturing methods for LOC devices

This chapter gives a more elaborate explanation of the various materials and manufacturing methods used for LOC devices. First, the various materials will be discussed. Second, the different manufacturing methods will be analyzed. These materials and manufacturing methods mainly focus on their application for LOC membranes. Lastly, membrane integration methods are studied.

### 3.1. Materials used for LOC devices

Zhang et al. [80] state that there are a considerable number of factors in the extracellular environment that control cell fate and tissue function. These include scaffold structure, physical parameters, biological cues, bioactive molecules, and electrical, magnetic, and chemical signalling among cells. These factors influence cell differentiation and proliferation, immune system response, and angiogenesis. Besides that, the mechanical characteristics of a scaffold or membrane also influence cell activity. For example, the geometric stiffness, elastic modulus, viscoelasticity, surface hardness, tension and compression, and shear stress all exert an influence [80]. Correspondingly, in choosing a suitable material for a LOC membrane, these mechanical characteristics should be considered.

Other material characteristics that are important in LOC membrane design include: optical transparency; the flexibility of the material; whether it ab- or adsorbs small molecules, and whether it is biocompatible and sterilizable. An overview of the advantages and disadvantages of the various promising or often used material groups is given in Table 3.1. These various material groups will be further discussed in this chapter.

#### 3.1.1. The downside of PDMS membranes

Most OOC models are made of poly(dimethylsiloxane) (PDMS) as their main structural and cell-interacting component [8][27][78][14][56][68]. PDMS is a soft and versatile polymer [60]. Its elastic modulus is generally around 1 MPa, but its stiffness can accurately be controlled between 0.8 MPa and 10 MPa, while still allowing 20% uniaxial strain [60]. PDMS can be used in a broad range of temperatures, spanning from -100 °C to 200 °C [60]. To fabricate PDMS structures, generally soft-lithography is used.

Using PDMS has several advantages; it is elastic, optically transparent, biocompatible, bioinert and has relatively good mechanical characteristics [78][8][11][60]. Its biocompatibility allows for long-term cell cultures [8]. Moreover, its flexibility allows recapitulating the strain and elasticity present in native tissues [8]. Furthermore, it has an excellent gas permeability, which is needed in an alveolar membrane [8][58]. Besides that, it is easy to mould and to use in soft-lithography, and it has a low cost [14][8].

Although this makes PDMS seem like a very suitable material for a LOC device, it is hydrophobic, so it needs surface treatment to enhance wettability, and cell adhesion [16]. Besides that, it has high adsorption and absorption of small hydrophobic molecules. Especially when there is a large surface-to-volume ratio, as is the case with a membrane. This ad- and absorption limits its application in drug evaluation studies [78][14][8].

Table 3.1: Overview of the advantages and disadvantages of various material groups.

Material group	Advantages	Disadvantages
<b>PDMS</b>	Elastic Optically transparent Biocompatible Gas permeable Relatively hydrophilic High gas permeability Ease of fabrication Low cost Sterilizable Robust mechanical properties	Ad- and absorption of small molecules Oligomer leaching High water vapor permeability Some autofluorescence Low throughput manufacturing
<b>Thermoplastics</b>	Low cost Robust mechanical properties Sterilizable Biocompatible Good optically transparent Low ab- and adsorption of small molecules Low oligomer leaching	Not elastic
<b>Glass and Silicon</b>	Optically transparent (only glass) Low ab- and adsorption of molecules Sterilizable Robust mechanical properties Biocompatible Low fabrication resolution Low oligomer leaching	Not elastic High cost of fabrication Low design freedom Not optically transparent (only silicon)
<b>Silicon Nitride</b>	Optically transparent Elastic Robust mechanical properties No ad- and absorption of small molecules Antibacterial properties Biocompatible	High elastic modulus Hydrophobic surface
<b>Elastomers</b>	Optically transparent Low ab- and adsorption of small molecules Flexible High throughput manufacturing possible and ease of fabrication Elastic Sterilizable Robust mechanical properties Gas permeable Biocompatible	Some oligomer leaching
<b>PCL</b>	Biocompatible Biodegradable Robust mechanical properties Elastic	Hydrophobic
<b>Hydrogels</b>	Potential for cell ingrowth Low cost Biocompatible Good cell viability Elastic Gas permeable Optically transparent	Weak mechanical properties Difficult sterilization Some ab- and adsorption of small molecules Some oligomer leaching Low design freedom

When the PDMS absorbs these molecules, there is (1) a reduction in the drug or cell-signalling compounds that exert an effect on the cell culture, (2) cross-contamination, (3) increased background fluorescence, and this all impairs accurate interpretations of the drug toxicity and efficacy/dose-response effect, thereby limiting drug evaluation studies [14][8]. Furthermore, uncured oligomers present in the PDMS can leach out into the surrounding environment [14]. Moreover, its intrinsic stiffness (1 MPa vs 2 kPa) and molecular composition are distinctly different from alveolar lung tissue [78]. It also has a high water vapour permeability, which causes osmolarity shifts and thus influences homeostasis [14]. Additionally, it is autofluorescent to some extent, and it is incompatible with organic solvents [8]. Finally, it also poses a challenge when high volume manufacturing is desired due to the development time when using master moulds [14][8].

When using PDMS, a possible solution for the ab- and adsorption of small molecules is to chemically modify and coat the PDMS surface, e.g. with chemically vapour deposited parylene or solution deposited Teflon AF. It was found that this reduces the absorption of specific hydrophobic molecules (rhodamine B and fluorescent dyes resp.) [14]. Besides that, it can also increase wettability. Also, coatings with ECM proteins such as collagen, gelatin, fibronectin, and laminin are possible [16]. Nonetheless, these coatings compromise other (mechanical) material properties, and they should remain stable throughout the entire experiment, possibly lasting several weeks [14][8]. Furthermore, dislodgement of cells from the PDMS surface is an issue for long-term cell cultures, especially under stretch conditions. This dislodgement is because of protein dissociation [16].

Therefore, other materials than PDMS need to be analyzed to create a new membrane design. For devices that recapitulate the physiological motion of breathing, highly elastomeric materials are desired [28]. Besides that, the membrane material must still be optically clear to facilitate high-resolution microscopic analyses [14]. Possible material groups include hydrogels, such as Matrigel or collagen-elastin/gelatin hydrogels. Moreover, in order to create more elastic membranes that still have a diminished small molecule absorption, elastomeric materials such as polyurethane, SEBS, tetrafluoroethylene-propylene (FEPM), PEGDA, POMaC, or PICO can be used [8].

### 3.1.2. Alternative materials

This subsection summarises the various alternative materials that have been used or are promising as an AOC membrane material.

#### Thermoplastic polymers

Often thermoplastic polymers are used as a PDMS replacement. Polymeric materials have a large variation in chemical groups, allowing for a broad spectrum of biomechanical properties [16]. In comparison with PDMS, they restrict small molecule absorption but also increase cell adhesion, without the need for coating [8]. Furthermore, thermoplastics are generally optically transparent, biocompatible and easy to manufacture. However, PDMS has more desirable characteristics in terms of elasticity; the elastic modulus of thermoplastics generally lies too high to use it to mimic breathing movements [8].

#### Silicon

Materials such as glass, silicon, resins and ceramics have a too high stiffness to use for fully flexible membranes. These materials can be used as a support material within membranes, such as is seen in the research by Laniece [40] and Zamprogno et al. [78]. Whereas silicon has been used in various OOC devices, it has so far been used as a relatively static part of the microfluidic device [31][52][48]. Oleaga et al. [48] designed a silicon cantilever that could measure the cardiomyocyte function through deflection, but this does not include large strains. A silicon membrane on which a strain is applied has not yet been produced for LOC devices.

#### Silicon Nitride

Another silicon-based material group is silicon nitride (SiNx). SiNx is a non-oxide ceramic [72]. No LOC membranes made of silicon nitride have been found in the literature. However, it is a promising material due to its elasticity and optical transparency. SiNx has a broad interest and application in the form of thin films [24]. These films can be produced with chemical vapour deposition (CVD), electron cyclotron resonance (ECR), and physical vapour deposition (PVD) [24]. SiNx thin films are promising in the application of hard coating in challenging environmental conditions [24]. SiNx has a high hardness, and optical transparency [24]. Recently, SiNx layers have been applied to a greater extent as flexible membranes [24].

The specific material properties of SiNx depend on the manufacturing method, the material structure, and membrane thickness. The main advantage of using SiNx is the well-established fabrication techniques. The electronics industry has been using silicon since the 1950s to manufacture MEMS devices with silicon structures [8][57]. Manufacturing techniques include: dry and wet etching; laser-drilling; direct, adhesive or anodic bonding; or sand-blasting [8]. Although, OOCs with silicon can still be labour-intensive and costly to manufacture [8].

Moreover, silicon-based materials are chemically inert, biocompatible, and they do not absorb small molecules [8][72]. The surface of silicon nitride (Si<sub>3</sub>N<sub>4</sub>) is highly hydrophobic [72]. It was also found by Webster et al. [72] that this silicon nitride has significant antibacterial properties during in-vivo experiments. However, the elastic modulus is high. Carlotti et al. [9] found an elastic modulus of 256 GPa and a Poisson's ratio of 0.28.

### Elastomers

Campbell et al. [8] proposes three different elastomers for LOC devices; polyester elastomers, tetrafluoroethylene propylene (FEP) elastomers, and thermoplastic elastomers. The advantage of elastomers is that they minimize the absorption of small molecules. Furthermore, they are elastic while containing robust mechanical properties, and they are biocompatible. This makes them promising for use as a flexible membrane.

An example of a polyester elastomer is poly(octamethylene maleate (anhydride) citrate) (POMaC), which is very long term stable and can be tailored to have nanoporosity [8]. Nano-porous membranes can be created by adding a porogen (e.g. PEGDM) to the mixture [79]. This material was used by Zhang et al. [79] in the scaffold in their AngioChip. They created POMaC with a bulk Young's modulus ranging between  $53 \pm 8$  kPa and  $1423 \pm 651$  kPa. They created a scaffold of several tens of microns thick. POMaC has the advantage that it is more elastic than other FDA approved polyesters, and since it is UV-polymerizable, it allows for easy manufacturing. POMaC has less ab- and adsorption of small molecules than PDMS, and it is a mechanically stronger material than hydrogels. Besides that, POMaC biodegrades by hydrolysis, and the degradation rate is in the order of weeks. [79]

Regarding the FEP elastomers, a collagen vitrigel membrane between two layers of FEP was designed by Sano et al. [58] to recapitulate the epithelial-endothelial interface. This layout allowed both fluid flow and mechanical strain to be incorporated in this design. FEP has exquisite chemical resistance, significantly diminishing ab- and adsorption of small hydrophobic compounds within this design when compared to the use of PDMS [58]. FEP is, however, just as POMaC, limited by its fabrication method due to its high glass transition temperature [8].

An example of a thermoplastic elastomer is styrene-ethylene-butylene-styrene (SEBS). SEBS elastomers have diminished absorption of small hydrophobic molecules while still having the advantages of flexibility, optical clarity [14]. Although, the ab- and adsorption is not completely eliminated in both FEP, POMaC, and SEBS [8]. Another main advantage of SEBS over PDMS is that it can be used in higher throughput manufacturing such as injection moulding and extrusion moulding [14].

Besides these elastomers, also, for example, the polyurethane (PU) elastomer researched by Domansky et al. [13], and off-stoichiometry thiol-ene polymer (OSTE), researched by Rimsa et al. [56] are promising alternatives. OSTE is, like PDMS, thermally or UV-curable, giving it the same ease of manufacturing. It is commercially available, and it has no small molecule diffusion and 80% less small molecule absorption when compared to PDMS. However, it does have a lower light transmission than PDMS, making the optical properties of the membrane challenging to be used under a confocal microscope [56].

A thermoplastic synthetic polyester that is elastic is polycaprolactone (PCL). PCL is regularly used in tissue engineering, especially in more recent research [16][68][6][34][11]. It is a biodegradable biomaterial, and it has good mechanical properties, providing tensile strength to hydrogels due to crosslinking when used in a hydrogel combination [6]. PCL is widely used as electrospun fibres. The material itself, however, is hydrophobic.

### Hydrogels

Hydrogels generally have high biocompatibility and physiochemical similarities to in-vivo ECM, increasing cell viability. Therefore a 3D matrix and microstructure can more closely resemble the real ECM than 2D or 2.5D structures. Due to this close resemblance, hydrogels are well-suited for use as a cell-contact material, such as in a tissue construct or a tissue interface barrier. The complex structures can be controlled very well during their manufacturing. They can be used in a 3D-(bio)printer, allowing a wide range of topologies and scaffold structures. Also, sacrificial moulding is a manufacturing method regularly used. [8]

There are three kinds of hydrogels. Natural hydrogels have limited mechanical strength, long-term stability and batch-to-batch reproducibility. Synthetic hydrogels can be adjusted more easily to have the desired reproducible mechanical properties, although they require additional chemical modifications for good cell adherence. Hybrid hydrogels are made with bio-sourced molecules such as hyaluronic acid and amino acids. Terrel et al. [70] state that the most important factors that need to be taken into consideration when selecting a hydrogel are cell compatibility, molecular diffusion rates, and mechanical properties. [70]

The elasticity of hydrogels allows for physiological movements, such as breathing, to be modelled [8]. It has been demonstrated that the matrix stiffness and topography of a hydrogel influences cell adhesion, morphogenesis, differentiation and viability [38]. Primary human alveolar type II cells seeded on Matrigel, a commercially available basement membrane, formed alveolar-like cysts. This is a sign that the in-vivo structure is well simulated [38]. A hydrogel membrane also provides the potential for cell ingrowth into the membrane. On gelatin methacryloyl (GelMA) cells were able to form a confluent alveolar epithelium containing tight junctions [26]. Other advantages include that it is generally an optically transparent and low-cost material [8].

Due to the high compliance of hydrogels, structural support materials are often needed to preserve their mechanical integrity and long-term use. When covering this support material, hydrogels reduce the contact between cells and the support material. Even though unwanted absorption of hydrophobic molecules is better in hydrogels than in PDMS, it might still pose a problem within the hydrogel or support material. Furthermore, hydrogels are not robust to all sterilization methods, possibly creating the need for a sterile fabrication environment. [8]

Moreover, hydrogels such as poly(ethylene glycol) diacrylate (PEGDA) swell when submerged in water. This swelling can influence the architecture and integrity of the membrane [40]. This aspect needs to be considered when, for example, a small pore size or a thin membrane is desired.

### Composite materials

Many hydrogels, such as chitosan (CS) and gelatin, have poor mechanical properties. To circumvent this problem, these hydrogels could be used in combination with other polymers. A possible combination is with pectin [6]. A second possibility is to combine it with polycaprolactone (PCL) [6][16]. The combination of PCL/CS has already been used to create an electrospun liver scaffold, and also Bennet et al. [6] proposed this combination to create a bioprinted scaffold. This combination has several advantages: good mechanical properties, hydrophilicity, good cell growth and attachment. Besides that, this composite exhibits good surface roughness, augmenting cell attachment [6].

This material combination also exhibits swelling due to water absorption. Bennet et al. [6] observed a swelling between 13% and 21% after 72 hours of incubation in PBS. The higher the PCL concentration, the lower the swelling and the higher the elastic modulus. They reported a strain of 0.39 under a stress of 0.0042 kPa. Degradation of the scaffold was also observed after 3 weeks, with a value between 28% and 71.5%, and with PCL having a slower degradation rate than CS. CS enhances wettability and permeability. Subsequently, this stimulates PCL's hydrolytic degradation rate. Bennet et al. [6] state that this composition is promising for developing in-vitro cell cultures.



### 3.1.3. Biodegradability of materials

An interesting characteristic that membrane materials can exhibit is biodegradability. A (partly) biodegradable membrane acts as a temporary structural support for tissue generation. It introduces time as a fourth dimension in tissue engineering. It thereby allows a change of mechanical and chemical characteristics of the membrane throughout the cell culture. Since these characteristics influence cell behaviour, as described previously, a biodegradable membrane can provide an environment that changes with the developing cell culture. It could give advantageous biochemical cues and represent the physical stimulation in a more adequate and complex manner. [80]

Over time the membrane will degrade and have changing features regarding the chemical, physical and mechanical properties [20][80]. The ideal biodegradable scaffold has a degradation rate that matches the regeneration rate of the tissue, and it should have the mechanical properties to support the tissue during generation [20]. For example, the membrane could be thicker or stiffer when a cell monolayer is still being formed and become thinner or more elastic when sufficient tight-junctions have been formed, and a stretch on the membrane is applied [16]. During degradation, the mechanical load can be shifted to the generated tissue. This load shift could ensure a more realistic loading case on cells since the cells can bear more load after the tight junction formation than they would have been able to at the start of the cell culture [80]. Moreover, the use of a degradable material can provide a changing pore size throughout the cell culture duration [16].

A promising example of a biodegradable membrane is by Zamprogno et al. [78], who created a thin biodegradable membrane (10  $\mu\text{m}$ ) mimicking the alveolar barrier, consisting of a collagen-elastin (CE) hydrogel integrated in a gold mesh. The hydrogel degraded after being exposed to an MMP-8 solution. This membrane forms due to surface tension, and when water evaporates from the mixture, the collagen molecules assemble into fibrils. Just as in a human lung's ECM, these fibrils provide a natural structural support. These robust, dried membranes can be shelved for at least three weeks. Another advantage of this biodegradable membrane is that it is still optically transparent (Figure 3.1). Furthermore, the ad- and absorption of the CE membrane were significantly lower than PDMS, making it a promising material for drug and toxicity studies. [78]

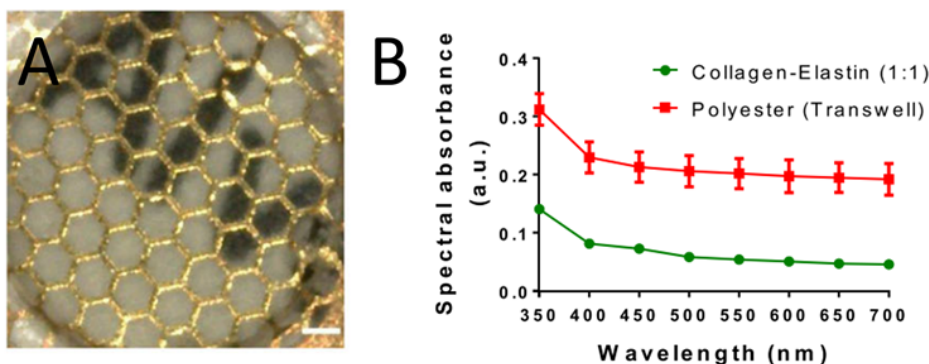


Figure 3.1: A) Optical properties of a 10  $\mu\text{m}$  collagen-elastin membrane integrated in a hexagonal gold mesh. Scale bar: 200  $\mu\text{m}$ . B) Optical properties of the collagen-elastin membrane compared with a standard transwell membrane. [78].

The degradation time of the membrane depends on the concentration of MMP-8 solution applied. Times ranging from one to seven hours were recorded [78]. Nevertheless, longer degradation times should also be obtainable by lowering the MMP-8 concentration. The membrane was subjected to a mechanical strain of up to 10% when lung epithelial cells were present. The membrane's stiffness can be adjusted based on the ratio between collagen and elastin concentrations. The stretchability of the CE membrane was also higher than that of PDMS: at a negative pressure of -2 kPa the radial strain of the CE-membrane was  $9.1\% \pm 2.5\%$ , instead of only  $2.7\% \pm 0.5\%$  for a PDMS membrane of the same dimensions [78]. For a 1:1 collagen-elastin ratio, the radial strain was roughly 5%, at a negative pressure of 1.0 kPa. This indicates an average tissue stiffness of roughly 20 kPa. The stiffness of human alveolar tissue is still about ten times lower [51]. Although it is one of the softer materials found in LOC devices.

Moreover, Zamprogno et al. [78] state that human primary alveolar epithelial cells and human lung microvas-

cular endothelial cells were successfully cultured on both sides of the membrane for at least three weeks. The effect of media flow on the membrane's mechanical properties and its degradation rate were not studied. However, as stated above, hydrogels have poor mechanical properties [68][20]. Thus, some support structure should be needed when using this material.

Fusaro et al. [20] state that instead of natural biodegradable materials, synthetic materials are required, due to their good elastomeric mechanical properties and controllable degradation rate, while still being biocompatible. However, synthetic materials do lack specific binding sites for cell interaction. They used a biodegradable electrospun membrane made of PBCE. This material is very flexible, biodegrades at a fast rate and exhibits good biocompatibility [20]. Biodegradable materials were also applied by Doryab et al. [16] who used a PCL-gelatin membrane to create a variable pore size. With this method, they could create a membrane with a thickness of less than 5  $\mu\text{m}$ , on which only epithelial cells could be cultured.

However, scaffold biodegradability can also adversely affect the cell culture. For example, acidic byproducts may be released during the breakdown of the aliphatic polyesters PLA and PGA. This release has a negative effect on pH, cell mobility, and angiogenesis [80]. Adverse effects, such as these, need to be taken into account. Besides that, the material should also withstand the shear forces and strains exerted on it by the media flow and have an adequate degradation rate. However, overall, a biodegradable material can provide adjustable mechanical or chemical properties and dimensions that recapitulate the native environment at various points in time and therefore can be desired throughout the cell culture to elicit the preferable cell behaviour.

## 3.2. Manufacturing methods for LOC devices

LOC devices are typically manufactured using soft-lithography. Other applied manufacturing techniques include electrospinning, micromoulding, microetching, micromilling, solid object printing, 3D printing, photopolymerization, laser etching, and injection moulding [38]. A LOC device ideally must be produced in a way that is low-cost, high throughput and applicable repetitively. In order to make LOCs low-cost and broadly available, the throughput must be on a significant scale or at least able to scale up. Besides that, in combination with the material, the manufacturing method has a significant influence on the device's eventual structural resolution and properties. Selecting a correct manufacturing method is therefore of great importance. Within the design of LOC devices, the main fabrication techniques found in the literature are soft-lithography, 3D printing and electrospinning. Therefore, these fabrication techniques will be discussed in this section, along with alginate bead moulding. First, the fabrication methods for LOC membranes are discussed. Second, the different ways of creating pores in these membranes are analyzed.

### 3.2.1. Soft-lithography based fabrication techniques

One of the most common fabrication techniques for LOC membranes is soft-lithography. This is a technique that is often used to fabricate PDMS structures and was applied by Huh et al. [28] and Sellgren et al. [61]. The name 'soft-lithography' is based on the fact that a patterned elastomeric polymer is used as a mask, stamp or mould to pattern soft materials [73]. Figure 3.2 shows the basic steps in soft-lithography. A master mould is fabricated by, for example, photolithography or 3D printing, on which PDMS is poured. This mould subsequently acts as a negative for the cured PDMS. Various types of soft-lithography include: replica moulding, microcontact printing, micromoulding in capillaries, microtransfer moulding, and moulding for microfluidics [73]. The technique is very low cost and has significant ease of manufacture. However, high throughput manufacture remains a challenge [46][73].

### 3.2.2. 3D (bio)printing

The development of 3D printing has assisted the design of scaffolds with innovative and previously unobtainable structures. Currently, shapes such as the ear, nose, heart and brain already have been mimicked using 3D printing [80]. As explained by Zhang et al. [80] the scaffold structure provides structural guidance for the cells to aggregate and to generate tissue in a shape dictated by the scaffold. The pore size and geometry influence gene expression, cell proliferation and differentiation. In literature, 3D-printing has been applied by Tas et al. [68], Mejias et al. [44], and Rezaei et al. [55].

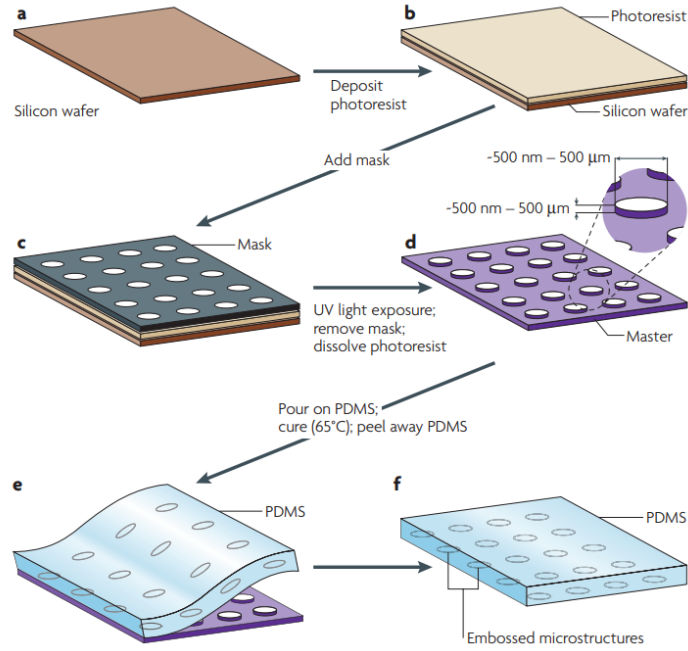


Figure 3.2: Schematic process of the soft-lithography technique to create PDMS structures [73].

### Cell-laden hydrogels

Zhang et al. [80] state that adding cells to the bio-ink allows for the printing of complex and heterogeneous tissues. Also, Tenenbaum et al. [69] and Huang et al. [26] state that bioprinting and cell-laden hydrogels are promising possibilities for the fabrication of more complex and biomimetic 3D structures [69][26]. Furthermore, concerning OOCs, they state that such technology has not been fully explored yet [69]. Moreover, also Huh et al. [29][28] state that growing cells within 3D ECM gels can improve tissue organization and tissue-specific functions. These models are already used in drug efficacy, and toxicity testing [29].

However, although 3D-bioprinting allows for a composition of a multitude of cell types in a shape closely resembling native organs, cell-laden hydrogels do not reconstitute key structural and mechanical features of living organs central to their function. This means two things. First, they fail to recreate an active tissue-tissue interface, which limits the transport of fluids, nutrients, immune cells, and other regulatory molecules [28][8]. Also, contributions of vascular and airflow are diminished [29][8]. Secondly, it restricts the application and transmittance of dynamic mechanical forces such as the breathing mechanism to be transferred between cells, which are crucial for their correct function and development [28]. Besides that, when using cell-laden hydrogels, there is a limitation on the control of cell alignments and diffusion restrictions since the cells may not be evenly dispersed throughout the gel [70].

For all the reasons stated above, the methodology using cell-laden hydrogels is less suitable for creating an alveolar membrane. A possible solution that Terrel et al. [70] propose for the control of cell alignments on hydrogels is the use of photolithography for precise gel localization. This method can, for example, be used to create hydrogel pillars using photomasks. These pillars serve as anchoring points for seeded cells, increasing control of the cell alignment. This approach may, however, generate phototoxicity issues [70]. Bennet et al. [6] also hypothesized that a hydrogel scaffold was more receptive to surface cell seeding than to a cell-laden culture. Thus, when using hydrogels, a separate structure should be made with the hydrogel, on which the cells are seeded afterwards.

Another drawback in using 3D printing is the printing resolution. Rezaei et al. [55] used a combination of CS and PCL to 3D bioprint a scaffold. They found that they could use a strand diameter of 360  $\mu\text{m}$ . The strand would have too weak mechanical properties if they reduced this diameter. However, this strand diameter is

already thicker than the overall thickness of most AOC membranes. Thus, the resolution of the printed structure is a limitation. Extrusion-based 3D printing technology has a resolution of around  $200\ \mu\text{m}$  and ink-jet technology of around  $20\text{--}100\ \mu\text{m}$ . If a smaller, submicron resolution is desired, other technologies such as electrospinning are favoured [80].

Also, in the design of OOCs, hydrogels are generally used in bioprinting. As explained in Section 3.1.2 on hydrogels, these materials have poor mechanical properties. For example, Rezaei et al. [55] were able to print a uniform scaffold with a porosity of 55% on which cells were able to grow, proliferate and migrate. The elastic region of this printed material was very small, with strains below 0.04% and stresses below 0.004 kPa. The weak mechanical properties underline the importance of using a support structure when larger strains are applied on a hydrogel.

### 3.2.3. Electrospinning

Flat, 2D surfaces do not accurately mimic the 3D structure of the ECM found in-vivo. Chen et al. [11] state that an ECM analogue scaffold is required in a cell culture, even if there is media flow present, in order to be able to simulate in-vivo conditions completely. Electrospinning is a good method to mimic this ECM structure because the use of nanoscale fibres allows for the mimicking of the fibrillar structures and porosity of the ECM architecture on the nanoscale (Figure 3.3) [71][70][15]. For example, Jin et al. [34] found that nanofiber membranes have greater cell adhesion than flat surfaces since the structure of nanofibrous membranes is more similar to the ECM of human tissue. Moreover, electrospun membranes have, like real ECM, a high porosity, spatial interconnectivity and high surface area [11].

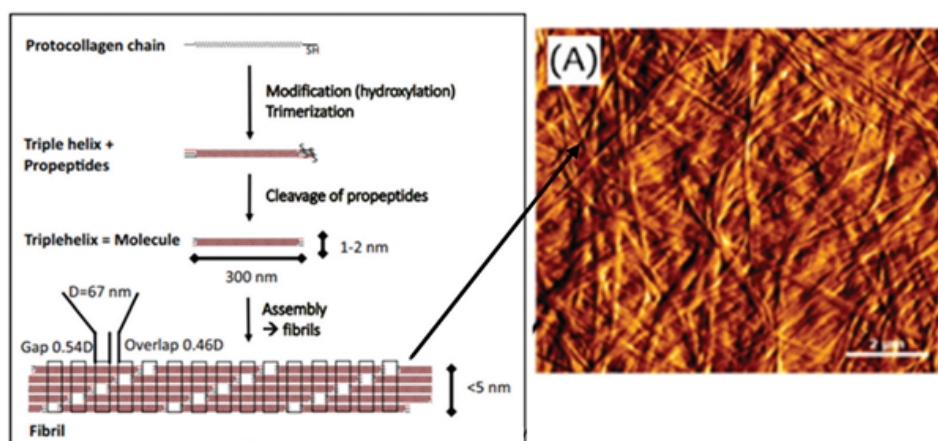


Figure 3.3: Collagen structure and assembly. Atomic force microscopy of dried reassembled collagen [70].

Another reason electrospun membranes could be very promising is that the electrospun fibres could mimic the 'nylon stocking effect'. The nylon stocking effect is the effect that under stretching conditions, the fibre response is a network effect, instead of an individual fibre response [10]. This effect is also seen within the ECM. Although the precise response of the fibre network also depends on the fibre orientation, distribution and thickness. Electrospun scaffolds are widely applied in mimicking the vascular systems, creating endothelial cell scaffolds, but also in bone and cartilage tissue engineering, and for in-vitro cell culture substrates [71][20][11]. Nonetheless, there has been limited research into recreating scaffolds that recreate the 3D ECM in a microfluidic device [11].

Electrospinning is a method where polymer solutions are transferred to fibres with a nano- or micro-sized diameter (Figure 3.4) [11]. An electrospinning machine generally consists of a high voltage power supply, a grounded collector and a syringe pump along with a syringe containing a metal needle (cannula) [20][11]. An electric field exists between the charged metal cannula, which contains the polymer solution, and the collector electrode. When the magnitude of this electric field exceeds the surface tension of the polymer solution, a Taylor cone is created. This cone is elongated towards the grounded collector due to the electrostatic force, creating fibres that dry up due to the evaporation of the solvent [11].

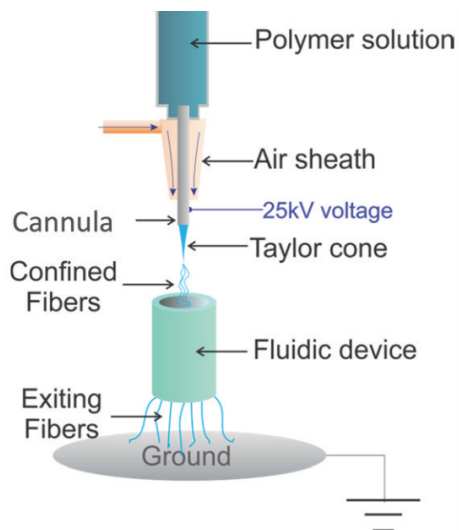


Figure 3.4: Schematic of the electrospinning process [11].

Besides electrospinning, phase separation and self-assembly have also been used to create nanofibrous scaffolds. The advantages of electrospinning are the wide possibility of materials, its easy and cost-effective manufacturing process, and the fact that it generates fibres with comparable dimensions to real ECM fibres. [71]

Materials with good mechanical properties can be used, allowing for applying large strains to be applied to the membrane [15]. Often polycaprolactone (PCL) is used [68][11][34], sometimes in combination with chitosan, gelatin or collagen [20][11]. But also, for example, gelatin fibers [54], p(BCE-co-TECE) [20] and PLGA fibers [76] are used. Although these materials generally achieve sufficient stretch conditions, they often have hydrophobic characteristics, which shows itself in limited cell growth and proliferation [15]. Thus, even though a large range of materials can be used, careful consideration needs to be taken in selecting the right material.

As stated briefly previously, electrospinning has several advantages. The first advantage is the large porous surface area of electrospun membranes. The large surface area to volume ratio in electrospun structures allows for the integration of bioactive molecules [1][15]. These bioactive components can increase cell proliferation, and differentiation [71]. The pore size and the number of pores can be controlled to a certain degree. However, the obtainable pore size is generally very small, limiting a 3D scaffold construction in which cells can migrate and infiltrate into the scaffold [1]. Furthermore, the pore size is often not specified or varies a lot throughout the membrane (Table 3.2). This challenges the creation of a reproducible membrane.

The second advantage of electrospinning is that it is possible to control the fibre orientation [1]. This allows mimicking of the anisotropy of the lung tissue material. To accurately simulate the native ECM and its anisotropic properties, a well-defined architecture with certain introduced alignments is necessary to mimic these mechanical properties [71]. Electrospun membranes have, for this reason, been widely studied in research on the blood vessels or cartilage [20].

This fibre orientation, along with fibre fusion at contact points, largely determines the overall mechanical properties of the membrane and has an influence on cell activity [20]. Moreover, aligned scaffolds can influence the cell orientation and extension and have an influence on the direction cells migrate to [71]. For example, Fusaro et al. [20] found that the cyclic stretching of aligned electrospun fibres had a beneficial effect on endothelial cell activity and proliferation when compared to random fibre orientation. All these variables (surface area, fibre orientation, pore size, porosity) influence cell differentiation, orientation, adhesion, infiltration and migration through the membrane [1][71].

Generally, the nanospun fibres have well controllable mechanical properties. Since the ECM has fibres in the range of 10 nm to 50 nm, fibres with a diameter smaller than 100 nm need to be created to mimic this architecture. Notwithstanding that, the porosity and pore size still needs to be large enough for cell migration, and

Table 3.2: Overview of membranes fabricated using electrospinning.

Author	Stretch	Media flow	Fiber thickness	Membrane thickness	Pore size
Chen et al. [11]	No	Yes	$1.6 \pm 0.6 \mu\text{m}$	$379 \pm 15 \mu\text{m}$	$113 \pm 19 \mu\text{m}^2$
Fusaro et al. [20]	Yes	Yes	$560 \pm 210 \text{ nm}$ $800 \pm 190 \text{ nm}$	-	-
Jin et al. [34]	No	No	200 - 500 nm	$70 \pm 10 \mu\text{m}$	$3 \mu\text{m} - 4 \mu\text{m}^a)$
Laniece [40]	Yes	Yes	-	$1 \mu\text{m}$	$2 \mu\text{m}^b)$
Tas et al. [68]	Yes <sup>c)</sup>	Yes	$441 \pm 1490 \text{ nm}$	$\sim 20 \mu\text{m}$	-
Yang et al. [76]	No	No	-	$2.3 \pm 0.2 \mu\text{m}$ to $9.1 \pm 1.2 \mu\text{m}$	-
Radiom et al. [54]	Yes <sup>d)</sup>	Yes	few 100 nm	100 - 500 nm	1 - 10 $\mu\text{m}$
Zhou et al. [82]	Yes	Yes	$2.5 \mu\text{m}$	$\sim 300 \mu\text{m}$	-

<sup>a)</sup> 77% between 1 - 10  $\mu\text{m}$ ; <sup>b)</sup> average pore size; <sup>c)</sup> duration: 2 hours; <sup>d)</sup> duration: 1 hour.

infiltration [71]. However, it is challenging to make nanofibers with a diameter of less than 10 nm that still have good mechanical properties [1]. Most fibre diameters used in LOCs do not reach below this 100 nm.

Subsequently, the major disadvantage of creating an alveolar membrane with this method is the possible membrane thickness. Although electrospinning seems an excellent option, it is critical to create a thin membrane when mimicking the alveolar-capillary barrier. Generally, 10  $\mu\text{m}$  is used as a membrane thickness, and the in-vivo alveolar barrier (including cells) is around 1  $\mu\text{m}$ . Besides that, the membrane also needs to be strong enough to be subjected to a cyclic strain of roughly 15%. Generally, electrospun membranes do not near the standard 10  $\mu\text{m}$  membrane thickness. If they do, they generally do not have exhibited mechanical properties that are good enough to culture cells under cyclic strain for multiple weeks.

An overview of the characteristics of several electrospun membranes found in literature can be found in Table 3.2. Additional information on these membranes can be found in Figure A.1 in Appendix A, which includes a table containing all LOC devices found in literature. Noteworthy is that many papers do not mention their specific (range of) pore sizes. Also, there is a large variation within the pore sizes and fibre thicknesses.

Laniece [40] found that each membrane patch that they used also varied regarding nanofibers configuration and specific porosity. She used thin gelatin nanofibers spread over a honeycomb PEGDA support structure to create a nanospun membrane for cell cocultures. This membrane is the thinnest electrospun membrane used to mimic the alveolar membrane seen so far ( $< 1 \mu\text{m}$ ) and nears the biological in-vivo dimensions of the membrane. Both a media flow and a cyclic stretch were exerted on the membrane. The cyclic strain they could obtain was 6.2%, which is below the physiological strain threshold. Also, the support structure bulged, adding to the total deformation (Figure 3.5). Besides that, the applied flow was not enough to induce physiological shear stress.

Another example of an electrospun mesh is by Chen et al. [11]. They made an airway-on-a-chip model by using a circular base structure of PDMS, on which a fibrous scaffold was deposited by electrospinning. Human dermal fibroblasts grown on the substrate resembled in-vivo regarding morphology and cell size, and they could adhere to the scaffold well. Furthermore, no fibre detachment was seen when the fluid flow was introduced. However, no cyclic stretch was applied. Yang et al. [76] also created a very thin membrane but did not include a cyclic stretch, by which the membrane thus could become thinner.

Both Radiom et al. [54] and Tas et al. [68] designed promising membranes with a thickness of 100 – 500 nm and about 20  $\mu\text{m}$  respectively. Both LOC designs included media flow, along with a cyclic stretch. However, it is unknown if these membranes are suitable for experiments spanning multiple weeks since their experiments, including stretch and media flow, did not span more than 1 hour and 2 hours, respectively.

Jin et al. [34] designed a nanofibrous membrane to look at the neutrophil displacement through the membrane. The membrane was electrospun with PCL and consisted of several electrospun layers of  $70 \pm 10 \mu\text{m}$  thick, making up a membrane of 150  $\mu\text{m}$  thickness overall. The membrane was placed between two PDMS



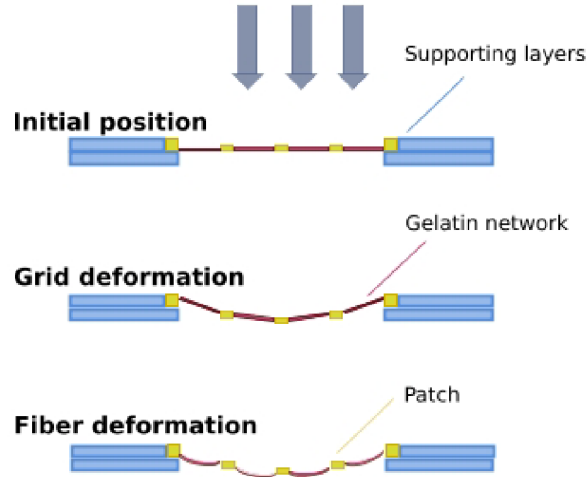


Figure 3.5: Bulging of the support structure under an orthogonal pressure [40].

chambers. The nanofibrous membrane had a dominant pore size of 3 to 4  $\mu\text{m}$ . Neutrophils were able to travel through this membrane, even though Jin et al. [34] found that many neutrophils remained stuck in the membrane.

Zhou et al. [82] designed a fibrous superhydrophobic membrane with a large obtainable biaxial strain (up to 700% under cyclic loading conditions). This membrane was produced by electrospinning poly(styrene-butadiene-styrene) p(SBS) combined with FAS. P(SBS) is biocompatible, and it can be produced on a large scale using a commercial product. Hysteresis, due to fibre reorientation, was found not to have a significant difference after the first 200 cycles. However, the membrane produced was significantly thicker than the thickness desired for an alveolar membrane, with a thickness of 300  $\mu\text{m}$ . [82]

In conclusion, an electrospun membrane that is strong enough to create long-term structural support for cells while withstanding cyclic strain and media flow is generally too thick. Furthermore, there is much variation in porosity, nanofiber and pore size and distribution. This variation poses a challenge when an easily reproducible membrane is desired. Therefore, an electrospun membrane is not the most suitable approach for designing a membrane mimicking the alveolar-capillary barrier. It might be a better approach for thicker membranes such as the larger airways.

#### 3.2.4. Alginate bead moulding

Another fabrication technique worth mentioning is the technique by Huang et al. [26], who fabricated a membrane with an alveoli-like 3D inverse opal structure by moulding GelMA hydrogel using dissolvable alginate beads (Figure 3.6). First, a lattice of uniform alginate microbeads was assembled, after which the GelMA solution was added to the voids between the beads and crosslinked. Subsequently, the alginate beads could be quickly removed using a M EDTA solution. Roughly 7050 microbeads, spread over three layers, provided a membrane with a thickness of about 546.4  $\mu\text{m}$  and a pore size of  $\sim 200 \mu\text{m}$ . This pore size was chosen because it resembles the dimensions of alveoli in the lung. This method resulted in an alveoli-like 3D hydrogel with uniform pores. Although this manufacturing method does not provide a thin membrane on which a coculture can be created, it can be used as an inspiration for manufacturing methods. [26]

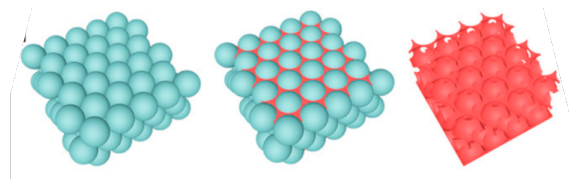


Figure 3.6: Schematic of the alginate bead molding process [26].

### 3.2.5. Creating pores in LOC membranes

Pores in a membrane are often created simultaneously and with the same manufacturing technique used to fabricate the membrane itself. For example, in soft-lithography, 3D printing and electrospinning, the pores can be formed during the fabrication process. However, these pores generally have a relatively large diameter. In soft-lithography, which uses moulding, pore sizes rarely are below  $10\ \mu\text{m}$ . In 3D printing, the printing resolution limits the pore size, which is already a limitation in the fabrication process. Electrospinning gives a wide range of possible pore sizes, depending on, e.g. the spinning time, fibre diameter and material used.

Other fabrication methods used to create pores in LOC membranes include: track etching, laser etched pores, block-copolymers and nanosphere lithography (NSL). Laser etching pores can, for example, be done with a femtosecond laser. This fabrication method is suited for small surfaces and pores larger than several micrometres [2]. Nanosphere lithography can achieve a resolution smaller than the conventional photolithography resolution limit of  $2\ \mu\text{m}$ . It relies on the use of self-assembling nanospheres in the etch mask fabrication [32]. As simple schematic of the process can be seen in Figure 3.7 [47]. Pores designed with this technique can reach below  $500\ \text{nm}$  [32].

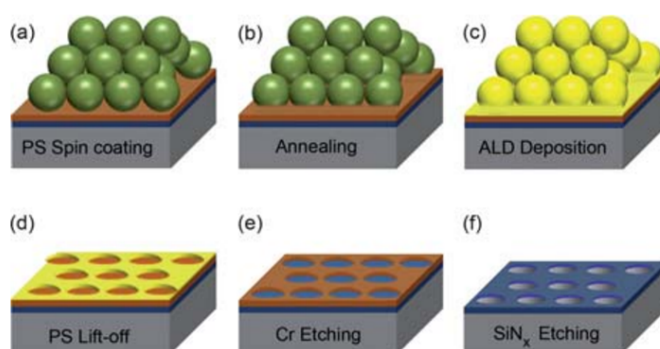


Figure 3.7: Schematic of the step-by-step fabrication of pores, using NSL [47].

Track etching is done on thin polymer membranes to create straight pores through the membranes. This is a well-known and widely used production technique, mainly used on PET transwell inserts (Figure 3.8). In this method, energetic ions are discharged at the material, altering its material properties. These regions are subsequently chemically etched, creating hollow channels [59]. The porosity and pore size can be independently varied in a wide range. The pore size can range from  $10\ \text{nm}$  to tens of micrometers, whereas the pore density can range from  $1$  to  $10^{10}\ \text{cm}^{-2}$  [3].

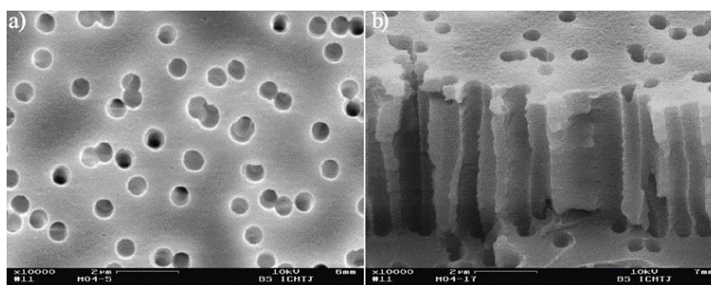


Figure 3.8: SEM image of a track etched PET membrane [59].

The block-copolymer technique uses a combination of block polymers, which microphase-separate (Figure 3.9). This creates a homogeneous, crosslinked nanostructured composite. By chemically etching, one of the block polymers can be etched away, leaving monoliths with a porous structure behind [62]. This technique is suited for relatively small surfaces and mesopores, which are pores between  $2$  and  $50\ \text{nm}$  [41].



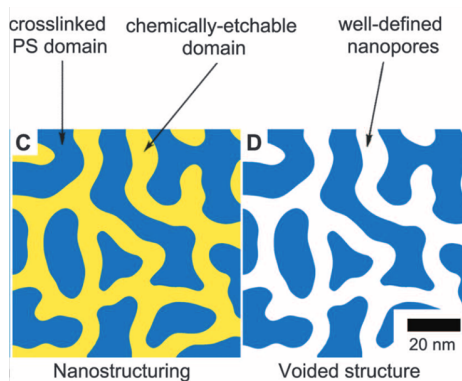


Figure 3.9: Schematic visualisation of block-copolymer nanopore fabrication [62].

### 3.3. Membrane integration methods

Besides the material and the manufacturing technique, the membrane's integration into the rest of the LOC device needs to be taken into account. The membrane itself should be leak-tight connected to the rest of the microfluidic device. This membrane integration is not always an easy task since this integration should remain intact and leak-tight while subjected to a cyclic strain. Several methods have been proposed to integrate a membrane into the device in the literature.

When no cyclic stretch needs to be applied, a standard integration frequently used with various membrane materials is to sandwich the membrane between 2 layers of PDMS. These layers are sealed together by slow-curing liquid PDMS between them. This was done by Nalayanda et al. [45], who used a porous PET membrane. This method, however, produces a membrane integration that is often not strong enough to remain intact when cyclic stretching is applied.

When using a PDMS membrane in a PDMS device, the integration bond is often a lot stronger than when using different materials, allowing for straining of the membrane. Oxygen plasma treatment can bond the membrane and the rest of the device together. This treatment was done in the devices of both Jain et al. [33], and Nissar [46]. Another bonding option when using PDMS on PDMS is using a corona treater. Douville et al. [17] irreversibly bonded a 100  $\mu\text{m}$  thick PDMS membrane, where a large bonding surface area was present. They were able to create a leak-tight membrane undergoing a cyclic bulging stretch. However, given that the membrane is irreversibly bonded to the chip, the membrane can not be reversibly taken out of the device for further analysis.

Regarding the integration of electrospun membranes, there are few reports. Chen et al. [11] proposed the solution of directly spinning the fibres onto the contact surface. However, this would bring several manufacturing challenges, and the membrane would not be easily retrievable. Laniece [40] did the integration of the membrane by adding a solid PEGDA outer ring for increased surface area and an extra PDMS middle layer to the membrane (Figure 3.10). The membrane in the chip was retrievable, allowing to take the membrane out of the device for analysis momentarily. The device itself was pressed together by an external casing to diminish any leakage. She detected that a leak-tight integration becomes more difficult when using handmade electrospun membrane patches. Because a few hundred microns difference can already cause a leakage in the membrane integration [40].

Laniece's [40] solution was to 'pre-bond' the membrane. The designed membrane had an outer solid ring, where no cells or structures were present and to which another layer could be attached. A middle PDMS layer was first bonded on top of the designed membrane. Afterwards, this middle layer was plasma bonded to the device's top and bottom PDMS parts, thereby fully sealing the membrane into the PDMS layers. The middle layer has a hole with a diameter a little bit smaller than that of the membrane. The overlap between the membrane and the middle layer was 4 mm. This method allows for bonding of the membrane and an open cell culture. [40]

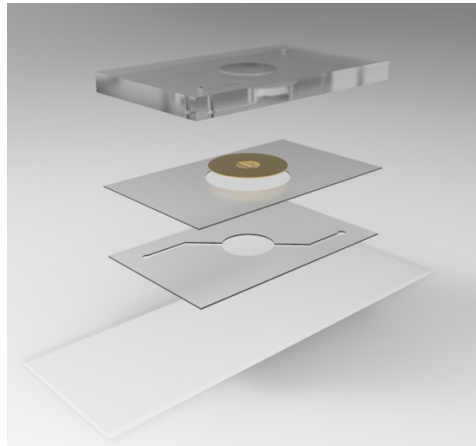


Figure 3.10: A burst view of the LOC device by Laniece [40].

In order to further increase the contact between the PDMS layers, Laniece [40] also proposed the use of a magnetic clamp, which exerts an equally divided pressure over the chip. She found that using such a clamping device, in combination with introducing a middle layer, prevented any leakage along the membrane, even though a pressure of at least 800 mbar was applied and the membrane was deflected out-of-plane.

For the design of a good membrane integration when an in-plane strain is applied on the membrane, several factors play a role: First, the materials of the contact surfaces of the membrane and the device should be compatible. This means that a strong bond between these surfaces should be possible. Second, the strength of this bond can be increased by a larger contact surface area or by 'pre-bonding' the membrane to a middle layer [40]. Last, a clamping device could help with further eliminating any possible leakage.

This chapter provided a more in-depth review of the possible membrane materials, manufacturing methods, and membrane integration methods for LOC devices found in the literature. Careful consideration of all the advantages and disadvantages needs to be made regarding the materials and methods, depending on the device's desired functionality. The next chapter will cover the membrane requirements that need to be considered when designing a membrane for an AOC.



# 4

## Membrane requirements

In order to obtain the required functionality within an AOC device, several requirements need to be taken into account. This chapter covers the various requirements for designing an adequate AOC membrane based on the literature.

The alveolar-capillary barrier that is aimed to be recreated is an elastic and exceptionally thin porous membrane. Doryab et al. [16] state that in order to allow for transport across the membrane barrier, three things need to be taken into account: a low membrane thickness ( $\leq 5 \mu\text{m}$ ); large pore size (up to  $8 \mu\text{m}$ ); and high porosity (around 9%). According to Doryab et al., two phases can be discerned during cell culture growth. In Phase 1, alveolar epithelial cells adhere to the membrane. They proliferate and grow into a connecting monolayer, forming tight junctions. In this phase, the membrane is still fully submerged on both sides, and no stretch is yet applied. In Phase 2, the cell layer will be further cultured under ALI conditions. This means that the media is interchanged with a gas flow on the apical side, initiating epithelial cell differentiation and acclimatization. During this acclimatization, cells will polarize and secrete surfactant. In the second phase, the cells are continuously secreting a cell-secreted ECM, which forms a layer underneath the cells between them and the membrane. After the cells have formed a monolayer during this phase, a cyclic strain can be applied. [16]

Table 4.1: Overview of membrane requirements.

Membrane requirement	Value
Chemical inertness	Minimal molecule ab- and adsorption and chemical reactivity
Biocompatibility	Long-term biocompatibility must be present
Wettability	$\text{WCA} < 70^\circ$
Stiffness	1 kPa - 0.3 Mpa
Actuation pressure	$\leq -800 \text{ mbar}$
Membrane diameter	3 mm
Membrane thickness	$\leq 10 \mu\text{m}$
Pore size	$\leq 3 \mu\text{m}$ in Phase 1, $\geq 3 \mu\text{m}$ and $\leq 8 \mu\text{m}$ in Phase 2
Permeability	$\sim 4.3 \times 10^{-6} \text{ cm/s}$ to proteins
Strain	$\geq 20\%$
Breathing frequency	0.2 Hz
Shear stress on endothelial cells	$\sim 1.54 \text{ N/m}^2$
Optical transparency	Adequate for confocal microscopy
Sterilizable	70% ethanol or 5% $\text{H}_2\text{O}_2$
Sustain x number of cycles	$\sim 5 \times 10^5 \text{ cycles}$
Membrane integration	Leaktight, detachable after experiments

Thus, for each phase, different membrane characteristics are desired. Figure 4.1 gives a schematic overview of how the different characteristics can change throughout the different phases. The phases begin with cell

seeding, after which a monolayer is formed. Once this layer has been formed, the ALI is introduced. In Phase 1, a membrane should be bioactive, promoting cell adhesion and growth, besides being wettable and non-porous or containing small pores. It should contain small pores so that cells do not travel through the membrane. These characteristics are optimal for cell monolayer formation. [16]

Then after the ALI has been introduced and the cells have differentiated, a strain can be introduced. For this second phase, the membrane needs to be permeable and porous to allow transport of nutrients and signalling molecules. Furthermore, the membrane also needs to have an elasticity that recapitulates the human lung's ECM while being tough enough to undergo a cyclic strain [16]. Table 4.1 gives a brief overview of the requirements for an AOC membrane. Each requirement is further elaborated on in the rest of this section.

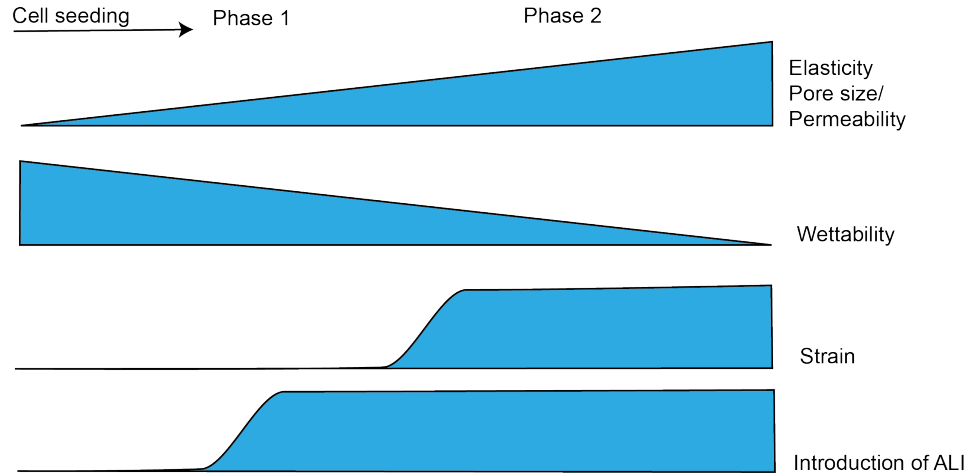


Figure 4.1: Schematic representation of the membrane properties throughout the cell culture. Based on Doryab et al. [16].

**Chemically inert and biocompatible:** The membrane should react minimally with any other chemical compounds present in the cell culture. Furthermore, it must be non-absorbent to molecules in the medium. These molecules can include drugs, proteins and growth factors [16]. This is relevant because this interaction with molecules can influence the accuracy of drug screening experiments [23].

Furthermore, the membrane material should be biocompatible. Both endothelial and epithelial cells should be able to create a confluent monolayer on the membrane without any cytotoxic effects [76][8]. Moreover, the material should remain biocompatible for the whole study duration so that long-term cell viability can be acquired. Although, once the cells have formed a confluent monolayer and they have started to secrete their own ECM, their contact with the membrane becomes less [1][15]. Thus, since the contact diminishes, the biocompatibility of the membrane also becomes less crucial.

**Hydrophilicity and wettability:** The cell substrate must have certain hydrophilicity and wettability, in order for cells to adhere adequately to the surface. A hydrophobic material would need a surface pre-treatment to enhance cell adherence. This surface treatment is, for example, done with a collagen coating, as is often done on a PDMS surface [56]. Regarding the wettability, Doryab et al. [16] state that a water contact angle of less than  $70^\circ$  is favourable ( $WCA \leq 70^\circ$ ). A WCA of less than  $90^\circ$  indicates a hydrophilic surface. Most synthetic materials used in OOC applications are hydrophobic. Therefore, this characteristic need to be taken into account when selecting materials.

The required wettability may also change throughout the cell culture stadia. A higher wettability is desired during the first phase to improve cell monolayer formation. In the second phase, the cells have started to secrete their own ECM, which creates a layer between the support membrane and the cell layer. Since the cells have already formed a continuous layer including tight junctions and are not in direct contact with the membrane anymore, the membrane may in this stage have a slightly diminished surface wettability (a larger WCA). [16]

**Stiffness:** The membrane must be stiff enough to support the adjacent cells, but also elastic enough to sustain cyclic breathing movements. The pressure actuator (Elveflow, OB1 MK3+ microfluidic flow controller) used for the AOC device by Nissar [46] can exert a negative pressure of 800 mbar on the membrane. The membrane should be elastic enough to provide the desired strain under this pressure or less.

Besides that, membrane stiffness also influences cell behaviour. The stiffness of the ECM has an influence on cell migration (e.g. by mechanotransduction), differentiation, cell division and maintaining homeostasis [22]. Zamprogno et al. [77] found, for example, that human fibroblast cell spread is reduced on soft surfaces compared to stiffer surfaces. The stiffness also influences cytoskeleton formation [22]. Softer membranes diminish tight junction formation and augment the distribution of actin, whereas stiffer membranes enhance the formation of F-actin cytoskeleton [16]. The stiffness of the membrane may also differ when various diseases are studied. For example, the collagen content increases in pulmonary fibrosis, which stiffens the alveolar-capillary barrier tissue.

Preferably, the membrane mimics the stiffness of the in-vivo basement membrane [49]. The stiffness of an alveolar wall ranges in the literature between a Young's modulus of 1 kPa [15], and a stiffness of 0.3 MPa [16]. Osario et al. [49] for example, stated an elastic modulus of 3.4 kPa in uniaxial tension, and Pasman et al. [50] stated a Young's modulus of lung tissue of 400 Pa or lower. It is relevant to note that in the design of a membrane, the overall membrane stiffness should be widely considered next to the material stiffness, since this greatly influences the membrane stretch that can be obtained and transferred to the adhered cells.

Throughout the cell culture the stiffness may vary. When no stretch is yet applied in the first phase, the membrane may be less elastic. In Phase 1 the membrane also largely has a support function and may therefore be stiffer than native alveolar-capillary barrier tissue. The elasticity becomes an important variable and needs to have a significant value when stretch is applied, and the membrane is deformed. This is also shown in Figure 4.1.

**Dimensions:** The membrane is designed to fit in the design by Nissar [46] and should therefore have suitable dimensions. These dimensions include a membrane diameter of 3 mm, excluding the membrane edges used for the membrane integration. Furthermore, a membrane with microscale thickness is needed to allow for efficient gas exchange [76]. The membrane thickness should mimic the alveolar-capillary barrier thickness as closely as possible, which is made up of 2 basement membranes of 50 nm each, creating a membrane with a thickness of 0.1  $\mu\text{m}$  overall [76]. Generally, an AOC membrane has a thickness around 10  $\mu\text{m}$  and few membranes have been designed to be thinner than that. Most membrane thicknesses have been determined by the manufacturing possibilities rather than a biologically based choice. This is due to the trade-off between membrane thickness and membrane strength, and due to the achievable manufacturing resolution. Thus, the thickness should adequately recapitulate the in-vivo properties while considering the materials and manufacturing methods. The device dimensions should also allow the cell culture to be studied under a confocal microscope. When using the device of Nissar [46], a membrane with a thickness of 10  $\mu\text{m}$  has been found to fit within the working distance of a confocal microscope (HCX PL Fluotar L 40x objective).

**Pore size and permeability:** Standard transwell inserts can generally be obtained with a pore size between 0.4  $\mu\text{m}$  and 8  $\mu\text{m}$  (Corning Incorporated, Corning, NY). Most LOC devices also contain pore sizes within this range, though some membranes do not contain pores [74][17][35][30]. However, many studies do not elaborate on their decision to choose a specific pore size.

A permeable and porous membrane is desired to facilitate nutrient and protein exchange through the membrane. For example, Pasman et al. [50] found that in static cell cultures, a higher cell density was possible on more permeable membranes since those facilitated a better nutrient supply. Furthermore, to measure lung inflammation, neutrophil movement needs to be observed. An indication of lung inflammation is the process of neutrophil displacement from the micro-vascular channel to the alveolar chamber [64]. Also, the cytokine interleukin-8 (IL-8) gene expression and subsequent protein release happen when inflammation is present [16][7]. This neutrophil and protein migration happens through the membrane, and thus a porous membrane must be incorporated. Moreover, pore size influences macrophage migration through the membrane. Besides that, pore size also influences cell differentiation, proliferation, adhesion, growth and viability

[80].

The membrane is expected to have an increased permeability under dynamic loading conditions compared to static conditions. This increase is because the pore size increases when strain is applied to the membrane. For example, Doryab et al. [16] found that pore size increased by a factor of 1.10 when a strain of 21% was applied. The device should have a watertight barrier between the upper and lower chambers even with this increased permeability. As a reference for the permeability value, Zhang et al. [79] stated that the permeability of mammalian capillaries to proteins is about  $4.3 \times 10^{-6}$  cm/s. Huh et al. [28] state the in-vivo level of protein permeability is 1-2%/hr. Regarding the porosity, Doryab et al. [16] aim at a porosity of 9%, whereas Nissar aims at a porosity of 3% - 3.5% [46].

Doryab et al. [16] state that in the first phase, no pores need to be present in the membrane. If pores are present, the maximum pore size is between 1-3  $\mu\text{m}$ , to avoid epithelial and endothelial cells from travelling through (or into) the membrane. This migration must be prevented since these cells need to form a confluent monolayer on their respective membrane sides. Zhang et al. [80] also state that 2.5 – 3.5  $\mu\text{m}$  is the minimum pore size which cells can infiltrate and through which they can migrate. However, there still needs to be sufficient nutrient supply in this phase, especially on a poreless membrane, where no nutrients can travel through the membrane. Pasman et al. [50] demonstrated that on a poreless membrane, compared to a membrane with pores, cells could grow more poorly.

Larger pore size was observed to allow cell penetration and immune cell recruitment in-vivo. Zhang et al. [79] noted that endothelial cells could migrate through 20  $\mu\text{m}$  pores, which indicates that a pore size of this dimension could be too large. This has also been determined by Doryab et al. [16] who stated that in Phase 2, a larger pore size of up to 8  $\mu\text{m}$  is desired. This pore size could allow for neutrophil and macrophage migration across the membrane. They determined that on pore sizes larger than 8  $\mu\text{m}$ , which is larger than a single epithelial cell, no confluent monolayers could be formed.

Thus the dilemma arises that when pore sizes are very small (e.g. the often used 0.4  $\mu\text{m}$ ), immune cells cannot pass through the membrane, but when the pore sizes are larger than 3  $\mu\text{m}$ , endothelial and epithelial cells can pass through the membrane, which hinders their adherence and monolayer formation.

A solution for this dilemma has been proposed by Doryab et al. [16] with their PCL and gelatin composite membrane (Figure 2.14b). They were able to create a membrane with a variable pore size up to 8  $\mu\text{m}$ , on which a confluent epithelial cell layer was cultured. Initially the membrane contained no pores. The porosity was also variable throughout the cell study up to  $9.4 \pm 0.2\%$ . Although a cyclic out-of-plane strain of 25% could be applied to this membrane, this was only experimentally tested for 48 hours under submerged conditions [16]. Besides that, this membrane only contained a monoculture of epithelial cells. Thus, although this is an improvement in the approach to pore sizes, the membrane in this design has not yet been proved suitable for use in long-term cocultures.

Furthermore, Huang et al. [26] demonstrated that uniform pores are preferable to random pores in experiments, even though the (average) pore size might be the same. Pasman et al. [50] also made the link between a less homogeneous pore distribution and a less confluent monolayer. This is noteworthy, since LOC devices often contain a range of randomly distributed pores and pore sizes [54][34][40][20][16].

Thus, an ideal membrane should have a uniform pore size below 3  $\mu\text{m}$  in the first phase, where a confluent monolayer is created. After this monolayer is created, a larger pore size is desired in order to mimic the in-vivo transmembrane processes such as neutrophil migration more closely. To date, little literature is present, however, on pore sizes and their effects in endothelial and epithelial in-vivo cell cultures.

**Cyclic stretch:** The membrane should be able to sustain cyclic stretch for several weeks. The physiological strain range is between 4% and 12% [54][15]. And strains over 20% are considered pathophysiological [7][68]. Since an adequate membrane should be able to recapitulate the complete (patho)physiological strain range, a strain of at least 20% must be sustained by the membrane in order to be able to mimic the whole range of physiological breathing movements and to also be able to recapitulate a pathophysiological environment.

The cyclic stretch, which exerts a strain on the cells, influences multiple cellular behaviours [28]. It enhances the formation of tight junctions [16]. Furthermore, it influences: pulmonary epithelial cell proliferation; differentiation; surfactant secretion; and migration [15]. It also influences disease onset and advancement. These effects occur since mechanical stimulation affects specific signalling pathways, which influence gene expression and protein synthesis [15]. For example, a strain between 15% and 20% on endothelial cells increases fibroblast growth factor release, activation of factor/monocyte chemoattractant protein-1 (MCAF/MCP-1), and production of the inflammatory cytokine IL-8 [7]. Besides that, overstretching of the alveolar membrane can cause a disruption of the tight junctions, causing damage to the cell monolayer and loss of cells [15][7]. This increases vascular leakage, which can lead to oedema [1]. Thus, mechanical stimuli are vital in recapitulating the (patho)physiological circumstances to study the effect of possible treatments in an in-vitro environment [15].

The type of cyclic stretch is often a sinusoidal cyclic stretch, as applied by Doryab et al. [15] and Stucki et al. [66], but it can also be a triangular cyclic stretch, as applied by Nissar [46] and Stucki et al. [67] three years later. The cyclic motion mimics the breathing motion, generally with a frequency of 0.2 Hz [26].

Various types of strain are present in LOC devices, as discussed in Section 2.4.2. Biaxial or triaxial stretch simulates the in-vivo environment more closely than uniaxial stretch. Huh et al. [28] observed that cells align to the loading direction perpendicularly when uniaxially stretched. This does not resemble the in-vivo cell behaviour and thus, biaxial or triaxial stretching should be selected over uniaxial stretching. In contrast, there is little information present in the literature on whether cells behave differently when subjected to a two-dimensional or three-dimensional stretch and whether this influences how well cells can be cultured.

Out-of-plane biaxial or triaxial stretching, or bulging, of small diameter membranes, does resemble the in-vivo type of stretching since the alveoli also exhibit a bulging of the membrane. However, often devices can not provide a media flow at the same time as bulging the membrane [66], because the same chambers are used for both purposes. Furthermore, if a media flow is provided, the shear stress exerted by the fluid flow passing by the membrane exerts a different effect on out-of-plane stretched membranes than on in-plane stretched membranes. The media will flow parallel to the membrane for in-plane stretched membranes, creating a uniform shear flow over the membrane. In out-of-plane stretch, the flow will not uniformly exert a shear on the membrane since the channel itself will not deform along with the membrane (Figure 4.2). This creates areas where shear stress will be higher than other areas. In the human body, the pulmonary vessel can generally be assumed to also deform along with the alveolar membrane, avoiding these local variations in shear stresses (Figure 4.3).

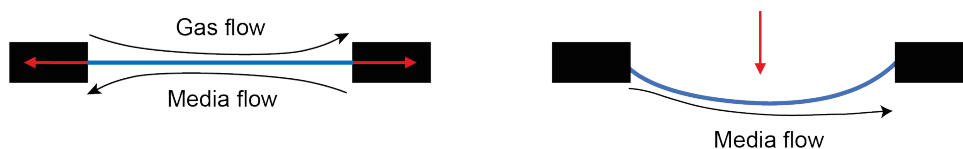


Figure 4.2: Schematic illustration of media and gas flow alongside an in-plane stretched membrane and an out-of-plane stretched membrane. Red arrows indicate the stretching direction.

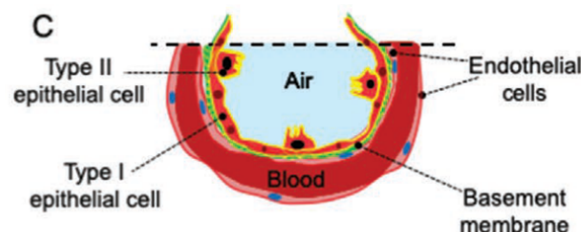


Figure 4.3: Schematic of the alveolar-capillary barrier [16].

Although the fluid flow in these devices is generally low, this aspect still needs to be considered. Besides



that, as explained previously in Section 2.4.2, on larger diameter membranes bidirectional in-plane stretching exerts roughly the same effect as triaxial out-of-plane stretching, regarding the applied surface area strain. Therefore, an in-plane biaxial stretch is best applied to the membrane. Furthermore, in a membrane that uses a bulging stretch, there is at least one actuation channel that exerts the pressure difference needed to bulge the membrane. Since this research aims to have two channels with medium flow (both gas and liquid), two flow channels should be present. The actuation for this membrane stretch is therefore controlled via separate actuation channels that run around the sides of the membrane (Figure 2.15).

**The air-liquid interface and shear stress:** The air-liquid interface (ALI) is an essential feature of healthy lungs. An ALI consists of the epithelial cell layer, on which a thin liquid surfactant layer is present and its boundary with the air. This surfactant layer separates the epithelial cells from the air [69]. The presence of air increases surfactant production, which is crucial in maintaining the stability of the membrane [64][69]. Furthermore, including airflow also introduces a more biomimetic permeability by decreasing the surface tension [64].

Douville et al. [17] note the importance of including both solid and fluid stresses within the device. Besides cyclic membrane straining, the AOC should also include a media flow on the basal side of the membrane and a gas flow on the apical side. Both flows, especially the media flow, can exert a shear stress on the adjacent cells, and this may play a role in the mechanoregulation of the cell layers [30]. It also plays a vital role in pathology, and disease mechanisms [17].

In conclusion, the LOC device should include both an ALI and physiological shear stress. The shear stress exerted on endothelial cells due to blood flow ranges between  $0.28 - 9.55 \text{ N/m}^2$ , with a mean value of  $1.54 \text{ N/m}^2$ . The shear stress in the smallest capillaries is in the higher range [39]. Besides mimicking the physiological shear stress, the ALI should remain intact under cyclic stretch: no medium leaches to the air interface side; and no cells detach from the membrane [16]. Furthermore, an open reservoir generally makes it difficult to create fluid stresses by a pressurized fluid flow, so the fluid channels should be able to be closed off if a pressurized fluid flow is desired [17].

**Handling requirements:** Various handling requirements also need to be met to make the chip suitable for laboratory use. These requirements include the possibility for direct on-chip cell seeding, confocal microscope analyses, ease of use and membrane recovery. Furthermore, the membrane needs to be designed such that it can be reproducibly manufactured. A closed chip configuration is unfavourable regarding the standard handling principles applied in both the Erasmus Medical Center, as well as in laboratories and the pharmaceutical industry [79]. Therefore, an open chip configuration is preferred to practically seed the cells on the chip and allow live imaging. The device by Nissar [46] contains a resealable chip configuration that can later be opened when cell seeding or imaging is done.

The device, including its membrane should also be sterilizable. At the Erasmus Medical Center this is done with 70% ethanol or 5%  $\text{H}_2\text{O}_2$ . Also Jin et al. [34], Tas et al. [68] and Shresta et al. [64], for example, used these sterilization methods. Other sterilization techniques found in literature include: UV sterilization [17][11][40][55], ozone sterilization [66][78], ethylene oxide [19] or a combination of ethanol and peracetic acid [53].

**Cell culture duration and cells used:** The chip is designed for studies ranging from 2 to 4 weeks. At a breathing frequency of 0.2 Hz a study of four weeks contains just less than  $5 \times 10^5$  stretching cycles. Therefore, the membrane must maintain its intended properties for this duration at least. The type of cells that are desired to be cultured on the membrane are primary endothelial and epithelial cells. Since these cells are relatively hard to culture, also cancer cells could be tested initially in order to obtain a proof of concept.

**Membrane integration:** The membrane should be detachable after the cell culture experiments to allow for additional testing. The membrane integration should therefore allow for suitable membrane removal. Besides that, the membrane integration should be robust enough to resist and prevent leakage or membrane detachment during cyclic stretching.

The requirements presented above should ideally all be taken into account when designing an adequate membrane for an AOC device. Based on the literature and these requirements, a conclusion and a design plan for designing a membrane will be proposed in the next chapter.

# 5

## Conclusion

This literature review covered membrane design for an alveoli-on-a-chip (AOC) device. It provides an in depth review of the state-of-the-art LOC devices designed to date. Furthermore, it gives a clear overview of the requirements that an AOC membrane should exhibit. Moreover, an explanation of the characteristics of the various material groups used for LOC membranes was provided. Commonly used manufacturing methods were also covered in detail.

It has become clear that there has been much advancement in the field of LOC devices in recent years, and to date, it is a broadly covered research topic in literature. Nevertheless, there are still many improvements possible in the current designs. For example, the use of PDMS as an OOC material is undesirable due to its high ad- and absorption of small molecules, which influences the accuracy of drug evaluation studies.

The alveolar-capillary barrier that is aimed to be recapitulated is an elastic and exceptionally thin porous barrier. To achieve an adequate membrane in-vitro, several requirements need to be met. The first is that a thin membrane must be incorporated. Besides that, the ALI, the gas and media flow, and the breathing motion should ideally also be included in the AOC model. Several conclusions were drawn in this literature review on whether devices contained these characteristics.

First, when not using PDMS as a membrane material, only a limited number of studies were able to include a thin ( $<10\text{ }\mu\text{m}$ ) membrane. These membranes were generally static and used in short-term cell culture studies. Second, a significant amount of the LOC devices found in literature do not include a cyclic stretch, along with media flow and an ALI at the same time. Thereby, these LOCs do not recapitulate the shear stress and the strain on the cells, as displayed in-vivo.

Third, various promising material alternatives for PDMS are proposed in the literature. Materials groups such as hydrogels, elastomers, thermoplastics, and silicon-based materials have been used in literature and subsequently these have been studied in more detail in Chapter 3. Most alternative materials were still incorporated in devices that did not mimic the breathing motion, often due to the rigidity or the limited mechanical strength of the used material.

Fourth, different phases of the cell culture may necessitate for or benefit from diverse membrane characteristics. Therefore, research containing dynamic membranes, which change throughout the cell culture, was studied in more detail in Chapter 4. In the first phase, a membrane should be bioactive, promoting cell adhesion and growth. Moreover, it should be wettable and non-porous or contain small-sized pores so that cells do not travel through the membrane. For the second phase, the membrane needs to be permeable and porous to allow transport of nutrients and signalling molecules across it. Furthermore, it has become clear that the membrane needs to be elastic enough to undergo a cyclic strain while being robust enough to last the entire cell culture.

The dilemma arises that when pore sizes are small, immune cells cannot pass through the membrane, but when the pore sizes are larger than  $3\text{ }\mu\text{m}$ , endothelial and epithelial cells can pass through the membrane

which hinders their adherence and monolayer formation. Regarding pore sizes, an ideal membrane should have a uniform pore size below  $3\ \mu\text{m}$  in the first phase, where a confluent monolayer is created. After this monolayer is created, a larger pore size is desired to more closely mimic the in-vivo transmembrane processes such as immune cell migration. However, little information is generally present on the motivation of the chosen pore size in LOC devices and its effect on the cell culture. Hence, more research on pore size and porosity throughout the cell culture is desired.

In conclusion, the need for a novel membrane for AOC devices became apparent in this review. The requirements for an ideal AOC membrane are set as follows: The membrane should sustain a cyclic in-plane stretch of at least 20%, an ALI along with a physiological fluid flow, and it should have a thickness of  $10\ \mu\text{m}$  or less. Furthermore, it should have an adequate pore size, be made of a material that has better ad- and absorption properties than the conventionally used PDMS, and it should be possible to culture cells for up to 2 to 4 weeks. Furthermore, more research on the effect of pore size and porosity needs to be undertaken.

### 5.1. Overall aim and research question

In this review, the concept of an ideal cell supporting membrane for an AOC was sketched, which is a membrane that recapitulates the alveolar-capillary barrier. The membrane should sustain a cyclic in-plane stretch of at least 20%, an ALI along with a physiological fluid flow, and it should have a thickness of  $10\ \mu\text{m}$  or less. Furthermore, it should have an adequate pore size, be made of a material that has better ad- and absorption properties than the conventionally used PDMS, and it should be possible to culture cells up to 2 to 4 weeks.

However, designing and testing a membrane on all these properties, next to testing and improving the prior AOC design by the PME Department [46], would be a too large knowledge gap and research subject to cover in the limited time span of this master's thesis. Therefore, a small part of this overall aim is researched. In this review, the need to establish adequate pore sizes in the membrane throughout the cell cultures became apparent. This includes both the initial starting pore size, which is used when culturing the monolayers and during cell differentiation, and secondly, the pore size which is desired when strain and an ALI are applied. As explained previously, these two pore sizes do not necessarily need to have the same diameter. Therefore, dynamically adjusting this pore size throughout the cell culture will be investigated as a possibility.

Thus, the research question of this thesis is: **What is the effect of a dynamic membrane pore size on the formation of a confluent alveolar epithelial and endothelial monolayer formation throughout the cell culture duration, under an ALI, with physiological fluid flow and cyclic stretch?** A physiological fluid flow should exert a shear stress on the endothelial cells of about  $1.54\ \text{N/m}^2$ , which is comparable to the in-vivo situation. Physiological cyclic stretch is defined as applying an in-plane linear cyclic strain to the cells between 4% and 20% at a frequency of 0.2 Hz. In order to answer this question, several subquestions need to be researched. The more elaborate design plan is discussed in Chapter 5.2.

First, it must be determined whether the base AOC device by Nissar [46] functions as expected regarding the fluid flow and membrane stretching and whether primary endothelial and epithelial cells grow as expected on the PDMS membrane located in the device. There are several subquestions for this phase (Phase A):

1. Can primary endothelial and epithelial cells form a confluent monolayer on PDMS?
2. Is it possible to create a leak-tight media flow in the base AOC device under which primary endothelial and epithelial cells can grow a confluent monolayer on a conventional membrane such as PET or PC?
3. How well can primary cells create a monolayer under media flow, and how well do cells remain confluent and adhered to the membrane under physiological strain on a PDMS membrane in the base AOC device?

These subquestions answer whether the base device works properly and set a control standard for any other membranes designed.

In Phase B, the effect of pore size will be taken into account. In this phase, the ideal pore size to start an alveolar cell culture will be determined. This ideal starting pore size will be determined to subsequently use it as the initial pore size in the membrane that will have a varying pore size throughout the cell culture. Then,

the effect of a varying pore size on monolayer formation and cell adherence is studied. Subquestions that are relevant in this phase are:

1. What is the effect of various static pore sizes in the cell supporting membrane on monolayer formation?
2. What is the effect of a dynamical pore size, which increases in diameter during the cell culture, on endothelial and epithelial monolayer formation and cell adherence?
3. Is a physiological strain, and media flow achievable on this dynamical membrane so that cells remain confluent and adhered to the membrane?
4. Are cell cultures of 2 to 4 weeks possible with the designed membrane?

These subquestions answer the question of what pores sizes can be incorporated throughout the cell culture to create a membrane that could support further research into the design of AOCs.

## 5.2. Design plan

The approach for this thesis project is first to check the base device in Phase A. Afterwards, the effect of variable pore size on monolayer formation and cell adherence is studied in Phase B. A Gantt chart of the thesis project planning is included in Figure 5.1. This chart is subdivided into Phase A, Phase B, and activities regarding the thesis report.

In Phase A, the device will first be checked on its fluidic capabilities by letting a media flow pass a conventionally used membrane, such as PET or PC. This is done to check the effect of media flow and the subsequent shear stress on cell viability since it is already established that endothelial and epithelial cells can form a confluent monolayer on these materials. Subsequently, the ability to grow a primary cell culture on a PDMS membrane will be checked first in a static culture. The membrane for this cell culture will be the membrane designed by Nissar [46], which is a 10  $\mu\text{m}$  thick PDMS membrane with a pore size of 8  $\mu\text{m}$ .

After establishing whether primary cells can grow on PDMS, this membrane will be tested within the base AOC device to see how well cells grow under both strain, an ALI and a media flow. It will be checked if the cells remain adhered in a confluent layer to the membrane when a physiological strain (4%-20%) is applied to the cells during the cell culture. These cells are ideally primary cells, but if primary cells prove too challenging to culture, lung cancer cell lines can also be seeded. With this, the base device and the control set-up are tested.

To check the monolayer integrity, transepithelial/transendothelial electrical resistance (TEER) measurements can be conducted. This is a reliable, non-invasive method that measures the resistance over the cell layer to signify the tightness of junctions and barriers and thus gives information on the integrity and permeability of the monolayer [35][37]. Furthermore, visual inspection of the cells on the membrane can be done with confocal microscopy. For example, after about a week, the lung cilia cells should show mucus production in the case of healthy cells, and this method can be used to check if there is no dramatic decrease in cell adherence throughout the cell culture. At the end of a cell culture, fluorescence microscopy can be applied to visualise the cell culture better, using, for example, DAPI and Phalloidin staining.

Subsequently, in Phase B, the effects of pore size on monolayer formation and cell adherence will be studied. Firstly, the effect of several static pore sizes (e.g. no pores, 0.4  $\mu\text{m}$ , 3  $\mu\text{m}$  and 8  $\mu\text{m}$ ) on epithelial and endothelial monolayer creation will be researched. This study is done to determine the most optimal starting pore size. An optimal starting pore size indicates that both endothelial and epithelial cells can form a confluent monolayer and that they are also able to differentiate on the membrane.

A dynamical pore size can be studied if this starting pore size has been determined. A membrane will be designed initially having the optimal starting pore size. This pore size will be increased throughout the culture duration to about 8  $\mu\text{m}$  [16]. The effect of this dynamical pore size, combined with cyclic stretch and a fluid flow, on the monolayer formation, integrity, and cell adherence to the membrane will be assessed. This assessment is done with TEER measurements and visual inspection, as explained above. The membrane will be placed in the same device as used in Phase A.

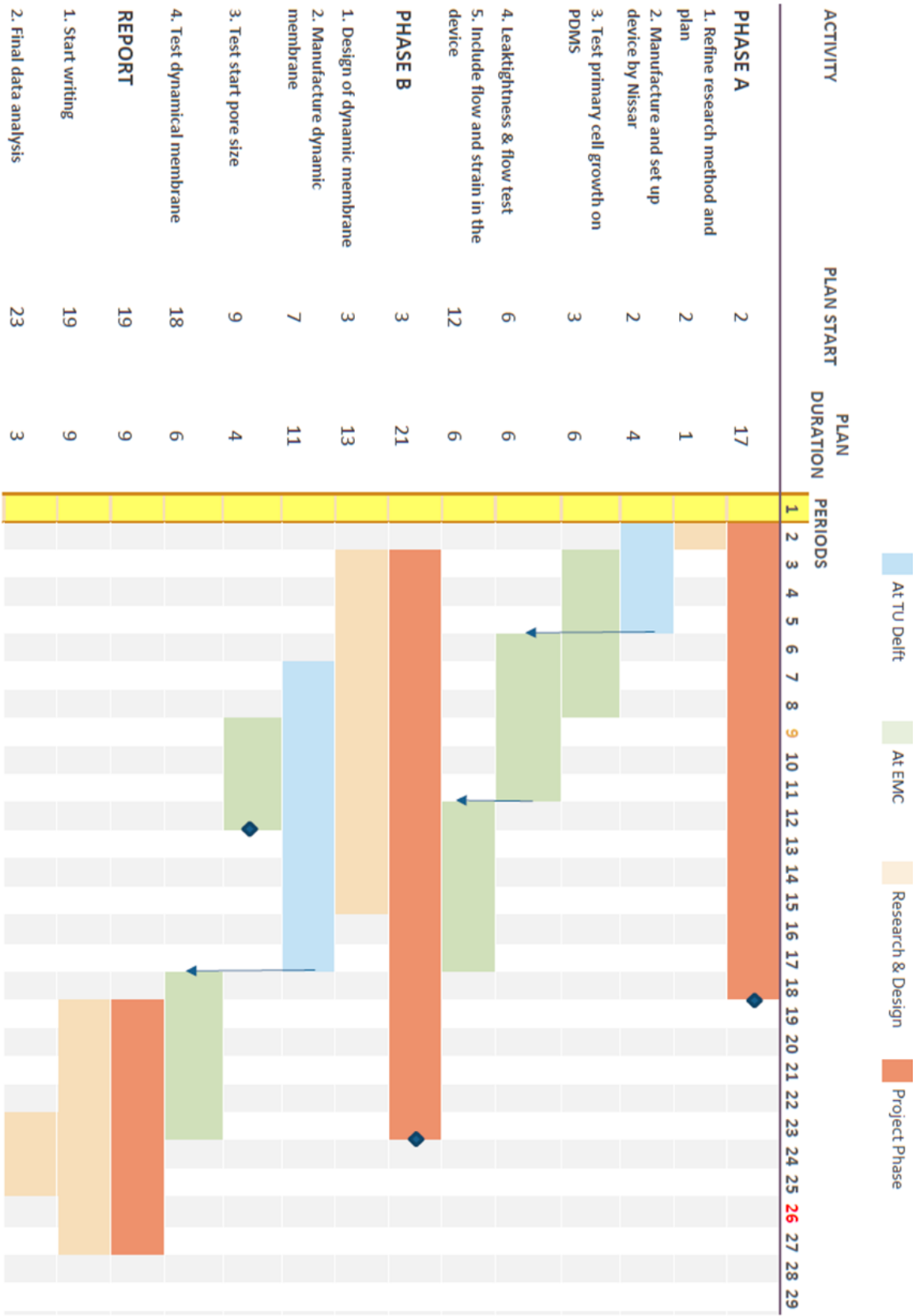


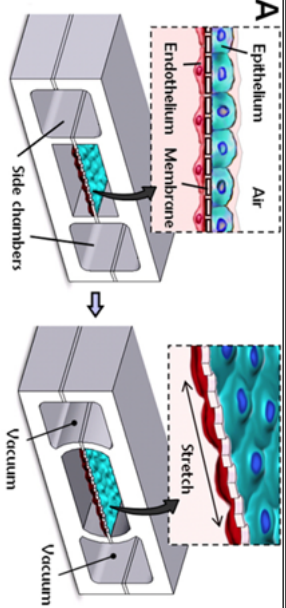
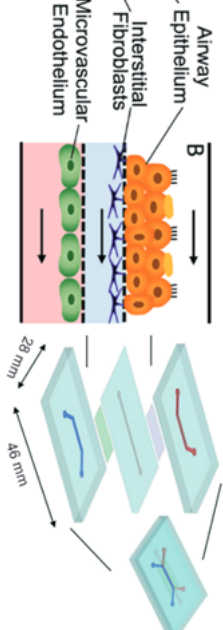
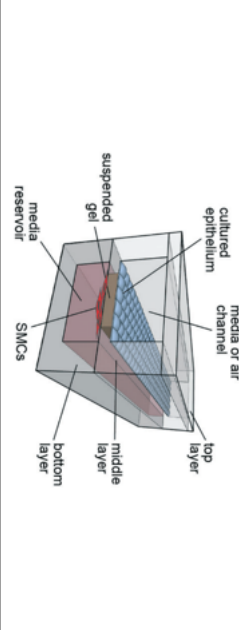
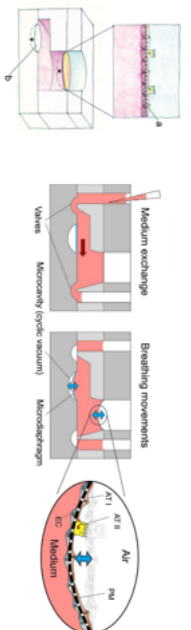
Figure 5.1: Gantt chart of the thesis project planning. Periods are in weeks, starting from week 1 2022.

# A

## Appendix A

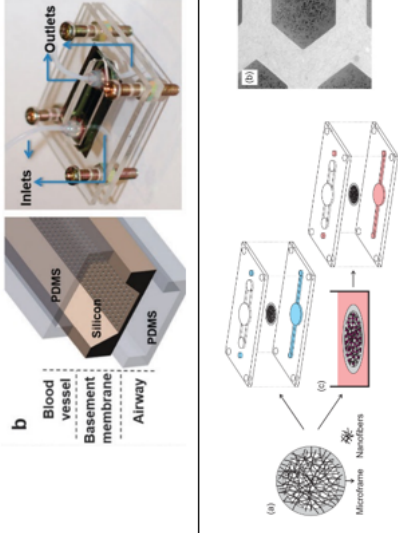
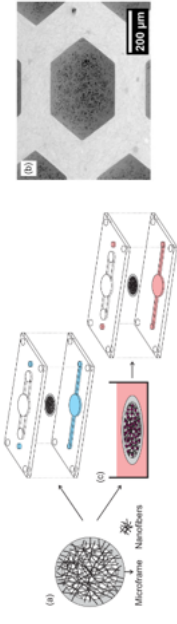
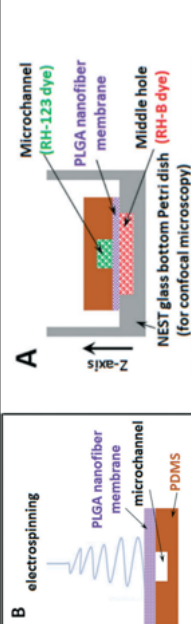
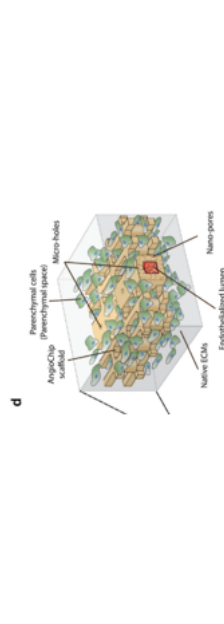
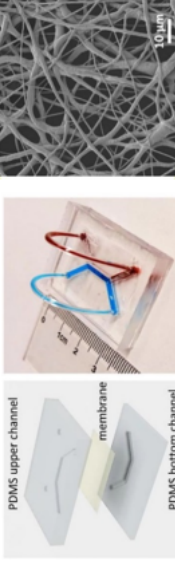
The figure containing the overview table can be found on the following page.

Literature Overview Table

	Author and Focus	Features: Cyclic stretch ALI/flow	Material Manufacturing method	Membrane thickness Driver	Pore size Porosity	Figure	Device lay-out
1	Huh et al. [28][29] AOC, alveolar membrane to study pulmonary inflammation and oedema	Cyclic stretch: Uniaxial ALI: Yes, Flow: Yes Conversion: No	Material: Membrane: PDMS Device: PDMS Manufacturing method: Soft-lithography, chemical etching	Membrane thickness: 10 $\mu$ m Driver: Manufacturing	Pore size: 10 $\mu$ m [28] 50 $\mu$ m [29] Porosity: -		Double stacked channels
2	Sellgren et al. [61] AOC, microarchitecture of the ALI with triple coculture	Cyclic stretch: No ALI: Yes, Flow: Yes Conversion: No	Material: Membrane 1: PTFE Membrane 2: PET Membrane 3: PC Device: PDMS Manufacturing method: Soft-lithography	Membrane thickness: PTFE: 40 $\mu$ m PC: 47 $\mu$ m PET: 10 $\mu$ m Total barrier: ~200 $\mu$ m Driver: -	Pore size: PTFE: 0.4 $\mu$ m PET: 0.4 $\mu$ m PC: 1 $\mu$ m Porosity: -		Triple stacked channels, double membrane
3	Humayun et al. [30] LOC, lung airway microenvironment with bronchial epithelial and smooth muscle cells	Cyclic stretch: No ALI: Yes, Flow: Yes <sup>1</sup> Conversion: No <sup>1</sup> : Only air flow	Material: Membrane: Matrigel and collagen Device: PMMA Manufacturing method: Micromilling & solvent bonding	Membrane thickness: 0.65 mm Driver: -	Pore size: - Porosity: -		Channel over media reservoir
4	Stucki et al. [66][67] AOC, alveolar barrier	Cyclic stretch: Triaxial bulging ALI: Yes, Flow: Media exchange Conversion: No	Material: Membrane: PDMS Device: PDMS, PC Manufacturing method: Soft-lithography	Membrane thickness: 3.5 $\mu$ m or 10 $\mu$ m Driver: Manufacturing	Pore size: 0.3 $\mu$ m, 8 $\mu$ m Porosity: 3 $\mu$ m: 8x 10 <sup>4</sup> pores/cm <sup>2</sup> 8 $\mu$ m: 6x 10 <sup>4</sup> pores/cm <sup>2</sup>		Chamber on top of reservoir

(a) Page 1

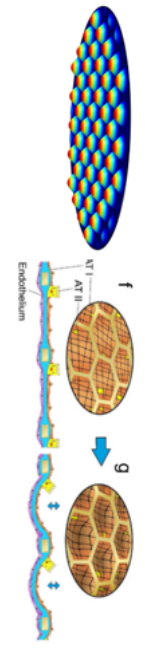
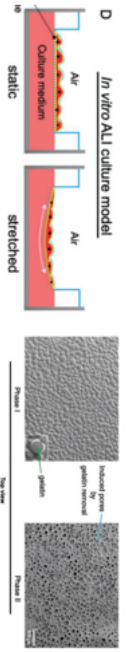
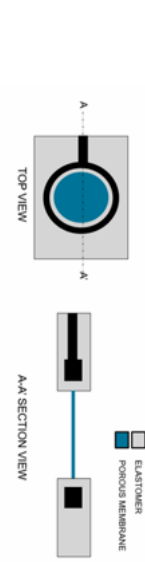

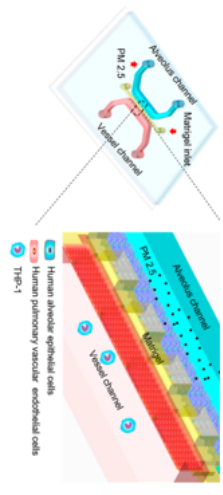
Figure A.1: Overview table of the various LOC devices found in the literature.

	Author and Focus	Features: Cyclic stretch ALI/flow Membrane conversion	Material Manufacturing method	Membrane thickness Driver	Pore size Porosity	Figure	Device lay-out
5	Punde et al. [52] LOC, bronchial epithelial lining	Cyclic stretch: No ALI: Yes, Flow: Yes Conversion: No	<b>Material:</b> Membrane: Silicon Device: PDMS  <b>Manufacturing method:</b> Etching	<b>Membrane thickness:</b> -  <b>Driver:</b> -	<b>Pore size:</b> 5 x 5 $\mu\text{m}$  <b>Porosity:</b> -		Double stacked channels
6	Radiom et al. [54] AOC, effect of periodic strain on alveolar cell layer formation	Cyclic stretch: Triaxial bulging ALI: Yes, Flow: Yes Conversion: No	<b>Material:</b> Membrane: Gelatin (fibers), Ormostamp (support) Device: PDMS  <b>Manufacturing method:</b> Lithography, electrospinning	<b>Membrane thickness:</b> < 1 $\mu\text{m}$ <b>Fibre thickness:</b> few 100 nm  <b>Driver:</b> Biological	<b>Pore size:</b> 1- 10 $\mu\text{m}$  <b>Porosity:</b> > 50%		Double stacked channels
7	Yang et al. [76] AOC, alveolar membrane to culture cancer cells	Cyclic stretch: No ALI: Yes, Flow: No Conversion: Not observed	<b>Material:</b> Membrane: PLGA Device: PDMS  <b>Manufacturing method:</b> Electrospinning, soft- lithography etching	<b>Membrane thickness:</b> 2.3±0.2 $\mu\text{m}$ – 9.1±1.2 $\mu\text{m}$ <b>Fibre thickness:</b> 3 $\mu\text{m}$  <b>Driver:</b> Biological	<b>Pore size:</b> -  <b>Porosity:</b> -		Double stacked channels
8	Zhang et al. [79] Scaffold, vasculature for endothelial cells (AngioChip)	Cyclic stretch: No ALI: No, Flow: Yes Conversion: Yes	<b>Material:</b> Scaffold: POMaC Device: glass  <b>Manufacturing method:</b> 3D-stamping	<b>Membrane thickness:</b> 25-50 $\mu\text{m}$  <b>Driver:</b> -	<b>Pore size:</b> 10 $\mu\text{m}$ , 20 $\mu\text{m}$  <b>Porosity:</b> 0.5%		Scaffold
9	Tas et al. [68] AOC, ventilator- induced lung injuries	Cyclic stretch: Biaxial bulging ALI: Yes, Flow: Yes Conversion: No	<b>Material:</b> Membrane: PCL Device: PDMS  <b>Manufacturing method:</b> Electrospinning, 3D-printing, replica moulding	<b>Membrane thickness:</b> ~20 $\mu\text{m}$ <b>Average fibre diameter:</b> 441 ± 1490 nm  <b>Driver:</b> Manufacturing	<b>Pore size:</b> -  <b>Porosity:</b> -		Double stacked channels

(b) Page 2

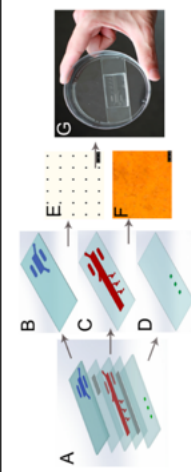
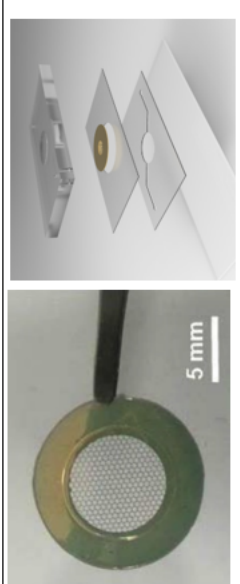
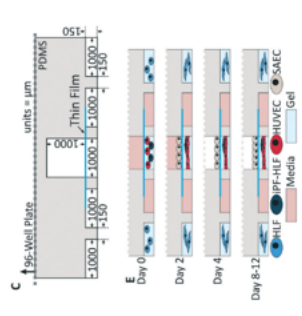
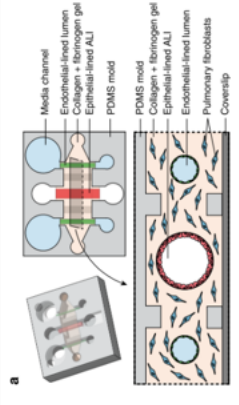
Figure A.1: Overview table of the various LOC devices found in the literature.



Author and Focus	Features: Cyclic stretch ALI/Flow Membrane conversion	Material Manufacturing method	Membrane thickness Driver	Pore size Porosity	Figure	Device lay-out
10 Zamprogno et al. [78] AOC, alveolar- capillary barrier	Cyclic stretch: Triaxial bulging ALI: Yes, Flow: No Conversion: Yes	Material: Membrane: CE-hydrogel Device: PDMS Manufacturing method: Soft-lithography, drop casting	Membrane thickness: Support: 18 $\mu$ m CE-membrane: 5-10 $\mu$ m Driver: -	Pore size: - Porosity: -		Double stacked chambers
11 Doryab et al. [16] AOC, alveolar epithelial microenvironment	Cyclic stretch: Triaxial bulging ALI: Yes, Flow: Yes* Conversion: Yes *Only airflow	Material: Gelatin & PCL Manufacturing method: Spincoating co-polymer emulsion	Membrane thickness: $\leq 5$ $\mu$ m Driver: Biological	Pore size: Variable up to 8 $\mu$ m Porosity: Variable up to 9.4 $\pm$ 0.2%		Open-air chamber on top of reservoir
12 Nissar et al. [46] AOC, alveolar-capillary barrier	Cyclic stretch: Biaxial in-plane ALI: Yes, Flow: Yes Conversion: No	Material: Membrane: PDMS Device: PDMS, glass Manufacturing method: Soft-lithography, replica molding	Membrane thickness: 10 $\mu$ m Driver: Manufacturing	Pore size: 8 $\mu$ m Porosity: 2.1%		Double stacked channels
13 Hou et al. [25] LOC, bronchial air-blood interface, to study the effect of cigarette smoke	Cyclic stretch: Triaxial bulging ALI: Yes, Flow: Yes Conversion: No	Material: Membrane: PDMS Device: PDMS Manufacturing method: Soft-lithography, replica molding	Membrane thickness: 40 $\mu$ m Driver: -	Pore size: 10 $\mu$ m Porosity: -		Stacked channels
14 Xu et al. [74] Zhang et al. [81] AOC, alveolar-blood barrier to study air pollutants	Cyclic stretch: No ALI: No, Flow: Yes Conversion: No	Material: Membrane: Matrigel Device: PDMS Manufacturing method: Soft-lithography	Membrane thickness: 80 $\mu$ m Driver: Manufacturing	No pores		Double stacked channels


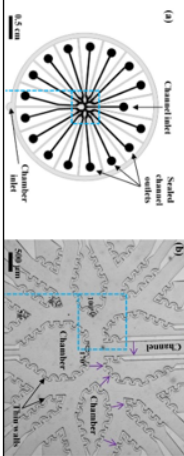
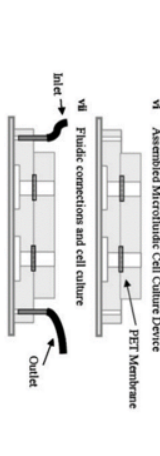
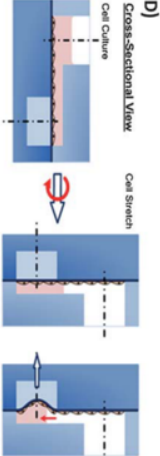
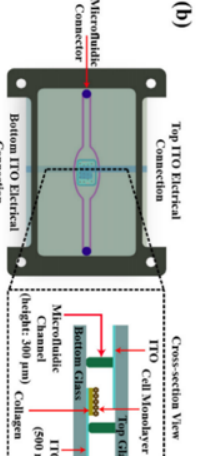
(c) Page 3

Figure A.1: Overview table of the various LOC devices found in the literature.

	Author and Focus	Features: Cyclic stretch ALU/flow	Material Manufacturing method	Membrane thickness Driver	Pore size Porosity	Figure	Device lay-out
15	Xu et al. [75] LOC, multi-organ chip to simulate lung cancer metastasis	Membrane conversion Cyclic stretch: Yes ALI: Yes, Flow: Yes Conversion: No	<b>Material:</b> Membranes: PDMS Device: PDMS <b>Manufacturing method:</b> Soft-lithography	<b>Membrane thickness:</b> 10 $\mu$ m <b>Driver:</b> -	<b>Pore size:</b> Microscale <b>Porosity:</b> -		Triple stacked channels, double membrane
16	Laniece [40] AOC, alveoli on a chip	Cyclic stretch: Triaxial bulging ALI: Yes, Flow: Yes Conversion: No	<b>Material:</b> Membrane: Gelatin (fibers), PEGDA (support) Device: PDMS, glass <b>Manufacturing method:</b> Photolithography, replica molding, electrospinning	<b>Membrane thickness:</b> Electrospun membrane: 1 $\mu$ m Overall membrane: 80 $\mu$ m <b>Driver:</b> Biological	<b>Pore size:</b> 2 $\mu$ m average <b>Porosity:</b> -		Double stacked channels
17	Mejias et al. [44] LOC, the blood vessel- interstitium fibroblast-epithelial microenvironment	Cyclic stretch: No ALI: Yes, Flow: No Conversion: No	<b>Material:</b> Membrane: vitriified fibrin-collagen hydrogel or PET Device: PDMS, PET <b>Manufacturing method:</b> Photolithography, 3D-printing	<b>Membrane thickness:</b> - <b>Driver:</b> -	<b>Pore size:</b> PET: 0.4 $\mu$ m <b>Porosity:</b> -		Channel on reservoir
18	Barkal et al. [4] LOC, bronchiole for pulmonary infection	Cyclic stretch: No ALI: Yes, Flow: No Conversion: No	<b>Material:</b> Membrane: Cell-laden collagen-fibrinogen gel Device: PDMS <b>Manufacturing method:</b> Soft-lithography, Replica molding	<b>Membrane thickness:</b> - <b>Driver:</b> -	<b>Pore size:</b> - <b>Porosity:</b> -		Reservoir

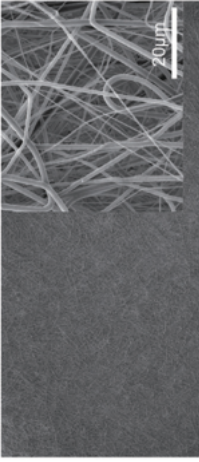
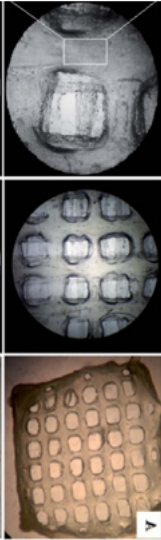
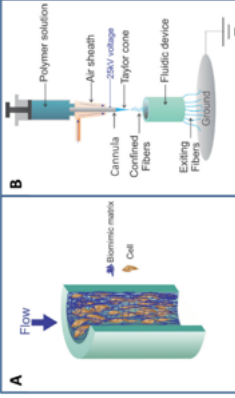
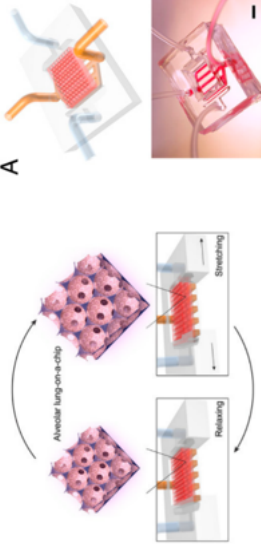
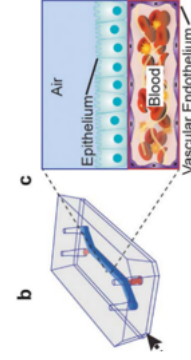
(d) Page 4

Figure A.1: Overview table of the various LOC devices found in the literature.

Author and Focus	Features: Cyclic stretch AL/flow Membrane conversion	Material Manufacturing method	Membrane thickness Driver	Pore size Porosity	Figure	Device lay-out
19 Benam et al. [5] LOC, bronchioles to model lung inflammatory disorder	Cyclic stretch: No ALT: Yes, Flow: Yes Conversion: No	Material: Polyester Device: PDMS Manufacturing method: Soft-lithography, Replica molding	Membrane thickness: 10 $\mu$ m Driver: Manufacturing	Pore size: 0.4 $\mu$ m Porosity: -		Double stacked channels
20 Fishier et al. [18] LOC, several generations of the acinar tree	Cyclic stretch: Yes ALT: Yes, Flow: Yes Conversion: No	Material: Membrane: PDMS Device: PDMS Manufacturing method: Soft-lithography, DRIE	Membrane thickness: ~45 $\mu$ m Driver: -	Pore size: - Porosity: -		Channels on top of reservoir
21 Nalayanda et al. [45] AOC, alveolar epithelium	Cyclic stretch: No ALT: Yes, Flow: Yes Conversion: No	Material: Membrane: PET Device: PDMS Manufacturing method: Photolithography, replica molding	Membrane thickness: - Driver: -	Pore size: 0.4 $\mu$ m Porosity: -		Open-air chamber on top of channel
22 Douville et al. [17] AOC, ventilator-induced lung injury (VILI)	Cyclic stretch: Triaxial bulging ALT: Yes, Flow: Yes Conversion: No	Material: Membrane: PDMS Device: PDMS Manufacturing method: Pre-polymer spinning	Membrane thickness: 100 $\mu$ m Driver: Manufacturing	No pores		Open-air chamber alongside channel
23 Khalid et al. [35] LOC, cancer environment	Cyclic stretch: No ALT: No, Flow: Yes Conversion: No	Material: Scaffold: Glass and collagen Device: Glass, ITO electrodes, Nusil silicone Manufacturing method: Inkjet printing	Scaffold thickness: 1.1 $\mu$ m Driver: -	No pores		Scaffold, single channel

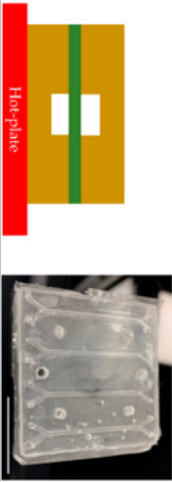
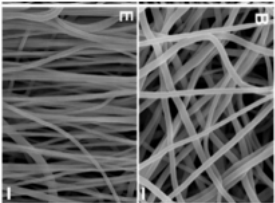
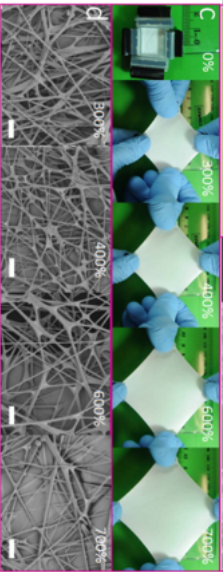
(e) Page 5

Figure A.1: Overview table of the various LOC devices found in the literature.

	Author and Focus	Features: Cyclic stretch ALI/flow Membrane conversion	Material Manufacturing method	Membrane thickness Driver	Pore size Porosity	Figure	Device lay-out
24	Jin et al. [34] Electrospun membrane, focus on the 3D migration of neutrophils	Cyclic stretch: No ALI: No, Flow: No Conversion: No	<b>Material:</b> Membrane: PCL Device: PDMS <b>Manufacturing method:</b> Electrospinning (DWES)	<b>Membrane thickness:</b> 70 ± 10 µm <b>Fibre diameter:</b> 200-500 nm <b>Driver:</b> -	<b>Pore size:</b> Dominant: 3-4 µm 77% between 1-10 µm <b>Porosity:</b> -		Double stacked reservoirs
25	Rezaei et al. [55] Porous scaffold for lung studies and to closely mimic ECM	Cyclic stretch: No ALI: No, Flow: No Conversion: Yes	<b>Material:</b> Scaffold: Chitosan/PCL <b>Manufacturing method:</b> 3D-printing	<b>Membrane thickness:</b> - <b>Fibre diameter:</b> 360 µm average <b>Driver:</b> -	<b>Pore size:</b> - <b>Porosity:</b> 55%		Scaffold
26	Chen et al. [11] OOC, ECM-resembling scaffold for microfluidic devices	Cyclic stretch: No ALI: No, Flow: Yes Conversion: No	<b>Material:</b> Membrane: PCL Device: PDMS <b>Manufacturing method:</b> Electrospinning, Replica molding	<b>Membrane thickness:</b> 379 ± 15 µm average <b>Fibre diameter:</b> 1.6 ± 0.6 µm average <b>Driver:</b> -	<b>Pore size:</b> 113 ± 19 µm <sup>2</sup> average <b>Porosity:</b> 55%		Scaffold
27	Huang et al. [26] AOC, the alveolar structure and ECM	Cyclic stretch: Biaxial In-plane ALI: Yes, Flow: Yes Conversion: No	<b>Material:</b> Membrane: GelMA Device: PDMS <b>Manufacturing method:</b> Hydrogel molding with alginate beads	<b>Membrane thickness:</b> 546.4 µm average <b>Driver:</b> Manufacturing	<b>Pore size:</b> 200 µm <b>Porosity:</b> -		Scaffold, double stacked channels
28	Jain et al. [33] AOC, inflammation- induced thrombosis using whole blood	Cyclic stretch: No ALI: Yes, Flow: Yes Conversion: No	<b>Material:</b> Membrane: PDMS Device: PDMS <b>Manufacturing method:</b> Stereolithography, replica molding, DRIE etching	<b>Membrane thickness:</b> 50 µm <b>Driver:</b> Manufacturing	<b>Pore size:</b> 7 µm, spaced 40 µm apart <b>Porosity:</b> -		Double stacked channels

(f) Page 6

Figure A.1: Overview table of the various LOC devices found in the literature.

	Author and Focus	Features: Cyclic stretch AI/Flow Membrane conversion	Material Manufacturing method	Membrane thickness Driver	Pore size Porosity	Figure	Device lay-out
29	Rimsa et al. [156] LOC, compare OSTe and PDMS as a LOC material	Cyclic stretch: No AI: Yes, Flow: Yes Conversion: No	Material: Membrane: PC Device: OSTe Manufacturing method: Replica molding, UV curing	Membrane thickness: - Driver: -	Pore size: 3 $\mu\text{m}$ Porosity: $6 \times 10^8$ pores/ $\text{cm}^2$		Double stacked channels
30	Fusaro et al. [20] Scaffold, mimic vasculature to culture human endothelial cells	Cyclic stretch: Biaxial In-plane AI: No, Flow: Yes Conversion: Yes	Material: Membrane: P(BCE-co-TECE) Manufacturing method: Electrospinning	Membrane thickness: - Fibre diameter: $800 \pm 190 \text{ nm}$ , $560 \pm 210 \text{ nm}$ Driver: -	Pore size: - Porosity: -		Scaffold
31	Zhou et al. [82] Fibrous membrane to study strain and hydrophobicity	Cyclic stretch: Biaxial In-plane AI: No, Flow: Yes Conversion: No	Material: Membrane: SBS coated with FAS Manufacturing method: Electrospinning	Membrane thickness: $\sim 300 \mu\text{m}$ Fibre diameter: $2.5 \mu\text{m}$ average Driver: -	Pore size: - Porosity: -		Scaffold

(g) Page 7

Figure A.1: Overview table of the various LOC devices found in the literature.

# Bibliography

- [1] Samad Ahadian, Robert Civitarese, Dawn Bannerman, Mohammad Hossein Mohammadi, Rick Lu, Erika Wang, Locke Davenport-Huyer, Ben Lai, Boyang Zhang, Yimu Zhao, Serena Mandla, Anastasia Korolj, and Milica Radisic. Organ-On-A-Chip Platforms: A Convergence of Advanced Materials, Cells, and Microscale Technologies. *Advanced Healthcare Materials*, 7(2):1–53, 2018. ISSN 21922659. doi: 10.1002/adhm.201700506.
- [2] Misturu Akashi, Takami Akagi, and Michiya Matsusaki. *Engineered Cell Manipulation for Biomedical Application*. Springer, Tokyo, 2014. ISBN 9784431551386. URL <https://link.springer.com/content/pdf/10.1007%2F978-4-431-55139-3.pdf>.
- [3] P. Apel. Track etching technique in membrane technology. *Radiation Measurements*, 34(1-6):559–566, 2001. ISSN 13504487. doi: 10.1016/S1350-4487(01)00228-1.
- [4] Layla J. Barkal, Clare L. Procknow, Yasmín R. Álvarez-García, Mengyao Niu, José A. Jiménez-Torres, Rebecca A. Brockman-Schneider, James E. Gern, Loren C. Denlinger, Ashleigh B. Theberge, Nancy P. Keller, Erwin Berthier, and David J. Beebe. Microbial volatile communication in human organotypic lung models. *Nature Communications*, 8(1770), 2017. ISSN 20411723. doi: 10.1038/s41467-017-01985-4. URL <http://dx.doi.org/10.1038/s41467-017-01985-4>.
- [5] Kambez H. Benam, Remi Villenave, Carolina Lucchesi, Antonio Varone, Cedric Hubeau, Hyun Hee Lee, Stephen E. Alves, Michael Salmon, Thomas C. Ferrante, James C. Weaver, Anthony Bahinski, Geraldine A. Hamilton, and Donald E. Ingber. Small airway-on-a-chip enables analysis of human lung inflammation and drug responses in vitro. *Nature Methods*, 13(2):151–157, 2016. ISSN 15487105. doi: 10.1038/nmeth.3697.
- [6] Tanya J. Bennet, Avineet Randhawa, Jessica Hua, and Karen C. Cheung. Airway-on-a-chip: Designs and Applications for Lung Repair and Disease. *Cells*, 10(1062), 2021. doi: <https://doi.org/10.3390/cells10071602>.
- [7] Konstantin G. Birukov, Jeffrey R. Jacobson, Alejandro A. Flores, Shui Q. Ye, Anna A. Birukova, Alexander D. Verin, and Joe G.N. Garcia. Magnitude-dependent regulation of pulmonary endothelial cell barrier function by cyclic stretch. *American Journal of Physiology - Lung Cellular and Molecular Physiology*, 285(4 29-4):785–797, 2003. ISSN 10400605. doi: 10.1152/ajplung.00336.2002.
- [8] Scott B. Campbell, Qinghua Wu, Joshua Yazbeck, Chuan Liu, Sargol Okhovatian, and Milica Radisic. Beyond Polydimethylsiloxane: Alternative Materials for Fabrication of Organ-on-a-Chip Devices and Microphysiological Systems. *ACS Biomaterials Science and Engineering*, 7(7):2880–2899, 2021. ISSN 23739878. doi: 10.1021/acsbiomaterials.0c00640.
- [9] G Carlotti, P Colpani, D Piccolo, S Santucci, V Senez, G Socino, and L Verdini. Measurement of the elastic and viscoelastic properties of dielectric films used in microelectronics. *Thin Solid Films*, 414: 99–104, 2002.
- [10] Francisco S A Cavalcante, Satoru Ito, Kelly Brewer, Hiroaki Sakai, Adriano M Alencar, Murilo P Almeida, S Andrade, Arnab Majumdar, Edward P Ingenito, S A Francisco, Satoru Ito, Kelly Brewer, Adriano M Alencar, Murilo P Almeida, S Andrade, Arnab Majumdar, Edward P Ingenito, and Suki Me. Mechanical interactions between collagen and proteoglycans: implications for the stability of lung tissue. *J Appl Physiol*, 98:672–679, 2005. doi: 10.1152/japplphysiol.00619.2004.
- [11] Chengpeng Chen, Benjamin T Mehl, Scott A Sell, and R Scott Martin. Use of electrospinning and dynamic air focusing to create three-dimensional cell culture scaffolds in microfluidic devices. *Analyst*, 141:5311–5320, 2016. doi: 10.1039/c6an01282e.



- [12] Edward D Crandall and Michael A Matthay. NHLBI Workshop Summary - Alveolar Epithelial Transport Basic Science to Clinical Medicine. *Crit. Care Med.*, 162(4):1021, 2001. URL <http://ajrccm.atsjournals.org/cgi/content/full/163/4/1021>.
- [13] Karel Domansky, Daniel C. Leslie, James McKinney, Jacob P. Fraser, Josiah D. Sliz, Tiama Hamkins-Indik, Geraldine A. Hamilton, Anthony Bahinski, and Donald E. Ingber. Clear castable polyurethane elastomer for fabrication of microfluidic devices. *Lab on a Chip*, 13(19):3956–3964, 2013. ISSN 14730189. doi: 10.1039/c3lc50558h.
- [14] Karel Domansky, Josiah D. Sliz, Norman Wen, Christopher Hinojosa, Guy Thompson, Jacob P. Fraser, Tiama Hamkins-Indik, Geraldine A. Hamilton, Daniel Levner, and Donald E. Ingber. SEBS elastomers for fabrication of microfluidic devices with reduced drug absorption by injection molding and extrusion. *Microfluidics and Nanofluidics*, 21(6):1–12, 2017. ISSN 16134990. doi: 10.1007/s10404-017-1941-4.
- [15] Ali Doryab, Sinem Tas, Mehmet Berat Taskin, Lin Yang, Anne Hilgendorff, Jürgen Groll, Darcy E. Wagner, and Otmar Schmid. Evolution of Bioengineered Lung Models: Recent Advances and Challenges in Tissue Mimicry for Studying the Role of Mechanical Forces in Cell Biology. *Advanced Functional Materials*, 29(39), 2019. ISSN 16163028. doi: 10.1002/adfm.201903114.
- [16] Ali Doryab, Mehmet Berat Taskin, Philipp Stahlhut, Andreas Schröppel, Darcy E. Wagner, Jürgen Groll, and Otmar Schmid. A Biomimetic, Copolymeric Membrane for Cell-Stretch Experiments with Pulmonary Epithelial Cells at the Air-Liquid Interface. *Advanced Functional Materials*, 31(10), 2021. ISSN 16163028. doi: 10.1002/adfm.202004707.
- [17] Nicholas J. Douville, Parsa Zamankhan, Yi Chung Tung, Ran Li, Benjamin L. Vaughan, Cheng Feng Tai, Joshua White, Paul J. Christensen, James B. Grotberg, and Shuichi Takayama. Combination of fluid and solid mechanical stresses contribute to cell death and detachment in a microfluidic alveolar model. *Lab on a Chip*, 11(4):609–619, 2011. ISSN 14730189. doi: 10.1039/c0lc00251h.
- [18] Rami Fishler, Molly K. Mulligan, and Josué Sznitman. Acinus-on-a-chip: A microfluidic platform for pulmonary acinar flows. *Journal of Biomechanics*, 46(16):2817–2823, 2013. ISSN 00219290. doi: 10.1016/j.jbiomech.2013.08.020.
- [19] Lisa E. Freed, Gordana Vunjak-Novakovic, Robert J. Biron, Dana B. Eagles, Daniel C. Lesnoy, Sandra K. Barlow, and Robert Langer. Biodegradable polymer scaffold for tissue engineering. *Nature Structural Biology*, 1(4):259–263, 1994.
- [20] Luca Fusaro, Chiara Gualandi, Diego Antonioli, Michelina Soccio, Anna Liguori, Michele Laus, Nadia Lotti, Francesca Boccafroschi, and Maria Letizia Focarete. Elastomeric electrospun scaffolds of a biodegradable aliphatic copolyester containing PEG-like sequences for dynamic culture of human endothelial cells. *Biomolecules*, 10(12):1–16, 2020. ISSN 2218273X. doi: 10.3390/biom10121620.
- [21] Olivier T Guenat and François Berthiaume. Incorporating mechanical strain in organs-on-a-chip: Lung and skin. *Biomicrofluidics*, 12:42207, 2018. doi: 10.1063/1.5024895. URL <https://doi.org/10.1063/1.5024895>.
- [22] Andrew M. Handorf, Yaxian Zhou, Matthew A. Halanski, and Wan Ju Li. Tissue stiffness dictates development, homeostasis, and disease progression. *Organogenesis*, 11(1):1–15, 2015. ISSN 15558592. doi: 10.1080/15476278.2015.1019687.
- [23] Shabir Hassan, Marcel Heinrich, Berivan Cecen, Jai Prakash, and Yu Shrike Zhang. Biomaterials for on-chip organ systems. *Biomaterials for Organ and Tissue Regeneration*, 26:669–707, jan 2020. doi: 10.1016/B978-0-08-102906-0.00019-2.
- [24] Nikolett Hegedüs, Katalin Balázs, and Csaba Balázs. Silicon Nitride and Hydrogenated Silicon Nitride Thin Films: A Review of Fabrication Methods and Applications. *Materials*, 14(19):5658, 2021. ISSN 19961944. doi: 10.3390/ma14195658.
- [25] Wei Hou, Siyi Hu, Yong Jie, and Zhang Hanbin. Cigarette smoke-induced malignant transformation via STAT3 signalling in pulmonary epithelial cells in a lung-on-a-chip model. *Bio-Design and Manufacturing*, 3(4):383–395, 2020. ISSN 2522-8552. doi: 10.1007/s42242-020-00092-6. URL <https://doi.org/10.1007/s42242-020-00092-6>.

- [26] Di Huang, Tingting Liu, Junlong Liao, Sushila Maharjan, Xin Xie, Montserrat Pérez, Ingrid Anaya, Shiwei Wang, Alan Tirado Mayer, Zhixin Kang, Weijia Kong, Valerio Luca Mainardi, Carlos Ezio Garciamendez-Mijares, Germán García Martínez, Matteo Moretti, Weijia Zhang, Zhongze Gu, Amir M. Ghaemmaghami, and Yu Shrike Zhang. Reversed-engineered human alveolar lung-on-a-chip model. *Proceedings of the National Academy of Sciences of the United States of America*, 118(19):1–10, 2021. ISSN 10916490. doi: 10.1073/pnas.2016146118.
- [27] Dongeun Huh. A human breathing lung-on-a-chip. *Annals of the American Thoracic Society*, 12(March): S42–S44, 2015. ISSN 23256621. doi: 10.1513/AnnalsATS.201410-442MG.
- [28] Dongeun Huh, Benjamin D. Matthews, Akiko Mammoto, Martin Montoya-Zavala, Hong Yuan Hsin, and Donald E. Ingber. Reconstituting organ-level lung functions on a chip. *Science*, 328(5986):1662–1668, 2010. ISSN 00368075. doi: 10.1126/science.1188302.
- [29] Dongeun Huh, Daniel C. Leslie, Benjamin D. Matthews, Jacob P. Fraser, Samuel Jurek, Geraldine A. Hamilton, Kevin Thorneloe, M. Allen McAlexander, and Donald E. Ingber. A human disease model of drug toxicity-induced pulmonary edema in a lung-on-a-chip microdevice. *Sci Transl Med.*, 4(159), 2012. doi: 10.1126/scitranslmed.3004249.A.
- [30] Mouhita Humayun, Chung Wai Chow, and Edmond W.K. Young. Microfluidic lung airway-on-a-chip with arrayable suspended gels for studying epithelial and smooth muscle cell interactions. *Lab on a Chip*, 18(9):1298–1309, 2018. ISSN 14730189. doi: 10.1039/c7lc01357d.
- [31] Jong Hwan and Michael L Shuler. A micro cell culture analog ( mCCA) with 3-D hydrogel culture of multiple cell lines to assess metabolism-dependent cytotoxicity of anti-cancer drugs. *Lab on a Chip*, 9: 1385–1394, 2009. doi: 10.1039/b901377f.
- [32] Lovro Ivancevic. OoC-integrated impedance spectroscopy for blood-brain barrier integrity analysis. Technical report, Delft University of Technology, Delft, 2021.
- [33] A. Jain, R. Barrile, A. D. van der Meer, A. Mammoto, T. Mammoto, K. De Ceunynck, O. Aisiku, M. A. Otieno, C. S. Loudon, G. A. Hamilton, R. Flaumenhaft, and D. E. Ingber. Primary Human Lung Alveolus-on-a-chip Model of Intravascular Thrombosis for Assessment of Therapeutics. *Clinical Pharmacology and Therapeutics*, 103(2):332–340, 2018. ISSN 15326535. doi: 10.1002/cpt.742.
- [34] Songwan Jin, Tae-Min Park, Kim Cho-Hee, Kim Jin-Soo, and Et Al. Three-dimensional migration of neutrophils through an electrospun nanofibrous membrane. *BioTechniques*, 58(6):285–292, 2015. doi: 10.2144/000114297.
- [35] Muhammad Asad Ullah Khalid, Young Soo Kim, Muhsin Ali, Byung Gul Lee, Young Jae Cho, and Kyung Hyun Choi. A lung cancer-on-chip platform with integrated biosensors for physiological monitoring and toxicity assessment. *Biochemical Engineering Journal*, 155(2020):107469, 2020. ISSN 1873295X. doi: 10.1016/j.bej.2019.107469. URL <https://doi.org/10.1016/j.bej.2019.107469>.
- [36] Lars Knudsen and Matthias Ochs. The micromechanics of lung alveoli: structure and function of surfactant and tissue components. *Histochemistry and Cell Biology*, 150(6):661–676, 2018. ISSN 1432119X. doi: 10.1007/s00418-018-1747-9. URL <http://dx.doi.org/10.1007/s00418-018-1747-9>.
- [37] Aditya Reddy Kolli, Mandy Brigitte Esch, Hasan Erbil Abaci, Balaji Srinivasan, Michael L Shuler, and James J Hickman. TEER measurement techniques for in vitro barrier model systems. *J Lab Autom*, 20(2):107–126, 2015. doi: 10.1177/2211068214561025.TEER.
- [38] Dipasri Konar, Mahesh Devarasetty, Didem V. Yildiz, Anthony Atala, and Sean V. Murphy. Lung-On-A-Chip Technologies for Disease Modeling and Drug Development. *Biomedical Engineering and Computational Biology*, 7s1:BECEB.S34252, 2016. ISSN 1179-5972. doi: 10.4137/bece.s34252.
- [39] Aristotle G Koutsiaris, Sophia V Tachmitzi, Nick Batis, and Maria G Kotoula. Volume flow and wall shear stress quantification in the human conjunctival capillaries and post-capillary venules in vivo. *Biorheology*, 44(5-6):375–386, 2007.



- [40] Alexandra Laniece. *Alveoli-on-a-chip: A close-contact dynamic model of the alveolar capillary barrier: micro-engineering , microfluidics and induced pluripotent stem cells*. Thèse de doctorat de phys, L ' Université Sorbonne Paris Cité, 2019.
- [41] Li Li. *Nanoporous Polymers for Membrane Applications*. PhD thesis, DTU Chemical Engineering, 2012.
- [42] Elaine N. Marieb and Katja Hoehn. *Human Anatomy Physiology*. Pearson Education, San Francisco, 10th edition, 2015.
- [43] Robert J. Mason. Biology of alveolar type II cells. *Respirology*, 11(SUPPL. 1):12–15, 2006. ISSN 13237799. doi: 10.1111/j.1440-1843.2006.00800.x.
- [44] Joscelyn C. Mejías, Michael R. Nelson, Olivia Liseth, and Krishnendu Roy. A 96-well format microvascularized human lung-on-a-chip platform for microphysiological modeling of fibrotic diseases. *Lab on a Chip*, 20(19):3601–3611, 2020. ISSN 14730189. doi: 10.1039/d0lc00644k.
- [45] Divya D. Nalayanda, Christopher Puleo, William B. Fulton, Leilani M. Sharpe, Tza Huei Wang, and Fizan Abdullah. An open-access microfluidic model for lung-specific functional studies at an air-liquid interface. *Biomedical Microdevices*, 11(5):1081–1089, 2009. ISSN 13872176. doi: 10.1007/s10544-009-9325-5.
- [46] Zabreen Nissar. *Lung-on-a-chip. Design and Manufacture of a Resealable Device for Recreating the Alveolar-Capillary Barrier in Vitro*. Thesis, Delft Univeristy of Technology, 2021.
- [47] Jeong Rok Oh, Jung Ho Moon, Hoo Keun Park, Jae Hyoung Park, Haegeun Chung, Jinhoo Jeong, Woong Kim, and Young Rag Do. Wafer-scale colloidal lithography based on self-assembly of polystyrene nanospheres and atomic layer deposition. *Journal of Materials Chemistry*, 20(24):5025–5029, 2010. ISSN 09599428. doi: 10.1039/b927532k.
- [48] Carlota Oleaga, Catia Bernabini, Alec S T Smith, Balaji Srinivasan, Max Jackson, William Mclamb, Vivien Platt, Richard Bridges, Yunqing Cai, Navaneetha Santhanam, Bonnie Berry, Sarah Najjar, Nesar Akanda, Xiufang Guo, Candace Martin, Gail Ekman, Mandy B Esch, Jessica Langer, Gladys Ouedraogo, Jose Coto, Lionel Breton, Michael L Shuler, and James J Hickman. Multi-Organ toxicity demonstration in a functional human in vitro system composed of four organs. *Scientific Reports*, (6):1–17, 2016. doi: 10.1038/srep20030.
- [49] Luana A. Osório, Elisabete Silva, and Ruth E. Mackay. A Review of Biomaterials and Scaffold Fabrication for Organ-on-a-Chip (OOAC) Systems. *Bioengineering*, 8(8):113, 2021. ISSN 23065354. doi: 10.3390/bioengineering8080113.
- [50] Thijs Pasman, Danielle Baptista, Sander van Riet, Roman K. Truckenmüller, Pieter S. Hiemstra, Robert J. Rottier, Naomi M. Hamelmann, Jos M.J. Paulusse, Dimitrios Stamatialis, and André A. Poot. Development of an in vitro airway epithelial–endothelial cell culture model on a flexible porous poly(Trimethylene carbonate) membrane based on calu-3 airway epithelial cells and lung microvascular endothelial cells. *Membranes*, 11(3), 2021. ISSN 20770375. doi: 10.3390/membranes11030197.
- [51] Samuel R Polio, Aritra Nath Kundu, Carey E Dougan, Nathan P Birch Id, Ezra Aurian-blajeni Id, Jessica D Schiffman Id, Alfred J Crosby, and Shelly R Peyton. Cross-platform mechanical characterization of lung tissue. *PLOS ONE*, 13(10):1–17, 2018. doi: 10.17605/OSF.IO/TNV7A.Funding.
- [52] Tushar H. Punde, Wen Hao Wu, Pei Chun Lien, Ya Ling Chang, Ping Hsueh Kuo, Margaret Dah Tsy Chang, Kang Yun Lee, Chien Da Huang, Han Pin Kuo, Yao Fei Chan, Po Chen Shih, and Cheng Hsien Liu. A biologically inspired lung-on-a-chip device for the study of protein-induced lung inflammation. *Integrative Biology (United Kingdom)*, 7(2):162–169, 2015. ISSN 17579708. doi: 10.1039/c4ib00239c.
- [53] Yan Ling Qiu, Xiao Chen, Ya Li Hou, Yan Juan Hou, Song Bo Tian, Yu He Chen, Li Yu, Min Hai Nie, and Xu Qian Liu. Characterization of different biodegradable scaffolds in tissue engineering. *Molecular Medicine Reports*, 49(5):4043–4056, 2019. ISSN 17913004. doi: 10.3892/mmr.2019.10066.
- [54] Milad Radiom, Yong He, Juan Peng-Wang, Armelle Baeza-Squiban, Jean François Berret, and Yong Chen. Alveolar mimics with periodic strain and its effect on the cell layer formation. *Biotechnology and Bioengineering*, 117(9):2827–2841, 2020. ISSN 10970290. doi: 10.1002/bit.27458.

- [55] Farnoush Sadat Rezaei, Ayeh Khorshidian, Farzaneh Mahmoudi Beram, Atefeh Derakhshani, Javad Esmaeili, and Aboulfazl Barati. 3D printed chitosan/polycaprolactone scaffold for lung tissue engineering: hope to be useful for COVID-19 studies. *RSC Advances*, 11(32):19508–19520, 2021. ISSN 20462069. doi: 10.1039/d1ra03410c.
- [56] Roberts Rimsa, Artis Galvanovskis, Janis Plume, Feliks Rumnieks, Karlis Grindulis, Gunita Paidere, Sintija Erentraute, Gatis Mozolevskis, and Arturs Abols. Lung on a chip development from off-stoichiometry thiol-ene polymer. *Micromachines*, 12(5), 2021. ISSN 2072666X. doi: 10.3390/mi12050546.
- [57] Tapani Ryhänen. Impact of Silicon MEMS—30 Years After. *Handbook of Silicon Based MEMS Materials and Technologies*, pages xv–xxxii, 2010. doi: 10.1016/b978-0-8155-1594-4.00053-x. URL <http://dx.doi.org/10.1016/B978-0-8155-1594-4.00053-X>.
- [58] Emi Sano, Chihiro Mori, Naoki Matsuoka, Yuka Ozaki, Keisuke Yagi, Aya Wada, Koichi Tashima, Shinsuke Yamasaki, Kana Tanabe, Kayo Yano, and Yu Suke Torisawa. Tetrafluoroethylene-propylene elastomer for fabrication of microfluidic organs-on-chips resistant to drug absorption. *Micromachines*, 10(11), 2019. ISSN 2072666X. doi: 10.3390/mi10110793.
- [59] B. Sartowska, W. Starosta, P. Apel, O. Orelovitch, and I. Blonskaya. Polymeric track etched membranes - Application for advanced porous structures formation. *Acta Physica Polonica A*, 123(5):819–821, 2013. ISSN 05874246. doi: 10.12693/APhysPolA.123.819.
- [60] R. Seghir and S. Arscott. Extended PDMS stiffness range for flexible systems. *Sensors and Actuators, A: Physical*, 230:33–39, 2015. ISSN 09244247. doi: 10.1016/j.sna.2015.04.011. URL <http://dx.doi.org/10.1016/j.sna.2015.04.011>.
- [61] Katelyn L. Sellgren, Elizabeth J. Butala, Brain P. Gilmour, Scott H. Randell, and Sonia Grego. A biomimetic multicellular model of the airways using primary human cells. *Lab on a Chip*, 14:3349–3358, 2014. doi: <https://doi.org/10.1039/C4LC00552J>.
- [62] Myungeun Seo and Marc A. Hillmyer. Reticulated Nanoporous Polymers by Controlled Polymerization-Induced Microphase Separation. *Science*, 336(June):1422–1425, 2012. doi: 10.4159/harvard.9780674333987.c22.
- [63] Jesus Shrestha, Maliheh Ghadiri, Melane Shanmugavel, Sajad Razavi Bazaz, Steven Vasilescu, Lin Ding, and Majid Ebrahimi Warkiani. A rapidly prototyped lung-on-a-chip model using 3D-printed molds. *Organs-on-a-Chip*, 1(November 2019):100001, 2019. ISSN 26661020. doi: 10.1016/j.ooc.2020.100001. URL <https://doi.org/10.1016/j.ooc.2020.100001>.
- [64] Jesus Shrestha, Sajad Razavi Bazaz, Hamidreza Aboulkheyr Es, Dania Yaghobian Azari, Benjamin Thierry, Majid Ebrahimi Warkiani, and Maliheh Ghadiri. Lung-on-a-chip: the future of respiratory disease models and pharmacological studies. *Critical Reviews in Biotechnology*, 40(2):213–230, 2020. ISSN 15497801. doi: 10.1080/07388551.2019.1710458. URL <https://doi.org/10.1080/07388551.2019.1710458>.
- [65] Bruce M. Stanton and Bruce A. Koeppen. *Berne Levy physiology*. Mosby/Elsevier, Philadelphia, 6 edition, 2008. ISBN ISBN 978-0-323-04582-7.
- [66] Andreas O. Stucki, Janick D. Stucki, Sean R.R. Hall, Marcel Felder, Yves Mermoud, Ralph A. Schmid, Thomas Geiser, and Olivier T. Guenat. A lung-on-a-chip array with an integrated bio-inspired respiration mechanism. *Lab on a Chip*, 15(5):1302–1310, 2015. ISSN 14730189. doi: 10.1039/c4lc01252f.
- [67] A.O. Stucki, G. Raggi, S. Sigrist, P. Zamprogno, N. Schneider-Daum, C.-M. Lehr, H. Huwer, J.D. Stucki, N. Hobi, and O.T. Guenat. Lung-on-a-Chip: The interplay of primary human epithelial and endothelial cells improves the alveolar barrier function. *Toxicology Letters*, 295(2018):S67–S68, 2018. ISSN 03784274. doi: 10.1016/j.toxlet.2018.06.074.
- [68] Sinem Tas, Emil Rehnberg, Deniz A. Bölükbas, Jason P. Beech, Liora Nasi Kazado, Isak Svenningsson, Martin Arvidsson, Axel Sandberg, Kajsa A. Dahlgren, Alexander Edthofer, Anna Gustafsson, Hanna Isaksson, Jeffery A. Wood, Jonas O. Tegenfeldt, and Darcy E. Wagner. 3D printed lung on a chip device with a stretchable nanofibrous membrane for modeling ventilator induced lung injury. *bioRxiv*,

- page 2021.07.02.450873, 2021. URL <https://www.biorxiv.org/content/10.1101/2021.07.02.450873v1%0Ahttps://www.biorxiv.org/content/10.1101/2021.07.02.450873v1.abstract>.
- [69] Janna Tenenbaum-Katan, Arbel Artzy-Schnirman, Rami Fishler, Netanel Korin, and Josue Sznitman. Biomimetics of the pulmonary environment in vitro: A microfluidics perspective. *Biomicrofluidics*, 12 (042209), 2018. ISSN 19321058. doi: 10.1063/1.5023034.
  - [70] John A. Terrell, Curtis G. Jones, Giraso Keza Monia Kabandana, and Chengpeng Chen. From cells-on-a-chip to organs-on-a-chip: Scaffolding materials for 3D cell culture in microfluidics. *Journal of Materials Chemistry B*, 8(31):6667–6685, 2020. ISSN 20507518. doi: 10.1039/d0tb00718h.
  - [71] Xianfeng Wang, Bin Ding, and Bingyun Li. Biomimetic electrospun nanofibrous structures for tissue engineering. *Materials Today*, 16(6):229–241, 2013. ISSN 1369-7021. doi: 10.1016/j.mattod.2013.06.005. URL <http://dx.doi.org/10.1016/j.mattod.2013.06.005>.
  - [72] T J Webster, A A Patel, M N Rahaman, and B Sonny Bal. Anti-infective and osteointegration properties of silicon nitride , poly ( ether ether ketone ), and titanium implants. *Acta Biomaterialia*, 8(12):4447–4454, 2012. ISSN 1742-7061. doi: 10.1016/j.actbio.2012.07.038. URL <http://dx.doi.org/10.1016/j.actbio.2012.07.038>.
  - [73] Douglas B. Weibel, Willow R. DiLuzio, and George M. Whitesides. Microfabrication meets microbiology. *Nature Reviews Microbiology*, 5(3):209–218, 2007. ISSN 17401526. doi: 10.1038/nrmicro1616.
  - [74] Cong Xu, Min Zhang, Wenwen Chen, Lei Jiang, Chunying Chen, and Jianhua Qin. Assessment of Air Pollutant PM2.5 Pulmonary Exposure Using a 3D Lung-on-Chip Model. *ACS Biomaterials Science and Engineering*, 6(5):3081–3090, 2020. ISSN 23739878. doi: 10.1021/acsbomaterials.0c00221.
  - [75] Zhiyun Xu, Encheng Li, Zhe Guo, Ruofei Yu, Hualong Hao, Yitong Xu, Zhao Sun, Xiancheng Li, Jianxin Lyu, and Qi Wang. Design and Construction of a Multi-Organ Microfluidic Chip Mimicking the in vivo Microenvironment of Lung Cancer Metastasis. *ACS Applied Materials and Interfaces*, 8(39):25840–25847, 2016. ISSN 19448252. doi: 10.1021/acsam.6b08746.
  - [76] Xingyuan Yang, Kaiyan Li, Xu Zhang, Chang Liu, Bingkun Guo, Weijia Wen, and Xinghua Gao. Nanofiber membrane supported lung-on-a-chip microdevice for anti-cancer drug testing. *Lab on a Chip*, 18(3): 486–495, 2018. ISSN 14730189. doi: 10.1039/c7lc01224a.
  - [77] Pauline Zamprogno, Giuditta Thoma, Veronika Cencen, Dario Ferrari, Barbara Putz, Johann Michler, Georg E. Fantner, and Olivier T. Guenat. Mechanical Properties of Soft Biological Membranes for Organ-on-a-Chip Assessed by Bulge Test and AFM. *ACS Biomaterials Science and Engineering*, 2021. ISSN 23739878. doi: 10.1021/acsbomaterials.0c00515.
  - [78] Pauline Zamprogno, Simon Wüthrich, Sven Achenbach, Giuditta Thoma, Janick D. Stucki, Nina Hobi, Nicole Schneider-Daum, Claus Michael Lehr, Hanno Huwer, Thomas Geiser, Ralph A. Schmid, and Olivier T. Guenat. Second-generation lung-on-a-chip with an array of stretchable alveoli made with a biological membrane. *Communications Biology*, 4(1):1–10, 2021. ISSN 23993642. doi: 10.1038/s42003-021-01695-0. URL <http://dx.doi.org/10.1038/s42003-021-01695-0>.
  - [79] Boyang Zhang, Miles Montgomery, M Dean Chamberlain, Shinichiro Ogawa, Anastasia Korolj, Aric Pahnke, Laura A Wells, Stéphane Massé, Jihye Kim, Abdulah Momen, Sara S Nunes, Aaron Wheeler, Kumaraswamy Nanthakumar, Gordon Keller, Michael V Sefton, and Milica Radisic. Biodegradable scaffold with built-in vasculature for organ-on-a- chip engineering and direct surgical anastomosis. *Nat Mater.*, 15(6):669–678, 2016. doi: 10.1038/nmat4570.Biodegradable.
  - [80] Fan Zhang and Martin W. King. Biodegradable Polymers as the Pivotal Player in the Design of Tissue Engineering Scaffolds. *Advanced Healthcare Materials*, 9(13):1–22, 2020. ISSN 21922659. doi: 10.1002/adhm.201901358.
  - [81] Min Zhang, Cong Xu, Lei Jiang, and Jianhua Qin. A 3D human lung-on-a-chip model for nanotoxicity testing. *Toxicology Research*, 7:1048–1060, 2018. ISSN 2045-4538. doi: 10.1039/c8tx00156a. URL <http://dx.doi.org/10.1039/c8tx00156a>.

- 
- [82] Hua Zhou, Hongxia Wang, Haitao Niu, and Tong Lin. Electrospun Fibrous Membranes with Super-large-strain Electric Superhydrophobicity. *Scientific Reports*, 5:1–9, 2015. ISSN 20452322. doi: 10.1038/srep15863.





